Role of secondary flows on flow separation induced by shock/boundary layer interaction in supersonic inlets

by

Rohan Morajkar

A dissertation submitted in partial fulfillment
of the requirements for the degree of
Doctor of Philosophy
(Aerospace Engineering)
in the University of Michigan
2017

Doctoral Committee:

Assistant Professor Mirko Gamba, Chair
Dr. John A. Benek , Wright-Patterson Air Force Base
Professor Steven L. Ceccio
Professor James F. Driscoll
Assistant Professor Karthik Duraisamy

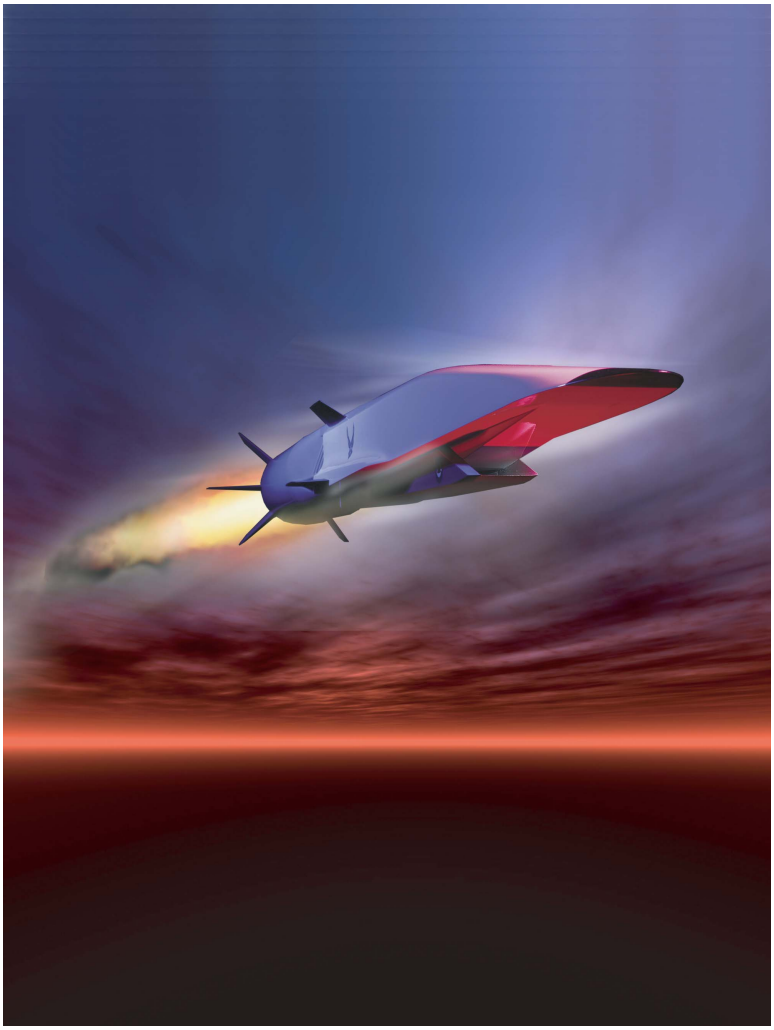

Rohan Morajkar
rohanrm@umich.edu
ORCID id: 0000-0003-3278-4471

Nothing is true, everything is permitted.

ACKNOWLEDGEMNTS

This work was made possible by a collective effort of countless individuals. Primarily I would like to extend my deepest thanks to my advisors Dr. Mirko Gamba and Dr. James Driscoll, thanks a lot for accepting me in your research group and providing me guidance throughout the process. I'm extremely grateful for your mentorship. Both of you have shaped my mind in a way I could have only hoped for. I particularly would like to thank Dr. Mirko Gamba for mentoring me, bestowing me with your knowledge and putting up an effort towards understanding my thoughts even in your many competing priorities; thank you and I wouldn't have done it without your guidance. You are a fantastic mentor and a sincere person and I have learnt a lot from you during these five years and I hope I can live up to the high standards set by you. I would like to thank my committee members, Dr. Karthik Duraisamy, Dr. Steven Ceccio and Dr. John Benek for their questions and enlightening discussions throughout the process. I would also like to thank Dr. John Benek towards partially funding my research.

Research work at the aerospace engineering department can never be conducted without the dedicated effort of the technical and office staff who keep the gears of the watch turning behind the scenes. My sincere thanks to Denise Phelps for her positivity and taking care of all important paper work. I also would like to thanks you for always letting me in my office every time I locked myself out which has happened countless times. Thanks to Kristin Parrish and Julie Power for taking care of all our purchase orders and reimbursements. Thanks to the excellent aero technical staff, Tom Griffin, Terry Larrow, Chris Chartier, Dave McClean, Late Martin Stenzel and Aaron Borgman without whom experimental work at FXB is impossible. Also thank you guys for allowing me to borrow (steal) tools, bolts, computer parts etc. from you when I needed them most. Thanks to Terry for making my drawings see reality. You make some of the most beautiful parts.

To all my teachers from my very first teacher Lakhshmi Viswanathan who taught me to read, write and think to my professors in undergraduate institute (National Institute of Technology, Nagpur, India) especially, Prof. Hemant Thorat, Prof. Animesh Chatterjee, Prof. Pramod Padole, Prof. Ashwin Dhoble and many others who took care of my professional development I dedicate this thesis to you for having laid the foundation of my personal development.

To all my friends in FXB, I'm fortunate to have walked the path with you. You guys have been one of the most important part of these five years. I would like to thank my partner in crime Robin Hunt for always having my back, it was a pleasure working with you. I also would like to extend my thanks to fellow experimentalists Senator Fabian Chacon, Padawan Jacob France, Logan White, Yasin Abul-Huda, Tim Wabel, Aaron Skiba and the younglings James Duvall and Louis Edelman

and wish you all the best through your journey. Thanks a lot for making experiments a lot more fun than they would have been if I was alone. To my late friend Abhinav Dasari, I thank you for always being there for us, for making sure all safety protocols of the lab were followed as well as keeping the lab organized apart from excelling in your research. We lost a really brilliant researcher, kind-hearted and hard working person. I would also like to thank my predecessor on the project Dr. Ethan Eagle for providing a foundation and direction to my research a. My fellow FXBers and their SOs, Yukiko Shimizu, Steve Kast, Doreen fan, Kai Ding, Chris Marley, Mr. President Chukwuka Mbagwu, Nicholas Anthiah Wolfgang Arnold-Medabalimi, Jungyeoul Maeng, Wai Li Chan, Yunta Chen, Kentaro Hara, Samuel Chen, Horatiu Dragnea, Devina Sanjaya, Brittany Essink, Daniil Adrienko and others whom I missed, thank you for making my experience at University of Michigan a memorable one. It won't have been the same without you guys. My office mates Maria Lang, Lori Groo, Astrid Raisanen and Kevin Neitzel, thanks a lot for bearing with me for all these years.

To my Martial arts friends at the Michigan Bujinkan Ninjutsu dojo, it was an honor training and fighting amongst you. My Sensei, Dr. Michael Z. Asuncion, thanks a lot for being my mentor outside of the academia. My seniors Gary Ciarkowski, Jay Zimmerman, Derek Arciniaga, Andy Dempz, Shweta Asuncion, Michael Bradbury and Sensei Michael Asuncion, thank you for showing me the path towards developing a good skill, martial spirit and an immovable heart. Also thank you for toughening me up. I will always strive to move forward in a direction you have led me. My training partners, Will Walker, Peter Wloszek, Rob Taylor, thank you for providing me a conduit for destressing. I had a lot of fun with you guys. To the Michigan dojo, I would not have done this without you, thank you for teaching me to not only face insanity but to thrive in it without letting it affect me.

To my imaginary friends, the CIA information extractor and the frat house throwing ice cream parties, thanks a lot for providing me an insight into understanding my research problem.

To all my roommates, previous roommates, nemesii, arch-nemesii and all other friends, Mayur Birla, Aditya Tayade, Tejas Pant, Kunal Javali, Neerad Phansalkar, Saumil Wagle, Krithika Swaminathan, Jhanani Selvakumar, Neel Desai, Subbuman, Priyank Ram, Shruti Bhave, Aunnasha Sengupta, Swaraaj Sankar, Teja Khetineni, Ritwika Banerjee, Shravya Reddy, Bharadwaj Mantha, Chirayu Chaudhari, Shrirang Deshpande, Bhavik Chauhan, Nikhil Bhosale, and many more, I have awesome friends. I really enjoyed those random weekend roadtrips, the destination of which was decided on reaching a destination. You guys made my stay in Ann Arbor a lot more fun than what it would have been. To my flight instructor Eric Taylor, thanks a lot for helping me get my

private pilot license and enjoy the freedoms of flying.

To my late Grand Parents who raised me, thank you for looking after me, developing me and making me the person I'm today. To my parents without whom I would never have done any of this, thanks a lot for having my back and letting me focus on what I like to do without having to worry about many other things.

To the human society, for giving me an opportunity to learn and grow at two of the finest institutes of excellence, I owe the society a debt which I will never be able to repay. For this I shall put to use the knowledge gained in these institutes towards a betterment of the world.

This thesis belongs to you all as much as it belongs to me. It was an honor to know and grow with you all and I can only imagine what life without you all would have been. Thank you for being there for me.

TABLE OF CONTENTS

LIST OF FIGURES

LIST OF TABLES

LIST OF APPENDICES

LIST OF ABBREVIATIONS

SBLI Shock Boundary Layer Interactions

PIV Particle Image Velocimetry

PLS Planar Laser Scattering

CCD Charge Couple Device

SPIV Stereo Particle Image Velocimetry

TDM Triple Decomposition of Motion

RMS Root Mean Squared

RANS Reynolds Averaged Navier Stokes

AVT Axial Velocity Thresholding

PDF Probability Density Function

PRF Probability of reverse flow

DNS Direct Numerical Simulation

LES Large Eddy Simulation

PTU Programmable Timing Unit

FFT Fast Fourier Transform

CVCCS Corner Vortex Centric Coordinate System

POD Proper Orthogonal Decomposition

ABSTRACT

Role of secondary flows on flow separation induced by shock/boundary layer interaction in supersonic inlets

by

Rohan Morajkar

Chair: Mirko Gamba

Flow separation in the scramjet air intakes is one of the reasons of failure of these engines which rely on shock waves to achieve flow compression. The shock waves interact with the boundary layers (Shock/ Boundary Layer Interaction or SBLI) on the intake walls inducing adverse pressure gradients causing flow separation.

In this experimental study we investigate the role of secondary flows associated with the corners of ducted flows and identify the mechanisms by which they affect flow separation induced by a shock wave interacting with the boundary layers developing along supersonic inlets. The coupling between flow three-dimensionality, shock waves and secondary flows is in fact a key aspect that limits the performance and control of supersonic inlets. The study is conducted at the University of Michigan Glass Supersonic Wind Tunnel (GSWT). This facility replicates some of the features of the three-dimensional (3D) flow-field in a low aspect ratio supersonic inlet. The study

uses stereoscopic particle image velocimetry (SPIV) to measure the three-component (3C) velocity field on several orthogonal planes, and thus allows us to identify the length scales of separation, its locations and statistical properties. Furthermore, these measurements allow us to extract the 3D structure of the underlying vortical features, which are important in determining the overall structure of separated regions and their dynamics. The measurements and tools developed are used to study flow fields of three cases: (1) Moderately strong SBLI (Mach 2.75 with 6° deflection), (2) weak SBLI (Mach 2.75 with 4.6° deflection) and (3) secondary corner flows in empty channels.

In the configuration of the initial work (moderately strong SBLI), the shock wave system interacts with the boundary layers on the sidewall and the floor of the duct (inlet), thus generating both a swept-shock and an incident-shock interactions. Furthermore, the swept-shock interaction taking place on the sidewalls interacts with the secondary flows in the corners of the tunnel, which are prone to separation. This interaction causes major flow separation on the sidewall as fluid is swept from the sidewall. Flow separation on the floor should be expected given the strength of the SBLI (moderately strong case), but it is instead not observed in the mean flow fields. Our hypothesis is that interacting secondary flows are one of the factors responsible for the sidewall separation and directing the incoming flow towards the center-plane to stabilize and energize the flow on the center of the duct, thus preventing or at least reducing, flow separation on the floor.

The secondary flows in an empty tunnel are then investigated to study their evolution and effects on the primary flow field to identify potential separation sites. The results from the empty tunnel experiments are then used to predict locations of flow separations in the moderately strong and weak SBLIs. The predictions were found to be in agreement with the observations.

CHAPTER 1

Introduction and Background

This work builds upon previous studies by Eagle [6] on full span highly three dimensional coupled Shock Wave / Boundary Layer Interaction (SBLI) generated by a an incident shock wave in a Mach 2.75 low-aspect ratio (approximately 1 : 1.9) duct flow. By linking SPIV measurements and oil flow pattern through critical point theory and secondary flow separation concepts, the work by Eagle [6] identifies the complexity of a 3D SBLI interaction as the interplay between a complex vortical system, that includes the corner vortex system, the vortex associated with swept SBLI and the vortex systems generated by the incident oblique SBLI on the bottom wall. The importance of corner flows on the properties of a normal SBLI was also identified by Bruce et al. [13] who identified how corner flow may affect centerline separation; an effect that was later confirmed and quantified by the computational studies of Benek et al. [14]. Although these previous works provide an initial view of 3D SBLI, they do not quantify secondary flows and their role on 3D interactions. For example,

- Most of the previous work falls short of quantifying the effects of the secondary flows towards generating flow separations and the relative strengths of various unit problems comprising the SBLI studied and describing the underlying mechanisms responsible for flow separations and configuration of the vortex structure observed.

- The interaction between the shock and the corner vortex on the sidewall was not studied and

it is this interaction that was found to produce the strongest flow separation in our studies [15].

- None of the previous works describe or quantify the baseline flow field that would exist in an undisturbed rectangular duct and the effects of this underlying flow field in governing the SBLI structure (primarily the flow separation).

These are critical gaps in the understanding of these problems that is addressed in this work. Specifically, the objectives of this thesis is to provide an in depth and quantitative description of the three-dimensionality and regions of flow separation in the 3D SBLI, as well as to quantify secondary flows in supersonic duct flows and how they affect the SBLI and flow separation.

In order to achieve this, Stereo Particle Imaging Velocimetry (SPIV) was applied to obtain all the components of velocity in the region surrounding the interaction to obtain flow fields along three orthogonally oriented planes. Validated dataset was then analyzed to obtain the 3D flow structure of the SBLI, large-scale vortex structure and a flow separation structure. The dynamics between the shock/ boundary layer interaction on the sidewall and the tunnel floor have been studied. It was found that the shock wave interaction with the corner secondary flows produces the strongest flow separation, which established the importance of the corner secondary flows. High resolution SPIV measurements were then conducted to study the effects of the corner secondary flows on the primary flows and the streamwise evolution of the secondary flows. The understanding gained from studying the empty tunnel corner flows helped in identifying the weak spots prone to flow separation in a flow field associated with a rectangular duct. These spots were found to be separated when a SBLI was introduced in the wind tunnel. Although some of the findings (for example the exact structure of the corner flows) might be specific to the wind tunnel used in the study, the relationship between vortical structure and propensity to flow separation when a shock wave is present are believed to be effects of a certain degree of generality.

1.1 Motivation

Understanding Shock wave/ Boundary Layer Interactions (SBLI) is of paramount importance if the Air Force's vision for having a long range strike craft operating within the regime of SCRAMJET (Supersonic Combustion Ramjet) engine is to be realized. Technology demonstrator programs like the X-51 waverider have been commissioned to explore the feasibility of this technology. One of the experiments of the X-51 program ended up in failure that was attributed to engine unstart, the process whereupon a shock propagates through the inlet and ends up outside the engine vastly reducing the airflow to combustor. This clearly demonstrates a need for better understanding of the complex inlet fluid dynamics in a scramjet. The phenomenon of engine unstart is primarily caused by blockage associated with flow separation in the inlet caused by adverse pressure gradients due to SBLI [16], boundary layer thickening and a complex vortical phenomena that are a focus of this thesis. Apart from internal flows confined within the engine air intakes, SBLIs are ubiquitous in most of the supersonic flows over surfaces like the wings of supersonic/transonic aircrafts or rocket nozzles, which makes understanding the flow physics associated with them of great significance.

Until recently SBLIs have been considered and treated as a two dimensional phenomena with relatively less attention being paid to the sidewalls and the inlet corner effects. Most of the computational/theoretical studies have considered symmetry or a two dimensional centerline flow-field while the experimental studies have focused on centerline flows in wide wind tunnels with large aspect ratios that are far from resembling realistic engine inlets like that of X-51, concorde or a supersonic combat aircraft.

This thesis primarily treats SBLI as a 3 dimensional phenomenon in its entirety. SBLI is studied in the Michigan Glass wind tunnel facility that has been described and characterized in great detail by Lapsa and Dahm [17]. The technique of Stereo Particle Image Velocimetry (SPIV) which allows us to study the secondary flows inclusively with the primary flow patterns in uncorrelated instances

has been used to study the SBLI and empty tunnel corner flows.

1.2 Shock Boundary Layer Interactions (SBLI)

The first experimental observation of SBLI was conducted back in 1940 by Antonio Ferri [18] on a wing profile in a supersonic wind tunnel. Using striometric visualizations and pressure measurements he was able to establish the importance of viscosity in the supersonic regime. During the early days of SBLI research, qualitative techniques like oil flow visualization, shadowgraphy and schlieren were used along with pressure measurements (pitot and wall) and hot wire anemometry for quantitative measurements. However due to the nature of SBLI flows, using intrusive techniques like pitot-static tube traversing and hot wire anemometry poses a challenge as these intrusions themselves cause shock waves that can influence the problem being studied by altering the flow in the vicinity of measurement. J. Green [19] conducted experiments using schlieren, oil flow visualizations and pressure measurements on oblique reflected SBLI at different shock strength (deflection angles). Green reported that as the shock strength increases, the reflected wave structure changes from a single shock to a compression fan followed by a compression fan embedded in which is an expansion fan. Green attributed the event of transition to onset of separation. From oil flow observations, Green also proposed a mechanism in which low momentum air is swept down the sidewall into the corner and towards the supposedly two dimensional interaction on the bottom wall. Thus indirectly, Green originally proposed the sidewall influence on the bottom wall interaction. However he did not report any effects on the two dimensionality. Settles et al. [20] conducted similar study (experimental and computational comparison) on compression ramps at Mach 2.85 for different deflection angles. They observed the transition of the SBLI from being completely attached at weaker angles (8°) through being incipiently separated at 16° to being fully separated at stronger angles (20° and 24°). It was noted that the computational solutions showed good agreement when the corner flow is not separated. Free interaction concept originally pro-

posed by Chapman et al. [21] was also investigated. The concept states that the viscous-inviscid interaction up to a point of boundary layer separation is independent of the downstream device which causes the interaction.

Since then tremendous advancements have been made in understanding and predicting the complex flow physics characterizing the SBLIs. However most of the theoretical advancements in understanding the SBLI problem have been towards two dimensional interactions. The physics of each unit problem in an unconfined configuration (2 dimensional problems of compression ramp and incident oblique SBLIs) have been extensively studied by researchers such as Adamson and Messiter [22], Korkegi [23], Zheltovodov [24], Dolling and Clemens [25] and Delery and Dussauge [26]. Adamson and Messiter [22] reviewed first attempts at simulating SBLIs using Reynolds Averaged Navier Stokes (RANS) equations with zero-, one and two-equation turbulence models to address the closure problem. It was concluded that one and two equation models could be fine-tuned in case of weak SBLIs with attached flow, however these were not universal results. Numerous review articles on the same interactions have also been published [27–29].

Traditionally the problem of SBLI has been divided primarily into various types of unit problems: 1) External Interaction, 2) Ramp flow, 3) Oblique/Normal incident SBLI, 4) Swept SBLI and 5) Shock-corner flow interaction. Each of these problems have typically been studied in isolation.

1.2.1 External Interaction

Transonic flows over wings, often due to accelerations may lead to formation of shock waves that then interact with the boundary layers present over the airfoil. This phenomenon can cause a sudden drop in the wing performance characteristics like loss of lift increased drag and possibly lead to a stall if the flow separates because of the adverse pressure gradient induced by the shock wave.

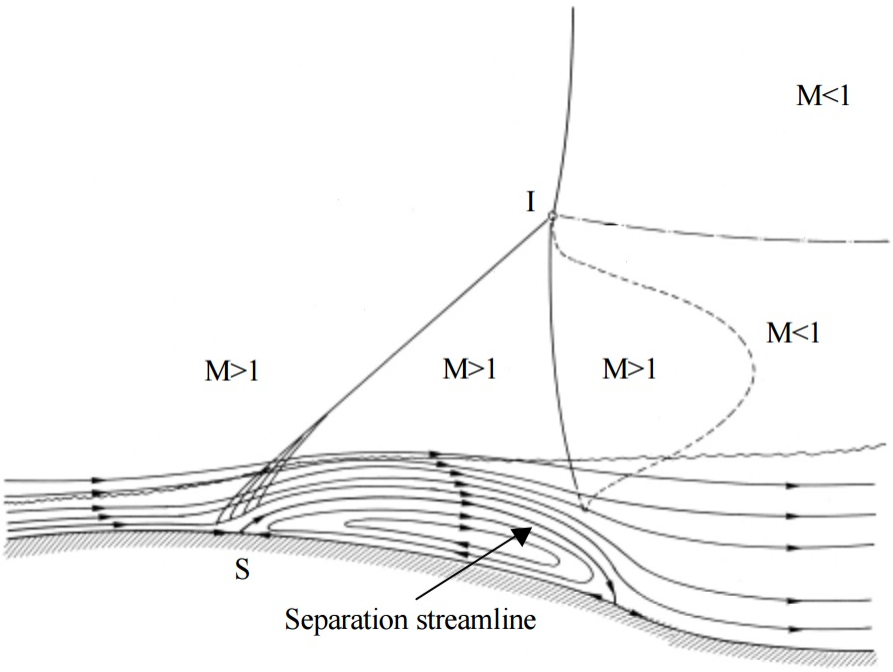

Figure 1.1: Structure of external SBLI, from Delery and Bur [1].

Figure 1.1 shows a schematic diagram of separated flow external SBLI. A normal shock away from the airfoil walls causes an adverse pressure gradient leading to flow separation. Point S is the separation point of the incoming flow. This results into a separation shock that is oblique with respect to the incoming flow, thus the flow behind the separation shock remains supersonic. The separation shock intersects the normal shock at point I causing a slip line ('- -') downstream of the intersection. The normal shock continues down the point I and is incident on the boundary layer around the region where the separated flow reattaches. The reader is referred to Delery and Bur [1] for further details.

1.2.2 Ramp Flow/ Compression Corner

A large portion of the SBLI literature is focused on this type of interaction. This type of study represents the type of flow field generated from supersonic flow interaction with control surfaces

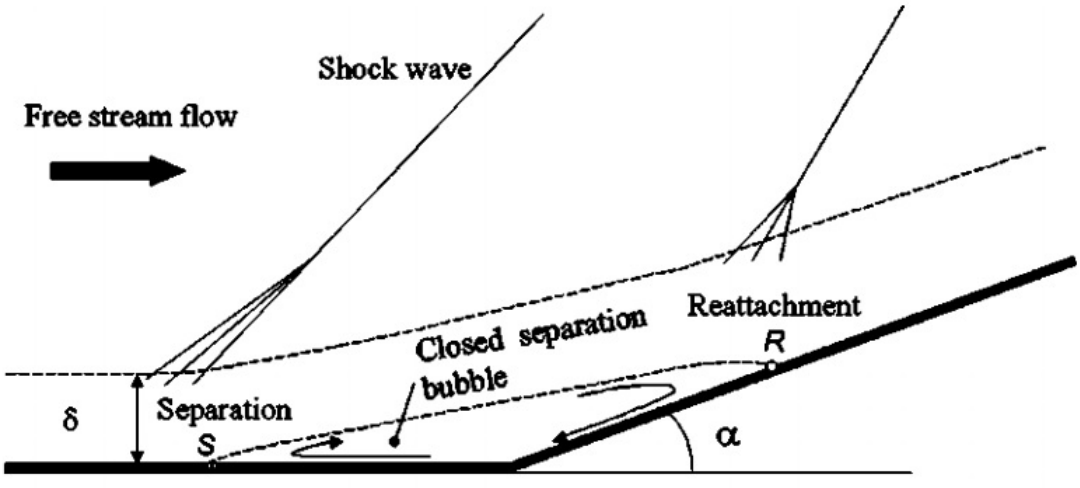

Figure 1.2: Structure of separated Ramp type SBLI, from Ostlund and Klingmann [2].

like ailerons, flaps, elevators etc. The reader is referred to studies conducted by Settles et al. [30], Martin group at Princeton [31–33] for further details of this type of interaction. Figure 1.2 (from Ostlund and Klingmann [2]) shows a SBLI case produced by an unswept, separated. The ramp causes a sudden change in the supersonic flow direction leading to formation of a shock wave and an associated pressure rise. A separation bubble may form depending on the Mach number and the inclination. In the case shown, point S is the separation point and the point R is the point of reattachment of the flow. A second shock wave is formed when the flow is turned parallel to the inclined wall as it reattaches. The two shock waves will intersect each other downstream of the corner formed resulting in a slip line similar to the one observed in external interaction.

1.2.3 Incident Oblique-Reflected Interaction

This type of interaction is representative of the flow pattern present within the air intakes of high speed aircraft engines (scramjets). These engines use the series of oblique shock waves to deceler-

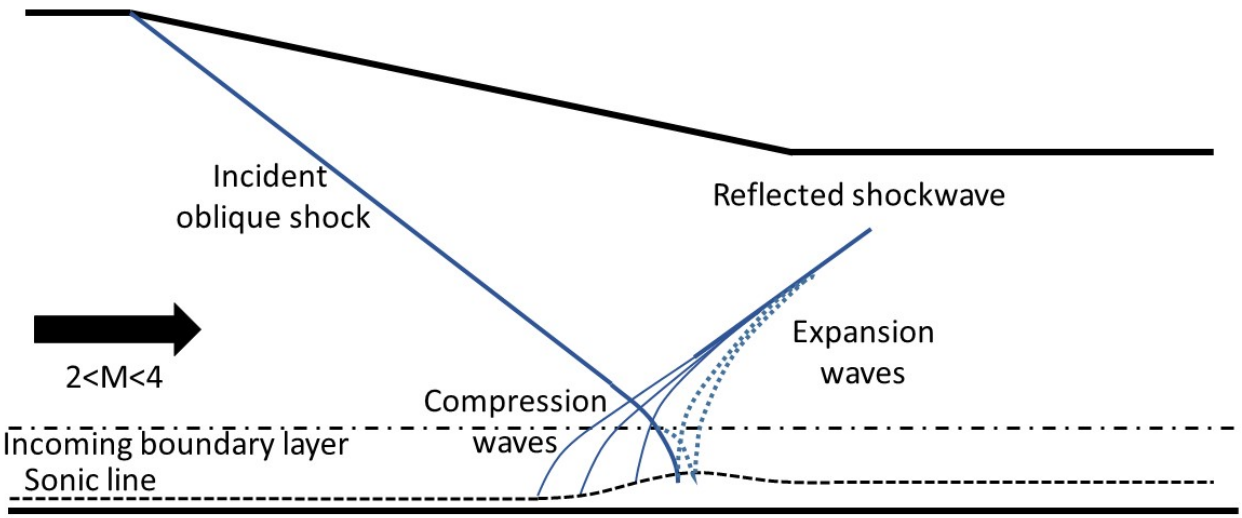

Figure 1.3: Structure of unseparated 2D incident SBLI.

ate and compress the incoming flow. The engine inlet must be carefully designed flow surfaces to minimize losses primarily caused by the SBLIs which can even be catastrophic as we have experienced in the case of X-51. Early reviews of this type of interaction have been done by Green [19], Hankey and Holden [34] and Adamson and Messiter [22].

Since this type of interaction is a part of the study presented here, it will be described in some detail. The physical description provided here is based on works by Babinsky and Harvey [27], Delery and Bur [1] and Delery and Marvin [35] and the reader is encouraged to refer to these publications for a more comprehensive review. An oblique shock wave impinging on a turbulent boundary layer may or may not cause a flow separation, which divides this type of interaction into two cases: Non-separated and Separated.

1.2.3.1 Unseparated Case

In this case the pressure gradient associated with the oblique incident shock wave is insufficient to cause a flow separation. A schematic of this type of interaction is shown in Figure 1.3.

As the shock wave penetrates the incoming turbulent boundary layer, the information of the adverse pressure gradient propagates upstream through the subsonic region (region bounded by the sonic line and the wall) near the wall. The pressure rise is therefore smeared upstream due to the viscous effects, which is termed as the upstream influence effect. The higher the turbulence of the incoming boundary layer, greater is the mixing leading to a thinner sonic region and weaker upstream influence effect. The adverse pressure gradient slows down the incoming flow causing a growth of subsonic region near the SBLI. This growth causes the streamlines above to be diverted away from the wall causing compression waves which coalesce into a reflected shock downstream. As the incident shock wave penetrates deeper into the boundary layer it weakens due to the slower flow and weaker pressure gradient caused by the upstream compression waves. The weakening causes the incident shock to spread as compression waves which are reflected from the free surface of sonic line as expansion waves. As the sub boundary layer flow progresses through the expansion waves, it accelerates leading to a recovery process and contraction of subsonic region. The interaction outside of the boundary layer in this case resembles an inviscid solution.

1.2.3.2 Separated Case

In this case the pressure gradient imposed by the incident shock wave is sufficiently strong to cause a flow separation. The resultant flow field is shown in Figure 1.4 As the incoming boundary layer encounters the SBLI, the strong adverse pressure gradient causes low momentum layers near the wall to turn upstream causing flow separation. Similar to the unseparated case, the subsonic region thickens in this case along with the boundary layer. The flow upstream of the thickening region turns away from the wall causing compression waves that coalesce into a reflected shock.

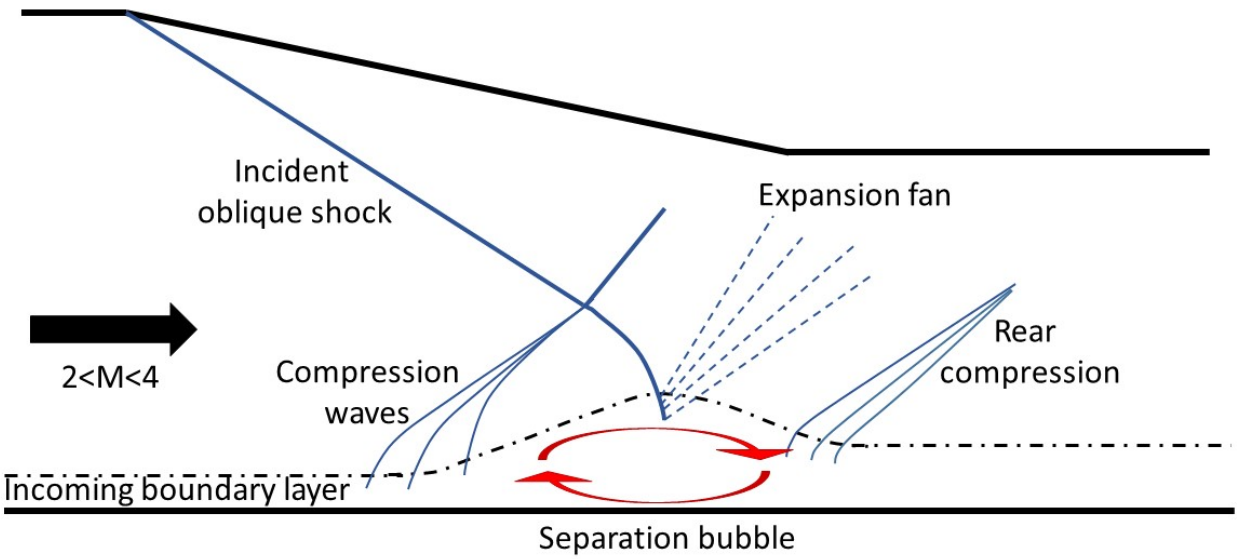

Figure 1.4: Structure of separated 2D incident SBLI.

Generally the compression waves coalesce into a reflected shock upstream of the incident shock causing the reflected shock to intersect the incident shock, and resulting in a slip line (not shown) which propagates downstream.

At the point of separation, the incoming boundary layer detaches to form a separated shear layer, just upstream of the separation bubble. The separated shear layer then encounters the incident shock causing it to weaken as it penetrates into a lower Mach number fluid. The weakening shock finally reflects as expansion waves as it hits the sonic line. As the separated shear layer passes through these expansion waves it accelerates and turns towards the wall and finally reattaches downstream of the separation bubble. The subsequent turning of the flow parallel to the wall leads to a series of compression waves that coalesce into a reattachment shock. Thus, a separated case of reflected SBLI will be characterized by three pressure jumps viz: incident shock, reflected shock and reattachment shock. The flow then undergoes a recovery process. However unlike the non-separated case, the flow doesn't conform to an inviscid solution.

1.2.4 Swept SBLI/ Fin Type Interaction

The three dimensional unit problem of swept SBLI, which will be encountered and studied in this work, has been studied by Alvi and Settles [4], Kubota and Stollery [3], Lu [36], Panaras et al. [37] and Knight et al [38]. All of these studies agree on the curved nature of the swept shock and the vortex structure that lies behind the curved part of the shock as shown in Figure 1.5. The general 2D structure (Figure 1.5b) away from the fin is similar to that of an external SBLI. The flow field is characterized by a vortex structure bounded by the shock foot and the walls that grows downstream producing a quasi-conical interaction structure as shown in Figure 1.5a. Due to the quasi-conical symmetry, the natural co-ordinates of choice would be spherical polar (r,β,ϕ) centered at the virtual conical origin, which is a point where various topological features of the interaction (upstream influence line, separation line and attachment line) converge. From the definition of conical flow, it follows that the r-direction is degenerate since conical flow properties are constant in r. Thus the flowfield associated with such an interaction can be considered 2D and completely represented by angular co-ordinates (β,ϕ). The separation associated with the swept SBLI was recently studied by Dou et al. [39]. It was found that the wall limiting streamlines behind the shock wave align themselves with a line from the virtual conical origin as the shock strength increases. An incipient separation bubble forms when the wall limiting streamline becomes perpendicular to the local pressure gradient.

A vortex is observed which is a result of the transverse gradients arising due to the curved nature of the swept shock giving rise to the three dimensionality of this particular type of interaction. Korkegi [40] suggested a correlation for determining whether a given case of Mach number and flow deflection angle due to the shock would produce incipient separation on the sidewall ($M\theta > 0.3^c$). The correlation was later reaffirmed by Dann and Morgan [41]. Recent works [6, 15] are conducted for a case just at the brink of incipient separation due to the swept shock as per Korkegis correlation. The study conducted as a part of this thesis is done at an incipient case and a weak

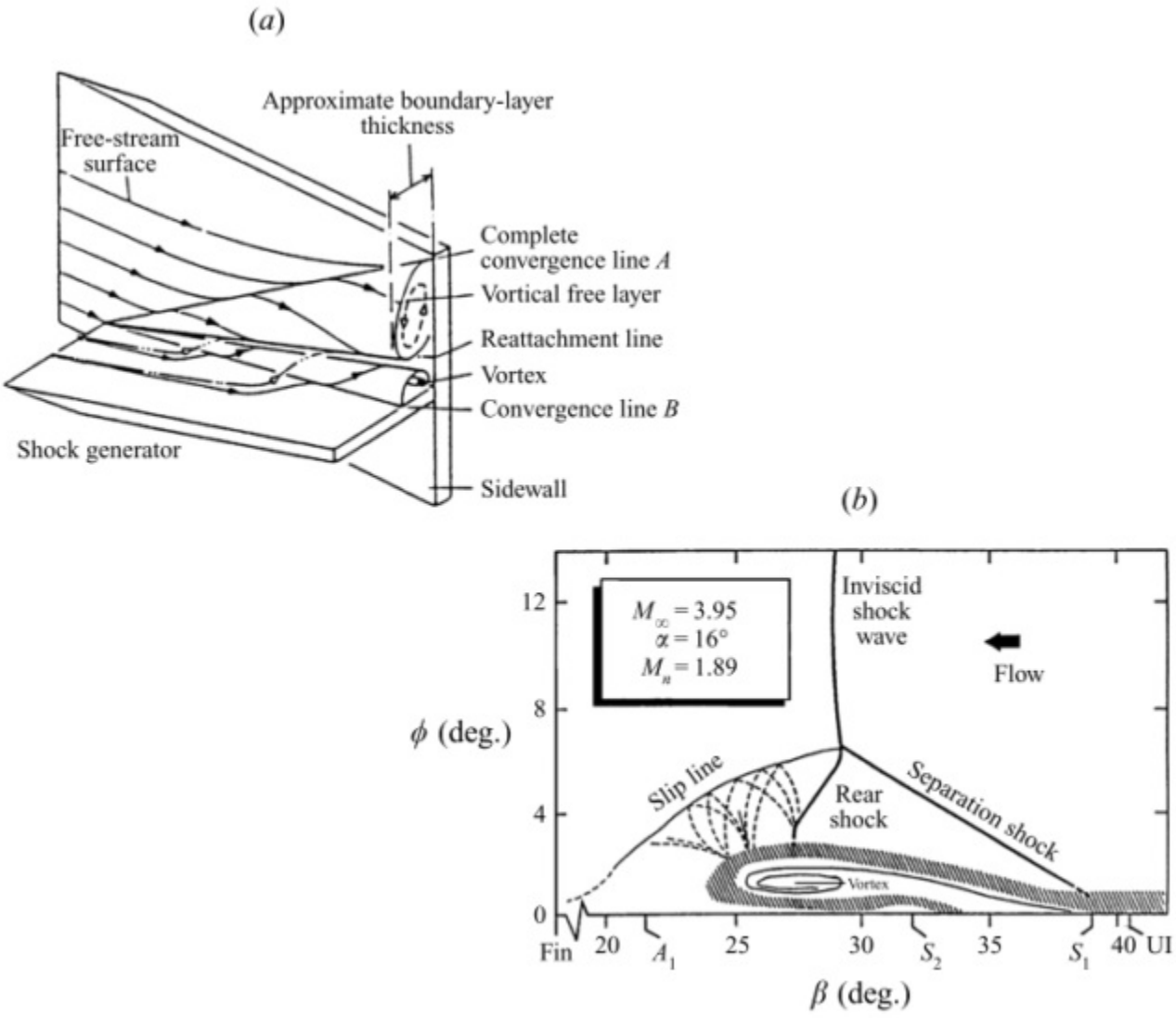

Figure 1.5: Structure of 3D fin-plate/swept SBLI: a: 3D model by Kubota and Stollery [3] b: 2D cross-section orthogonal to the shock from Alvi and Settles [4].

interaction case and the relative locations of these cases with respect to the Korkegii's correlation are shown in Figure 1.9.

1.2.5 SBLI Unsteadiness

SBLI systems are known to be unsteady as has been qualitatively observed by Bogdonoff [42] and Chapman et al. [21]. Kistler's [43] experiments in studying the fluctuating wall pressures under the separated supersonic over a forward facing step indicated a presence of low frequency unsteadiness associated with the shock. The source of this unsteadiness has been sourced to mechanisms driven by flow structures both upstream and downstream of the interaction. Dolling and Or [44] studied the shock foot unsteadiness over compression ramps using pressure measurements. They observed large pressure fluctuations at the separation and reattachment points as well as the intermittent region under the shock structure. The power spectra of the pressure fluctuations uncovered that the frequencies couple of orders of magnitudes lower than the characteristic frequency of the boundary layer had a significant contribution to the unsteadiness in the intermittent region. Beresh et al. [45] used PIV measurements coupled with pressure readings to show that the downstream motion of shock wave is associated with instantaneous packets of fuller velocity profiles and vice versa. Ganapathisubramani et al. [46] used PIV and Planar Laser Scattering (PLS) techniques and discovered streamwise elongated coherent structures of uniform momentum in the incoming boundary layer at Mach 2 greater than 40δ where δ is the boundary layer thickness. The frequency of the shock foot oscillations correlated well with the characteristic frequency of these coherent structures. A study by Erengil and Dolling [47] found only weak correlation between incoming boundary layer and shock motion. They argued that large streamwise structures would be required in the incoming flow to cause the observed low frequency shock oscillation. Instead, they proposed that it was a low frequency disturbance associated with the downstream flow separation bubble that was responsible for the shock motion. Downstream mechanism associated with flow separation

bubble controlling shock foot association was also supported by Large Eddy Simulation (LES) by Touber and Sandham [48] and Hadjadj et. al. [49], Direct Numerical Simulation (DNS) of Dr. Martin's group [32, 33] as well as experimental studies by Dupont et al. [50] and Piponniau et. al. [51]. Souverein et. al. [52] experimentally studied oblique-reflected SBLI and observed that both upstream and downstream mechanisms were responsible for shock motion with stronger interactions being dominated by downstream mechanism. A comprehensive review of mechanisms responsible for shock unsteadiness was given by Clemens and Narayanaswamy [29].

1.2.6 3D SBLIs

It has been long known of the secondary flows that developed in a rectangular streamwise corner due to gradients in Reynolds stresses and the counter-rotating vortex pair associated with such a flow. Gessner et al. [53] and Davis et al. [7] outline characteristics of such a flow that will be studied in detail in chapter 4. However, relatively less in known about the effect of a swept shock incident on such a flowr. Reda and Murphy [54], Bruce and Babinsky [55], Burton and Babinsky [56] Eagle et al. [6,57], Benek et al. [58], Helmer et al. [59] established the importance of the sidewall in three-dimensional low-aspect-ratio duct flows, while Morgan et al. [60, 61] and Moreno et al. [62] used various CFD models to demonstrate the importance of the sidewalls. Reda and Murphy [54] were the first to note the separation as a result of interaction between the swept shock and the secondary corner flow. Once the SBLI was isolated from the sidewall effects, they observed a reduction in incipient separation pressures and reduction in the scale of separated flows. Batcho and Sullivan [5] conducted pressure, oil flow, local vapor screen and color schlieren measurements of a coupled 3D SBLI and successfully identified 3 vortex systems associated with different SBLI unit problems present in a full span compression corner type interaction. Their flow structure is shown in Figure 1.6. Doerffer and Dallmann [63] studied the effects of Reynolds number on asymmetry of the flow structure observed. They conducted pressure, schlieren and oil flow measurements on an

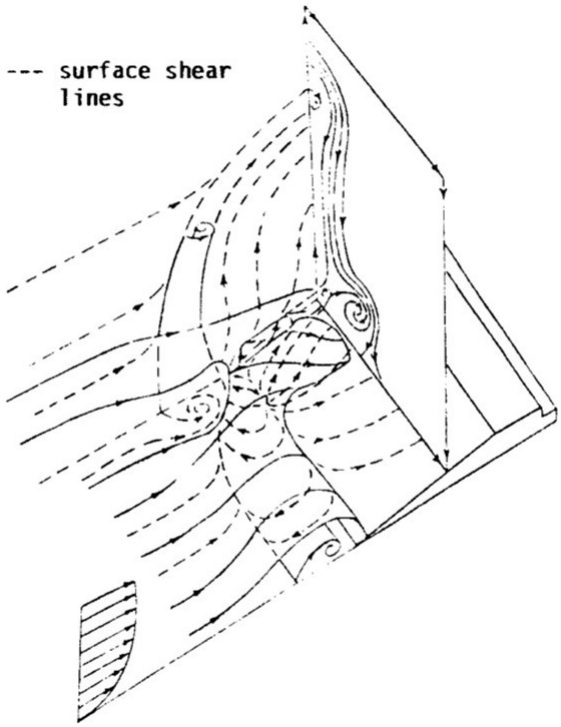

Figure 1.6: Coupled SBLI vortex structure of a full span compression corner, from Batcho and Sullivan [5].

experiment varying the incoming Reynolds number of a normal SBLI on a convex wall. A decrease in centerline separation length with an increase in Reynolds number was observed with a highly three dimensional flow field inside the separated zone. A sharp drop in coefficient of friction with an increase in static pressure was observed upstream of the flow separation. They observed increased asymmetry sourced from SBLI at higher Reynolds numbers.

Recently, Eagle et al. [64] and Morajkar et al. [15] used stereo-PIV to record a comprehensive database that includes the three components of velocity along 25 orthogonal measurement planes which was further analyzed as a part of this work. Their initial work [15] described a case that would be just at the brink of separation (case of Mach 2.75 and 6° deflection, see Figure 1.9) on the sidewall produce relatively strong separation on the sidewall which was primarily attributed to the interaction of the swept shock with the corner flow. Multiple studies describing the flow

structure resulting from the corners in SBLIs have been reported for various configurations such as those by Batcho and Sullivan [5], Cresci et al [65]. Doerffer and Dallmann [66] conducted experimental studies by varying Reynolds number (*Re*) of the flow and found that the flow structure or the layout of the vortices produced as a result of the interaction changes dramatically with *Re*. The vortices originating from near the corner or the sidewall which were inferred from the oil flow measurements were proposed to be the principal mechanism in determining the separation point on the centerline. It was also suggested that the shear layer roll up caused by multiple streamwise vortices (which have been detected in our work [15]) produced structural instability that led to asymmetries with increasing *Re*. However, no evidence of the 3D structure or the underlying mechanism responsible for such a behavior was presented. The role of corner interactions in generating flow asymmetries was further confirmed by Morris et al. [67] who observed that mass removal from the bottom wall boundary layer caused the sidewall/corner boundary layer to grow unstable and develop asymmetries. Bruce et al. [13] showed both experimentally and computationally the development of asymmetries in the case the opposite corner flows grow large enough to interact with each other. However, none of these studies propose a mechanism for the cause of such asymmetries. Perhaps the vortices originating from the opposite corner interactions come in close proximity and produce asymmetries. However in order to be certain a complete flow-field around the corner interaction is required to be studied which is the heart of this thesis.

Burton and Babinsky [56] and Bruce et al. [68] established the coupling of the corner/sidewall SBLI. They conditioned the corner of the incoming boundary layer without affecting the centerline boundary layer by adding corner vanes that eliminated the separation on the centerline, increased the corner separation and reduced the sidewall separation. Corner suction on the contrary produced increased separation on the centerline and sidewall whereas decreased the corner separation. They suggested that the corner separation bubble produced 3D compression waves that propagated towards the centerline and smeared the adverse pressure gradient. Another observation

put forth by them was that there was a channel of attached flow between the corner separation and centerline separation, which probably also lies in approximately the same region where one of the corner vortices was displaced to due to the corner SBLI as observed in our work [15]. However, most of these studies do not consider the role of the already present secondary corner vortices in providing possible explanations for the observed phenomena as it has been observed in our journal paper that the interaction between the swept shock and the corner vortices can produce major separation on the sidewall even though the correlation model proposed by Korkegi [23] suggests existence of a very weak separation. Benek et al. [58] conducted RANS CFD simulations using the code overflow for various parameters like aspect ratio, mach number and the flow deflection angle to ascertain the role of the corner interactions. It was found that three dimensionality can significantly influence separation parameters with respect to their equivalent 2D values. The hypothesis they propose is that compression waves originating at the corners result in reduction or elimination of centerline separation. This hypotheis was partially substantiated by the existence of compression waves detected in the RANS solutions although few cases resulted into stronger corner and centerline separation that contradicts the hypothesis. Perhaps another mechanism that acts as a communication link between the centerline and corner interaction regions is the vortex structure of the flow. The major disadvantage of their study is its inability to resolve secondary corner flows that have a major role to play in governing the global dynamics such as separation as seen in our work [15]. Recently Eagle and Driscoll [69] using SPIV and oil flow measurements presented a qualitative three dimensional picture of the structure of the coupled SBLI as shown in Figure 1.7. Their results highlighted the significance of secondary flows on global flow structure by proposing a vortex and separation structure of the flow field. The proposed flow structure also seemed to strengthen the hypothesis proposed by Burton and Babinsky [56] that the corner and bottom wall flow separations are linked by compression fans caused by boundary layer thickening resulting from sidewall/corner flow separations.

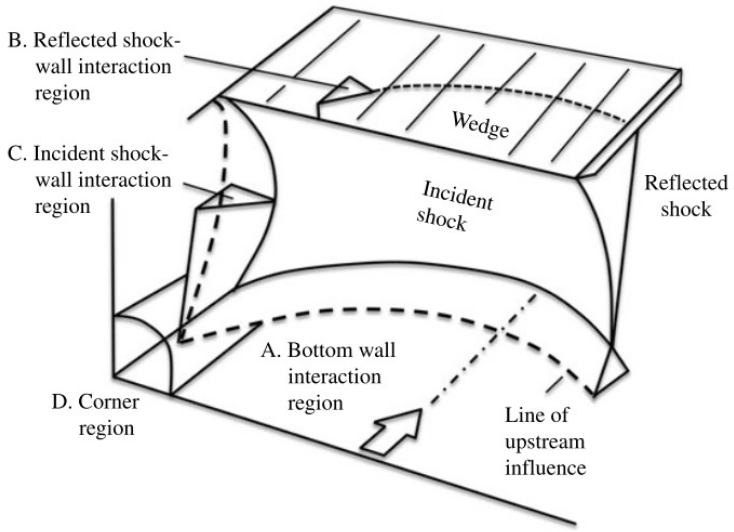

Figure 1.7: Coupled SBLI structure, from Eagle and Driscoll [6].

1.3 Corner Flows in Rectangular Ducts

The fluid flow that exists at the intersection of two walls is characterized by secondary motion, which is defined as flow motion due to velocity components normal to the principal flow direction. Ridha [70] published a review article describing many of the theoretical studies of the corner flow boundary layer that have been conducted. Rubin [71] initially developed an analytical model to describe the laminar corner flow. He divided the flow cross-section into 4 parts: the two boundary layers along the two walls forming the corner, the corner overlap between the boundary layers and the core flow. The terms of the Navier-Stokes (N-S) and boundary layer equations were then expanded into an infinite series and the constants matched up to second degree in order to match the values of various components of velocity that asymptote towards the core flow and in the boundary layer overlap region. He thus obtained a numerical solution describing the flow in the corner region.

Prandtl in 1952 formally divided the secondary flows into two categories: secondary flows of the first and second kinds, which have been further explained by Bradshaw [72]. Secondary flows of

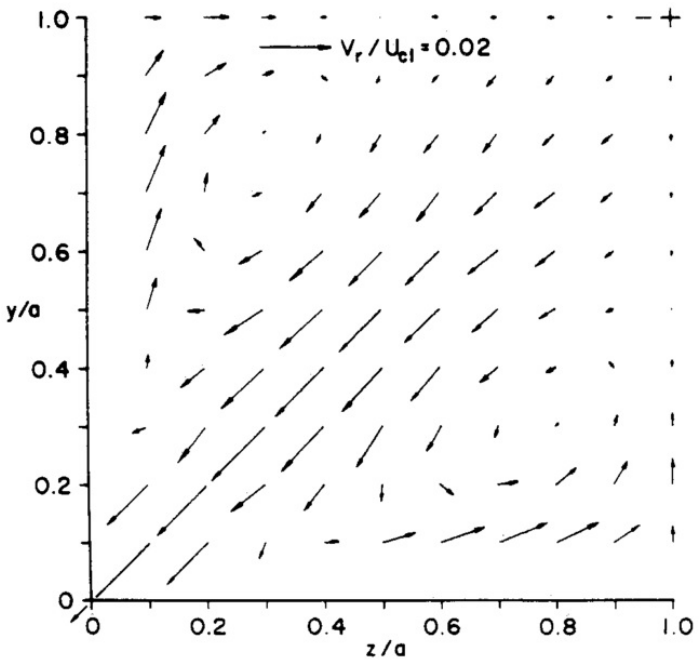

Figure 1.8: Proposed canonical corner secondary flow structure, from Davis and Gessner [7].

the first kind originate because of mean flow skewing (i.e., due to the tilting and stretching term in the vorticity equation), and are relatively well understood. However, much is to be known about secondary flows of the second kind, which are a result of anisotropic variations of Reynolds stresses [70, 73]. The streamwise corner flows that exist at the intersection of two surfaces intersecting in the principal flow direction fall into the second kind.

It is believed that secondary corner flows are characterized by streamwise vortices that arise due to the production of vorticity by Reynolds stresses. The pair of streamwise vortices that would exist in ideal symmetric flow conditions is shown in Figure 1.8.

Perkins [74] explains the formation of these vorticies from the (steady) x-vorticity conservation equation written after the Reynolds decomposition and averaging is performed; thus taking into

account the Reynolds stresses, the steady state vorticity equation can be written as:

$$U\frac{\partial \omega_x}{\partial x} + V\frac{\partial \omega_x}{\partial y} + W\frac{\partial \omega_x}{\partial z} = \nu\nabla^2\omega_x + \omega_x\frac{\partial U}{\partial x} + P1 + P2 + P3 + P4 \tag{1.1}$$

where the terms on the left-hand-side represent the convection of the streamwise component of vorticity (ω_x). The first two terms on the right-hand-side are the viscous diffusion and vortex stretching, respectively. The third term is

$$P1 = \omega_y\frac{\partial U}{\partial y} + \omega_z\frac{\partial U}{\partial z} \tag{1.2}$$

and describes the production of streamwise vorticity by skewing of the mean flow field and thus represents the secondary flow of the first kind. The fourth terms is

$$P2 = \frac{\partial}{\partial x}\left(\frac{\partial \overline{u'v'}}{\partial z} - \frac{\partial \overline{u'w'}}{\partial y}\right) \tag{1.3}$$

and describes the formation of vorticity due to streamwise gradients of the primary Reynolds shear stress gradients. This term is often ignored from most of the studies due to assumption of zero pressure gradients; whether this term is important in flows with strong pressure gradients (e.g., in locations where a shock wave induced pressure gradient is present) is currently not known. The fourth term in the vorticity equation is

$$P3 = \frac{\partial^2}{\partial y \partial z}\left(\overline{v'^2} - \overline{w'^2}\right) \tag{1.4}$$

and represents the formation of vorticity due to anisotropy in direct turbulent stresses. This term is believed to be the prominent quantity that leads to creation of streamwise vortices in a corner. Unlike the isotropic nature of the turbulence in the undisturbed boundary layers away from the corner, the kinetic energy is distributed unequally along different directions in the corner region,

which leads $P3$ to take non-zero values. The final term in the vorticity equation is

$$P4 = \left(\frac{\partial^2}{\partial z^2} - \frac{\partial^2}{\partial y^2} \right) \overline{v'w'} \tag{1.5}$$

and describes the formation of streamwise vorticity due to gradients in the secondary stress $\overline{v'w'}$. Together $P2$, $P3$ and $P4$ represent the quantities responsible for the development and sustenance of the secondary flow of the second kind. These terms are important in corner flows.

Gessner [73] experimentally evaluated the terms in the energy and vorticity balance equations using pressure taps and hot wire measurements. His results suggest that the transverse secondary flow is initiated as a direct result of the primary turbulent stress gradients normal to the corner bisector and that the anisotropy of the stresses does not play a major role in the secondary flow generation as suggested by Perkins [74]. He suggests that the variations in the curvature of iso-contours of the axial velocity that occur in the flow undergoing laminar-to-turbulent transition result into turbulent stress gradients along the iso-contour which necessitate the development of a secondary flow from the concave to the convex side of the iso-contour. Brundrett and Baines [75] conducted experimental investigation using hot-wire measurements in order to characterize regions of vorticity creation and diffusion. Their results suggest that the diffusion of vorticity peaks near the wall while the production of vorticity is associated with the region near the corner bisector; however, it is zero on the corner bisector itself while being of opposing signs on either side of it. They suggest that it is because of this distribution that the vortices have a tendency to convect towards the walls. The zone of peak vorticity production is characterized by a vortex on each side of the corner bisector with opposite signs. It was found that the vorticity production is independent of the Reynolds number, but the vortex diffusion is not. They suggested this to be the reason for the secondary flow to be pushed towards the wall as the Reynolds number is increased. Kornilov and Kharitonov [76] studied the structure of the corner flows in asymmetric configurations featuring unequal boundary layer thicknesses on the walls forming corners. One of their most important

findings was that the vortex located towards the thicker boundary layer is stronger and larger than that towards the thinner boundary layer.

The unstable nature of these flows have been reported by various stability studies conducted by Alizard et al. [77], Zamir [78] and Balachandar and Malik [79]. As a result of this unstable nature it is highly likely that any intrusive form of measurement would lead to a disturbed flow, thus yielding false measurements of the corner flow properties, especially in supersonic flow wherein the effect of shock wave / flow interaction resulting from the probe can propagate upstream through the viscous region and change the characteristics of the incoming flow as it has been explained by Chapman et al. [21] and reported by Kornilov [80]. Because of this, it is necessary to characterize the flow using non-invasive experimental techniques, such as the particle image velocimetry (PIV) technique. Motivated by this observation, Park et al. [81] conducted PIV measurements in the corner flow in a plane oriented along the corner bisector in the streamwise direction. They majorly focused on capturing the developing boundary layer on this plane. Their findings are in agreement with the theoretical studies in that the velocity distributions were found to follow self-similar profiles and that the corner velocity profiles correspond to the Blasius branch of the theoretical solutions. However in order to fully understand the secondary flows, it is necessary to obtain non-intrusive high resolution measurements in the plane where such secondary flows are observed. Uruba et al. [82] conducted POD analyses to elucidate the most energetic modes of secondary flows in the rectangular corner.

This work builds on these earlier efforts, and aims to provide additional insights into the behavior of vorticies in the corner region. The earlier efforts mentioned in this section primarily look at the corner flows from a purely RANS perspective which is not a physical picture if the instantaneous flow field is investigated. Additionally the previous work conducted on corner flows have never mathematically or physically defined the corner vortex making it difficult to study its properties. This study proposes a systematic way to define the corner vortex pair in instantaneous turbulent

vector fields where the identification of the vortex pair is masked by a forest of small-scale vortices associated with the underlying turbulent flow of the boundary layer. Once the corner vortices have been defined, it is possible to statistically study their behavior in the corner and the roles they play in affecting the primary flow field. Thus, a part of this thesis (Chapter 4) will majorly be focused on analyzing the instantaneous structure of the corner flow from a set of instantaneous PIV measurements that focus into the turbulent boundary layers merging at the corner.

1.4 Objectives and New Contributions

While previous studies mentioned in section 1.2 have investigated the importance of secondary flows on a 3D SBLI, they have mainly focused on the effects of the secondary flows on the centerline interaction ignoring the swept SBLI on the sidewall. In addition, no studies have considered the effects of the baseline flow field characteristics of a rectangular duct on the structure of the SBLI that would be present in the duct.

The work presented in this thesis aims at providing a complete description of the entire SBLI flow field including the swept SBLI, incident oblique SBLI and the swept shock-corner flow interaction. Thus, the first objective is to obtain quantitative velocity measurements using SPIV in SBLI flow fields. In particular, measurements are taken on planes orthogonal to the primary flow direction (i.e., on cross-sectional planes) to enable to study of the baseline secondary flows characteristic of the wind tunnel, as well as their effects on the 3D SBLI. The analysis of the flow field revealed the dominance and complexity of the sidewall SBLI over the centerline SBLI, as well as it revealed the importance of the corner flow. Thus, the second objective is to obtain SPIV measurements planes orthogonal to the principal flow direction in the empty tunnel to facilitate the quantification and study of secondary flows of the baseline flow. The instantaneous flow fields obtained in the empty tunnel are then analyzed statistically to quantify the turbulence properties of the secondary

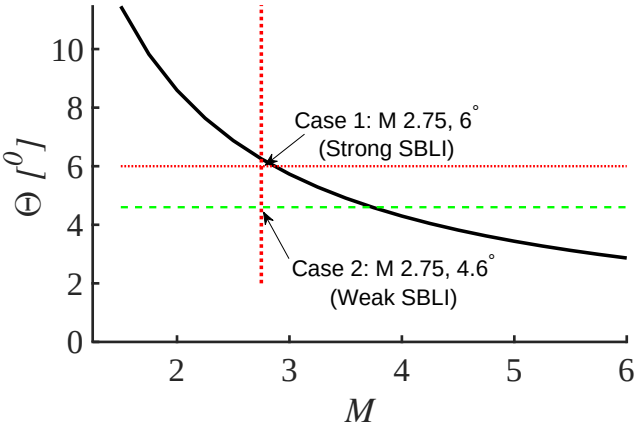

Figure 1.9: Locations of the current study on Korkegii's correlation for incipient separation on the sidewall for swept shock.

flow in a spatially phase average sense rather than interpreting them in the RANS point of view developed in previous work (see section 1.3), which is a view with limited physical meaning in a highly unsteady flow field as that found in this work. The lessons learnt from studying the baseline flows in this manner are applied to the SBLI flow fields particularly to the weak SBLI case (Mach 2.75 4.6° deflection) in order to make predictions on sites of most probable flow separation.

1.5 Thesis Outline

After the introduction to the problem presented in this chapter, this thesis is structured to address the following topics. Chapter 2 provides the details of the experimental techniques used. Chapter 3 outlines the SPIV results of our first case of SBLI using a moderate strength interaction (Mach 2.75 with 6° flow deflection) that establish the highly 3D nature of the flow around the interaction region. In this chapter, triple decomposition of motion (TDM) will be used to extract the large-scale vortex structure around the interaction region using the dataplanes aligned in all three orientations. Flow separation was quantified and the importance of the sidewall interaction over that of centerline was established. Linking the vortex structure to the flow separation also elucidates the role of

secondary flows, especially the corner flows in causing flow separation on the sidewall. Building on this established importance, Chapter 4 studies the empty tunnel corner flows in detail. Two sets of data were recorded, one at Mach 2.75 and the other at Mach 2.0. Both the datasets were in agreement with each other over the general flow features and made it possible to mathematically define the corner vortices. Various characteristics of the corner vortices, the turbulence and their streamwise evolution were studied. After further studying the interaction of the SBLI system with corner flows, in chapter 5 the effects of the corner vortices on the evolution of primary flow field were used to build a hypothesis providing explanations for flow separations. This hypothesis was then used to predict the locations of flow separation in a different case of weak interaction (Mach 2.75 with 4.6° flow deflection). A stronger case of interaction was attempted at Mach 2.75 and 7° deflection. However, under these conditions wind tunnel unstart was observed. Unstart was observed also in the case of 4.6° deflection at Mach 2.0, thus limiting the range of conditions that could be studied with the current wind tunnel configuration.

All the figures presented in this thesis are dimensional due to the three dimensional nature of the problem studied. The reader is directed to Section 4.1 in order to get an idea of boundary layer variation.

CHAPTER 2

Experimental Setup and Analytical Tools

2.1 Experimental Setup

2.1.1 Stereo Particle Image Velocimetry (SPIV)

2.1.1.1 Principle of PIV

Particle Image Velocimetry (PIV) is a non-intrusive method of measuring flow velocities at large number of points withing the fluid simultaneously. The flow is seeded with particles that are assumed to exactly follow the flow without altering it. One crude example of PIV would be sawdust in a flowing river, which makes certain primitive behavior like swirling behind rocks obvious.

In a quantitative sense, a flow is seeded with particles with calculated characteristics within a certain tolerance, and a pair of images are recorded within a finite time interval (Δt). The flow velocity at a point X is obtained by the displacement within Δt of the particles in the defined neighborhood of point X. A typical arrangement for conducting PIV is shown in Figure 2.1.

The particle images shown in Figure 2.1 by two square boxes containing filled and hollow circles representing particles are obtained by illuminating the medium by a laser sheet in quick succession separated by Δt, such that $\Delta t = t' - t$. The light scattered by the particles at t and t' is recorded on two separate frames by the Charge Couple Device (CCD) camera/s. The images are then divided into finite parts called interrogation windows that define the neighborhoods of various points in

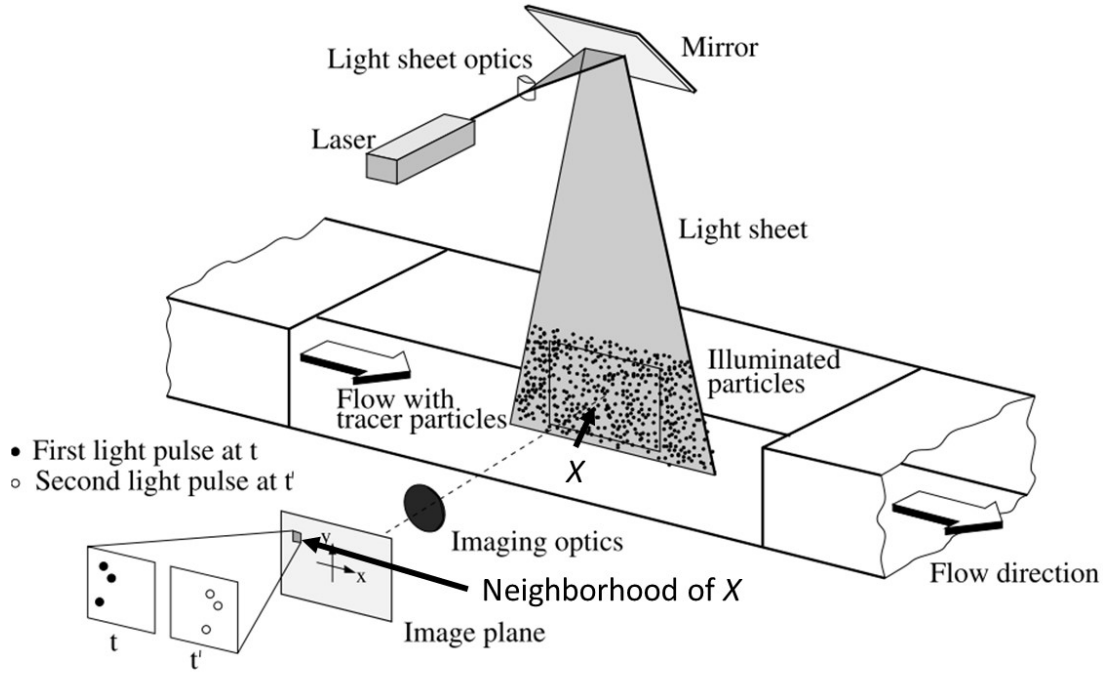

Figure 2.1: Experimental arrangement for a typical PIV system, Adapted from Raffel et al. [8].

the image. Cross correlations are then used to determine the most likely displacements of particles in the interrogation windows within both the images. Let $I_1(i,j)$ and $I_2(i,j)$ be the light intensity recorded fields within an $m \times n$ interrogation window at times t and t' respectively for pixel (i,j). Cross-correlation($C(dx,dy)$) is then carried out by shifting $I_1(i,j)$ around $I_2(i,j)$ by a displacement vector (dx,dy) and summing the products of all overlapping pixel intensity fields at each shift (dx,dy) which is given as

$$C(dx,dy) = \sum_{i=1}^{m}\sum_{j=1}^{n}\left[I_1(i+dx,j+dy) - \overline{I_1(i,j)}\right]\left[I_2(i,j) - \overline{I_2(i,j)}\right] \tag{2.1}$$

where $\overline{I_1(i,j)}$ and $\overline{I_2(i,j)}$ are the averages of $I_1(i,j)$ and $I_2(i,j)$ respectively. $C(dx,dy)$ is then normalized using the standard deviation ($\sqrt{\sigma}$, where $\sigma = \sum_{i=1}^{m}\sum_{j=1}^{n}\left[I(i,j) - \overline{I_1(i,j)}\right]^2$) from each win-

dow. Thus the normalized form of cross-correlation function is given by

$$c(dx, dy) = \frac{C(dx, dy)}{\sqrt{\sigma_1}\sqrt{\sigma_2}} \tag{2.2}$$

The maxima value of $c(dx, dy)$ represents the most probable displacement within that interrogation window. Note that this displacement ($\mathbf{d}(\mathbf{X}, \mathbf{t})$) although referred to as *instantaneous displacement* is the displacement of the particles averaged over Δt within the interrogation window. The instantaneous velocity ($\mathbf{v}$) (averaged over Δt) is then obtained by $\mathbf{v} = \frac{\mathbf{d}(\mathbf{X},\mathbf{t})}{\Delta t}$. When PIV is conducted by imaging the same planar area using two cameras in stereoscopic orientation, it is possible to obtain the 3rd out of measurement plane component of velocity due to the stereoscopic view. The following sections contain a brief description of various subsystems of the SPIV used in this study.

2.1.1.2 Seed Particles

The challenge associated with choosing the right seeding particles for a PIV experiment is that they should be small and light enough to track the flow effectively, but sufficiently large to scatter enough light. If the mass of the particle can be considered as negligible, then the particles' flow following property is a function of its shape, size, particle density (ρ_p), fluid density (ρ_f) and fluid dynamic (μ) or kinematic ($\nu = \mu/\rho_f$) viscosity. The equation of motion for spherical particles in a fluid was derived by Melling [83] which for a case of PIV using oil droplets in air (large $\frac{\rho_p}{\rho_f}$) reduces to

$$\frac{dU_p}{dt} = \frac{U_p - U_f}{\tau_p} \tag{2.3}$$

where U_p is the particle velocity, U_f is the fluid velocity and τ_p is the characteristic particle time lag obtained from Stokes drag law. A modified version of Stokes drag law for supersonic flows was provided by Scarano [84] as

$$\tau_p = \frac{\rho_p d_p^2}{18\mu_f}(1 + 2.7Kn_d) \tag{2.4}$$

where Kn_d is the Knudsen number based on the particle diameter d_p. Zucrow and Hoffman [85] show that Knudsen number can be expressed as

$$Kn_d = 1.26\sqrt{\gamma\left(\frac{M_{\Delta u}}{Re_{d_p}}\right)} = 1.26\sqrt{\gamma\left(\frac{u_{pre} - u_{post}}{a_{pre}Re_{d_p}}\right)} \tag{2.5}$$

where γ is the gas constant (1.4 for air) a_{pre} is the pre-shock sonic velocity (taken to be constant 217.1 m/s, computed using a stagnation temperature of 296 K and free stream velocity of 597 m/s) and Re_{dp} is the droplet Reynolds number in pre shock state. The particle seeding of the flow used in this study was generated by a TDA-4B portable Laskin nozzle aerosol. The generator consists of an array of six Laskin nozzles that create poly-dispersed sub-micron particles using Poly-Alpha Olefin-4 (PAO-4) oil with density of 819 kg/m^3. The generated particles were found to be well suited for PIV studies in supersonic flows due to their sub-micron sizes and high refractive index. However, all these factors considered it is possible that the particles coalesce into larger particles downstream, thus an assessment of uncertainty in flow following properties of the particles is conducted in Section B.2.

2.1.1.3 Particle Imaging

An example of the particle images obtained is shown in Figure 2.2. The tracer particles scatter the illumination used for viewing them through a finite aperture lens system due to which they form a Fraunhoffer diffraction pattern consisting an Airy disk surrounded by Airy rings [8]. The Airy disk diameter (d_{diff}) represents the smallest particle image that can be obtained from the PIV system and hence is of prime importance. It is a function of $f\#$ (ratio of focal length f and aperture diameter d_a), wavelength of illumination λ and the magnification M (ratio of distance between image plane and lens v and lens and object plane u) of the imaging system used. The diffraction

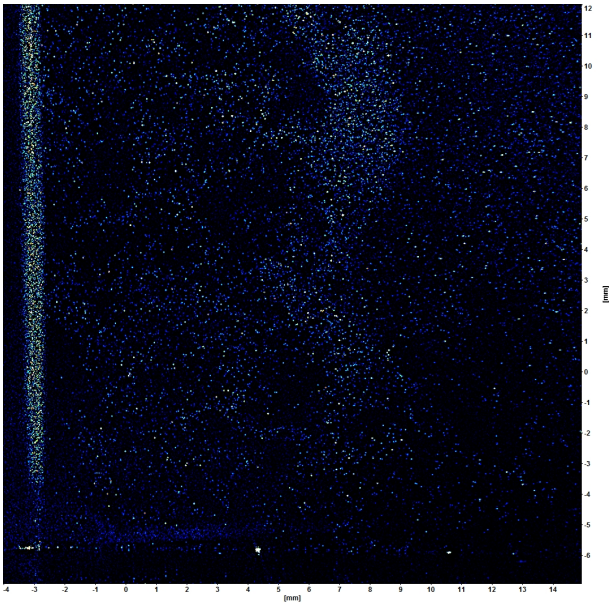

Figure 2.2: An example of the particle image obtained in the corner with flow out of the plane. The light strip on the left indicates the reflection on the sidewall.

limited minimum diameter d_{diff} is given by,

$$d_{diff} = 2.44 f\#(M+1)\lambda \tag{2.6}$$

For the configuration used $M \approx -0.15$, $f\# = 22$, $\lambda = 532$ nm, we have $d_{diff} = 24\ \mu$m. As per Adrian [86] total particle image diameter (d_i) of a finite-diameter particle is the convolution of the Airy function with the geometric image of the particle. Approximating [86] both the functions by Gaussian leads to the minimum image diameter of:

$$d_i = \sqrt{M^2 d_p^2 + d_{diff}^2} \tag{2.7}$$

For the sub-micron sized particles and $|M| < 1$, the image diameter $d_i \approx d_{diff} = 24\ \mu$m. It is important to note that $d_i \approx 2d_{pix}$, where $d_{pix} \approx 13\ \mu$m is the physical pixel size. It is required that the particle image diameter be at least 2 pixels wide in order to avoid biasing phenomenon such as peak locking, where improper sub-pixel particle detection leads to integer values of displacement

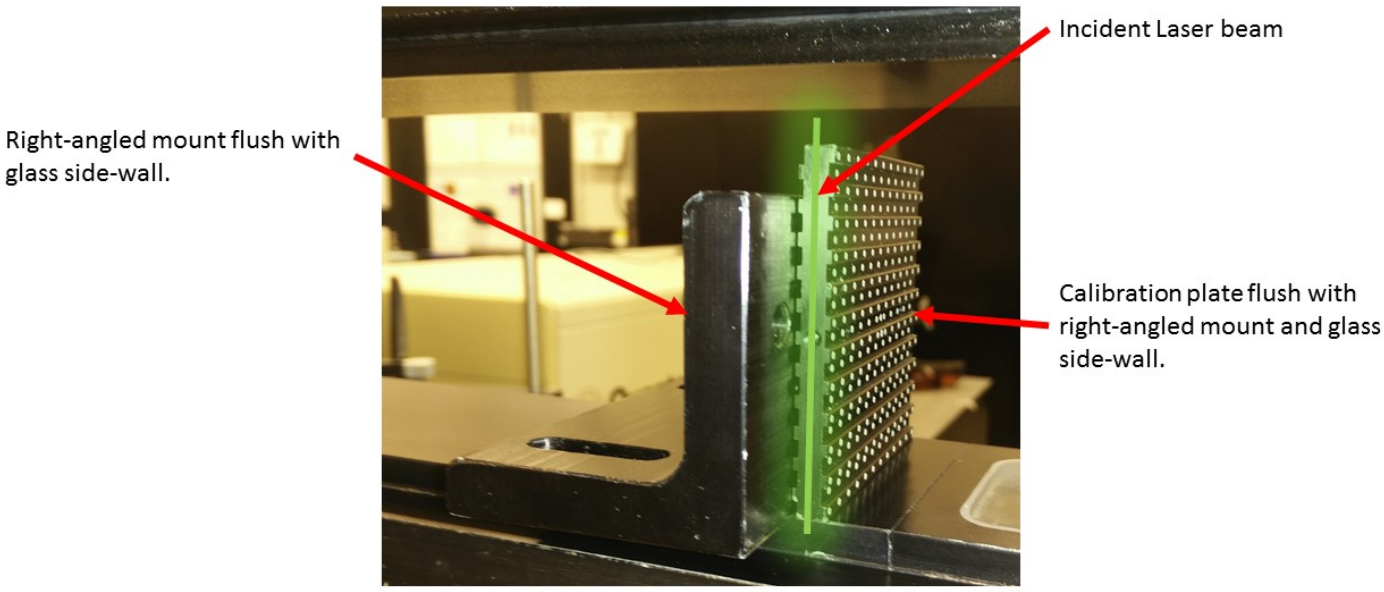

Figure 2.3: Calibration plate placement in the wind tunnel.

in pixel space. The data recorded in this experiment was checked for peak locking in Appendix B.5, where none was observed.

2.1.1.4 Calibrations

The SPIV calibrations were conduted by using a LaVision Type-7 3D calibration plate. The calibration plate was placed at the location of the incident laser sheet and it was ensured to be perpendicular to the side glass wall using laser reflections. A machined right angled mount is used to ensure the calibration plate is perpendicular to the sidewall as shown in Figure 2.3. The uncertainty associated with location of the laser sheet with respect to the calibration plate was investigated in Appendix B.3. Camera calibration was accepted if the average deviation of the dewarped mark positions to the ideal grid value and RMS fit error was less than 0.3 pixels.

Stereo PIV self-calibration was then conducted to minimize the errors associated with uncer-

tainty in location of the laser sheet (A detailed analysis is conducted in Section B.3). Around 100 recorded images are used to conduct SPIV self-calibration at each dataplane. Self calibration is then conducted starting with a window size of 128×128 with 75% overlap and 3 passes. The process is refined at the same resolution until the average deviation decreases below 0.001 pixel while making sure that the sidewall laser reflection images from both the cameras are overlapping at each step. Window size is then reduced to 64×64 and process repeated. The final window size used for self calibration is 32×32 with an overlap of 75%.

2.1.1.5 Experimental SPIV Arrangement

A schematic arrangement of the SPIV data acquisition system is shown in Figure 2.4. Two interline transfer 12-bit CCD cameras (LaVision Flowmaster/PCO Sensicam QE) recording at 3.33 Hz with a resolution of 1376×1040 pixel were used for the imaging. The cameras were placed in a stereoscopic, forward-scattering configuration effectively oriented at 33° with respect to the measurement plane normal direction, using scheimpflug adapters turned at 6° as shown in Figure 2.4. The cameras feature a minimum interframe time delay of about 500 ns. The cameras were equipped with Sigma $70-300$ mm lenses operated at a focal length of about 100 mm and $f_{\#}$ of 22.

The double-pulse illumination of the flow is provided by a pair of low repetition rate, frequency-doubled Nd:YAG lasers (one Spectra-Physics Quanta-Ray Pro-250 and one Spectra-Physics GCR-3) producing an output of 532 nm beam with a total energy of 200 mJ/pulse. The lasers are triggered at 10 Hz with a time delay (Δt) of 600 ns/650 ns/700 ns in between the two pulses depending on the case investigated (see Table 2.1) and pulse duration of 10 ns. The delay is measured with a ThorLabs DT10A/M photodiode that has a 1 ns response time and a LeCroy Waverunner 6030 350 MHz digital oscilloscope and then ensured by adjusting the time delay between the trigger signals using a LaVision Programmable Timing Unit (PTU) controlled through Davis 7 or 8 software. The PTU can control the pulses within 5 ns. In order to optimize the particle

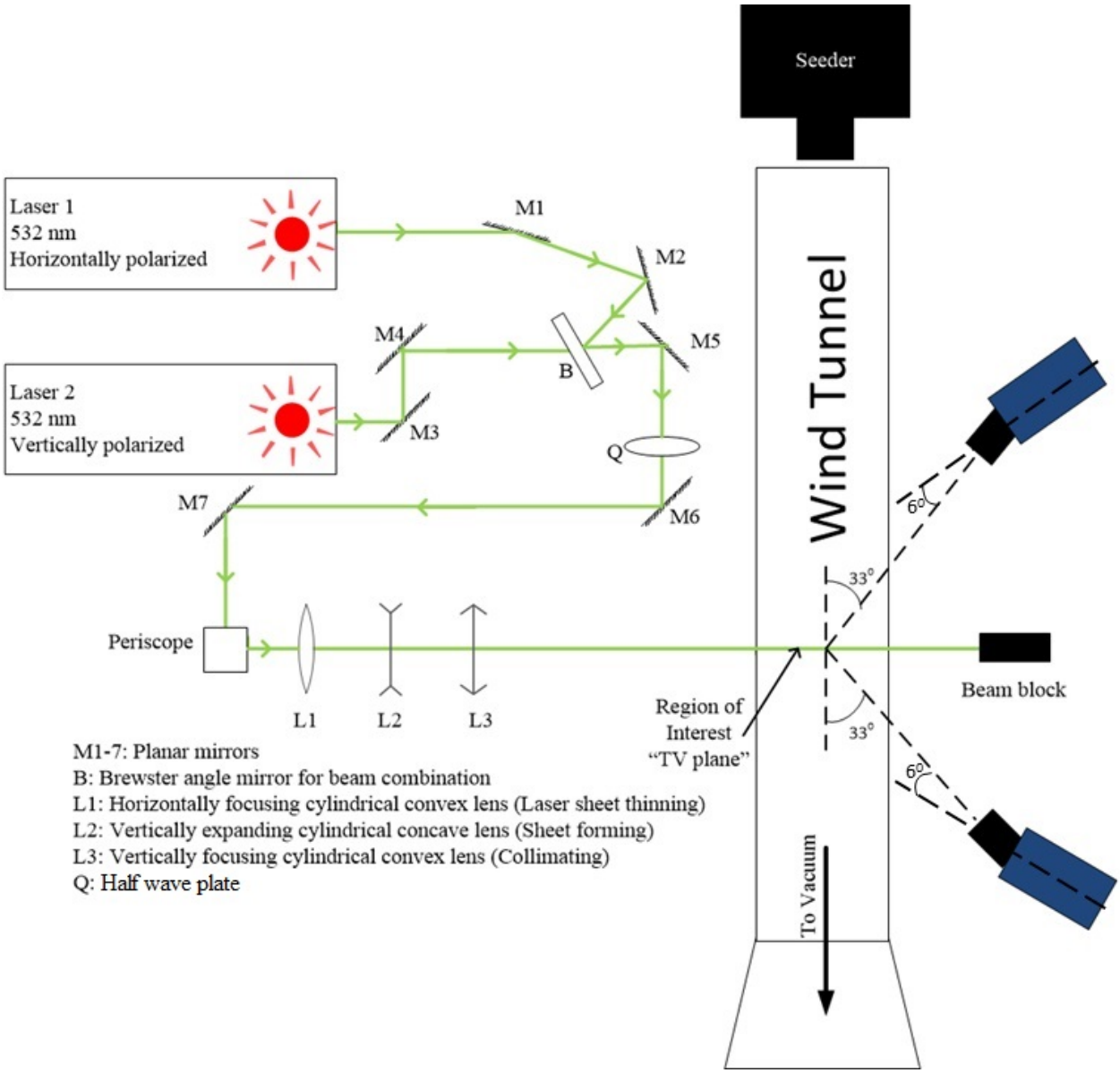

Figure 2.4: Schematic diagram of SPIV arrangement for transverse-vertical plane (Top view).

dropout and volumetric effects, laser sheet thickness is set using expanding-collimating optics to approximately 4 times the out of plane displacement of a particle within the measurement domain as suggested by Adrian and Westerweel [87]. The beam width was measured to be 1.45 ± 0.25 mm, which is approximately 3.6 times the particle displacement (approx. 400 μm) in 650 ns at the free-stream speed. Measurements of beam profiles using knife edge technique are given in Appendix B.1.

2.1.1.6 Image Processing and Post-processing

The LaVision DaVis 7 or 8 software is used for the acquisition of the measurement and processing of the data. The three-component velocity fields are reduced from the particle images using Davis 7 or 8. A multi-pass with reducing interrogation window size is used. Two passes were conducted using an interrogation window size of 64x64 pixels with a 50% overlap and a circular 1:1 weighting. The final size of the interrogation windows after two further passes was 32x32 pixels with an overlap of 75% or 50% and circular 1:1 weighting, the physical details of which are tabulated in Table 2.1. Standard $I1 * I2$ correlation function via Fast Fourier Transform (FFT) with zero padding was used for all passes. Post processing within multiple passes included deleting a vector if its correlation value was less than 0.8 as well as removing groups with less than 4 vectors. Post processing was also conducted once all the passes were completed by removing vectors with a peak ratio (Q) less than 1.2. Laser sheets were oriented perpendicular to the flow, spanning a fraction the cross-section of the tunnel. Multiple such images (about 1000 instances at each measurement location) were recorded to construct statistics of various flow properties. Data was recorded along 25 SPIV planes in different orthogonal orientations to investigate the 6° SBLI case, 3 planes oriented orthogonal to streamwise direction for each of the empty tunnel cases (Mach 2.75 and Mach 2) and 4 planes orthogonally oriented to streamwise direction to investigate the 4.6° SBLI case with and without the SBLI. They have been labeled as *(1) Transverse Vertical (TV)* that are oriented in $y-z$

plane orthogonal to the principal plane direction, *(2) Streamwise Horizontal (SH)* that are oriented in $x-y$ plane and *(3) Streamwise Vertical (SV)* that are oriented in $x-z$ plane. The schematic of the arrangement of these planes for 6° SBLI case is shown in Figure 2.5. The coordinate system is discussed in Section 2.1.3. Experimental parameters used for recording data in various cases and the geometric extents of the data planes are summarized in Table 2.1.

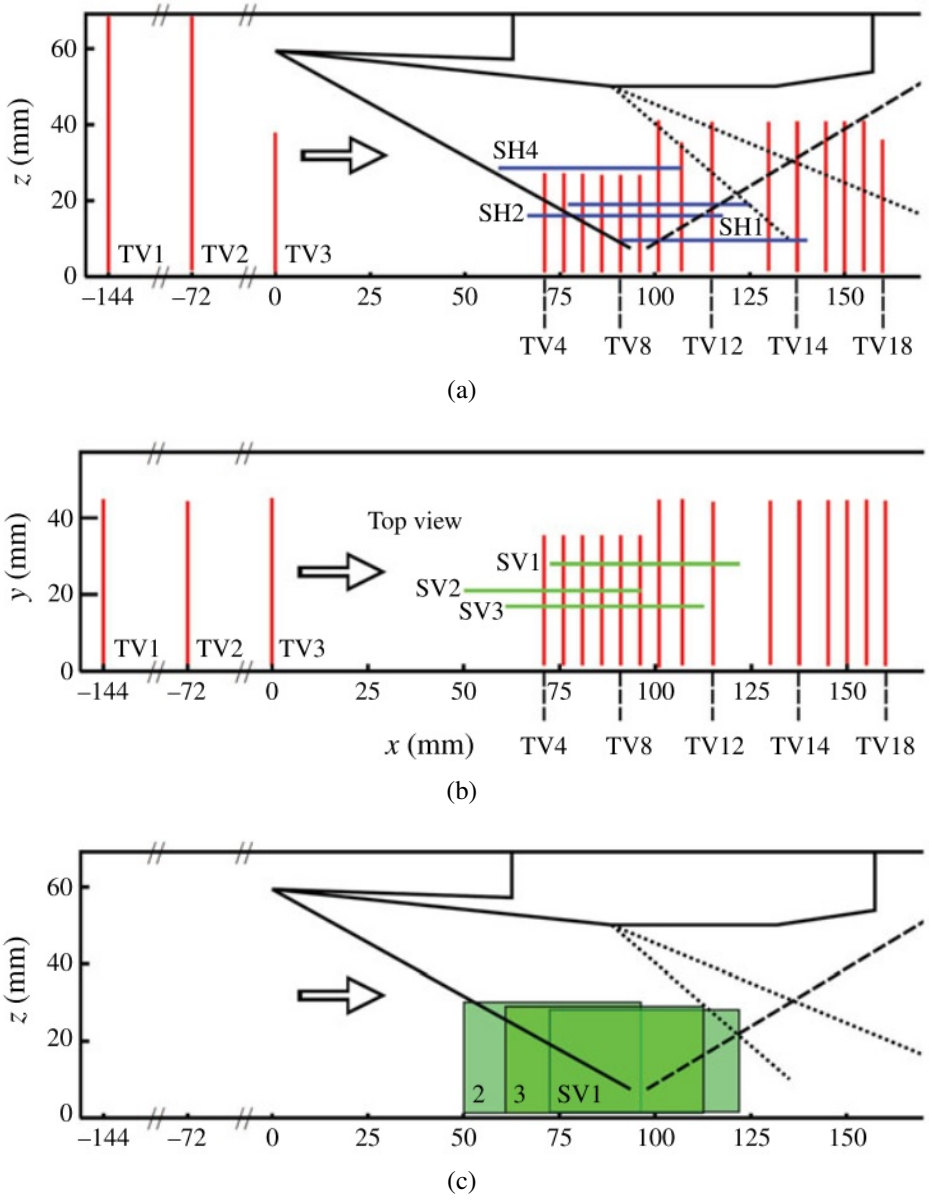

Figure 2.5: Orientation of SPIV data planes for the case of 6° SBLI.

Plane	**x** [mm]	**y** [mm]	**z** [mm]	**Pulse delay [ns]**	**Number of images**	**IW sizes** [mm x mm]	**Resolution** [mm x mm]
Mach 2.75 empty corner							
		Transverse	*Vertical*				$\Delta y \times \Delta z$
TV1	-100	0.56-16.5	0.5-16.5	650	489	0.608×0.608	0.152×0.152
TV2	-50	0.45-16.6	0.45-16.6	650	798	0.603×0.603	0.151×0.151
TV3	75	0.53-16.5	0.56-16.5	650	1602	0.587×0.587	0.147×0.147
Mach 2 empty corner							
		Transverse	*Vertical*				$\Delta y \times \Delta z$
TV1	-100	0.49-16.5	0.53-16.5	700	1475	0.448×0.448	0.112×0.112
TV2	-50	0.54-16.5	0.55-16.5	700	1993	0.444×0.444	0.111×0.111
TV3	0	0.53-16.5	0.55-16.5	700	1963	0.298×0.298	0.075×0.075
SBLI Mach 2.75 6°							
		Transverse	*Vertical*				$\Delta y \times \Delta z$
TV1	-144	1.3-45	1.3-68	600	2000	1.296×1.296	0.648×0.648
TV2	-72	1.8-44	1.6-68	600	1950	1.274×1.274	0.637×0.637
TV3	0	1.2-4.5	1.2-38	600	1902	1.204×1.204	0.602×0.602
TV4	71	1.5-35	1.1-27	600	402	0.426×0.426	0.213×0.213
TV5	76	1.5-35	1.1-27	600	402	0.426×0.427	0.213×0.213
TV6	81	1.5-35	1.1-27	600	402	0.426×0.428	0.213×0.213
TV7	86	1.5 35	1.1-27	600	402	0.426×0.429	0.213×0.213
TV8	91	1.5-35	1.1-27	600	402	0.426×0.430	0.213×0.213
TV9	96	1.5-35	1.1-27	600	402	0.426×0.431	0.213×0.213
TV10	101	1.1-45	1.2-41	600	1800	0.676×0.676	0.338×0.338
TV11	107	1.6-45	1.4-35	600	1100	1.152×1.152	0.576×0.576
TV12	115	1.6-44	1.4-41	600	1700	1.354×1.354	0.677×0.677
TV13	130	1.8-44	1.5-41	600	1800	1.354×1.354	0.677×0.677
TV14	137	1.5-45	1.2-41	600	1650	1.366×1.366	0.683×0.683
TV15	145	1.5-45	1.2-41	600	1400	1.366×1.366	0.683×0.683
TV16	150	1.5-45	1.2-41	600	1468	1.366×1.367	0.683×0.683
TV17	155	1.6-45	1.4-41	600	1800	1.366×1.368	0.683×0.683

			Streamwise Vertical				$\Delta x \times \Delta z$
SV1	72-122	28	1.6-28	600	500	1.206×1.206	0.603×0.603
SV2	51-96	21	1.2-30	600	670	0.596×0.596	0.298×0.298
SV3	61-113	17	1.2-30	600	1050	0.398×0.398	0.631×0.631
			Streamwise Horizontal				$\Delta x \times \Delta y$
SH1	91-141	14-45	9.5	600	500	1.246×1.246	0.623×0.623
SH2	77-125	11-42	19	600	800	1.262×1.262	0.631×0.631
SH3	59-107	12-44	29	600	1030	1.304×1.304	0.652×0.652
SBLI Mach 2.75 4.6°							
			Transverse Vertical				$\Delta y \times \Delta z$
TV1 empty	67	0.56-29.1	0.67-29.1	625	451	0.841×0.841	0.21×0.21
TV1	67	0.56-29.1	0.67-29.1	625	3099	0.841×0.841	0.21×0.21
TV2 empty	82	0.49-37	0.83-28.9	625	419	0.84×0.84	0.21×0.21
TV2	82	0.49-37	0.83-28.9	625	2373	0.84×0.84	0.21×0.21
TV3 empty	102	0.66-37	1.09-33	625	157	0.84×0.84	0.21×0.21
TV3	102	0.66-37	1.09-33	625	1734	0.84×0.84	0.21×0.21
TV4 empty	122	0.55-31	0.83-31	625	342	0.842×0.842	0.21×0.21
TV4	122	0.55-31	0.83-31	625	1889	0.842×0.842	0.21×0.21

Table 2.1: SPIV dataplane measurement properties.

The data (each snapshot/instantaneous field) was further validated in Matlab using the criterion proposed by Nogueira et al. [88]. An image was deleted if it had more than 3% missing vectors. The missing data was then interpolated using a fourth order differential equation [89]. The method leaves all known values intact. The data was lowpass filtered using a Gaussian filter with a standard deviation corresponding to 2.5 vector spacing and a kernel size of 5×5 points. All of the SPIV data was analyzed using PIVMAT [90] modified to use a least-square finite difference scheme for computing derivatives except at the edges where forward and/or backward differencing was used. A direct cosine transform based penalized least-square method [91] developed by Garcia [92, 93]

was also used for interpolating-smoothing.

The performance of the SPIV system in stagnant flow to evaluate the detectability and noise limit of the arrangement is given in Appendix B.7.

2.1.2 Pressure Measurements

Static pressure measurements were obtained at bottom- and sidewalls locations instrumented with pressure taps. Pressure tap sizing was based on the results of Mckeon et al. [94], Chue [95] and Shaw [96] in order to minimize measurement errors and the effects of the presence of wall pressure tap on the fluid flow. Recess-mount pressure taps were used where the tap diameter and length were 0.8 mm and 7.6 mm, respectively (depth-to-diameter ratio of approximately 9); stainless steel tubing (inner diameter 0.8 mm, outer diameter 1.6 mm) was press fitted into the walls to connect the pressure tap to the pressure transducer. Different tap spacings were used: 25 mm upstream of the interaction, 6.35 mm around the interaction region, and 12.7 mm downstream of the interaction. Tygon B-44-4X flexible tubing (inner diameter 1.6 mm, outer diameter 3.2 mm) was used to connect the pressure taps to a differential pressure sensor array scanner (Scanivalve model DSA 3217). The accuracy of the pressure sensor array was 0.009 kPa.

A reference wall pressure tap was located on the top-wall at $x = -85$ mm. Measurements at this location were used to reference and monitor all runs, and to reference all other differential measurements. Absolute pressure measurements were performed at this location with two different transducers: a pressure gauge (Omega model DPG2001B-30A, accuracy 0.5 kPa) or a vacuum capacitance manometer (MKS Baratron 627D, accuracy 0.12% of reading). All pressure measurements reported here are time-average measurements over a minimum averaging time of 30 seconds.

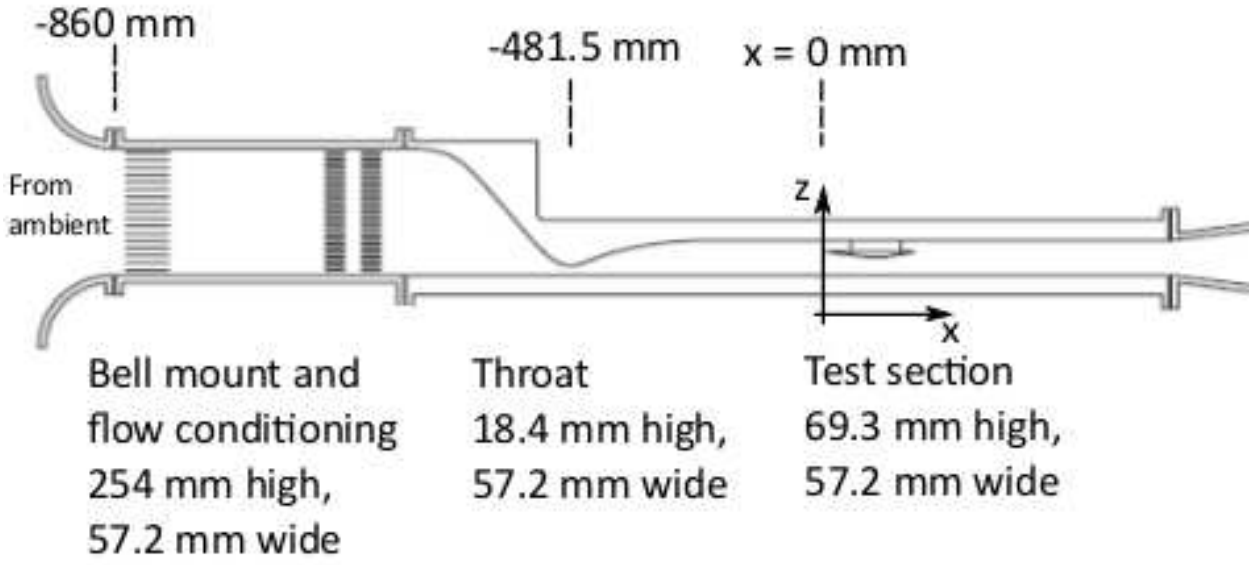

Figure 2.6: Wind tunnel schematic diagram with Mach 2.75 nozzle (not to scale).

2.1.3 Wind Tunnel

The experiments presented here were carried out at the Michigan Glass Wind Tunnel (GWT) facility. A schematic diagram of the configuration used in the study is shown in Figure 2.6. The coordinate system selected for this study is a right handed x-direction being the streamwise direction with $x = 0$ being the tip of the shock generator described in Section 2.1.4, z-direction being perpendicular to the bottom wall as shown in Figure 2.6 and the y-direction satisfying the right hand rule with the x and z-directions points towards the tunnel centerline perpendicular to the right sidewall looking downstream with this sidewall being $y = 0$. A 3D schematic of the coordinate system is shown in Figure 2.10b.

It is a low aspect ratio suction supersonic wind tunnel $y_T \times z_T = 57.2\text{ mm} \times 69.3\text{ mm}$ (2.25 in $\times$ 2.75 in) in cross-section capable of being configured to operate nominally at Mach 2.75 and Mach 2 with stagnation pressure and temperature of 98.1 kPa and 294 K, respectively. The effective (measured) Mach number is approximately 2.72 for Mach 2.75 configuration and 1.99 for Mach

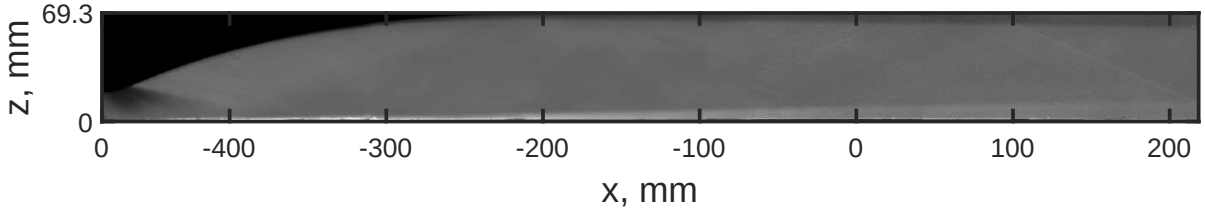

(a)

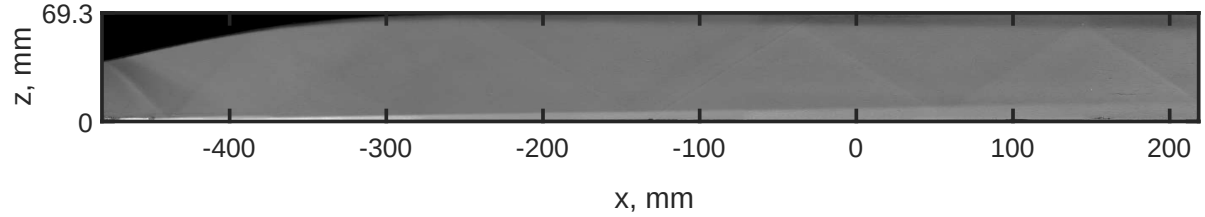

(b)

Figure 2.7: Mean Schlieren fields in empty tunnel at (a): Mach 2.75 and (b): Mach 2.

2 configuration. The tunnel is composed of a one-sided two-dimensional converging-diverging nozzle followed by a constant area test section. This design was selected to produce an equilibrium flat plate boundary layer [17] in an attempt to minimize pressure gradients history effects and Görtler vortices on the boundary layer developing on the bottom wall (floor) of the wind tunnel. The averaged empty tunnel Schlieren measurements done by Klomparens [97] are shown in Figure 2.7. The wind tunnel in both the configurations does feature a weak uncanceled wave originating from the converging-diverging nozzle as seen in Figure 2.7 which possibly is due to its one-sided nature. However this disturbance was deemed sufficiently weak to disturb the large-scale features of the SBLIs studied here.

Figure 2.8 shows the evolution of mean absolute wall static pressure in both the configurations of the empty wind tunnel. It should be noted that in the Mach 2 configuration a shock train rests downstream of $x = 150$ mm, however this configuration features only empty tunnel data recorded

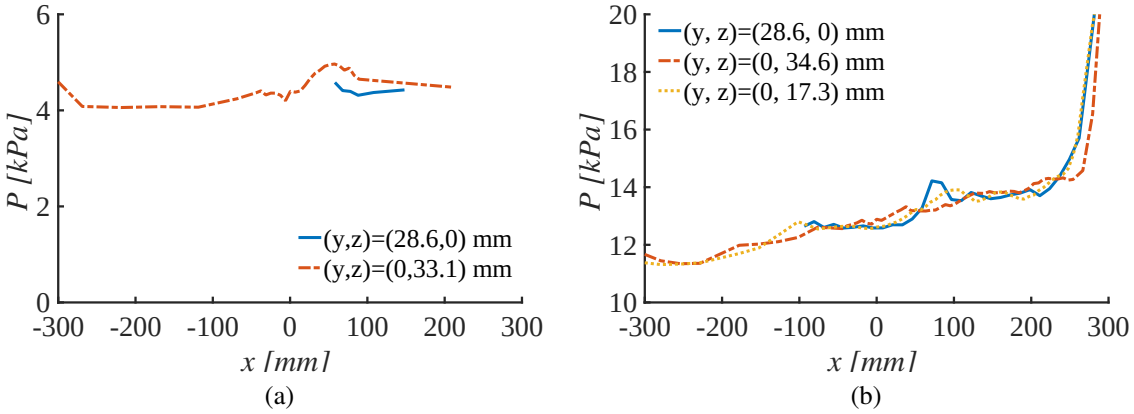

Figure 2.8: Mean wall static pressure in empty tunnel at (a): Mach 2.75 and (b): Mach 2.

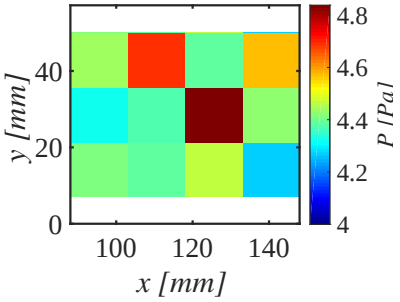

Figure 2.9: Mean bottom wall static pressure in empty tunnel at Mach 2.75.

at locations up to $x = 0$ mm. Because the test section in both the configurations has constant area, the static pressure increases along the (empty) tunnel as a result of boundary layer growth. The increase in pressure was quantified by the pressure gradient parameter defined as $\beta = \frac{\delta}{\rho U_\infty^2}\frac{\partial P}{\partial x}$ and was calculated from the sidewall pressure measurements conducted in the empty tunnel at half the tunnel height. The value of this parameter was found to be 5×10^{-4} for Mach 2.75 nozzle and 9×10^{-4} for Mach 2 nozzle. The empty tunnel bottom wall pressure obtained at Mach 2.75 at the location of the 6° SBLI is shown in Figure 2.9.

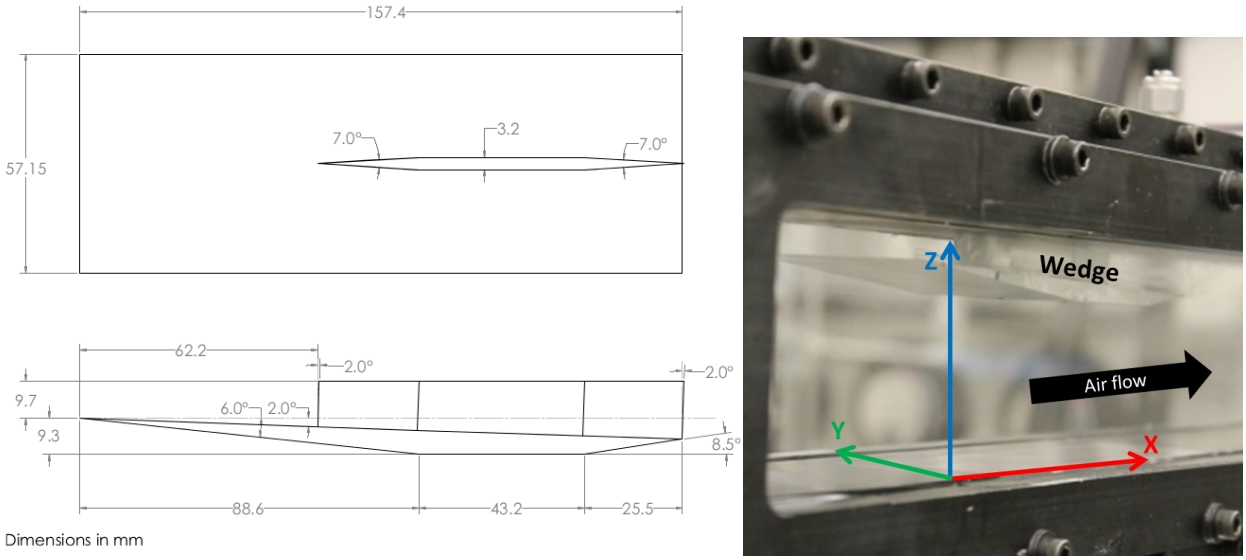

(a) (b)

Figure 2.10: (a): Drawing of full span shock generating wedge and (b): shock generating wedge as installed and the co-ordinate system used.

2.1.4 Shock Generator

The wedge geometry is shown in Figure 2.10a, where relevant dimensions (in millimeters) are reported. The wedge is suspended by a strut (see Figure 2.10), such that the leading edge of the wedge is 9.7 mm below the top wall of the wind tunnel and outside of the top-wall boundary layer. The leading edge of the shock generated is located 481.5 mm downstream of the nozzles throat, and it is taken to be at $x = 0$ in the coordinate system used throughout this work. The oblique shock wave thus formed is anchored very steadily to the leading edge of the wedge and is incident on the bottom wall on the centerplane of symmetry of the tunnel at a streamwise distance of 96 mm from the leading edge (i.e., at $x = 96$ mm). However, owing to the shocks curved nature, the point of impingement moves upstream as one moves away from the centerplane. The shock curvature will be discussed in detail in Chapter 3. The upper surface of the wedge diverges by 2° in order to prevent choking in the channel formed between the wedge and the top wall by providing expansion.

A weaker SBLI was obtained by placing a few spacers in between the top surface of the shock

generating wedge and the strut resulting in a shock generating angle of 4.6°. The leading edge of the wedge is 14.1 mm below the top wall of the wind tunnel and outside of the top wall boundary layer. The oblique shock wave generated is incident on the bottom wall boundary layer on the centerline of the tunnel at a streamwise location of x = 102 mm as observed from the Schlieren measurements. The upper surface of the wedge is slightly converging in this configuration, however no choking of the flow over the wedge that could affect the SBLI studied is observed from the schlieren images.

Since the study is focused on a 3D SBLI configuration and this work is a continuation of our previous SBLI work [6, 15, 57, 64, 98, 99], the origin of the coordinate system is centered at the location of the leading edge of the full-span 6^o shock generator wedge (which is about 481.5 mm downstream of the nozzle throat) used in our previous work on 3D SBLI. The unit Reynolds number of the flow at Mach 2.75 near the interaction region is 8.9×10^6 /m with an incoming boundary layer thickness (δ_{99}) of 10 mm measured at x = 75.5 mm and y = 28.6 mm (i.e., on the vertical midplane of the test section) in an empty tunnel [17]. A complete summary of the experimental conditions along with their respective uncertainties is provided in Table 2.2. Optical access to the test section is provided from both sides of the wind tunnel by glass windows that run along the whole length of the wind tunnel, including the nozzle throat region.

2.2 Analytical Tools

2.2.1 Flow Separation Bubble Profiles

Two criteria were identified and applied to determine separation and its properties. In particular, separation was identified by using the following two criteria as applied by Souverein et al. [52] and Piponniau et al. [51]:

Empty tunnel conditions			
Mach 2.75		**Mach 2**	
Mach number (Mach 2.75) M^1_∞	2.70 ± 0.01	Mach number (Mach 2) M^1_∞	2 ± 0.002
Mach number (Mach 2.75) M^2_∞	2.72 ± 0.03		
Free stream velocity at Mach 2.75 U^3_∞	593 ± 2 m/s	Free stream velocity at Mach 2 U^3_∞	512 ± 2 m/s
Throat height (Mach 2.75) [4]	18.4 ± 0.1 mm	Throat height (Mach 2) [4]	36.8 ± 0.2 mm
Wall static pressure (Mach 2.75) ($x = -85$ mm)[4]	4.15 ± 0.05 kPa	Wall static pressure (Mach 2) ($x = -85$ mm)[4]	11.79 ± 0.09 kPa
Static Temperature (Mach 2.75) T^3_∞	119 ± 1 K	Static Temperature (M2) T^3_∞	163 ± 1 K
Stagnation Pressure [4]		98.5 ± 0.2 kPa	
Stagnation Temperature [4]		294 ± 2 K	
Test section width [4]		57.2 ± 0.1 mm	
Test section height [4]		69.3 ± 0.2 mm	
SBLI, Mach 2.75 tunnel			
Wedge leading edge	$x = 0$ mm	Throat to wedge leading edge distance [4]	481.5 ± 1 mm
Mean center of bottom wall separation (Mach 2.75 6° SBLI)	$x = 96$ mm	Mean center of bottom wall separation (Mach 2.75 6° SBLI)	$x = 102$ mm

[1] Computed from a direct measure of stagnation and static pressure assuming isentropic expansion.
[2] Computed from a direct measure of the ratio of stagnation pressure and test section pitot pressure.
[3] Uncertainty estimated from error propagation rule.
[4] Uncertainty includes both measurement accuracy and day-to-day variability.

Table 2.2: Summary of experimental conditions.

2.2.1.1 Method 1: The "h-criterion"

A canonical structure of a typical laminar flow separation bubble is shown in Figure 2.11. The

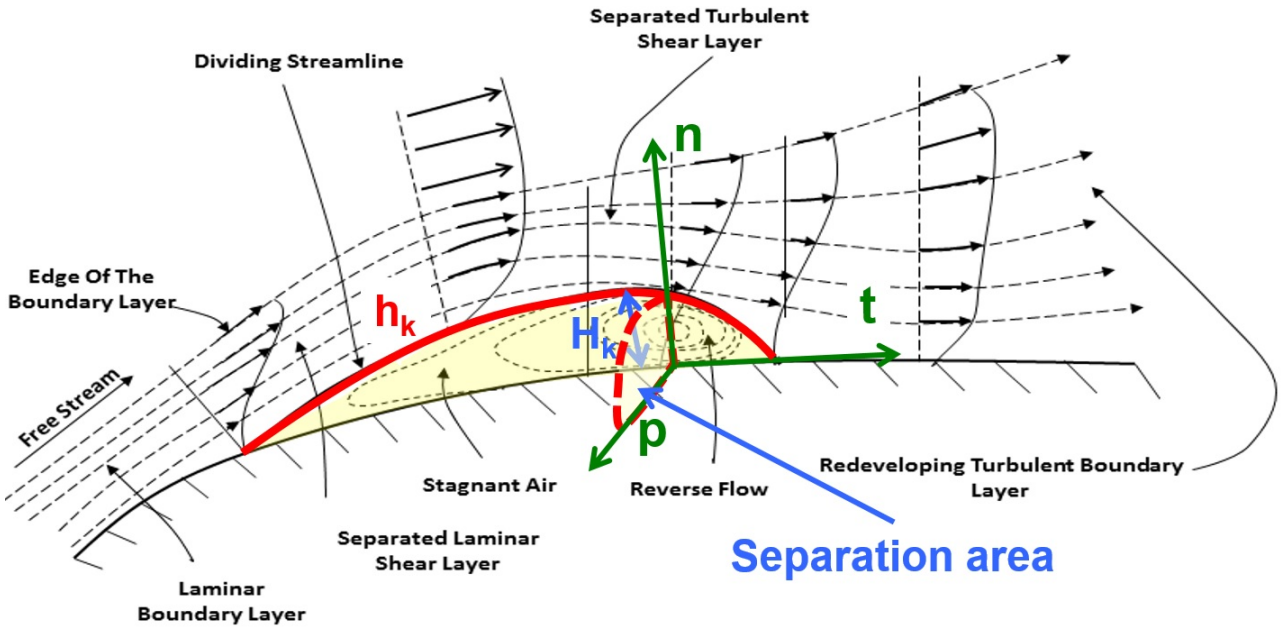

Figure 2.11: Section view of a typical laminar separation bubble, adapted from Karasu et al. [9].

separation bubble profile $h_k(p,t)$ of k^{th} image as a function of the wall surface location (p,t), is defined to be:

$$h_k(p,t) = \{\eta \mid \int_0^{\eta} u_k(p,t,n) \cdot dn = 0\} \tag{2.8}$$

where **t** is the direction tangent to the wall pointing in the general streamwise direction, **n** is the direction normal to the wall, **p** is the direction perpendicular to **t** and **n** out of the plane of the schematic shown in Figure 2.11 and $\mathbf{u_k}(\mathbf{p},\mathbf{t},\mathbf{n})$ is the local streamwise velocity at the (p,t,n) point. The quantity h_k is computed for each measurement instant k. By definition, if separation is not detected, $h_k = 0$. The ensemble average separation bubble profile, here denoted by h, is computed by averaging the set of local values h_k. This parameter effectively describes how much of wall

normal space is reduced because of separation. This is equivalent to that region being unavailable to the incoming flow but it must be noted that the current measurements do not include the effect of density. This quantity is limited by the accuracy of velocity measurements near the wall and by the overall spatial resolution of the measurements, however being an integral quantity it is fairly robust with respect to noise.

From each profile instantaneous h_k profile, the maximum value of the profile is extracted and denoted by H_k. This quantity is simply referred to as separation bubble height and provides a global instantaneous measure of the wall-normal extent of separation. Unlike the quantity h_k which is a function of wall coordinate direction, H_k is a constant for a particular image. The ensemble average separation bubble height H is then computed from the set of instantaneous values.

The separation bubble cross sectional area perpendicular to the principal flow direction referred to as separation area $A_{k_{sep}}$ for k^{th} image is defined as

$$A_{k_{sep}}(t) = \int_0^{p_{max}} h_k(p,t)dp \tag{2.9}$$

where p_{max} is the extent of the surface. Thus by definition an instant with value of $A_{k_{sep}} = 0$ will correspond to attached flow. The volume of the flow separation bubble given by $\int A_{k_{sep}}(t)dt$ may be regarded as the volume of a bluff body placed in the flow.

2.2.1.2 Method 2: Axial Velocity Thresholding (AVT)

The probability of separated flow at each point in the measurement domain was defined and computed as the fraction of the total number of realization where the local instantaneous streamwise velocity was less than a threshold value, here taken as 20 m/s. The quantity thus computed represents the probability of the local velocity to be less than the threshold value at a particular location in a data plane. A threshold value of 20 m/s is chosen to make the method resistant to errors aris-

ing from the SPIV dynamic resolution. As a consequence, this definition identifies regions where both reverse and low-velocity regions exist. Thus, it tends to overestimate the distribution and size of the region where reverse flow might exist. In any case, this definition is used to identify the regions that are most affected by the shock interaction process and we loosely refer to them as regions of probable separation. All points with a probability greater than 50% were said to lie near a separated zone. The isoconotur line of 50% probability, denoted as h_{AVT}, was chosen as the dividing line between disturbed and undisturbed flow . The area under the dividing line h_{AVT} can be understood as the separation or blockage area similar to h_k. . This definition of separated flow is more robust than the corresponding one that could be defined from the separation profile h because it is less prone to the experimental limitations near the wall as a low velocity region resulting from separation can extend towards the core flow away from the wall, where the accuracy of SPIV is sufficient. However, it incorporates an arbitrary parameter (50% intermittency) that hinders identification of highly unsteady separation. To address this latter issue, different threshold values were considered and similar conclusions were made to those reached with the value shown here.

2.2.2 Triple Decomposition of Motion (TDM)

To better identify vortical structures, we compute from the available velocity measurement a quantity called the rigid-body rotation vorticity ω_{RR}, which is one component of the vorticity field. Basic fluid motion can be categorized into rigid-body rotation, irrotational straining, and pure shearing [100] as shown in Figure 2.12.

The traditional Cauchy–Stokes decomposition of the velocity gradient tensor $\nabla\mathbf{u}$ separates the flow into two parts: the rate of strain $\mathbf{S}$, and rate of rotation $\mathbf{\Omega}$ tensors:

$$\nabla\mathbf{u} = \mathbf{S} + \mathbf{\Omega} \tag{2.10}$$

where the rate of rotation tensor $\mathbf{\Omega}$ is related to vorticity ω. However, in this form, we cannot

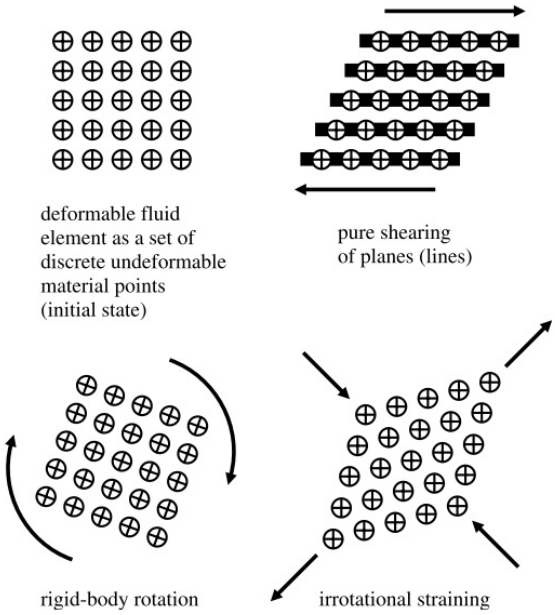

Figure 2.12: Basic parts of fluid motion, from Kolar [10].

differentiate between vorticity contribution due to pure shear with that due to rigid-body rotation about an axis (swirling). In the flow-field studied here, shear dominates the flow-field, and thus makes rigid-body vorticity detection difficult. Thus, an alternative decomposition used for vortex identification is used. In particular, we choose the triple decomposition of motion method of Kolar [10], from which rigid-body rotation vorticity ω_{RR} can then be defined. Other vortex identification strategies have been proposed and used in the literature [101–104]. Here, we use a 2D surrogate of the TDM because it provides us a representation of rigid-body rotation (vortical features) analogous to other vortex identification schemes (e.g., swirling strength) while preserving the sense of rotation (i.e., sign of the rigid-body vorticity), unlike other methods. In the following is a brief summary of the TDM, adapted to a 2D field to reflect the planar nature of the measurements, taken from the original work of Kolar [10]. It has to be emphasized that the TDM applied here is a planar (2D) surrogate of the full 2D form.

Triple decomposition allows one to decompose the flow-field motion into an irrotational straining

rigid-body rotation and a pure shearing motion. Thus, it allows one to extract the rigid rotation component, which is used here to identify vortical flow structures. The decomposition into these three components is effective in identifying rigid rotation only in a particular frame of reference in which pure shear is maximum. The TDM method first requires identifying this particular frame of reference, and only then extracting rigid rotation. Consider the 2D surrogate of the true 2D velocity gradient tensor defined on a TV plane as

$$\nabla \mathbf{u} = \begin{bmatrix} v_y & v_z \\ w_y & w_z \end{bmatrix} \tag{2.11}$$

which can be computed from the gradient components available from the planar measurements on our TV planes. The term $()_j$ indicates the derivative along direction j for any quantity. We can apply the rotation operator $\mathbf{Q}_\alpha$ to $\nabla \mathbf{u}$ to introduce an arbitrary rotation by an amount α to the laboratory frame of reference, and we obtain the velocity gradient tensor in the rotated frame of reference $\nabla \mathbf{u}'$:

$$\mathbf{Q}_\alpha \nabla \mathbf{u} {\mathbf{Q}_\alpha}^T = \mathbf{Q}_\alpha \mathbf{S} {\mathbf{Q}_\alpha}^T + \mathbf{Q}_\alpha \mathbf{\Omega} {\mathbf{Q}_\alpha}^T \tag{2.12}$$

The rotation operator is defined as

$$\mathbf{Q}_\alpha = \begin{bmatrix} cos(\alpha) & -sin(\alpha) \\ sin(\alpha) & cos(\alpha) \end{bmatrix} \tag{2.13}$$

Rewriting the terms of equation 2.12 as single variables,

$$\nabla \mathbf{u}' = \mathbf{S}' + \mathbf{\Omega}' \tag{2.14}$$

where $\mathbf{S}'$ and $\mathbf{\Omega}'$ are the rate of strain and rate of rotation tensors in the rotated frame of reference obtained from applying the Cauchy–Stokes decomposition to $\nabla \mathbf{u}'$. We can then find the particular frame of reference rotated by an angle $\alpha = \theta$ such that pure shear in this rotated frame of reference is maximum. It can be shown [10] that this condition corresponds to finding the angle θ such that

$|S'_{12}\Omega'_{12}|$ is maximum, or simply

$$\theta = \left\{ \alpha : \frac{d}{d\alpha} |S'_{12}\Omega'_{12}| = 0 \right\} \tag{2.15}$$

In this particular rotated frame of reference, the velocity gradient tensor can be decomposed in two terms (tensors): a pure shear tensor $\mathbf{H}$ (which is maximum), and a term that is referred to as the residual tensor $\mathbf{R}$:

$$\mathbf{Q}_\theta \nabla \mathbf{u} \mathbf{Q}_\theta{}^T = \mathbf{R} + \mathbf{H} \tag{2.16}$$

The residual tensor $\mathbf{R}$ in this frame contains motion associated only with rigid-body rotation and irrotational straining. It can either be a symmetric or an antisymmetric tensor. For the 2D case, the residual tensor is given by

$$\mathbf{R} = \begin{bmatrix} v'_y & sign(v'_z)min(|w'_y|, |v'_z|) \\ sign(w'_y)min(|w'_y|, |v'_z|) & w'_y \end{bmatrix} \tag{2.17}$$

where the primed terms are the components of $\nabla \mathbf{u}$ that are known once θ has been found. Once the residual tensor is known, it is rotated back to the original laboratory frame of reference where it is decomposed further into pure strain $\hat{\mathbf{S}}$ (symmetric part) and pure rotation $\hat{\mathbf{\Omega}}$ (antisymmetric part) using the Cauchy–Stokes decomposition:

$$\mathbf{Q}_{-\theta} \nabla \mathbf{u} \mathbf{Q}_{-\theta}{}^T = \hat{\mathbf{S}} + \hat{\mathbf{\Omega}} \tag{2.18}$$

Finally, the cross-diagonal term of the pure rotation tensor $\hat{\mathbf{\Omega}}$ gives the x component of rigid-body rotation vorticity, which we define as $\omega_{RR,x}$. This quantity is used to mark the vortical flow features in our flow.

Note that the definition of solid-body rotation vorticity ω_{RR} [Eq. 2.18] is similar to that of vorticity

ω [Eq. 2.10], but vorticity is defined directly from $\nabla\mathbf{u}$ (through $\mathbf{\Omega}$), whereas rigid-body rotation vorticity is defined from $\nabla\mathbf{u}$ after the pure shear component is separated from it using the TDM method (i.e, from $\hat{\mathbf{\Omega}}$). Thus, the rigid-body rotation vorticity computed by this method is different than the corresponding vorticity computed directly from $\nabla\mathbf{u}$, i.e., $\omega_{RR,x} \neq \omega_x$.

Although the description of the method is given for the specific case of measurements on a TV plane, it can be applied to any other plane. The method was applied to all the mean TV planes to obtain $\omega_{RR,x}$, the mean SV planes to obtain $\omega_{RR,y}$, and the mean SH planes to obtain $\omega_{RR,z}$, respectively.

CHAPTER 3

Structure of 3D Coupled SBLI

This chapter will cover the flow structures observed in the case of Shock boundary layer interactions taking place at Mach 2.75 with a deflection angle of 6° using a full span wedge.

3.1 General Flow Features

3.1.1 Mean Incoming Flow Field

To set the stage for the observations that will be discussed, and because it is important to understand the incoming baseline flow, we will first briefly describe the properties of the flow generated by the wind tunnel coming into the interaction region. Figure 3.1 shows a time-averaged schlieren image of the flow around the interaction region where the main flow features are labeled and introduced in the discussion that follows. C_1 and C_2 indicate the incident and reflected shock waves, respectively; E indicates the expansion wave from the shoulder of the shock generator; W is the expansion wave associated with the interaction; and U is the upstream shock that results from the disturbed (thickened and/or separated) boundary layer, which continues as the reflected shock C_2. I is the nominal interaction point, which is defined as the intersection point of C_1 and C_2. D is a weak disturbance wave generated by a slight mismatch between the floor and the bottom access window; this wave is found to be inconsequential to the flow properties. The expansion wave E is sufficiently downstream of the interaction so that it does not disturb the flow at the

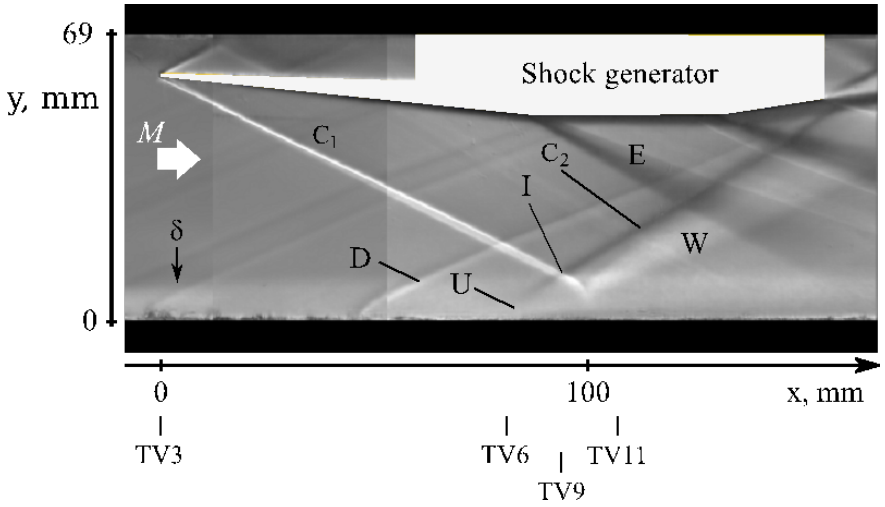

Figure 3.1: Average schlieren image of the 6° SBLI.

interaction point I. The wedge that generates the incident oblique shock is positioned such that the incident shock reaches the nominal interaction point nearly 582 mm downstream of the throat; this location corresponds to $x = 96$ mm in our coordinate system (plane TV9). Lapsa [105] showed that this location was sufficiently downstream of the throat for the incoming turbulent boundary layer to reach an equilibrium state with properties similar to those of a zero-pressure-gradient flat-plate turbulent boundary layer. In particular, Lapsa and Dahm [17, 105] performed high-resolution SPIV measurements in the empty tunnel at two downstream locations to characterize the boundary layer properties. Just upstream of the location of the nominal interaction point, and specifically at $x =$ 76 mm (which corresponded to the location of plane TV7), they estimated a (99%) boundary layer thickness δ of 10 mm with a friction velocity of $u_\tau = 30.9$ ms which is of same order of magnitude as the value computed at this location in Section 4.10. This corresponds to local Reynolds numbers of $Re_\delta = 89000$ and $Re_\theta = 9600$, where the momentum thickness θ here is based on the incompressible form.

Their assessment, however, was only limited to the state of the boundary layer near the symmetry plane of the test section. Because of the importance of the incoming flow to the properties of the

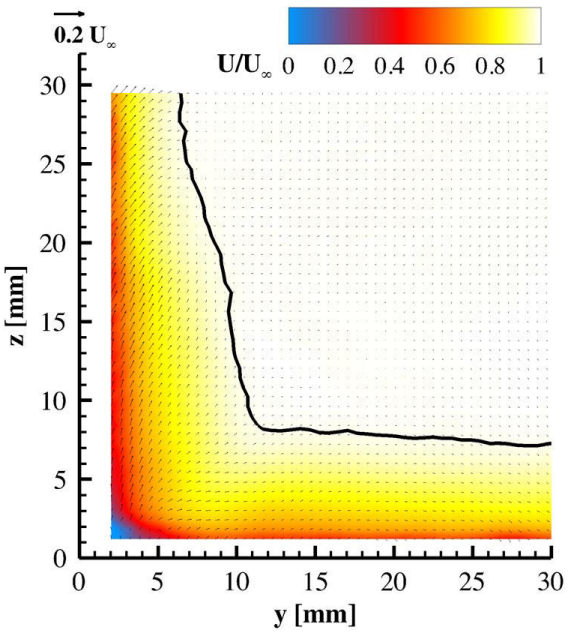

Figure 3.2: Mean velocity distribution on TV3 plane (inlet conditions). For reference, y_T = 57.2 mm, z_T = 69.3 mm.

interaction, the properties of the incoming flow, and particularly near the corner and sidewall, will be investigated first. Planes TV1, TV2, and TV3 are well upstream of the interaction region, and therefore can serve to quantify the state of the incoming flow, as well as serve as inflow boundary conditions for possible computational fluid dynamics computations. Planes TV1 and TV2 span the full width and height of the wind tunnel, whereas plane TV3 only spans the lower right quadrant (as one looks downstream) and is located at $x = 0$ mm (i.e., at the leading edge of the shock generator). As the TV3 plane is the closest of these three undisturbed planes to the interaction region, it will be discussed in more detail here.

The mean velocity field on the TV3 plane is shown in Figure 3.2, where the mean in-plane velocity components are shown as vectors and the out-of-plane component (streamwise velocity) is shown as a color contour. The solid black line indicates the local (99%) boundary layer thickness. All velocity components shown here are normalized by the freestream undisturbed value U_∞. The flow outside of the boundary layer is uniform. The boundary layers on the bottom walls and

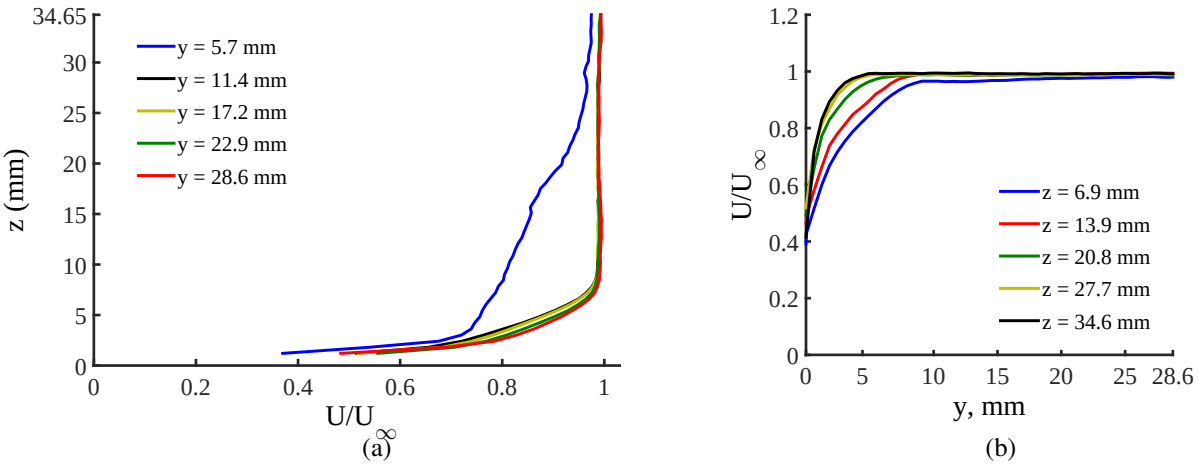

Figure 3.3: Mean streamwise velocity profiles normal to (a): bottom wall and (b): sidewall. For reference, $y_T = 57.2$ mm, $z_T = 69.3$ mm.

sidewalls develop differently. A similar trend is observed for the TV1 and TV2 planes, although the nonuniform corner region grows in size from TV 1 to TV3. Wall-normal and spanwise streamwise (mean) velocity profiles taken at different distances from the side- walls and bottom walls are shown in Figs. 3.3a and 3.3b, respectively.On the bottom wall, the boundary layer remains similar to the centerline profile up to $y = 11.5$ mm; its (99%) thickness varies from about 7.7 mm on the centerline to 8.5 mm at $y = 11.5$ mm. Conversely, the boundary layer on the sidewall has a similar profile in the upper portion of the plane ($z > 34.6$ mm), but it quickly thickens as the corner ($y = 0$, $z = 0$) is approached. In particular, the sidewall boundary layer is 6.4 mm thick at $z = 34.6$ mm and 11.1 mm at $z = 10.5$ mm. Thus, the sidewall boundary layer is thinner ($\approx 17\%$) than that on the bottom wall far from the corner but thicker as the corner is approached. The difference in boundary layer thickness between the sidewalls and bottom walls is possibly due the one-sided nature of our nozzle, which induces different pressure time histories and gradients experienced by the boundary layer on the sidewalls and bottom walls, and thus result in different boundary layer profiles on the different walls of the tunnel. This effect is also reported by Sebacher [106].

3.1.2 Mean Streamwise Oriented Flow Field around Interaction Region

In this section, we will discuss the global flow structure of the interaction from ensemble-averaged velocity fields. Figure 8 shows the mean velocity field on two SV planes where the streamwise velocity is indicated in the color contour with superimposed in-plane streamlines. The sonic line, which is here defined as the iso-contour line of streamwise velocity equal to the speed of sound evaluated at the stagnation temperature, is also shown as a dashed line for reference as a convenient way to approximately indicate the extent over which the boundary layer is affected by the interaction: no particular physical meaning is necessarily attached to this iso-contourline. Figure 8a shows the SV1 plane, which is on the centerplane of the duct and is centered on the interaction region (I in Figure 5). On this plane, the overall flowfield resembles the classical two-dimensional interaction described by Babinsky and Harvey [27] and Dlery and Dussauge [26], and it is generally consistent with the schlieren image of the flow in Figure 3.1. The labels in Figure 8a follow the flow features described in Figure 3.1. Note that the ensemble-averaged field presented here is compiled from all realizations and does not show mean separation on the centerplane (at least within the measurement region). In the SV3 plane (Figure 8b), which is located at about y = 17 mm from the sidewall, the overall flow structure begins to change as a consequence of the sidewall, as observed by Helmer et al. [59]. In particular, the effect of the reflected shock begins to smear out. Furthermore, the projected point of incidence of the incident shock on the bottom wall moves upstream relative to SV1 (from about x = 120 mm to x = 110 mm, respectively), although the shock angle remains unchanged. It has to be pointed out that both the incident and reflected shock angles are somewhat larger than the inviscid solution, whereas the flow deflection past the incident shock is estimated from the velocity measurements to be about 5.2° on centerline and reduces to 3.8° as the wall is approached (y = 17 mm plane). Furthermore, the two-dimensional streamlines on planes approaching the sidewall become curved past the incident shock, unlike inviscid theory would predict. This deviation, which is contrary to the observation by Helmer et al. [59], is most

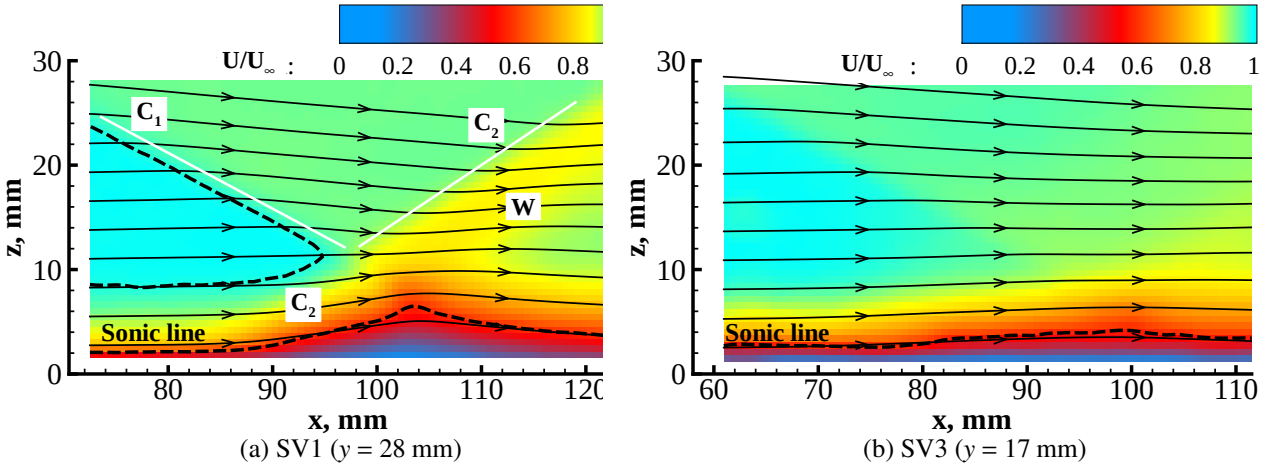

(a) SV1 (y = 28 mm) (b) SV3 (y = 17 mm)

Figure 3.4: Ensemble averaged streamwise velocity fields in SV planes.For reference, y_T = 57.2 mm, z_T = 69.3 mm.

likely due to the lateral flow effects caused by the swept-shock/corner flow interactions.

3.1.3 Pressure Variation around the Interaction Region

The free interaction theory [35] predicts that, for our flow configuration, the pressure increase across the interaction region for incipient flow separation is about 2.2: a pressure ratio which is also equal to the value of an inviscid 2D interaction. A similar conclusion is also valid for the sidewall interaction that is described by Korkegi [40]. Figure 3.5 shows the pressure distribution measured along the wind tunnel at different locations on the bottom walls and sidewalls. Consider first the pressure profile measured on the bottom wall. It was measured along the centerline (corresponding to SV1; Figure 3.4a). The wall pressure is seen to rise smoothly across the interaction region, peaks at a value of about 2.3 near x = 105 mm, drops and remains constant at about 2.2 up to x = 140 mm, and then decreases. The decrease afterward is attributed to the presence of the expansion wave originating from the end of the compression surface on the shock generator (see E in Figure 3.1). Therefore, although significant thickening of the boundary layer near the centerline is observed, mean flow separation does not occur. In this respect, the interaction can be classified as weak on

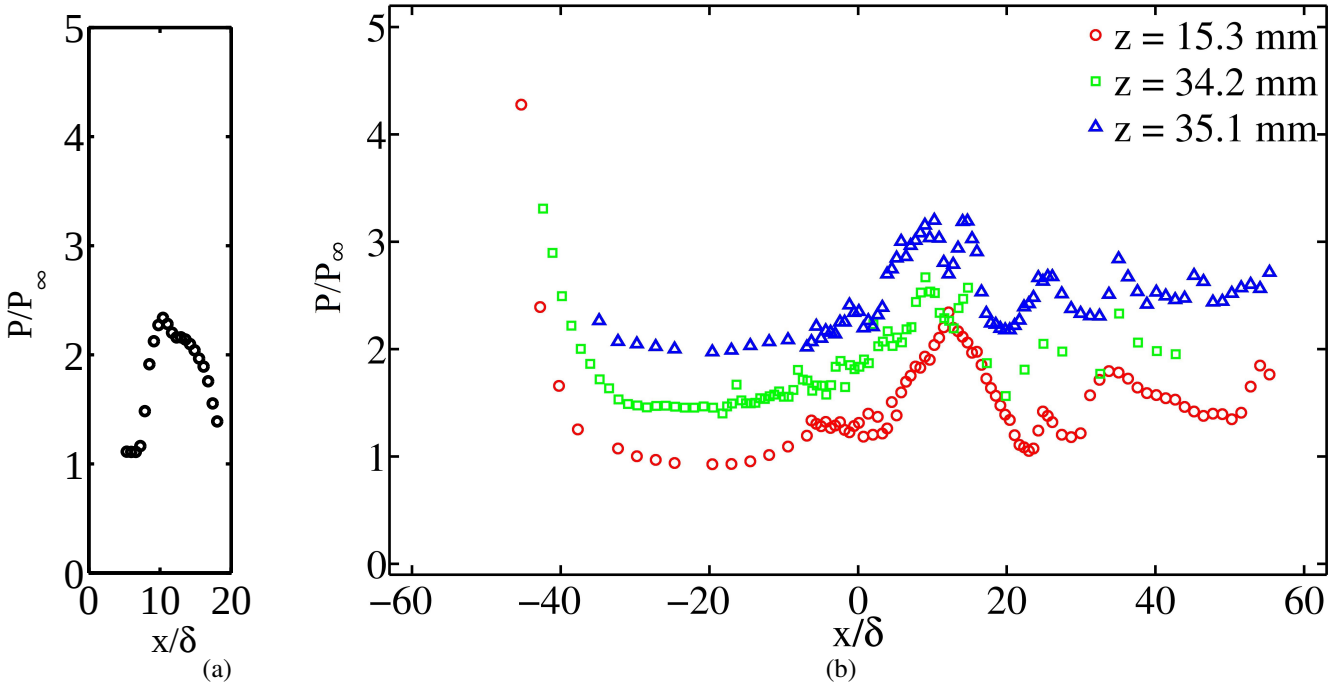

Figure 3.5: Average pressure distribution on the (a) centerline of the bottom wall and at (b) various wall-normal locations on the sidewall ($y = 0$) of the wind tunnel. Pressure data at ($z = 34.2$ mm and 35.1 mm) have been offset vertically by one unit for clarity.

the centerline; overall, it has features similar to a purely two-dimensional interaction. We will see, however, that, overall, the interaction is highly three-dimensional and the properties of the interaction on the SV1 plane are the result of SV1 being a plane of symmetry. On the sidewall, the pressure distribution follows a profile similar to the one on the bottom wall as if the pressure increase due to the interaction is spread equally across the span. The main difference is the presence of a local minimum at about $x = 120$ mm, which is attributed to the intersection of expansion wave W, E with C_2. After the interaction region, the pressure distribution decreases again due to expansion wave E.

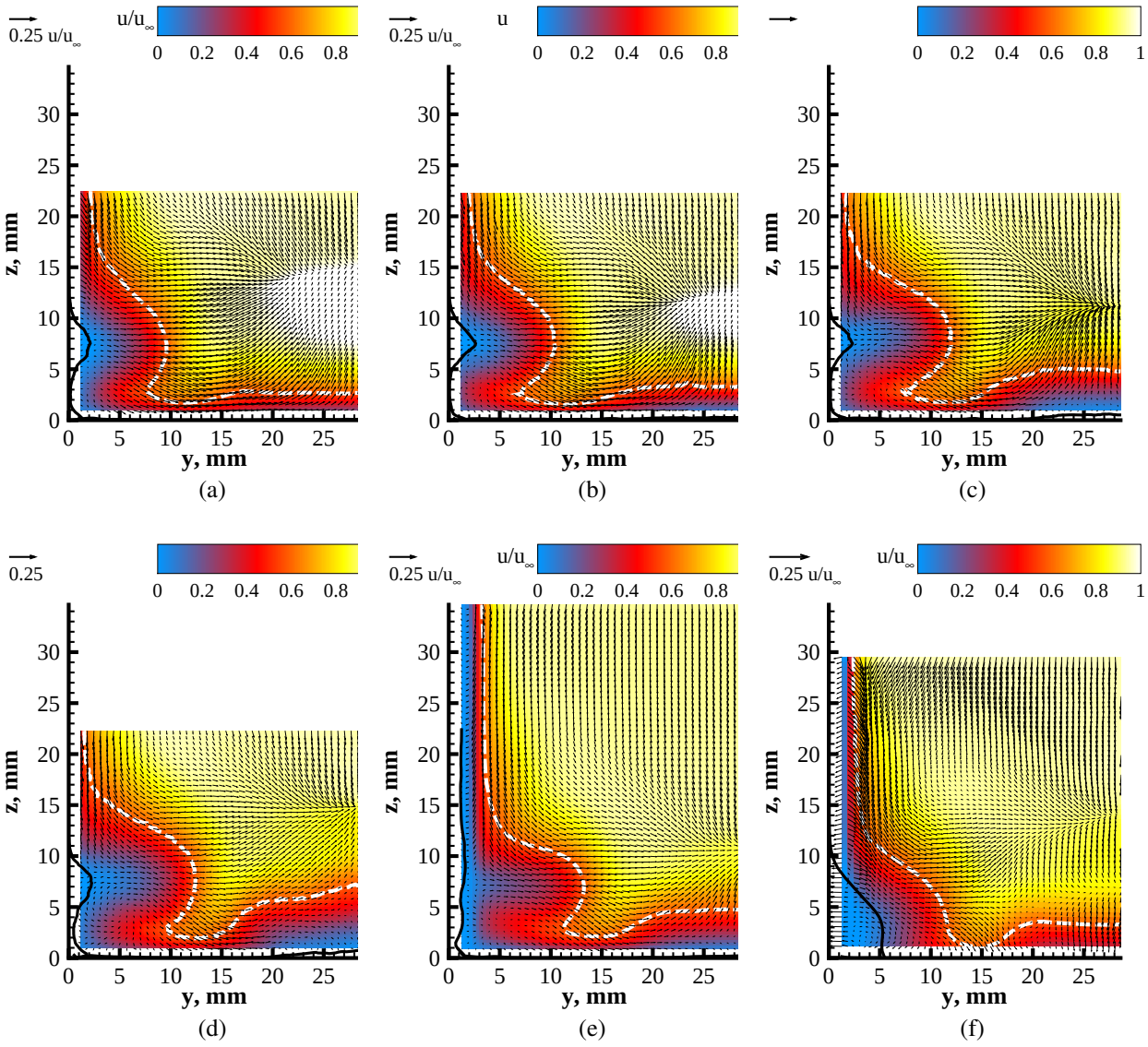

Figure 3.6: Average velocity fields on cross-sectional TV planes (a)-(f): TV6-TV11. For reference, $y_T = 57.2$ mm, $z_T = 69.3$ mm.

3.1.4 Cross-sectional Flow Field and Shock Structure

The effect on the flow field of the sidewall and corner region is better visualized by the set of measurements on selected TV planes, shown in Figure 3.6. The selected TV planes span the region immediately upstream and downstream of the nominal interaction region. In particular, Figure 3.6 shows planes TV6 through TV11, which cover a region from 15 mm(1.5δ) upstream of I to 10 mm(1δ) downstream of I. In these figures, the white dashed line indicates the sonic line as defined previously, whereas the black solid line indicates the edge of the separated flow h as defined in section 2.2.1. The measurement region on these planes approximately spans the lower right corner of the wind-tunnel cross section when looking in the direction of the flow. Plane TV6 (Figure 3.6a) is approximately located at the beginning of the region of upstream influence, where the boundary layer near the centerline has not yet thickened (see Figure 3.4a). With reference to the earlier Figure 6, we observe that the flow at the corner has strongly evolved: from just a thickening of the boundary layer at the corner (Figure 3.2) into a bulge with a strong velocity defect on the sidewall that protrudes into the core flow. The modification of the corner flow region into what we observe is primarily due to the presence of the incident shock wave interacting with the sidewall boundary layer and the corner flow itself. As the flow evolves downstream, the velocity defect bulge grows deeper into the flow, reaching about one-quarter of the span by TV10. In plane TV7, a low velocity region near the tunnels centerline also begins to appear and grows up to plane TV9, after which it collapses and disappears by TV11. This is the region on the bottom wall affected by the interaction (which does not separate in the mean, as we will assess subsequently), and it is consistent with that shown by the field in plane SV1 (Figure 3.4a). Note also that this region is located only around the centerplane of the tunnel,but it does not reach the sidewall. In fact, it appears to close as the low-velocity bulge near the corner is reached. Thus, at least in the specific case of this study, the bottom wall and sidewall boundary layer interactions are not directly connected to each other.

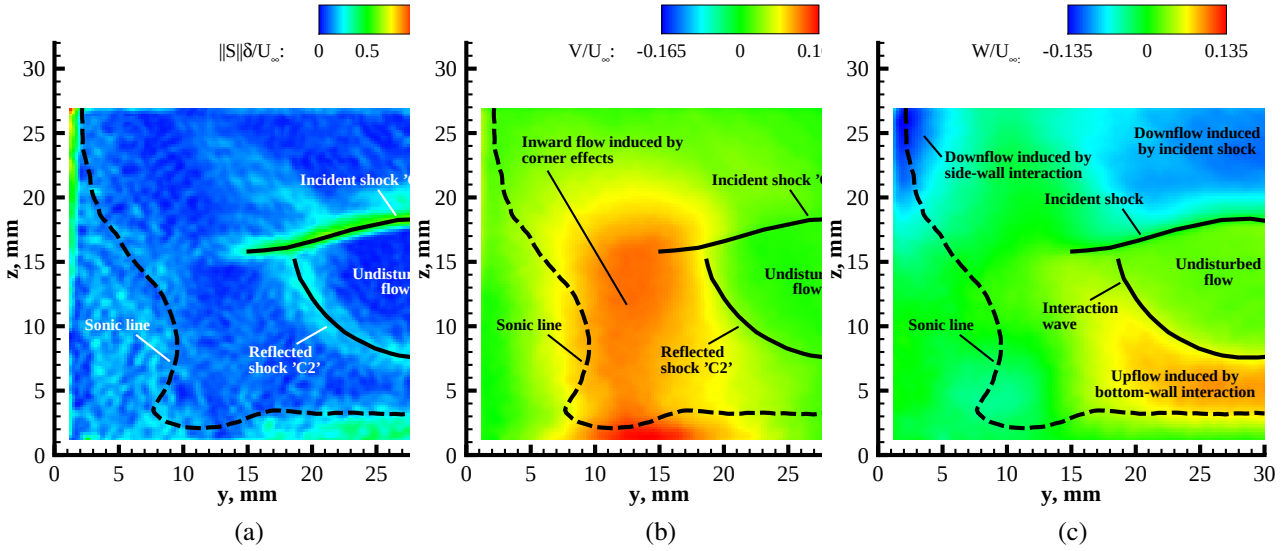

Figure 3.7: Average fields at TV6 showing (a): in-plane strain norm, (b): velocity component V,(c): velocity component W. For reference, $y_T = 57.2$ mm, $z_T = 69.3$ mm.

To further investigate the flowfield structure in relation to the incident/reflected shocks, the shock structure is extracted from a measure of the in-plane strain inferred from the in-plane spatial gradients that the measurements allow. In particular, the norm of the in-plane strain rate is defined as

$$\|S\| = \sqrt{S_{yy}^2 + S_{zz}^2 + S_{yz}^2} \tag{3.1}$$

where $S_{yy} = \frac{\partial V}{\partial y}$, $S_{zz} = \frac{\partial W}{\partial z}$, and $S_{yz} = \frac{1}{2}\left[\frac{\partial V}{\partial z} + \frac{\partial W}{\partial y}\right]$ are the in-plane strain components obtained from the measurements.

Figure 3.7a shows the norm of the in-plane strain rate on the TV6 plane, with the major shock and flow structure identified by black lines. The incident shock wave is identified as the region of maximum strain. Unlike a truly 2D interaction, the incident shock is somewhat curved, as has been studied by Alvi and Settles [4], Kubota and Stollery [3],Lu [36], Panaras [37],Wang et al. [107], and Knight et al. [38]; it does not extend to the sidewall but, rather, it dies out at about one-quarter of the span from the sidewall. This is consistent with the previous observation that the bottom wall

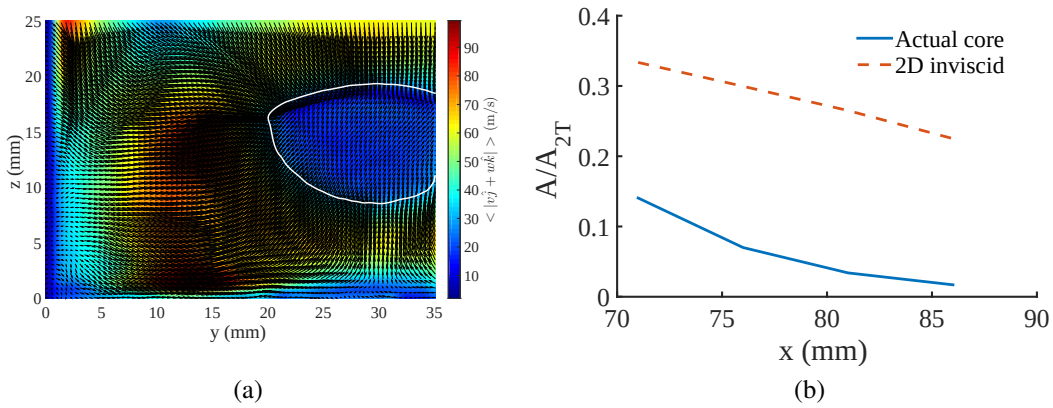

Figure 3.8: (a) Plot showing mean $|v\hat{j} + w\hat{k}|$ in TV6 with iso contours of $0.1U_\infty$ showing the core flow area (b) Streamwise evolution of core flow area. For reference, $y_T = 57.2$ mm, $z_T = 69.3$ mm.

interaction extends only up to about one-quarter of the span. The sidewall does not appear to be affected by regions of concentrated large strains. This effect could be attributed to the existence of shock waves. In general, the incident shock exhibits characteristics similar to those shown for plane TV6 (Figure 3.7) on TV planes up to plane TV9. Below the incident shock, we can also observe the formation of the reflected wave induced by the thickening of the boundary layer on the centerplane, which begins at about $x = 86$ mm. The reflected wave in Figure 3.7 would form the upstream part of the incident shock lambda structure reported in many previous studies [22, 26, 45]. In contrast to the incident shock, the reflected wave is highly curved upward and terminates at the incident shock. To the left of the point where the incident and interaction waves meet, the flow is disturbed by the presence of the sidewall and, more importantly, by the low-velocity region (bulge) identified in Figure 3.6. Between the incident and reflected shock is the undisturbed flow, which at this location only covers a small area of the full cross section of the wind tunnel (see also Figure 3.6a). For example, at this location, if the interaction of the incident shock were 2D and inviscid, then the region of undisturbed flow would be the region below the $z = 18$ mm line, or about five times the size (area) of what we observe in this 2D interaction. Thus, the strong three-dimensionality of the interaction results in a significantly reduced core cross-sectional area, even at the early stages of

the interaction. This effect of three dimensionality can be observed by quantitatively comparing the streamwise core flow area of the current configuration with inviscid theory as shown in Figure 3.8b. The core flow area is defined as the area enclosed by the iso-contour of $0.1U_\infty$ on the contour map of mean magnitude of secondary flow vectors (Figure 3.8a). The general shock structure shown on plane TV6 is also observed for planes upstream of the nominal interaction location, i.e., up to TV8. At plane TV8 (not shown), the incident and reflected waves intersect and cross. The distortion of the flowfield resulting from confinement effects can also be further visualized by the V and W -velocity color contours of Figures 3.7b and 3.7c (superimposed on the shocks identified in Figure 3.7a). With reference to Figure 3.7b, the presence and evolution of the low-velocity region at the corner induces a strong inward (i.e., from the sidewall toward the centerplane) flow; this inward flow region does not reach the centerplane, but it is bounded by the incident and interaction waves. Similarly, the interaction of the incident shock on the centerplane induces an upflow from the wall into the core flow; the region of upflow is bounded by the bottom wall and the upwardly curved interaction wave. Similarly, the incident shock induces a downflow (bounded by the wedge surface) in the region around the centerplane only. Finally, a strong downflow (about 10% of the undisturbed streamwise speed) on the sidewall is also present. This region is bounded in a narrow region at the sidewall for z larger than 21 mm in this case. Although the 2D strain field computed from the measurements does not reveal the presence of a sidewall shock, we conjecture that this downflow is induced by the presence of a swept-shock-like interaction on the sidewall generated by the incident oblique shock. Many of these wall-normal velocity features were also observed by Helmer et al. [59].

3.2 Intermittent Flow Separation

The boundary layers on the bottom walls and sidewalls do not separate in the mean but only intermittently. The characteristics of the intermittent separation are investigated by extracting the edge

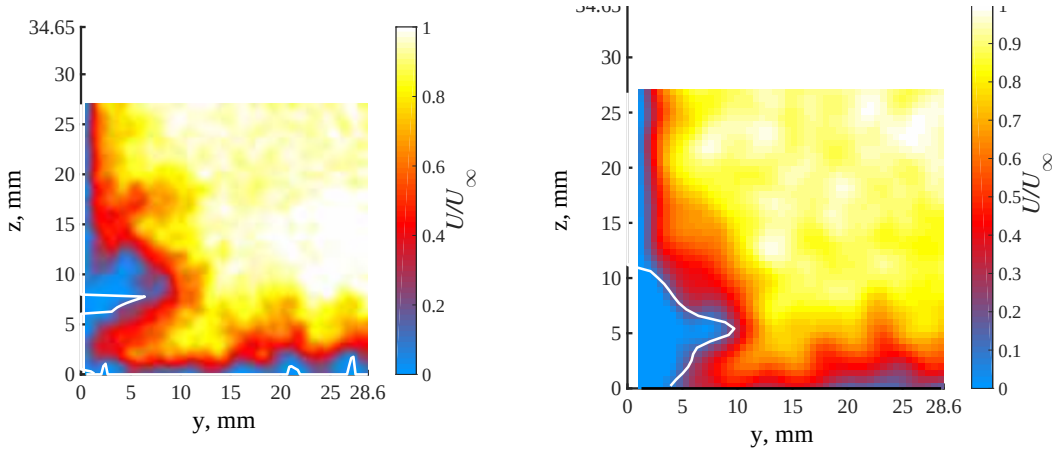

Figure 3.9: Instantaneous u-velocity fields superimposed by separation bubble profile at (a): TV6 (x = 81 mm) and (b): TV11 (x = 107 mm). For reference, y_T = 57.2 mm, z_T = 69.3 mm.

of the separated flow from the set of uncorrelated instantaneous measurements used to construct the ensemble-averaged fields shown previously. Two different methods as discussed in section 2.2.1 have been used. In the first method (AVT), an intermittency of separation map was constructed by computing the local probability of finding an instantaneous streamwise velocity less than a threshold value indicative of separation[i.e., by defining a probability of reverse flow, PRF]. Different threshold values ranging from 0 to 60 m/s ($0.1U_\infty$) were considered, but all cases showed similar results. Here, we show a case with threshold value of 25 m/s, which is about twice the minimum velocity we can measure with our setup and instrumentation. This value was selected to account for limitations of our measurement configuration in measuring low velocities.

We compute the separation bubble extent and properties as defined in Section 2.2.1.1 using the other method. TV5 to TV13 planes, which lie around the interaction region, are analyzed for detecting separated flow. Transverse-vertical planes are chosen for this analysis, since they provide for a cross-sectional projection of the separation bubble perpendicular to the core flow direction, which is then used to infer the effective area unavailable to the flow.

Figures 3.9a and 3.9b show a representative instantaneous view of the separation bubble height profile h_k (black solid line) superimposed on the streamwise (out-of-plane) velocity color contour of planes TV6 (1.5δ upstream of the incident shock impingement) and TV11 (1δ downstream of the incident shock impingement). The first observation to be made is that the region of separated flow on the sidewall is larger than that on the bottom wall, and it is most prominent near the corner of the tunnel. For the location and specific instant shown for plane TV6, the sidewall separation close to the corner is already developed, whereas the bottom wall boundary layer near the centerplane of the tunnel is not strongly influenced by the incident shock yet. It is apparent from comparing Figures 3.9a and 3.9b that the region of separated flow on the sidewall in TV11 is larger than that in TV6, indicating growth of the separation through the SBLI. This result is also seen in the ensemble-averaged profile h (shown by solid lines in Figure 3.6) and from inspection of the probability of reverse-flow maps (shown subsequently in Figure 13).

The ensemble-averaged separation bubble height profiles h corresponding to the planes of Figures 3.9a and 3.9b are indicated in Figures 3.6a and 3.6f by the solid black line. The ensemble-averaged bottom wall separation bubble height was found to be negligible (at least within the limitations of the current measurements) and is not visible in the figures, whereas the corresponding profile on the sidewall has a non-negligible value in the mean. The area under these curves is a representation of the region in the wind tunnel where there is no net streamwise flow on average and behaves as a bluff body obstructing the incoming flow. Comparing Figures 3.6a and 3.6f, flow blockage is larger in the TV11 plane than in TV6, as the instantaneous case has also shown. Most of the contribution to the blockage comes from the sidewall separation in both planes. The bottom wall separation is nearly nonexistent in the mean at these two locations and only appears in the immediate vicinity of the expected centerline interaction. This behavior can be ascribed to the significant three-dimensional effects arising as a result of the low aspect ratio of the wind tunnel and the complex curved shock structure of the incident shock as the corner flow is approached.

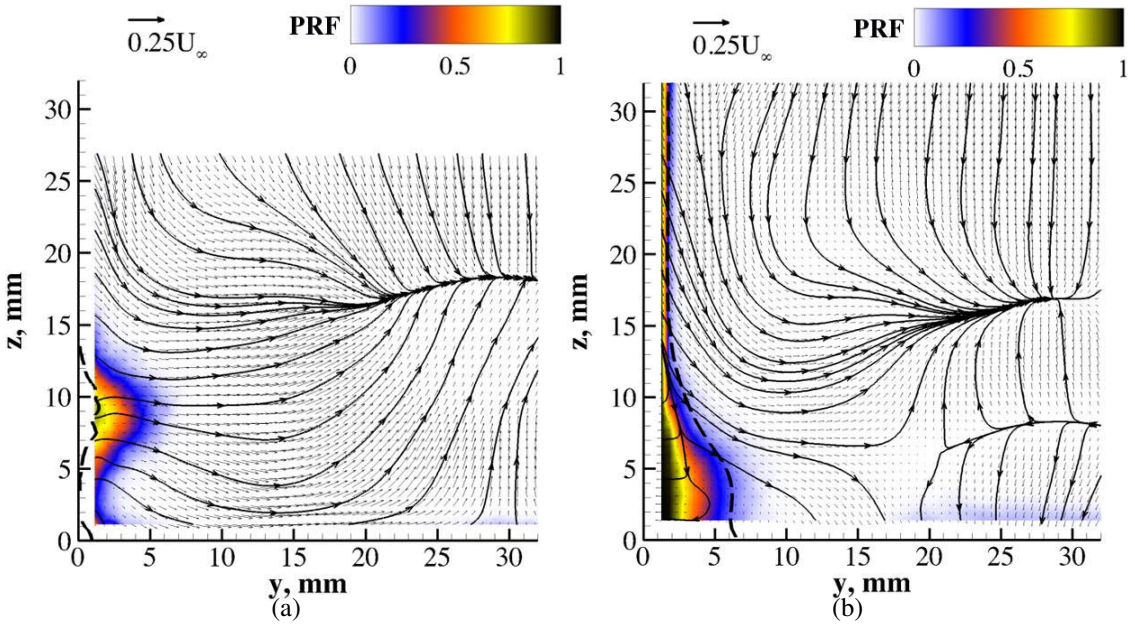

Figure 3.10: Probability of reverse flow (PRF) superimposed by separation bubble profile at (a): TV6 (x = 81 mm) and (b): TV11 (x = 107 mm). For reference, y_T = 57.2 mm, z_T = 69.3 mm.

To quantify the likelihood of observing flow separation, the probability of reverse flow for planes TV6 and TV11 is shown on Figure 13. The figures show the probability superimposed on the mean h profile (thick, black, and dashed line), in-plane velocity vectors, and two-dimensional (projected) streamlines. We observe that, on TV6, the probability of finding separated flow on the bottom wall near the tunnels centerplane is much less than 50% (within the measurement region); whereas on the sidewall, we can have flow separation up to 50% of the time within the region where the low- velocity bulge identified previously is found. For the TV11 plane, no separation is, in practice, observed on the bottom wall, whereas the sidewall and corner experience flow separation a significant fraction of the time. In the corner region, for example, flow separation approaches 100%. In both cases, the separation bubble height profile h is a good indicator of separated flow and agrees well with the probability map.

Figure 3.11a shows the probability density function (PDF) distribution of sidewall separated flow

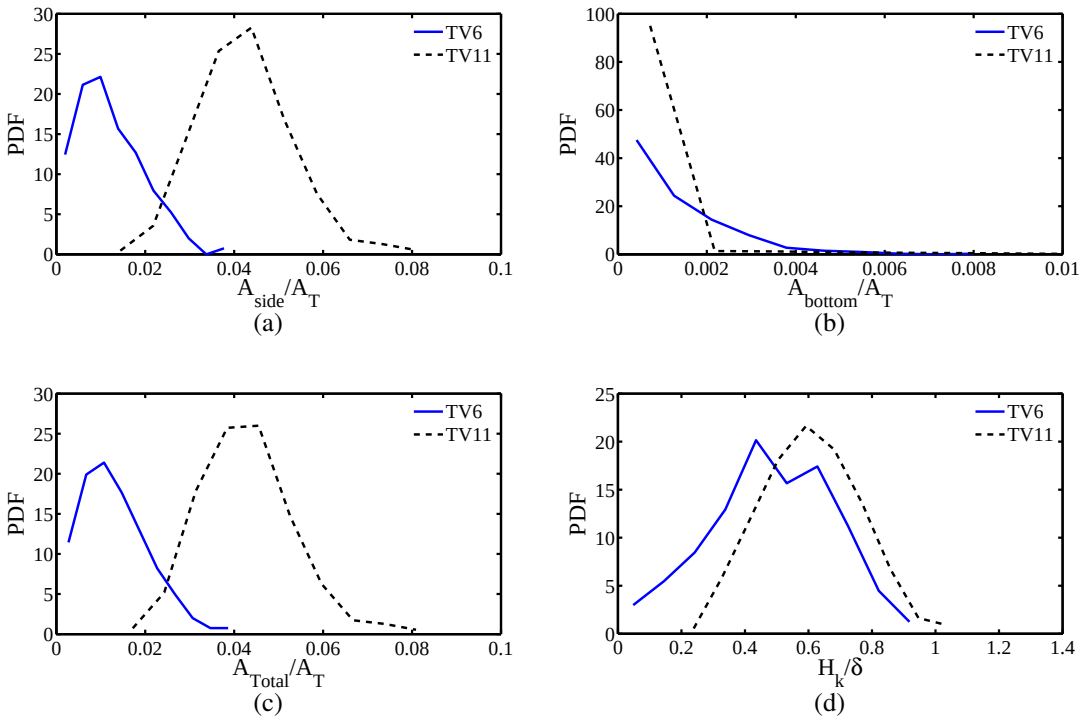

Figure 3.11: PDFs of various separation characteristics at TV6 and TV11 planes.

area A (normalized by A_T, which is one-fourth of the cross-sectional area of the tunnel) compiled over all instants for the TV6 and TV11 planes. The results are normalized with one-fourth of the tunnel cross-sectional area, as only the bottom quarter of the tunnel is studied in detail in this work; this choice gives the equivalent fraction if computed over the full cross-sectional area. The ratio AA_T indicates the fraction of the total area blocked to the incoming flow by separation. Flow is considered attached if $A = 0$. The upstream plane (TV6) has a smaller sidewall separated flow area, and separation is more intermittent than sidewall flow separation at the downstream location (TV11), as inferred from Figure 3.11a. Comparing Figures 3.11a and 3.11b, we conclude that, on the sidewall, the flow state at TV6 is more likely to be attached, whereas the flow is always separated in TV11. On the contrary, the bottom wall is more likely to be attached at both locations. However, note that the finite resolution of the measurements (relative to the boundary layer thickness and, possibly, to the size of separation that might be present) and practical limitations in measuring the flow velocity as the wall is approached could bias the measurement toward higher velocity, thus preventing correct detection of negative velocities for thin (compared to the size of the PIV interrogation window) reverse-flow regions.

Further downstream, the most probable value of the sidewall separated flow area in the TV11 plane is about 3% of the quarter-tunnel cross-sectional area A_T, and there is no case of non-separated flow, as seen in Figure 3.11a. At the most, the sidewall separation on the TV11 plane amounts to up to 6% of the wind-tunnel quarter-cross-section area.

PDF distributions of the bottom wall separation area for the TV6 and TV11 planes are shown in Figure 3.11b. It is evident that the bottom- wall separation is more probable at the upstream location of TV6; although, at both locations, the predominant state is attached flow. The hypothesis put forward by Delery and Dussauge [26] to explain reattachment is that the incident shock wave impinges on the flow around a separation bubble, which acts as a free boundary, causing an expansion wave to be reflected in the downstream direction. The expansion wave curves the detached

shear layer toward the wall, eventually reattaching it downstream of the interaction. At the same time, the influence of high pressure developed behind the shock is propagated upstream through the viscous boundary layer. This smears the adverse pressure gradient upstream of the point where the shock impinges the boundary layer on the bottom wall and causes the flow to separate. In Figures 3.11a and 3.11b, it can be seen that most of the flow separation in our flow configuration comes from the interaction of the shock with the sidewall boundary layer and the corner flow, and not from the interaction with the bottom wall.

PDF distributions computed for the total separated flow area (i.e., the sum of the separated area on the sidewalls and bottom- walls) from all the images of the TV6 and TV11 planes are shown in Figure 3.11c. For the most part, these PDF distributions follow the profiles for the corresponding sidewall separated flow area. Separation is more probable and larger in the region downstream of the interaction than the upstream plane.

Figure 3.11d shows the PDF distribution of the sidewall (maximum) separation bubble height H_k (normalized by δ) for the two planes considered here. This quantity represents how far the region of separated flow stretches into the undisturbed flow. A value of H_k equal to zero corresponds to a nonseparated case. It is worth noting that, past the interaction zone, the separation bubble is more likely to stretch toward the core flow than in the upstream region. On the upstream plane, the separation bubble height extends up to 0.5δ; whereas on the downstream plane, it reaches one boundary layer thickness.

The analysis presented previously was repeated for the planes around the interaction region to obtain the variation of separated flow properties with respect to the streamwise direction x. The streamwise variations of the ensemble-averaged total, bottom wall, and sidewall separated flow areas (computed over all instances) are shown in Figure 3.12. Since the relevant measurements started at a streamwise location of $x = 76$ mm, the data are linearly extrapolated to zero (solid lines) to obtain the upstream point of separation, which is found to be around $x \approx 70$ mm. It can also be

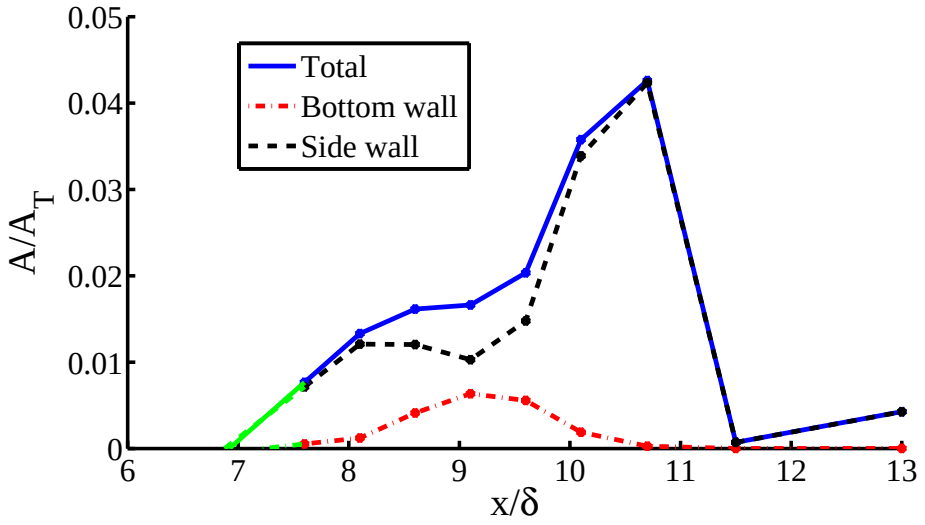

Figure 3.12: Streamwise distribution of mean separation area.

seen that the bottom wall separation bubble reattaches upstream of the sidewall reattachment at about $x \approx 110$ mm. These values are also supported by the static wall pressure measurements made on the bottom wall centerline, as shown in Figure 3.5. It can be seen from the pressure measurements that a sharp adverse pressure gradient is developed at about $x \approx 75$ mm, causing the flow to (intermittently) separate, whereas a strong favorable pressure gradient between $x \approx$ 100 mm and 120 mm causes the flow to reattach on the bottom wall. The static wall pressure measurements on the sidewall follow the same trend of the streamwise variation of separated flow area. In particular, the decrease in the sidewall separated flow area around $x \approx 90$ mm corresponds to the local dip in pressure and the favorable pressure gradient observed about the vertical midplane ($z = 34.7$ mm), whereas the maximum of the sidewall separated flow area corresponds to the second peak in the pressure plots observed about the vertical midplane ($z = 34.7$ mm) around $x \approx 110$ mm. Note that the local minimum around $x \approx 90$ mm is not observed in the pressure plots taken at $z = 15.2$ mm. The absence of the pressure minimum at this position could be caused by corner effects and the resulting shock system that may tend to smear out pressure variations.

It can be seen from Figure 3.12 that most of the contribution to the total separated flow area

comes from the sidewall separation. This is particularly true after the nominal interaction. The area of separated flow on the bottom wall grows from $x = 70$ mm, peaks around the nominal interaction location ($x \approx 96$ mm), and then decreases to zero immediately after the interaction. On the other hand, the sidewall separated flow area increases above the value for the bottom wall in the region leading to the nominal interaction region, drops to a local minimum value around the nominal interaction region, and then further increases after the nominal interaction location. At the nominal interaction location, where separation on the bottom wall is at its strongest, the bottom wall separated flow area accounts for about 35% of the total separated flow area. Thus, overall, separation on the sidewall is the largest contribution to areas of separated flow. We note that, at least for a low-aspect-ratio duct, this result could impact the placement and testing of various boundary layer control devices and injection systems that have previously been installed primarily on the bottom walls of supersonic inlet geometries, such as in the studies by Bruce and Babinsky [55], Lapsa [105], Lu et al. [108], and McCormick [109], to name a few.

The dominance of separated flow on the sidewall is attributed to the strong three-dimensionality of the flow caused by the SBLI. In the region just before the nominal interaction location, the bottom wall separation zone strengthens due to the adverse pressure gradient from the shock that is felt upstream, and it may cause the sidewall separation zone to weaken (relative to the incoming state) in the same region. Nevertheless, the contribution of sidewall separated flow to the total separated flow remains greater than the contribution of bottom wall separated flow. After the nominal interaction location, the bottom wall separation reattaches due to the expansion fan reflected from the incident shock. But, at this position, the 2D effects of the interaction associated with sidewall-induced flow deflection toward the center of the duct (and, overall, important because of the low aspect ratio of the tunnel) dominate. As the centerline interaction is diminishing, the separation bubble size on the sidewall continues to grow in the downstream direction. The strengthening of one separation and the weakening of the other seem to indicate the existence of some coupling

between sidewall and bottom wall separated flow regions. Analysis of the separated flow size among instantaneous images did not yield any correlation between sizes, however. Another behavior worth noticing from the extrapolated curves is that the sidewall separation bubble seems to start much further upstream (around $x \approx 68$ mm) of the central interaction, whereas the bottom-wall separation bubble starts at around $x \approx 72$ mm. It is postulated that this result may be caused by the shock being curved upstream toward the sidewalls, along with viscous effects introduced by the sidewall boundary layer that tend to smear the pressure rise further upstream, thus inducing flow separation on the sidewall earlier than on the bottom wall.

3.3 Large Scale Vortical Structure in the Interaction Region

Vortex structure of the flow field was extracted using the TDM procedure described in section 2.2.2 applied to mean vector fields. A few examples of the rigid-body rotation vorticity ω_{RR},as defined in section 2.2.2 are shown in Figure 3.13 for TV planes TV5, TV9, TV12, TV13, and TV14. The TV5 data plane (Figure 3.13a) was chosen, as it offers a clear view of the vortices in the incoming flow. At this location, the flow is characterized by three primary vortices. Vortices *A* and *B* correspond to a counter-rotating corner vortex pair. Vortex *A* rotates counter-clockwise (positive vorticity), whereas vortex *B* rotates clockwise (negative vorticity). These are consistent with the findings of Davis and Gessner [7], who observed a similar vortex pair. Empty tunnel corner flows will be investigated in detail in the next chapter 4. The geometry of the vortices in our case is skewed because the wind-tunnel nozzle is contoured only on the top side. Vortex *C* is caused by the swept-shock interaction with the sidewall boundary layer. A description of the properties of a swept-shock/boundary layer interaction can be found in the work by Alvi and Settles [4]. As the flow evolves downstream, it is observed that, as the incident shock wave approaches the bottom wall, the clockwise rotating vortex *B* is constrained by the corner and its magnitude increases. It should also be noted that the structure of vortex *B* in Figure 3.13b seems to be a distorted version

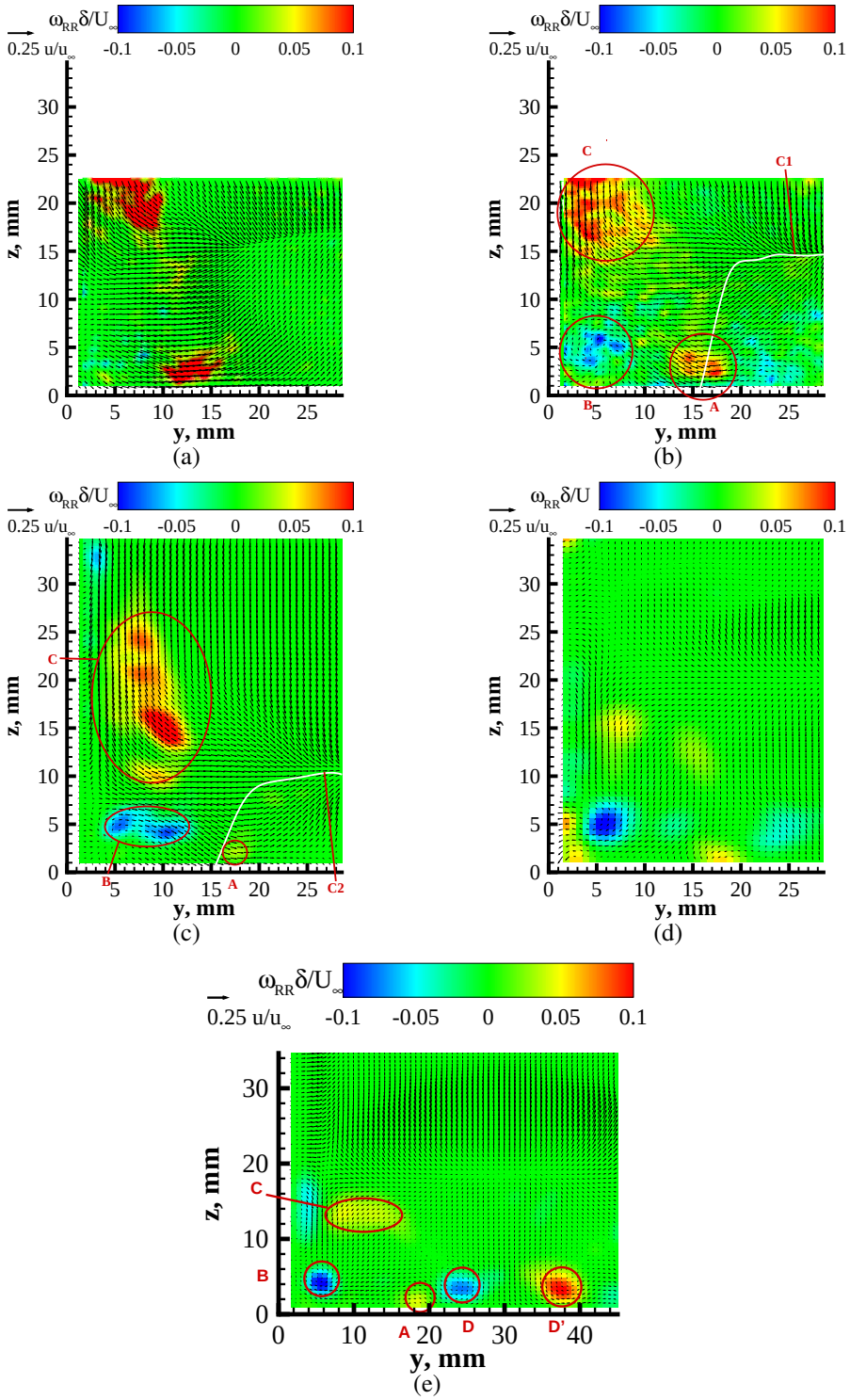

Figure 3.13: ω_{RR} fields at (a): TV5 (x = 76 mm), (b): TV9 (x = 96 mm), (c): TV10 (x = 101 mm), (d): TV13 (x = 130 mm), and (e): TV14 (x = 137 mm). For reference, y_T = 57.2 mm, z_T = 69.3 mm.

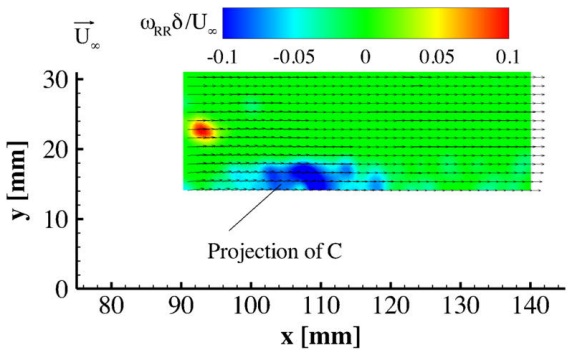

Figure 3.14: Rigid rotation z-vorticity contours with in-plane velocity vectors on SH1. For reference, y_T = 57.2 mm, z_T = 69.3 mm.

of vortex structure observed after a moderate strength oblique shock-streamwise vortex interaction in the computational studies of Zudov and Pimonov [110].

Figure 3.13d shows that, as the flow further develops downstream, vortex *C*, which is associated with the swept shock, is reflected upward from the corner vortex *B*, and it is then further deflected upward by the reflected shock.From Figures 3.13d and 3.13e, it appears that the expansion wave *W* deflects the vortex, which then strengthens and is convected downward by the stronger expansion fan E that follows. The results of Figure 3.13 also show that the corner vortex *A* moves toward the center, whereas vortex *B* is strengthened and remains near the corner. The bending of vortex *A* away from the sidewall would divert the core flow away from it, which is consistent with the oil flow visualization and the surface streamlines described by Burton and Babinsky [56] and Benek et al. [58].

Figure 3.14 shows the z-vorticity contour map on the SH1 plane (z = 9.5 mm). The negative vorticity toward the sidewall is the projection of the vorticity associated with the incoming swept shock (vortex *C*) on the streamwise-horizontal plane. The close proximity of this vortex to the bottom wall is thought to be responsible for the increased sidewall separation in the corner region.

A fourth vortex, labeled *D*, is identified on plane TV12 and the following planes. This vortex is seen to persist downstream and evolve while remaining close to the bottom wall.To better iden-

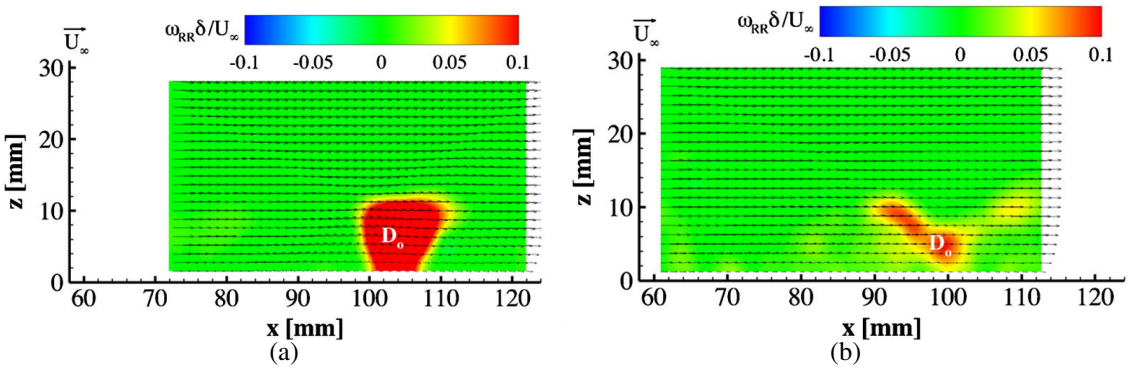

Figure 3.15: Rigid rotation y-vorticity contours with in-plane velocity vectors on (a): SV1 (y = 28 mm) and (b): SV3 (y = 17 mm) planes. For reference, y_T = 57.2 mm, z_T = 69.3 mm.

tify the origin of this vortex, we compare it with the vorticity field extracted on other planes. In particular, Figure 3.15a shows rigid-body rotation y vorticity on plane SV1, and we can identify a strong region of concentrated vorticity (indicated by D_o in Figure 3.15) about 1δ downstream of the nominal interaction region. This region of concentrated vorticity is not associated with the (intermittent) separation on centerline, but it is associated with the flow passing through the interaction above the region of separated flow. As shown in Figure 3.9, the height of the region of separated flow extends, at most, up to z = 1.7 mm, whereas the region of intense vorticity is centered around y = 5.7 mm and extends outward up to y = 8.6 mm while remaining within the boundary layer. We speculate that vortex D and vortex D_o observed on SV1 are somehow related. Specifically, our assessment suggests that they are the same vortex that forms near the centerline of the duct as a spanwise vortex (positive y vorticity), and it is then tilted symmetrically with respect to the duct centerline to aligned itself in the direction of the flow downstream to form a counter-rotating vortex pair. What we observe in Figure 3.15a is the cross section of the vortex projected on the symmetry plane as the vortex is formed at the interaction, whereas Figure 3.13e captures both legs (feature D and D')of the deflected and tilted vortex on a cross-sectional plane. Note that measurements on this plane are full span and capture the counter-rotating nature of the vortex pair DD'. (Note also the near symmetry of the flow field and vortex distribution.) The observed alternating negative-

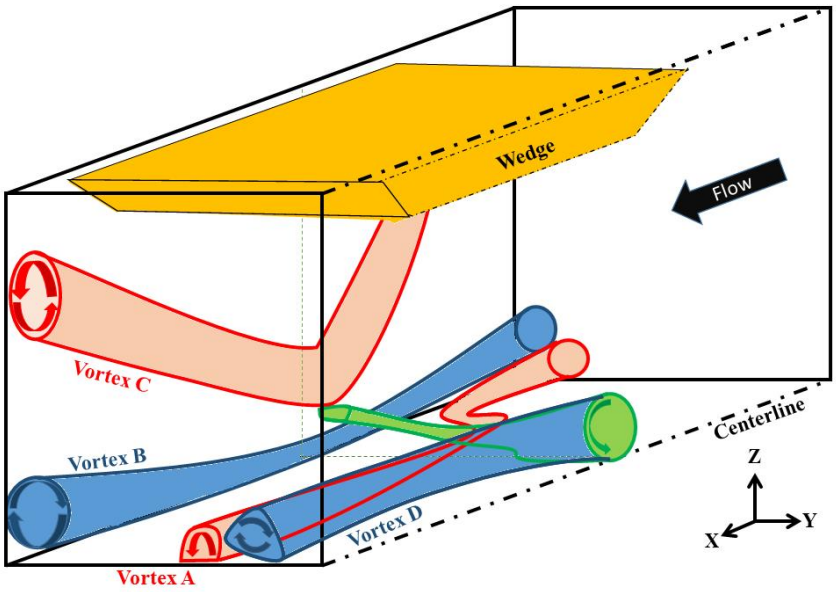

Figure 3.16: Schematic diagram of the vortex structure associated with the 3D SBLI.

positivenegative vortex tubes conforming the bottom wall would cause alternating separation and reattachment lines, as proposed by Kornilov [80], downstream of the oblique incident SBLI. The overall structure of vortex DD0 is similar to that of a horseshoe vortex formed around a bluff body in a flow. In this flow, we can relate the intermittent separation bubble on the bottom wall or even the local thickening of the boundary layer near the centerline of the duct as the bluff-body disturbance that generates the horseshoe vortex we identify in the vortex pair DD'. To conclude, note that, from a comparison of consecutive TV planes, we can also observe that the counter-rotating vortex pair DD' tends to move toward the bottom wall because the vortex dynamics drives them downward. As a result, they cause a net downward velocity on the centerline, which may then promote flow reattachment or delay any further separation on the bottom wall.

A schematic diagram that summarizes the possible 2D structure, distribution, and dependencies of the vortex systems is shown in Figure 3.16.

3.4 Role of Vortices in inducing Flow Separation

3.4.1 Corner Vortices $A-B$

Vortex pair $A-B$ is associated with secondary flows developing in the corner (described in detail in Chapter 4) that originate from the full time history of the corner flow forming the flow coming into the interaction. Thus, it is reasonable to assume that the details and response of the vortex pair to a shock may differ from one duct flow to another one. For example, recalling Figure 3.2 and the description of the incoming flow properties, the corner flow in our wind tunnel is not symmetric about the corner bisector due to the non symmetric nature of our nozzle that induces different pressure gradient and time histories on the developing boundary layer developing on the side and floor of the tunnel merging into the corner [106]. Because the corner vortex pair evolves in a flow field controlled by two opposing shock interactions on either side of the corner, the evolution of the vortex pair is strongly linked to and responds to the evolution of the other two vortex systems (C and D).

3.4.2 Swept Shock Vortex C

Vortex C develops on the sidewall and assumes the shape seen in Figure 3.13c, which is comparable to what was observed by Panaras [37] in his computations. The curved nature of the incident and reflected shocks is also apparent in Figures 3.13a3.13c, which is caused by the simultaneous existence of the two coupled shock interaction systems (swept and oblique incident SBLIs) and the low aspect ratio of the duct. Vortex C is associated with the relatively weak swept-shock interaction on the sidewall that develops as the incident shock approaches the bottom wall and then continues as part of the reflected shock system.

Using the physical model of the free (i.e., not confined by or reflected from walls) swept-shock interaction of Alvi and Settles [4] for a Mach 2.7 and 6° flow deflection angle considering the shock

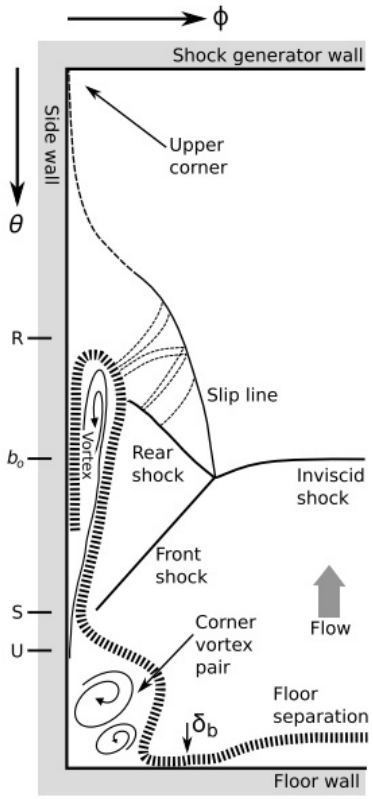

Figure 3.17: Schematic SBLI structure on a plane perpendicular to the incident shock.

normal Mach number $M_n = 1.2$ and measured $P_{post\ shock}/P_{pre\ shock} \approx 2.2$, it would be expected that the interaction results in what they referred to as a primary separation case in which flow separation consists of a single flattened spiral vortex. In our case, the interaction is relatively weak compared to the range of cases they studied, but it still falls under the primary separation case as they defined it. A schematic diagram showing the flow structure generated by a swept shock is shown in Figure 3.17. It has been adapted starting from the description of Alvi and Settles, with the addition of the confinement of the bottom wall and the other vortex features that resulted from the interaction. Because of the conical symmetry of the swept-shock flowfield, it is more appropriate to describe the flowfield in a plane perpendicular to the incident swept shock and in a conical coordinate system (ϕ, θ). What is shown in Figure 3.17 follows this view.

The separation map of the interaction along with a planar representation of the incoming and reflected shocks is shown in Figure 3.18 that will be discussed in detail in Section 3.4.3. In a swept-shock interaction with primary separation, the pressure increase due to the incident shock lifts the

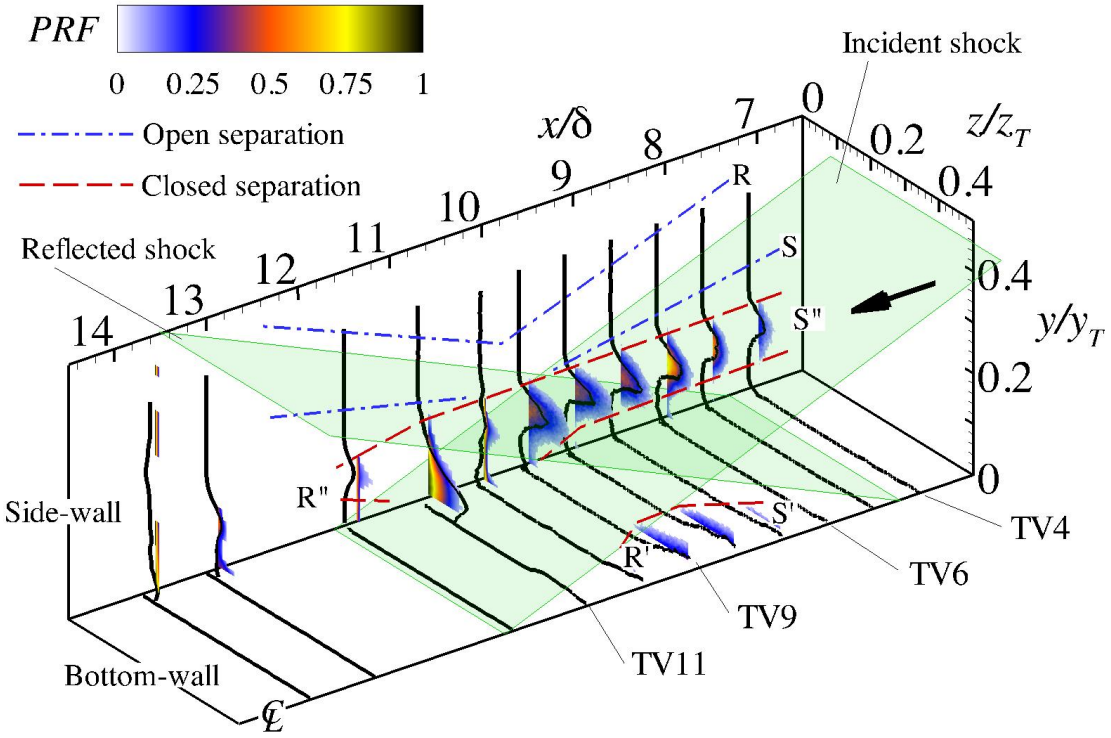

Figure 3.18: Three-dimensional plot of probability reverse flow PRF (color contour) and separation bubble height h(solid line) around the interaction region. S' and R' indicate separation and re-attachment points of the closed separation region on the bottom wall resulting from the incident shock interaction; S" and R" indicate separation and re-attachment of the closed recirculation region on the sidewall resulting from the corner; S and R are the (approximate) separation lines of the open separation from the swept shock interaction. Incident and reflected shock waves are indicative.

boundary layer (S in Figure 3.18) and folds it into the spiral vortex once it reattaches (reattachment R in Figure 3.18). The influence of the formation of this vortex propagates upstream to some point U. The separation and reattachment lines are conical, and thus is the spiral vortex itself. Because of the conical structure of the flow field, reverse flow in the laboratory frame of reference (i.e., negative streamwise velocity) might not be expected at all times, especially for weak interactions (reverse flow is, however, present in the conical coordinate system and refers to flow moving away from flow coming into the interaction, as seen in the conical coordinate system). In this respect, the conical vortex might be considered a form of open-type separation region [111–114], as discussed by Alvi and Settles [4]. The separation vortex then induces a branching of the incident shock (i.e., the creation of a λ foot) with a front and a rear shock wave. In our flow, we identify vortex C as the primary separation conical vortex in the free swept-shock interaction.

In our case, we do not have a free swept-shock interaction because of the presence of the corner and bottom wall. Furthermore, the two other vortex systems interact with vortex C, and the swept shock (along with vortex C itself) ultimately reflects from the bottom wall. To reconcile the free swept-shock model with our more complex flow field, consider the following (refer also to Figures 3.16 and 3.17). Early in the evolution, the incident swept-shock flow field forms and evolves independently and undisturbed by the constraints imposed by the corner and bottom wall. We observe the presence of vortex C on planes upstream of the interaction close to the sidewall and centered at about $z = 20$ mm from the bottom wall (see Figure 3.13), but we do not observe reverse flow (in the mean flow in laboratory frame of reference) at this location (Figures 3.6 and 3.10). This would be consistent with vortex C being a conical spiral vortex induced by the swept shock on the sidewall and providing a region of open-type separation. Below vortex C,we do observe the low streamwise velocity bulge and (intermittent) flow separation in a region close to the sidewall centered at $y = 7$ mm (Figures 3.6 and 3.10); but, this feature is associated with the asymmetric corner vortex pair, and its role in weakening the flow at the corner (i.e., by making it more prone

to separation) by asymmetrically reorganizing high- (into the lower portion of the corner close to the bottom wall) and low-momentum (away from the corner, in the upper part of it) fluids. As a result, the flow weakly separates in the bulge region upstream of the nominal interaction point away from the bottom wall (Figures 3.6a and 3.10a). Separation in this region is initiated by the adverse pressure gradient associated with the incident shock interaction (see Figure 3.5). Then, the flow more strongly separates right at the corner once the incident shock reaches the bottom wall and the corner (Figures 3.6f and 3.10b). This larger and stronger separation appears to be associated with fluid originating from the region of separated flow starting upstream and being swept down toward the corner vertex. Note that the point of maximum wall pressure is observed near TV11, which is where strong flow separation at the corner vortex is observed in Figures 3.6f and 3.10b. Note also that this region of separated flow in the corner region is of the closed type (the methods based on defining the separation bubble height profile h and the probability of reverse-flow map, shown in Figures 3.6 and 3.10, are capable of identifying closed separation only). Thus, vortex C defines a sidewall open separation due to the swept shock, whereas vortex pair $A-B$ indirectly induces a closed separation in the corner itself. Vortex C and the vortex pair $A-B$ mutually interact as the incident shock closes on the bottom wall corner to create the conditions for generating and sustaining the region of stronger separated flow near the channel corner. This thus establishes the importance of the secondary flows that exist due to a streamwise corner of a channel and necessitates their further study (Chapter 4).

The interaction between the two vortex systems also affects their trajectory. From the set of vorticity plots in Fig 3.13, we can also observe that the trajectory of vortex C is downward toward the bottom wall (see also Figure 3.16). As vortex C approaches the bottom wall, it displaces vortex B further down towards the bottom wall, which then drives vortex A toward the centerline of the tunnel, and which is ultimately bounded by vortex D and the plane of symmetry (the centerplane of the channel). Then, as the flow proceeds through the interaction, vortex C begins to follow an

upward trajectory and induces a secondary counter-rotating vortex bounded by the sidewall (Figure 3.13e). Thus, this vortex dominates the vortex system associated with the reflected shock wave near the corner (Figure 3.13d).

3.4.3 Vortex *D* and Vortex Branching

The first two vortex systems discussed so far are associated with the swept-shock interaction of the incident shock on the sidewall, the presence of the corner, and the corner vortex pair. As the incident shock finally reaches the bottom wall boundary layer, a third vortex system is formed. A signature of this third vortex system was identified by vortex D in Figure 3.13 and vortex D_o in Figure 3.15 in both SV1 and SV3. We also observe that vortex D_o appears to split in SV3. Because of the somewhat limited set of measurements, we do not have a complete view of the origin of this third vortex system. However, starting from what we discussed so far, we here attempt to reason about its origin and the overall structure from the available data. Vortex D appears to be relatively decoupled from the flow evolution on the sidewall and at the corner, although its presence may limit the evolution of the vortex pair $A-B$, which tends to be displaced outward toward the centerplane by vortex C. Combining the information inferred from Figures 3.13 and 3.15 about vortex D in the previous section, we speculate that vortex D may be part of a horseshoe vortex system generated by the boundary layer thickening or separation near the centerline of the tunnel. However, even this interpretation might be incomplete. Previous work in our tunnel by Eagle et al. [6, 115] focused on the study of the topology of the flow field primarily through oil flow visualization. That work identified some of the vortex features studied in more detail here, but it also identified a region of recirculation on the sidewall near the bottom wall interaction point. This region was associated with a focus point existing on the sidewall, and it was observed that the size of the swirling region increased with the strength of the interaction (i.e. with increasing flow deflection angle of the shock generator). Its origin was not clear, but we currently have two hypotheses about its relation

to the vortex D system.

The first hypothesis is that the swirling observed at the sidewall is associated with the closed recirculation region observed at the corner, and it is solely a result of the corner flow; whereas vortex D is the horseshoe vortex described previously. If this were true, we would expect that a similar recirculation region exists on the bottom wall at a corresponding position. Thus, the closed recirculation region would have a shape of a toroidal sector that terminates on the bottom walls and sidewalls, with one focus on either wall. Unfortunately, the oil flow visualization [57] does not show the existence of a second focus point on the bottom wall (may be due to unsteadiness or intermittency of the flow), nor do we have stereo-PIV measurements available close to and parallel to the bottom wall that could provide more insight on this possibility.

The second hypothesis we consider is that the focus point on the sidewall observed from the oil flow visualization, the vortex D_o in SV1 and SV3, and vortex D are somehow linked, as schematically shown in Figure 3.16 through a vortex branching process. The hypothesis is that a vortex spans the full width of the duct and it is anchored on the sidewall; whereas a symmetric U-shaped branching occurs somewhere between the centerplane of the duct and the sidewalls to form vortex D, which we observe on TV planes. The direction of rotation of the vortex pair DD' observed in TV planes is consistent with this hypothesis. The vortex D_o spanning the bottom wall along the y direction observed in the SV planes has a positive y vorticity. If this vortex tube were turned by 90 deg in the positive z direction of rotation, it would have a rotation in the negative x vorticity, which is consistent with the sign of rotation of vortex D in the TV planes. Similarly, the sign of rotation of vortex D' is consistent with the turning of vortex D_o by 90 deg in the negative z direction of rotation.

Spanwise vortices associated with flows past finite-span bluff bodies attached to a flat surface are widely observed and discussed in the literature [116, 117]. In our case, a streamwise adverse pressure gradient exists at the nominal interaction region. Pressure is, however, nearly uniform

across the span (refer back to Figure 8); thus, the spanwise vortex can terminate on the sidewall and it does not spill over the sides, as in the case of flow around finite-span bluff bodies [116, 117].

The studies of Tropea and Martinuzzi [116] and Chou and Chao [117] showed that the spanwise vortex formed at the bluff body could branch into a number of horseshoe U vortices as the ratio between the length L of the bluff body causing the vortex to its height d is increased. In our case L corresponds to the span of the bottom wall interaction or width of the tunnel and d corresponds to the thickened bottom wall boundary layer as a result of the interaction which would act similar to a bluff body for the incoming flow. We define this ratio as the slenderness ratio, $L^* = Ld$, and we refer to this process as U branching. In our case, we take the length to be the width of the tunnel ($L = y_T$) and the height of the thickened boundary layer at the interaction on SV1 (specifically, we take the maximum height of the sonic line in Figure 3.4a as the representative height of the body blocking the flow, and which is approximately on the order of $\delta/2$). Thus, in our case, $L^* = y_T d \approx 10$. Chou and Chao [117] considered slenderness ratios ranging from 5 to 20, and they observed the formation of no branches, one branch, two branches, and three branches as the value of L^* increased over this range. The first branching occurred for a slenderness ratio near 10. Thus, our case might exhibit vortex U branching. Note, however, that their study was performed in water flows at low Reynolds numbers, and our estimate of the size of the equivalent bluff-body size is somewhat arbitrary.

The flow recirculation structure visualized by the oil flow visualization of a stronger interaction (Mach 2.0, 10 deg deflection SBLI; study by Eagle et al. [57]) in the same wind tunnel corresponds to a case of smaller L^* (owing to larger representative blockage or d caused by the stronger interaction) and is similar to the structure of the vortex cross section observed by Chou and Chao [117] for a case of $L^* = 5.33$, where they observed no branching. However, no quantitative data are available from the stronger interaction study [57] to confirm the nonexistence of DD' in the case with a stronger interaction.

3.5 Summary

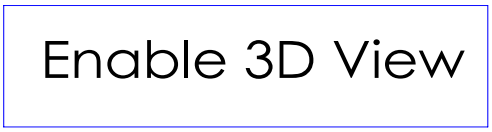

Figure 3.19: 3D interactive figure of flow structure.

Based on the quantitative and qualitative assessment of the different flow properties presented so far, a 2D schematic diagram showing the distribution of the different vortex systems is presented in Figure 3.16 (An interactive 3D version is provided in Figure 3.19). The alternating arrangement of positive and negative vortex tubes conforming to the bottom wall would be a likely cause of the alternating regions of separation and reattachments observed by Kornilov [80]. Furthermore, a 2D plot showing the probability of reverse flow (contour), the profiles of separation bubble height h (black solid line), and a schematic representation of the various separation (S, S', and S") and

reattachment (R, R', and R") lines are shown in Figure 3.18. For clarity, only the TV planes were used to construct Figure 3.18. Open-type (dasheddotted lines) and closed-type (dashed lines) separations are differentiated by the line type. For closed separation, the separation and reattachment lines are defined as qualitatively bounding regions of significant probability of reverse flow. The region between the S and R lines are only qualitatively located to represent the location of the sidewall vortex induced by the swept shock, which we associate to an open separation consistent with the primary separation flow structure of a weak swept-shock interaction (shown in Figure 3.17). Neither the probability of reverse flow nor the separation bubble height methods are capable of identifying this open separation region because these quantities are defined on the detection of reverse flow, whereas close separation does not involve reverse flow [114]. The planes are a qualitative representation (neglecting shock curvature) of the incident and reflected shock wave (angles extracted from the schlieren image of Figure 3.1).

The region of closed separation associated with the bottom wall interaction is confined in a relatively small region on the bottom wall. Its streamwise extent $L_{sep,BW}$ is only about 2δ long (somewhere between TV6 and TV10), extends laterally to about $\pm\delta$ from the duct centerplane, and is about 13δ high at most. Separation on the bottom wall is only intermittent, and the probability of observing reverse flow is only 25%.

The closed separation at the corner starts upstream of TV4 and terminates past TV12, which corresponds to a streamwise extent $L_{sep,SW}$ of at least $\approx 5\delta$ and penetrates into the duct for about 0.8δ, whereas it remains confined on the sidewall but off the corner itself until the reattachment shock is formed. The most upstream point is where flow reversal is at about 2.5δ upstream of the nominal interaction point (TV4) and shows a probability of reverse flow around 25%. The probability increases as the flow evolves in the corner, and it reaches a value near 75% at the interaction itself (around TV9). Up to the interaction point, separation is only intermittent however. Completely separated flow(i.e., 100% probability of finding reverse flow) is found only 1δ downstream of the

interaction and is observed right at the corner of the duct. The region of separated flow then slowly closes downstream at a position about 2δ downstream of the interaction (past TV12). Thus, the sidewall region is characterized by a larger region of more likely separated flow than the bottom wall region. In this sense, the sidewall interaction is said to be the dominant feature.

Recently Bruce et al. [13] and Benek et al. [14] investigated the effects of corners, sidewalls, and confinement effects on the different shock wave/boundary layer interaction configurations. Specifically related to this work, the recent computational work of Benek et al. [14] was aimed at investigating the effect of the duct aspect ratio ($y_T z_T$) and boundary layer thickness on the regions of separated flow induced by different-strength incident SBLI cases. Their results showed that, independent of the strength of the shock and duct aspect ratio, the boundary layer thickness-to-duct-width ratio (δy_T) had a primary role in determining the balance between the size and shape of the bottom wall and sidewall regions of separated flow and the overall structure of the vortical flows. In particular, their parametric study showed that, as δy_T increased, the overall morphology of the interaction and separated flow regions was strongly affected. More significantly, they found a non monotonic trend between the bottom wall separation length and δy_T: there existed an intermediate value of δy_T at which $L_{sep,BW}\delta$ was maximum. A phenomenological explanation of this behavior was that, for low values of δy_T, the two interactions developed in a decoupled fashion (effectively, one being a 2D incident SBLI, and the other a free swept SBLI); as δy_T increased, the two interactions coupled to affect each other and to limit their development. But, the dominant flow mechanism controlling the coupling was primarily the region at the corner, and not the sidewall interaction itself. For sufficiently large δy_T, the development (growth) of the bottom wall separation was effectively hindered by the constraining of the sidewall separation at the corner (not at the swept SBLI itself), which now dominated the domain with large recirculation regions and vortical structures. The swept shock might have had a role by sweeping sidewall boundary layer fluid toward the corner. Furthermore, as a result of the displacement of the sidewall flow toward the

center, the bottom wall separation size was reduced (in both the lateral and streamwise extents). The dominance of the sidewall/corner separated flow over the bottom wall centerline separation was enabled by the fact that the footprint of the interaction was convex (i.e., the influence of the bottom wall interaction was more upstream as the sidewall/corner was approached): the corner flow began to develop undisturbed upstream of the centerline separation, whereas the centerline bottom wall separation developed in the wake of the corner flow separation.

Although our study considers only two interaction strengths (freestream Mach number and shock deflection angle), the second of which will be discussed in Chapter 5 and one case of aspect ratio ($y_T z_T = 0.83$, $\delta/y_T = 0.17$), it supports the general observations of Benek et al. [14] on the dominance of the sidewall and corner interactions in low-aspect-ratio supersonic duct flow: although, quantitatively, the response of different flow properties might be somewhat different from theirs.

3.6 Conclusions

In this work, the three-dimensionality of the properties and flow structure of a shock wave/boundary layer interaction in a low-aspect- ratio supersonic duct flow was investigated. SPIV measurements on several orthogonal planes around the interaction regions were used for the study. Measurements on cross-sectional planes were of particular significance for understanding the properties and the coupling between the bottom wall (incident SBLI) and sidewall (swept SBLI) interactions. It was observed that the incident shock was deformed (curved) toward the core flow, which was in agreement with the simulations of Wang et al. [107]. Because the interaction was relatively weak (6° deflection angle), only intermittent separation was observed, which agreed with the findings from some of the cases of Souverein et al. [52]. From the data of Figures 3.6 and 3.18 on TV planes, it was found that the largest velocity defect and the highest likelihood of separation occurred near the corner region. The topology and location of these regions were different from those observed

in the oil flow experiments by Bruce et al. [13, 68] and Burton and Babinsky [56]; the primary reason for this difference would likely be the swept-shock interaction present on the sidewall in this experiment. Three-dimensional representations of the areas of flow separation (Figure 3.18) and of vortical features (Figure 3.16) were constructed to identify key features in the flow and their relative location. They revealed the complex 2D vortical flowfield that coupled that sidewall and bottom wall interactions, with the corner region being constrained by the vortices and having a larger tendency to separate. Thus, for the current low-aspect-ratio duct flow, it was concluded that the corner flowfield dominated the interaction in the sense that it was the location of the largest and more probable flow separation. The shape of the flow-separation bubble on the bottom wall was similar to that observed in the simulations of Bermejo-Moreno et al. [62, 118]. The presence of the attached flow region on the bottom wall between the bottom wall separation and the corner separation was consistent with the results of Wang et al. [107]. Furthermore, it was demonstrated that the (rigid-body rotation) vorticity was affected by the interaction of the incident shock system on the bottom wall and sidewalls, and it resulted in a system of vortices on both walls. It is noted, however, that the reconstructed structure of the vortical features was conducted from a two-dimensional surrogate of the velocity gradient tensor, which might put a limit on how these vortical features are identified.

The current flow configuration was unsteady with intermittent separation. Similar results for the case of a high Reynolds number and weak incident shock were observed on the bottom wall by Souverein et al. [52]. Conditional statistics were used to identify and quantify the locations, areas, and probabilities of separation. Maps quantifying the local probability of reverse flow and the separation bubble height h along with its statistics were constructed. Three regions of separated flow were identified from these quantities: 1) the bottom wall centerplane separation; 2) the corner flow separation; and 3) the sidewall interaction and separation. The first two regions were of the closed-type separation, whereas the third region was of the open type. The sidewall flow was

controlled by a conical vortex induced by the swept-shock interaction with no reverse flow (in the laboratory frame of reference). Bottom-wall flow (closed-type) separation was present, but the probability of observing it was only about 25% on a relatively small region. At most, its length was limited to about 2δ. The three regions were coupled, and their mutual interaction balanced their strength and size, as suggested by the study of Benek et al. [14]. In fact, the ratio of the boundary layer thickness relative to the duct size was within the range of values for it to play a controlling role on the growth of the bottom wall separated flow region, as indicated by Benek et al. [14]. A closed separation (up to 75% probability of observing reverse flow) was also found at the corner on the sidewall of the duct around TV11 (see Figures 3.10 and 3.18). This was the dominant closed separation region. The sidewall separation began well upstream (2.5δ) than the bottom wall separation and closed well downstream (2.5δ) of it. Its location, size, and strength (probability of finding separated flow) were the result of a balance between the competing development of the sidewall shock interaction, the bottom wall interaction, and the asymmetric weak corner flow generated by the one-sided nozzle.

The underlying 2D vortex structure was identified by applying the triple decomposition of motion to isolate the rigid-body rotation vorticity from the shear-related one. This decomposition was applied to a 2D surrogate form of the velocity gradient tensor that was defined based on the components made available by the current measurement configuration while neglecting the effect of compressibility. This approach provided an effective way to identify swirling motion only, as well as to reconstruct the location and 2D structure of vortical flow features that dominated the interaction. The method identified three systems of vortices: 1) the corner vortex pair (vortex AB); 2) the swept-shock vortex on the sidewall (vortex C); and 3) a horseshoe-like vortex originated from the bottom wall interaction, and possibly connected to the corner separation through a branching process. The three vortex systems approached each other at the nominal interaction region, and their combined rotational velocities exerted a strong velocity away from the wall, which tended to pro-

mote separation, particularly at the sidewall corner region (This interaction is studied in detail in Chapter 5). The bulk of the structure proposed was similar to the structure proposed by Eagle and Driscoll [6] however, the lifted type-2 vortex pair was not observed in the TDM results, possibly indicating it was a result of shear or straining phenomena. The alternating negativepositivenegative vortex tubes conforming the bottom wall would also reaffirm the propositions of alternating separation and reattachment lines, as proposed by Kornilov [80], downstream of the oblique incident SBLI.

CHAPTER 4

Empty Tunnel Corner Flows

In this chapter a description of secondary flows residing in the corner of a rectangular wind channel will be presented. The data presented here has been recorded in the Michigan glass wind tunnel at both Mach 2.0 and Mach 2.75. The corner flow structure and properties for the two Mach number cases are mostly similar. Therefore, although two cases were studied in detailed, here we report only results for the Mach 2.75 case, with some additional or representative results of the Mach 2 case for completeness and to show a few instances of the Mach 2 case.

4.1 Analysis of Velocity Fields

4.1.1 Instantaneous Flow Characteristics

An example of instantaneous velocity fields at an upstream ($x = -100$ mm) and a downstream ($x = 75$ mm) location at Mach 2.75 is shown in Figure 4.1. The in plane velocity fields are shown as vectors ($v\hat{j} + w\hat{k}$) while the out of plane velocity component (u) is shown by color contours. The $y = 0$ line represents the sidewall and the $z = 0$ line represents the bottom wall. The flow near the corners is turbulent and characterized by eddies which will be clearer in the vorticity fields in subsequent sections. We can observe that at $x = -100$ mm location, high momentum flow dominates most of the interrogation region as shown in Figure 4.1a. As we proceed downstream, we can see from Figure 4.1c that a low momentum layer is formed near the walls. A strong

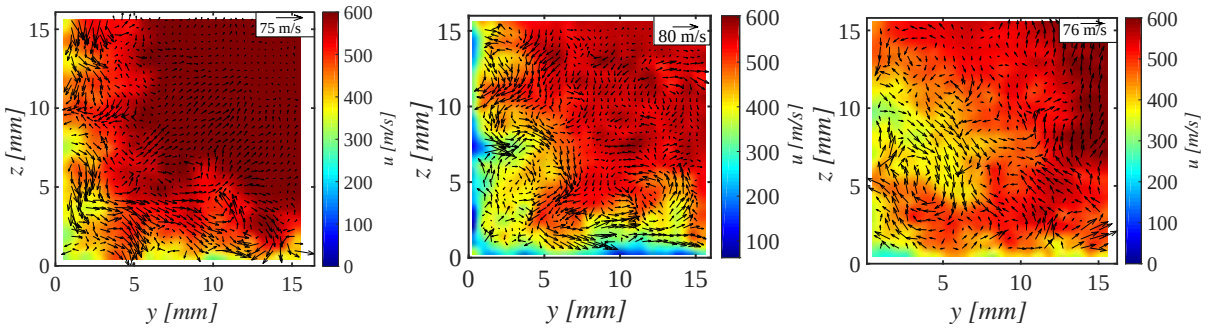

Figure 4.1: Example of instantaneous velocity field at Mach 2.75 from (a): TV1 ($x = -100$ mm), (b): TV2 ($x = -50$ mm) and (c): TV3 ($x = 75$ mm) at Mach 2.75. In plane velocity components are represented by vectors while the out of plane component is shown by the contour map. For reference, $y_T = 57.2$ mm, $z_T = 69.3$ mm.

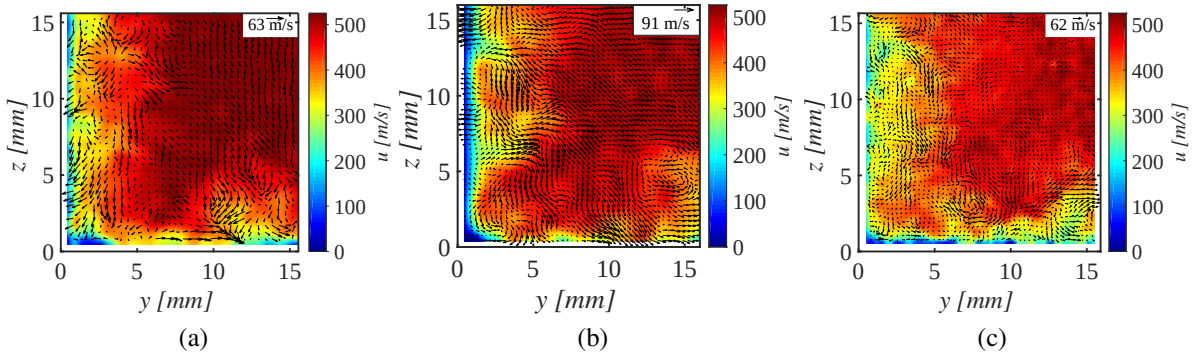

Figure 4.2: Example of instantaneous velocity field from (a): TV1 ($x = -100$ mm), (b): TV2 ($x = -50$ mm) and (c): TV3 ($x = 0$ mm) at Mach 2. In plane velocity components are represented by vectors while the out of plane component is shown by the contour map. For reference, $y_T = 57.2$ mm, $z_T = 69.3$ mm.

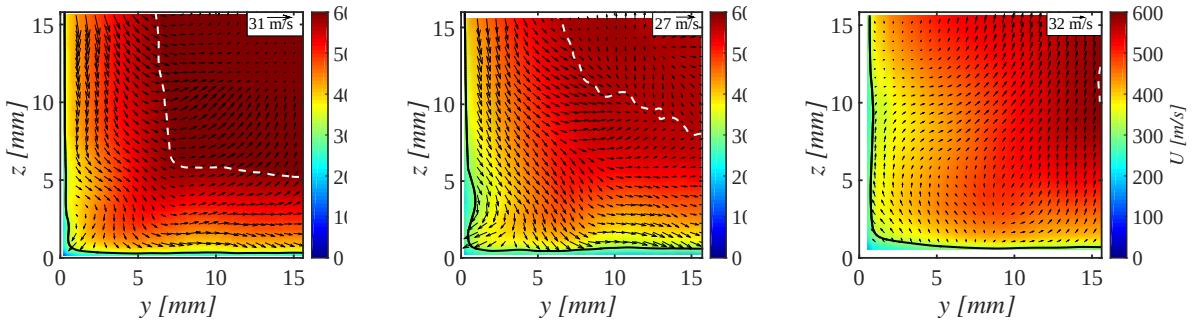

Figure 4.3: Mean velocity field on (a): TV1 ($x = -100$ mm); (b): TV2 ($x = -50$ mm); and (c): TV3 ($x = 75$ mm) at Mach 2.75. In-plane velocity components are represented by vectors while the out-of-plane component is shown by the contour map. The white dashed line represents the δ and the solid black line represents the contour of sonic velocity. For reference, $y_T = 57.2$ mm, $z_T = 69.3$ mm.

secondary turbulent flow is observed in Figure 4.1c away from the sidewall at a height of about 10 mm from the bottom wall which convects the low momentum sidewall boundary layer fluid towards the core flow. For comparison instantaneous velocity fields at Mach 2.0 are shown in Figure 4.2. The flow grows more turbulent just like Mach 2.75 fields with high momentum fluid region region being confined away from the corner towards the core flow. Low x-momentum fluid regions are observed on the sidewall and bottom wall around $z = 10 - 15$ mm and $y = 10 - 15$ mm in the TV3 plane (Figure 4.2c).

4.1.2 Mean Primary Flow Field

The mean flow fields obtained from uncorrelated sequence of images obtained at the same locations in Mach 2.75 wind tunnel are shown in Figure 4.3. The number of instances used for averaging for each location is tabulated in Table2.1. Sampling uncertainty was carried out using the least number of instances available (see Appendix B.4). Figure 4.3a shows the streamwise velocity contours of the most upstream data-plane with the streamwise flow being out of the plane. It can be seen that

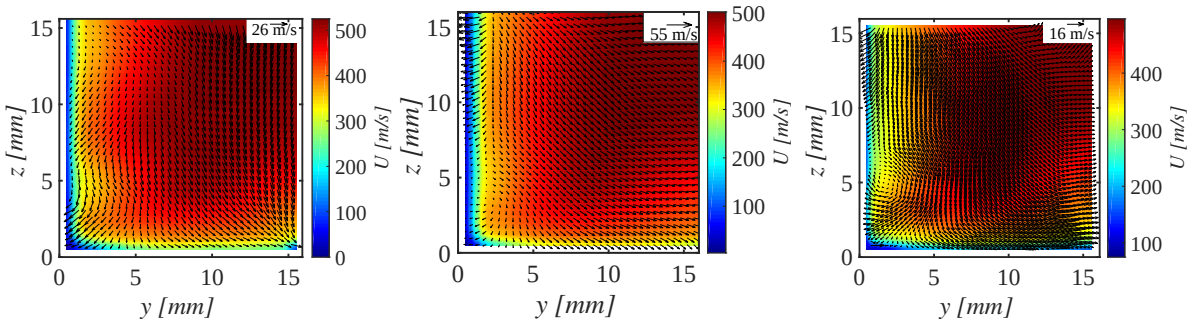

Figure 4.4: Mean velocity field on (a): TV1 ($x = -100$ mm); (b): TV2 ($x = -50$ mm); and (c): TV3 ($x = 0$ mm) at Mach 2. In-plane velocity components are represented by vectors while the out-of-plane component is shown by the contour map. For reference, $y_T = 57.2$ mm, $z_T = 69.3$ mm.

the boundary layer thickness, defined by the 99 % iso-contour line, is fairly uniform without any curvature indicating that the flow is fairly symmetric relative to the corner at this location. Also the close proximity of the sonic line to the sidewall indicates that the flow is mostly supersonic throughout the cross-section of the tunnel at $x = -100$ mm. The sonic line was computed using the local speed and assuming a calorifically perfect gas with unit Prandtl number and a T_∞/T_w value of 0.37 for Mach 2.75 and 0.41 for Mach 2 by interpolating the experimental values compiled by Spina et al. [119].

It can be seen from Figure 4.3b (plane at $x = -50$ mm) that the sidewall 99% boundary layer thickness has started to thicken towards the bottom wall before it merges with the bottom wall boundary layer. On the contrary, the boundary layer on the bottom wall remains fairly undisturbed. The sonic line now extends along the entire walls of the tunnel. Also a fair portion of the flow is subsonic at the corner.

Further downstream at TV3 ($x = 75$ mm), it is to be noted that boundary layer flow now occupies nearly the entire domain of interrogation. Low momentum region (yellow zone of the contour) can be seen bulging out (at a height of about 10 mm from the bottom wall) from the sidewall

towards the core flow indicating a momentum transport due to secondary flow. At the same time a high momentum region (red zone of the contour) can be seen penetrating towards the corner. This effect of curvature of iso-tach (constant velocity) lines has been observed by Gessner et al. [53,73], Brundrett and Baines [75] and it was associated with the underlying vortical momentum transport by Perkins [74].

Another important conclusion that can be drawn from Figure 4.3 is that the observed flow field is asymmetric unlike the symmetric/anti-symmetric flow fields about the corner bisector discussed in previous studies [7, 53, 73–75]. The primary reason for this irregularity is suspected to be the one-sided nozzle and the low aspect ratio characteristic of the wind tunnel.

Figure 4.5 shows the velocity profiles of average streamwise velocity U perpendicular to the bottom and sidewalls. As is expected the flow at the most upstream location TV1 sports a near canonical mean velocity profile (see also [120]) without any visible inflection points and seems to be similar to that of an attached flow (see $y = 5$ mm and $z = 5$ mm in Figure 4.5a and Figure 4.5b). At the downstream location $x = -50$ mm, it can be seen from Figure 4.5c and Figure 4.5d that the velocity profile now sports an inflection point near the corner ($y = 5$ mm and $z = 5$ mm). Also the velocity profile at the location of TV2 near the corner $y = 5$ mm and $z = 5$ mm sports a velocity defect compared to the profiles away from the corner as seen in Figure 4.5c and Figure 4.5d. The mean flow profile at the downstream TV3 location shows similar characteristics to the flow at TV2 location with a relatively higher velocity defect in the profile at $y = 5$ mm. Further downstream at $x = 75$ mm where the secondary flow (see section 4.1.3) is relatively well developed, it starts affecting the mean primary flow which can be seen in the velocity profiles. The streamwise velocity profile at $y = 5$ mm (Figure 4.5e is seen to have a minimum point at about $z = 8$ mm indicating that momentum transport occurs). A detailed comparison of the observed velocity profiles to the theoretically established turbulent boundary layer profiles is conducted in Section 4.11. Similar trends of momentum transport influencing the structure and morphology of primary flow field

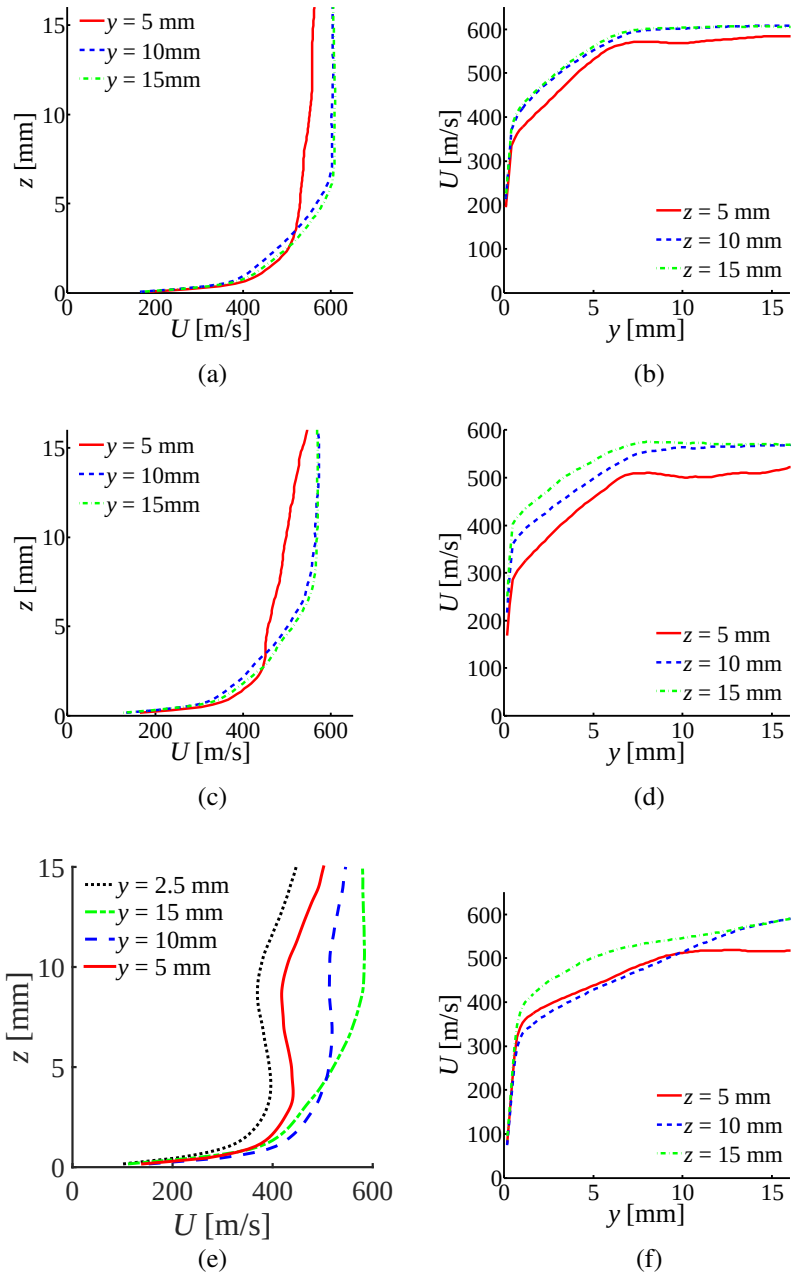

Figure 4.5: Mean streamwise velocity component profiles from (a): $U(z)$ on TV1; (b): $U(y)$ on TV1; (c): $U(z)$ on TV2; (d): $U(y)$ on TV2; (e): $U(z)$ on TV3; (f): $U(y)$ on TV3 at Mach 2.75. For reference, $y_T = 57.2$ mm, $z_T = 69.3$ mm.

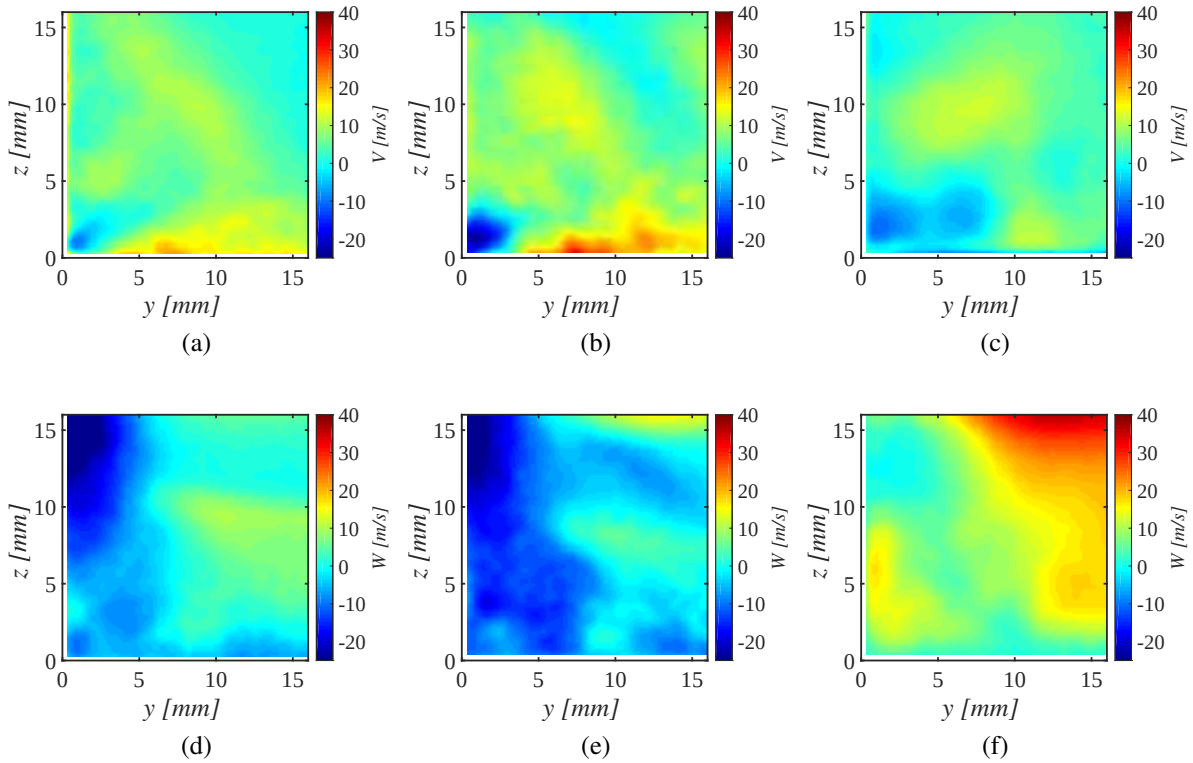

Figure 4.6: Mean secondary velocity components at Mach 2.75. Top Row: V-velocity, bottom row: W-velocity. Left column: TV1 ($x = -100$ mm), middle column: TV2 ($x = -50$ mm) and right column: TV3 ($x = 75$ mm). For reference, $y_T = 57.2$ mm, $z_T = 69.3$ mm.

were observed in the data obtained from Mach 2 shown in Figure 4.4.

4.1.3 Mean Secondary Flow Field

Contour plots at Mach 2.75 of the transverse (in-plane) velocity components are shown in Figure 4.6. Although the streamwise velocity field at $x = -100$ mm is fairly uniform, the study of the transverse velocity component field that will be presented further below reveals the presence of a weak secondary flow in proximity of the corner as is seen in Figure 4.6a and Figure 4.6d. The V-component at these locations is directed towards the corner in the immediate vicinity of the corner and then reverses direction away from the corner along the sidewall and bottom wall. As

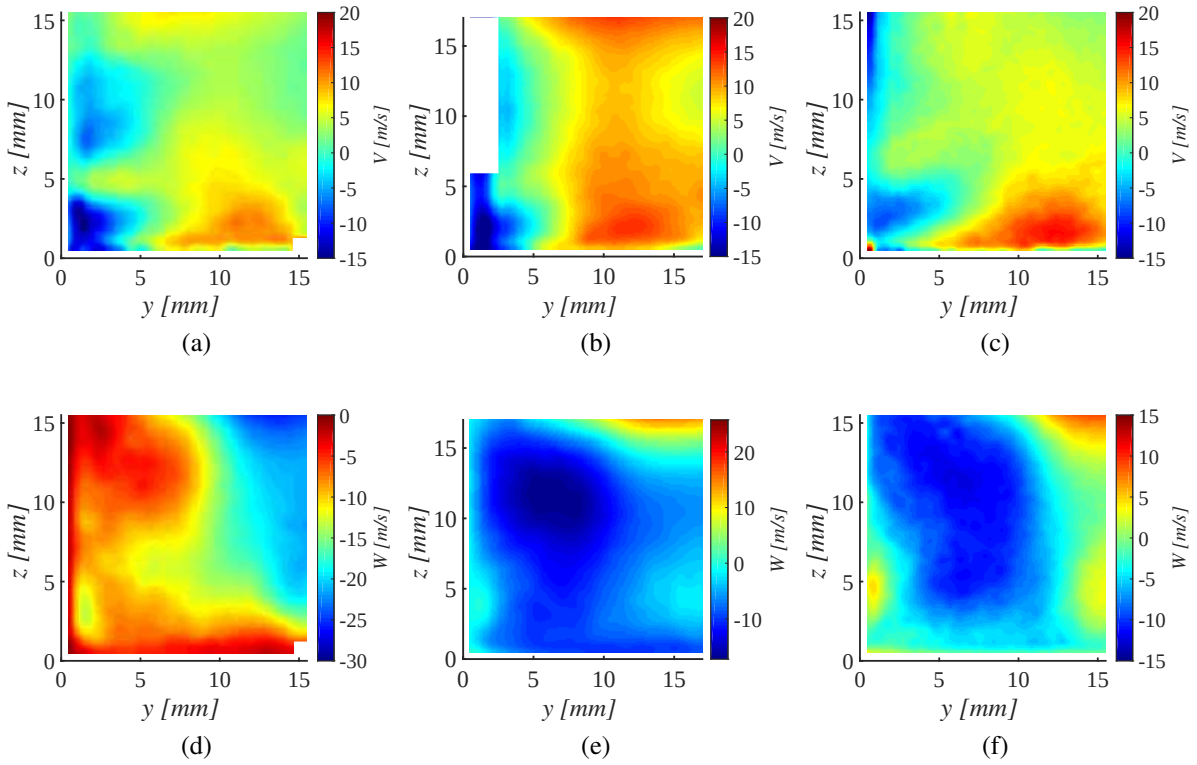

Figure 4.7: Mean secondary velocity components at Mach 2. Top Row: V-velocity, bottom row: W-velocity. Left column: TV1 ($x = -100$ mm), middle column: TV2 ($x = -50$ mm) and right column: TV3 ($x = 0$ mm). For reference, $y_T = 57.2$ mm, $z_T = 69.3$ mm.

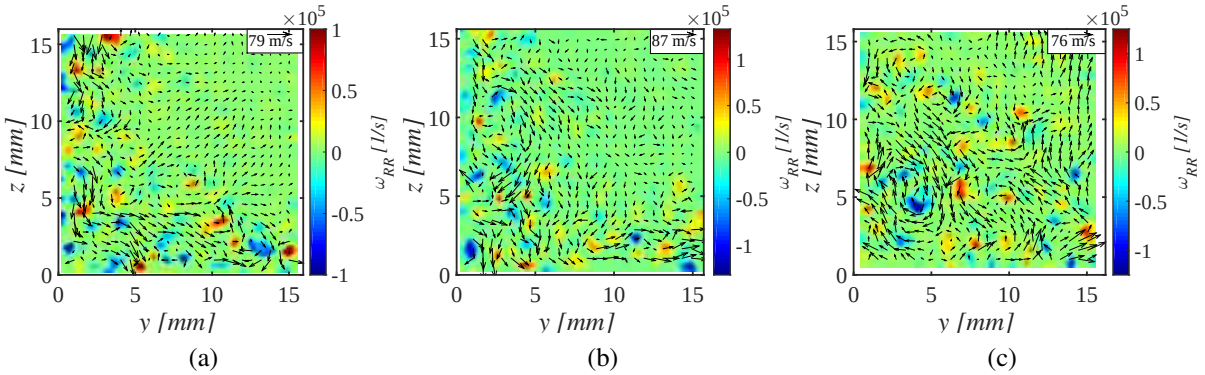

Figure 4.8: Instantaneous rigid rotation vorticity field of instantaneous vector fields shown in Figure 4.1 from (a): TV1 ($x = -100$ mm), (b): TV2 ($x = -50$ mm) and (c): TV3 ($x = 75$ mm) at Mach 2.75. For reference, $y_T = 57.2$ mm, $z_T = 69.3$ mm.

we proceed downstream the magnitude of this negative V-region initially increases at $x = -50$ mm and then decreases at $x = 75$ mm, however the size of the region increases as seen from Figure 4.6c respectively. We attribute this to an increase in spatial unsteadiness of the secondary flows at these locations. Similar observations were made at Mach 2 (See Figure 4.7).

4.2 Vortex Analysis

4.2.1 Instantaneous Vortex Fields

Because the flow in the corner is dominated by heavy shear and strain, traditional Cauchy Stokes' decomposition of motion into symmetric part (shear) and anti-symmetric (vorticity) is insufficient. The shear and strain mask the vorticity associated with vortex tubes and makes identifying the corner vortices difficult. Thus, TDM discussed in Section 2.2.2 was used to determine only the part of vorticity associated with rigid-body rotation (ω_{RR}), which makes identifying the vortex cores clearer.

Figure 4.8 shows the instantaneous rigid rotation vortex fields obtained from the instantaneous

velocity fields shown in Figure 4.1 at Mach 2.75. As we can see no large-scale distinctive corner vortex system discussed in the previous studies [7, 53, 73–75] is observed in instantaneous fields. Instead, the flow within the boundary layer near the corner is dominated by a forest of vortices or vortex tubes if a complete 3D picture is considered. The vortices tend to spread away from the walls as we proceed downstream due to boundary layer growth.

4.2.2 Mean Vortex Fields

Rigid rotation vorticity fields obtained from the complete mean flow fields of Figure 4.3 are given in Figure 4.9. It can be observed that a counter-rotating vortex system can be found conforming to the sidewall (negative vortex) and the bottom wall (positive vortex). Although this system has signs consistent with a canonical corner vortex system, its location is fairly displaced from the corner. Moreover this system is geometrically asymmetric, which may be due to the asymmetric nature of the wind tunnel. At the most upstream location of TV1, we can observe from Figure 4.9a that a negative vortex exists along the sidewall at about $z = 4$ mm while traces of positive vortex exist along the bottom wall around $y = 6$ mm. As we proceed downstream to $x = -50$ mm, it can be seen from Figure 4.9b there is a slight increase in the strengths of the negative and positive vortices which remain fairly at the same location. At the location of $x = 75$ mm the traces of negative vortex can be seen at about $z = 5$ mm (4.9c) while there exist only a few weak traces of the positive corner vortex. The general lack of strong corner vortices identified by the averaging process is attributed to the unsteady nature of the vortex system that washes out the mean structure of the vortex pair.

An alternative way to evaluate the average location of vortices is to compute the mean value of the instantaneous rigid rotation vorticity fields (i.e., by averaging fields like that of Figure 4.8 rather than computing ω_{RR} from the mean fields of Figure 4.13 to obtain the fields of Figure 4.9). Fields obtained in this way are shown in Figure 4.10, but do not match the vorticity fields computed from the mean flow (This is because TDM does not commute with ensemble averaging). We can

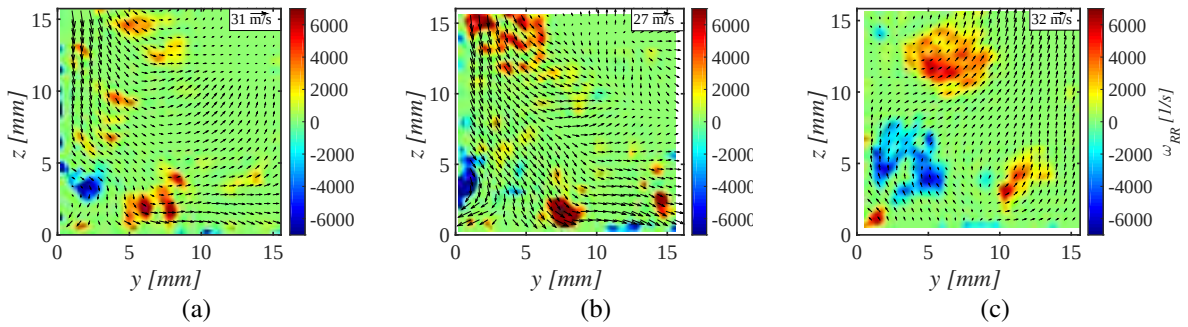

Figure 4.9: Rigid rotation vorticity field of mean vector fields shown in Figure 4.3 at (a): TV1 ($x = -100$ mm), (b): TV2 ($x = -50$ mm) and (c): TV3 ($x = 75$ mm) at Mach 2.75. For reference, $y_T = 57.2$ mm, $z_T = 69.3$ mm.

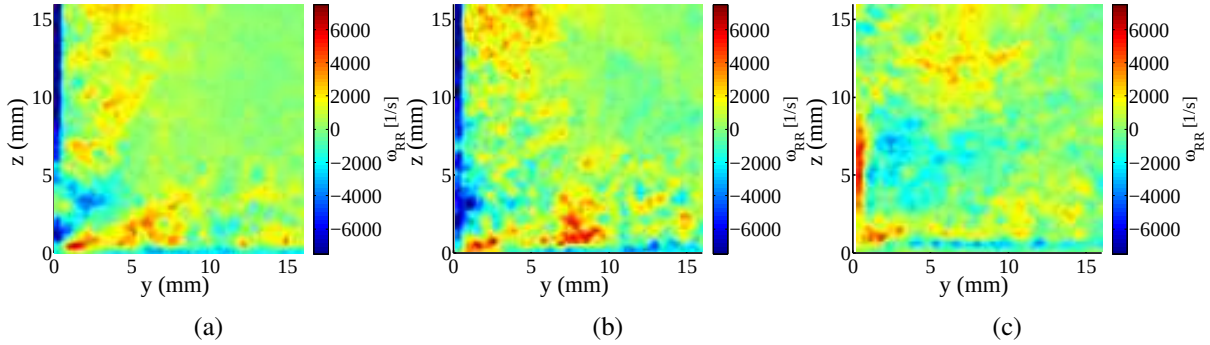

Figure 4.10: Ensemble average of instantaneous rigid rotation vorticity fields at (a): TV1 ($x = -100$ mm), (b): TV2 ($x = -50$ mm) and (c): TV3 ($x = 75$ mm) at Mach 2.75. For reference, $y_T = 57.2$ mm, $z_T = 69.3$ mm.

observe from Figure 4.10a that an anti-symmetric (both in sign as well as geometry) vortex system is likely to exist in the corner, but its structure thus identified is not consistent with the canonical corner vortex pair. In fact, the distribution of ω_{RR} is not concentrated in a well-defined region, but it spreads over the entire corner region, although some symmetry in the sign (negative above and positive below the corner bisector) is maintained. We attribute this property to an inherent unsteadiness of the corner vortex system. Marching downstream, it can be seen from Figure 4.10b that the anti-symmetric vortex system has increased in size since the corner region occupied by ω_{RR} has increased. In Figure 4.10c, we can observe that the amplitudes of mean rigid rotation vorticities associated with the positive and negative corner vortex system have weakened, however they are now spread over a larger area. This might imply a growth of spatial unsteadiness as it will become clear in later sections (Section 4.7.1).

4.3 Flow Field Scale Decomposition

According to our observations in sections 4.1.1 to 4.2.2, the canonical structure of secondary corner flows as shown in Figure 1.8 is not observed. Instead the flow in the corners is dominated by a forest of small-scale vortices. Thus, we hypothesize that there exist two superimposed scales of motion: a small-scale, high amplitude component, which is essentially comprised of the flow turbulence, superimposed to an underlying large-scale, low amplitude component, which is comprised of the secondary corner flows. One convenient way to identify these two components is to implement a decomposition of scales that isolates each of the two components. In practice, this requires to extract the large-scale field from a low-pass filtered representation of the flow field, while the small-scale field is the remaining component.

The instantaneous three-component velocity field is decomposed using two decompositions of motion. First, a scale-dependent decomposition of motion into a large and small-scale contribu-

tion is applied. Then, the resulting flow fields are additionally decomposed into a fluctuating and ensemble-average components using the Reynolds decomposition of motion.

Let $\mathbf{u} = u\hat{\mathbf{i}} + v\hat{\mathbf{j}} + w\hat{\mathbf{k}}$ be the three-component velocity field in the domain. The flow can be decomposed into a large-scale and a small-scale contribution as

$$\mathbf{u} = \mathbf{u}_L + \mathbf{u}_S \tag{4.1}$$

where we refer to $\mathbf{u}_L$ as the velocity field of the large-scales and $\mathbf{u}_S$ is the velocity field of the small-scales. More specifically, the large/small-scale decomposition is conducted by defining a (filtered) velocity field over a scale Λ:

$$\mathbf{u}_L(\mathbf{x}, t) = \frac{\iiint_\Lambda h(\mathbf{s})\mathbf{u}(\mathbf{x}+\mathbf{s}, t)\mathrm{d}\mathbf{s}}{\iiint_\Lambda h(\mathbf{s})\mathrm{d}\mathbf{s}} \tag{4.2}$$

where $h(\mathbf{s})$ is an appropriate low pass filtering kernel function (e.g., a top-hat filer). Here the filtering kernel function is a top-hat filter spanning a square approximately $0.5\delta \times 0.5\delta$ locally (i.e.$\Lambda = 0.5\delta$). We select this filter length scale under the assumption that the secondary corner flow be of order of the boundary layer thickness. This would be consistent with what known of corner flows in the literature [53, 71, 73, 75] and observations offered so far. The small-scale contribution is then defined as:

$$\mathbf{u}_S(\mathbf{x}, t) = \mathbf{u}(\mathbf{x}, t) - \mathbf{u}_L(\mathbf{x}, t) \tag{4.3}$$

This decomposition can be extended to average fields due to the linearity of the averaging and field decomposition processes. Additionally, we invoke the Reynolds decomposition where the velocity field is decomposed as the sum of an average field and an instantaneous fluctuation component

$$\mathbf{u} = \mathbf{U} + \mathbf{u}' \tag{4.4}$$

Finally, we can combine the two decompositions due to the linearity of each step. Thus we can

write

$$\mathbf{u} = (\mathbf{U}_L + \mathbf{u}'_L) + (\mathbf{U}_S + \mathbf{u}'_S) \tag{4.5}$$

Substituting in the continuity equation, under the incompressible assumption due to the lack of density information, we have

$$\nabla \cdot (\mathbf{u}_L + \mathbf{u}_S) = 0 \tag{4.6}$$

from which it also follows

$$\nabla \cdot (\mathbf{U}_L + \mathbf{U}_S) = 0 \tag{4.7}$$

and thus

$$\nabla \cdot (\mathbf{u}'_L + \mathbf{u}'_S) = 0 \tag{4.8}$$

We then apply this decomposition of motion to the momentum equation, from which we can derive a corresponding form of the three-component vorticity equation in terms of the propose decomposition of scales. In index notation, the resulting vorticity equation can be written as:

$$U_i \frac{\partial}{\partial x_i}\overline{\omega_j} = \overline{\omega_i}\frac{\partial}{\partial x_i}U_j + \frac{\partial}{\partial x_i}(\overline{\omega'_i u'_j} - \overline{\omega'_j u'_i}) + \nu\frac{\partial^2}{\partial x_i^2}\overline{\omega_j} \tag{4.9}$$

where $\overline{(\,\cdot\,)}$ represents ensemble average of the quantity under the bar. In particular, because in this study we are primarily interested in analyzing vortical features organized along the streamwise direction, the corresponding $x-$component of the vorticity equation 4.9 becomes:

$$\left[U\frac{\partial\overline{\omega_x}}{\partial x} + V\frac{\partial\overline{\omega_x}}{\partial y} + W\frac{\partial\overline{\omega_x}}{\partial z}\right] = \left[\overline{\omega_x}\frac{\partial U}{\partial x} + \overline{\omega_y}\frac{\partial U}{\partial y} + \overline{\omega_z}\frac{\partial U}{\partial z}\right] + \left[\frac{\partial}{\partial y}\left(\overline{\omega'_y u'} - \overline{\omega'_x v'}\right) + \frac{\partial}{\partial z}\left(\overline{\omega'_z u'} - \overline{\omega'_x w'}\right)\right] + \\ + \nu\left(\frac{\partial^2\overline{\omega_x}}{\partial x^2} + \frac{\partial^2\overline{\omega_x}}{\partial y^2} + \frac{\partial^2\overline{\omega_x}}{\partial z^2}\right) \tag{4.10}$$

where the different terms of equation 4.10 can be reorganized and grouped into $P1$, $P2$, $P3$ and $P4$ defined previously in equation 1.1.

The vortex tilting term is

$$P1 = \overline{\omega_y}\frac{\partial U}{\partial y} + \overline{\omega_z}\frac{\partial U}{\partial z}$$

For the case of small adverse pressure gradient ($|\beta| << 1$), it can be approximated by noting that

$$|\partial V/\partial x| \;\&\; |\partial W/\partial x| << |\partial U/\partial y| \;\&\; |\partial U/\partial z|$$

The approximations are justified by invoking the boundary layer approximation and the observation from our measurements that the streamwise changes in $\overline{v}$ and $\overline{w}$ across different streamwise measurement locations remains small even as the corner is approached. This assumption will be is a form of boundary layer approximation and can be represented mathematically as $\frac{\partial}{\partial x} \simeq 0$. One implication of this approximation is that the vorticity components in a plane perpendicular to the flow direction can be approximated as

$$\overline{\omega_y} \simeq \frac{\partial U}{\partial z}$$

and

$$\overline{\omega_z} \simeq -\frac{\partial U}{\partial y}$$

which would imply that $P1 \simeq 0$, i.e., the mean vorticity and shear would not contribute to the reorganization of existing vorticity into the streamwise direction to form the corner vortex pair.

The different terms of the approximate equation 4.10, which is still written in terms of the ensemble-average quantities, can then be decomposed using the scale decomposition proposed above. Thus, the following form of the terms on the right-hand-side of equation 4.10 can be obtained: These can then be decomposed into large-scale, small-scale and interscale components of vorticity production.

$$P1 = (\overline{\omega_{L_y}} + \overline{\omega_{S_y}})\frac{\partial (U_L + U_S)}{\partial y} + (\overline{\omega_{L_z}} + \overline{\omega_{S_z}})\frac{\partial (U_L + U_S)}{\partial z} \tag{4.11}$$

$$P2 = \frac{\partial}{\partial x}\left[\frac{\partial[\overline{(u'_L + u'_S)(v'_L + v'_S)}]}{\partial z} - \frac{\partial[\overline{(u'_L + u'_S)(w'_L + w'_S)}]}{\partial y}\right] \tag{4.12}$$

$$P3 = \frac{\partial^2}{\partial y \partial z}\left[\overline{(v'_L + v'_S)(v'_L + v'_S)} - \overline{(w'_L + w'_S)(w'_L + w'_S)}\right] \tag{4.13}$$

$$P4 = \left(\frac{\partial^2}{\partial z^2} - \frac{\partial^2}{\partial y^2}\right)\left[\overline{(v'_L + v'_S)(w'_L + w'_S)}\right] \tag{4.14}$$

The terms analyzed in detail in this work are $P3$ and $P4$, which can be decomposed into a large-scale ($P3_L$, $P4_L$), a small-scale ($P3_S$, $P4_S$) and an interscale (representing the effect of large-scale motion on the small-scale motion and vice versa) ($P3_{LS}$, $P4_{LS}$) contribution as

$$P3_L = \frac{\partial^2}{\partial y \partial z}\left[\overline{(v'^2_L)} - \overline{(w'^2_L)}\right] \tag{4.15}$$

$$P3_S = \frac{\partial^2}{\partial y \partial z}\left[\overline{(v'^2_S)} - \overline{(w'^2_S)}\right] \tag{4.16}$$

$$P3_{LS} = 2\frac{\partial^2}{\partial y \partial z}\left[\overline{(v'_L v'_S)} - \overline{(w'_L w'_S)}\right] \tag{4.17}$$

$$P4_L = \left(\frac{\partial^2}{\partial z^2} - \frac{\partial^2}{\partial y^2}\right)\left[\overline{v'_L w'_L}\right] \tag{4.18}$$

$$P4_S = \left(\frac{\partial^2}{\partial z^2} - \frac{\partial^2}{\partial y^2}\right)\left[\overline{v'_S w'_S}\right] \tag{4.19}$$

$$P4_{LS} = \left(\frac{\partial^2}{\partial z^2} - \frac{\partial^2}{\partial y^2}\right)\left[\overline{(v'_L w'_S + v'_S w'_L)}\right] \tag{4.20}$$

where $P3_L$ and $P4_L$ are the production of vorticity due to spatial unsteadiness of the large-scale corner flows, $P3_S$ and $P4_S$ are the production of vorticity due to small-scale turbulence and $P3_{LS}$ and $P4_{LS}$ are the interscale vorticity production terms due to interaction between the two scales.

4.4 Large and Small-scale Velocity Fields

The original vector fields near the walls comprised of small-scale motions. The vector fields are decomposed into large-scale and small-scale fields by the use of a spatial averaging filter spanning (e.g. 24×24 pixels) which is equivalent to a characteristic length of 3.65 mm or $\delta/2$ at the location

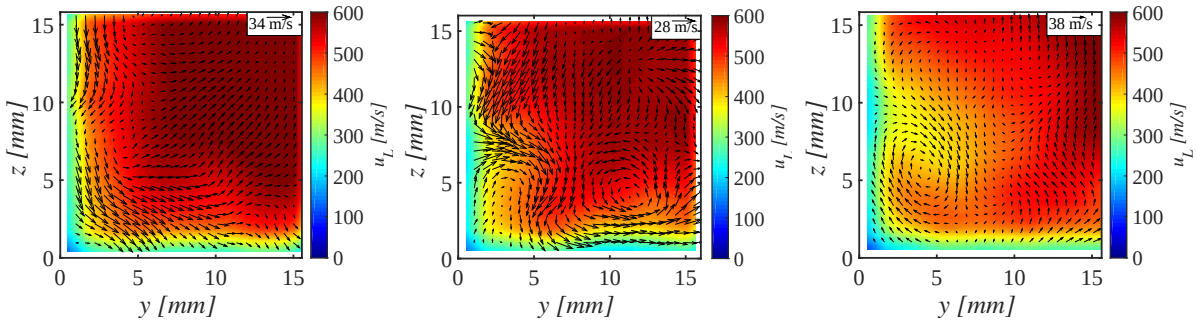

Figure 4.11: Instantaneous large-scale velocity vector fields obtained by decomposing instantaneous fields in Figure 4.1 at (a): TV1 ($x = -100$ mm), (b): TV2 ($x = -50$ mm) and (c): TV3 ($x = 75$ mm) at Mach 2.75. For reference, $y_T = 57.2$ mm, $z_T = 69.3$ mm.

of TV1.

Instantaneous vector fields at the large-scales obtained by decomposing the instantaneous flow field at Mach 2.75 shown in Figure 4.1 are shown in Figure 4.11. The large-scale swirling motion characteristic of canonical corner flows is more discernible from the in plane vector fields as compared to the original fields (Figure 4.1). This observation establishes the necessity of scale decomposition. We can observe that as we go downstream the swirling motion in the instantaneous field is stronger and larger. The background contour of the streamwise velocity component is smoother but similar to the original field. The large-scale flow at the most downstream location (TV4) is observed to be dominated by a strong negative vortex that seems to be responsible for the momentum transport in the corner. A bulge of low momentum region is observed stretching away from the sidewall towards the core flow from the location where this vortex is drawing low momentum fluid from the near sidewall fluid flow. The instantaneous small-scale velocity fields (Figure 4.12) associated with the described instant showed no discernible structure, but are characterized by a forest of small-scale vortices.

Mean flow fields at different scales were obtained by averaging multiple uncorrelated instances at

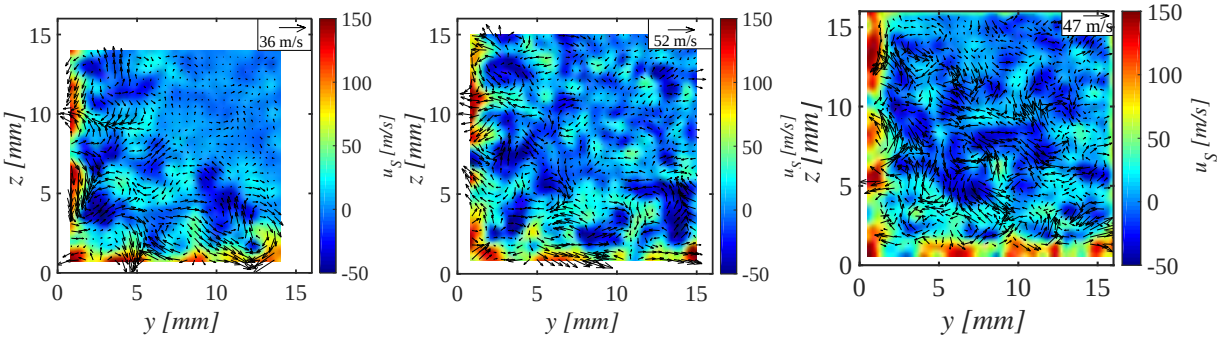

Figure 4.12: Instantaneous small-scale velocity vector fields obtained by decomposing instantaneous fields in Figure 4.1 at (a): TV1 ($x = -100$ mm), (b): TV2 ($x = -50$ mm) and (c): TV3 ($x = 75$ mm) at Mach 2.75. For reference, $y_T = 57.2$ mm, $z_T = 69.3$ mm.

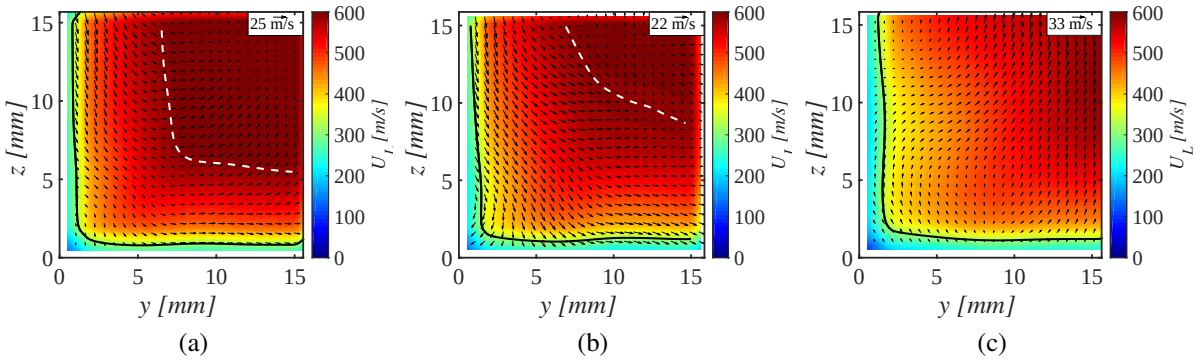

Figure 4.13: Mean large-scale velocity vector fields from (a): TV1 ($x = -100$ mm), (b): TV2 ($x = -50$ mm) and (c): TV3 ($x = 75$ mm) at Mach 2.75. For reference, $y_T = 57.2$ mm, $z_T = 69.3$ mm.

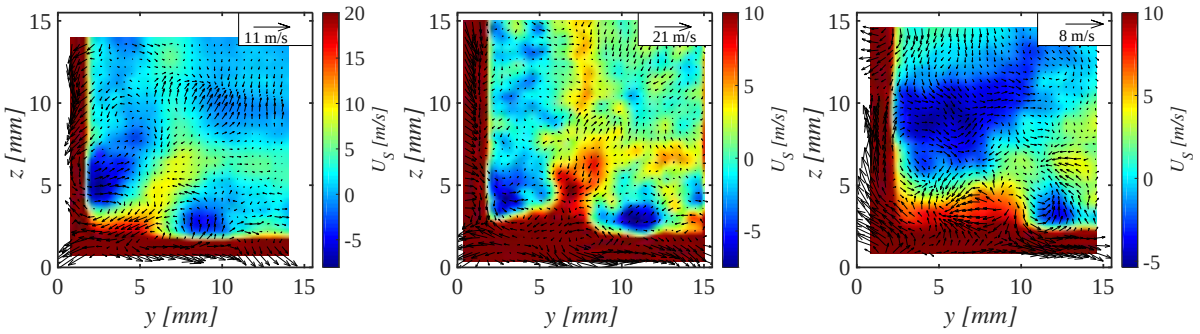

Figure 4.14: Mean small-scale velocity vector fields from (a): TV1 ($x = -100$ mm), (b): TV2 ($x = -50$ mm) and (c): TV3 ($x = 75$ mm) at Mach 2.75. For reference, $y_T = 57.2$ mm, $z_T = 69.3$ mm.

the corresponding scales. The mean large-scale velocity fields are shown in Figure 4.13. The mean large-scale fields follow the same general trend as the mean complete fields in Figure 4.3, however they are characterized by a thicker subsonic region which is an artifact of spatial filtering near the wall used in decomposition. Mean small-scale velocity fields are shown in Figure 4.14. Comparing the amplitudes in Figures 4.13 and 4.14, it can be observed that the small-scale fields are at a much lower amplitude (less than 10%) as compared to the large-scale velocity fields. The effect of streamwise momentum transport (Section 4.9) due to large-scale secondary flows is however much more evident in the small-scale velocity fields in the form of negative streamwise velocity. Regions of negative streamwise small-scale velocity component can be observed in Figures 4.14a and 4.14b at about $(y,z) = (2.5\text{ mm}, 5\text{ mm})$ and $(y,z) = (9\text{ mm}, 2.5\text{ mm})$ for TV1, $(y,z) = (2.5\text{ mm}, 5\text{ mm})$ and $(y,z) = (11\text{ mm}, 2.5\text{ mm})$ for TV2. These are the locations from where the secondary flows draw the lower momentum fluid from near the walls towards the core flow. Further downstream (Figure 4.14c) at the location of TV3 ($x = 75$ mm) the regions of negative streamwise small-scale velocities move away from the corner with the pocket of negative streamwise velocity along the sidewall growing in size and strength, now located at about $(y,z) = (4\text{ mm}, 9\text{ mm})$ and $(y,z) = (12\text{ mm}, 3\text{ mm})$. These are the locations from where the momentum is transferred away from the walls as shown

in Figure 4.32. A strand of positive streamwise velocity is observed in between the regions of streamwise negative velocity extending away from the corner. This region corresponds to the momentum transport due to the large-scale secondary flows from the core towards the corner. The in plane streamwise momentum transport is discussed in Section 4.9.

The mean large-scale in plane velocity (V_L, W_L) fields have a similar structure with slightly weaker magnitudes with respect to the complete fields (Figure 4.6). The mean small-scale in plane velocity fields show no discernible structure.

4.5 Large-scale Vortex Fields

4.5.1 Large-scale Intantaneous Vortex Fields

Applying TDM to the large-scale velocity fields presents a clear picture of the large-scale vortices present in the corner. The large-scale instantaneous rigid rotation vorticity fields are shown in Figure 4.15. The rigid rotation vorticity field is now dominated by a few large-scale vortices, the locations and direction of which resemble those described in the previous studies (Section 1.3). In the downstream planes of TV2 and TV3 where the secondary flow is relatively well developed, a pair of counter-rotating vortices are observed that convect the high momentum fluid from the core flow towards the corner. In TV2 (Figure 4.15b) a large-scale negative vortex belonging to the corner system as defined in Section 4.6 is observed near the sidewall centered at about z = 6 mm along with a positive corner vortex centered at about y = 12 mm along the bottom wall. A similar layout can be observed in the TV3 plane, however the instance presented shows a weaker positive corner vortex unlike the instance showed in Figure 4.17 showing a typical corner rigid rotation vorticity field at TV3. Small-scale rigid vorticity fields are comprised of a forest of smaller vortex cores similar to the rigid rotation vorticity fields shown in Figure 4.8.

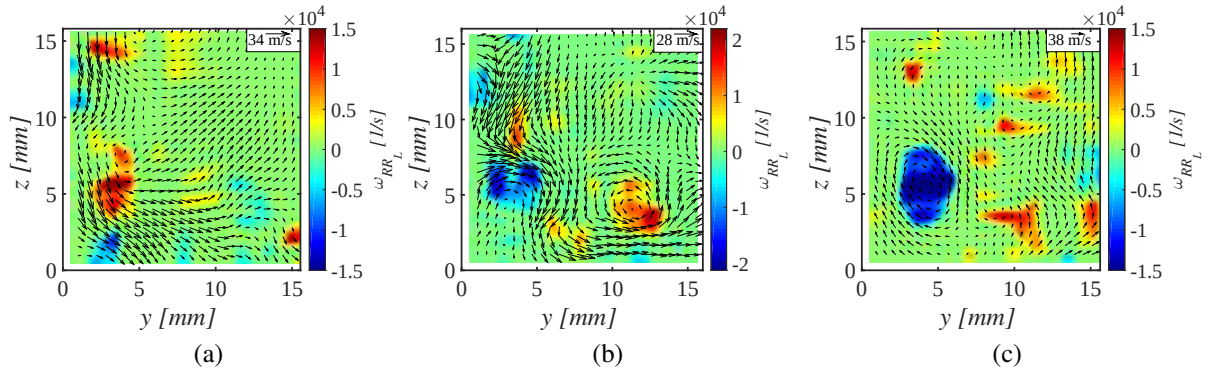

Figure 4.15: Instantaneous rigid rotation vorticity field obtained using TDM on instantaneous large-scale vector fields shown in Figure 4.11 at (a): TV1 ($x = -100$ mm), (b): TV2 ($x = -50$ mm) and (c): TV3 ($x = 75$ mm) at Mach 2.75. For reference, $y_T = 57.2$ mm, $z_T = 69.3$ mm.

4.5.2 Mean Large-scale Vortex Fields

Mean vorticity field obtained by averaging rigid rotation fields of large-scale velocity fields are shown in Figure 4.16. The scale decomposition allow us to more clearly identify the existence of the corner vortex system. Distinct negative and positive zones of vorticity associated with the corner system can be observed. In TV1 and TV2 (Figures 4.16a and 4.16b) there exists a region of mean negative vorticity near the corner along the sidewall at about $z = 3$ mm and the positive vorticity associated with the corner system is found along the bottom wall in the range $y = 5 - 10$ mm. Further downstream at TV3 (Figure 4.16c), it can be observed that the negative vorticity region associated with the corner vortex system has grown in size; this may indicate constrained spatial unsteadiness, while the region associated with the positive corner vortex has significantly decreased in size which may be due to increased unsteadiness.

4.6 Definition of Corner Vortex and its Properties

Now, that the flow field decomposition revealed a flow structure that would be characteristic of a canonical corner structure as described in the Section 1.3, it is required to define an instantaneous

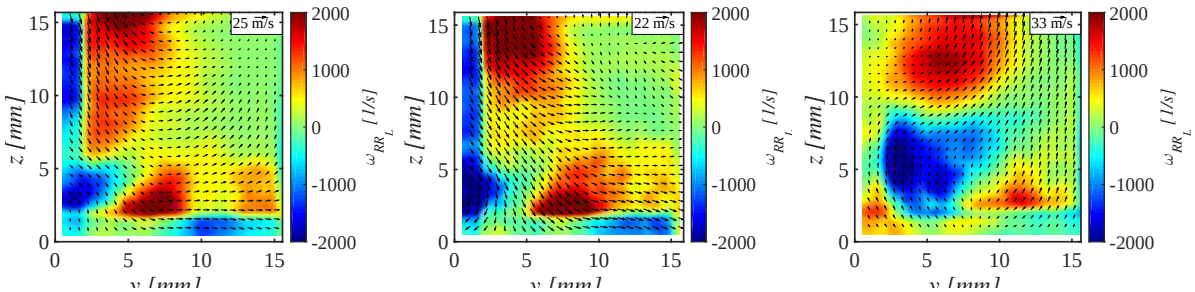

(a) (b) (c)

Figure 4.16: Ensemble average of instantaneous rigid rotation vorticity fields obtained from large-scale instantaneous vector fields at (a): TV1 ($x = -100$ mm), (b): TV2 ($x = -50$ mm) and (c): TV3 ($x = 75$ mm) at Mach 2.75. For reference, $y_T = 57.2$ mm, $z_T = 69.3$ mm.

corner vortex in order to statistically investigate the corner flows.

The instantaneous velocity vector fields (full and scale decomposed fields) obtained from SPIV planes were decomposed into rigid rotation vorticity as described in Section 2.2.2. Since we apply the definitions on the large-scale component field ($\mathbf{u}_L$), we here define the method based on this component and the corresponding ω_{RR_L} extracted from $\mathbf{u}_L$. (ω is here used to indicate the streamwise component of vorticity since in our measurements we only have access to the streamwise component.) The planar projection of an instantaneous vortex tube (φ) referred to as vortex henceforth, is defined as the area enclosed (A) by an iso-contour closed loop ($|\omega_{RR_L}| = 10$). The effects of varying the threshold on statistics of different properties of a corner vortex are investigated in Appendix C.1 and it was found that the statistics of interest here shown subsequently, as well as the conclusions drawn from them, are independent of the choice of threshold partially because of the large separation between rigid rotation vorticity associated with the background and that of the vortex tubes. The centroid of the iso-contour closed loop defines the vortex center $(\tilde{y}, \tilde{z})$ for TV planes. This was then used to define a corner vortex as follows, discarding vortices less than 3 pixels in size.

Suppose an instantaneous vector field m is characterized by a set ϕ of n distinct vortices, $\phi =$

$[\varphi_1, \varphi_2, ..., \varphi_k, ...\varphi_n]$, an ordered set α of corresponding areas $\phi = [A_1, A_2, ..., A_k, ...A_n]$ and a set of corresponding ordered pairs of vortex center co-ordinates $VC = [(\tilde{y}_1, \tilde{z}_1), (\tilde{y}_2, \tilde{z}_2), ..., (\tilde{y}_k, \tilde{z}_k), ...(\tilde{y}_n, \tilde{z}_n)]$. A negative (positive) corner vortex is defined as a coherent lump of vorticity whose integrated value is negative (positive) and the magnitude of the integrated value is the largest among the set of n vorticies in one instant bounded by the corner region. The negative corner vortex (Φ_-) of the instantaneous vector field m is mathematically defined as follows:

$$\begin{aligned} \Phi_- \coloneqq \Bigg\{ \varphi_k \,|\, \varphi_k \in \phi, \int_{A_k} \omega_{RR_L} dA_k < 0, \int_{A_k} \omega_{RR_L} dA_k = \\ = \min \left[\int_{A_n} \omega_{RR_L} dA_n \,|\, \varphi_n \in \phi \right], \tilde{y_k} \leq \delta, \tilde{z_k} \leq 1.5\delta, \tilde{z_k} > K\tilde{y_k} \Bigg\} \end{aligned} \tag{4.21}$$

where K is the aspect ratio of the wind tunnel defined by ($K = z_T / y_T$) and dA_k is the differential area element in the area enclosed by the the vortex tube boundary of k^{th} vortex. Similarly the positive corner vortex (Φ_+) of vector field m is mathematically defined as:

$$\begin{aligned} \Phi_+ \coloneqq \Bigg\{ \varphi_k \,|\, \varphi_k \in \phi, \int_{A_k} \omega_{RR_L} dA_k > 0, \int_{A_k} \omega_{RR_L} dA_k = \\ = \max \left[\int_{A_n} \omega_{RR_L} dA_n \,|\, \varphi_n \in \phi \right], \tilde{y_k} \leq 1.5\delta, \tilde{z_k} \leq \delta, \tilde{z_k} < K\tilde{y_k} \Bigg\} \end{aligned} \tag{4.22}$$

If no vortices satisfying the above definitions are found in an instantaneous field which may happen if no vortex bigger than 3 pixels was observed, that field is discarded from further statistical analyses. Less than 1% of the images were ever discarded from any dataplane due to this condition. The characteristic length λ of a corner vortex Φ is defined as

$$\lambda \coloneqq \sqrt{A_\Phi} \tag{4.23}$$

where A_Φ is the area of corner vortex Φ.

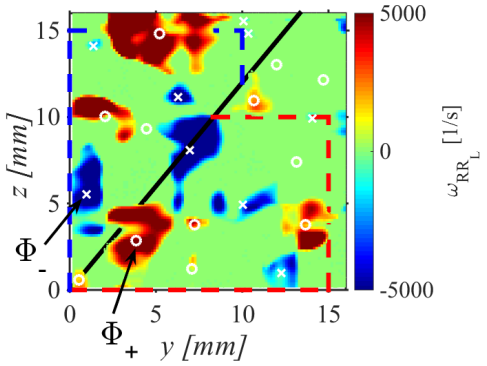

Figure 4.17: An instantaneous image in TV3 showing the vortex center detection and the pair of corner vortices as defined in equations 4.21 and 4.22. The region bounded by blue dashed lines and the solid black line is the domain of existence for the negative corner vortex. Similarly the region bounded by red dashed lines and the solid black line is the domain of existence for the positive corner vortex.

The spatial unsteadiness of the corner vortex is quantified as

$$\sigma = \sqrt{\frac{\sum_{i=1}^{n} [(\tilde{y}_i - \bar{y})^2 + (\tilde{z}_i - \bar{z})^2]}{n}} \tag{4.24}$$

where $\bar{y}$ and $\bar{z}$ are the mean vortex centers of a corner vortex (negative $_-$ or positive $_+$). This quantity represents the root mean square of the distance an instantaneous corner vortex is away from the mean position.

An example of instantaneous rigid rotation vorticity field is shown in Figure 4.17. The black solid line $z = Ky$ represents the diagonal of the wind tunnel rectangular channel. Thus the center belonging to the negative corner vortex must lie above this line as per the definition 4.21 while the center belonging to the positive corner vortex must lie below it (definition 4.22). The vertical dashed red line ($y = 1.5\delta$) and horizontal red dashed line ($z = \delta$) are the vertical and horizontal bounds below $z = Ky$ that bound the region of existence of the positive corner vortex. Similarly the vertical blue dashed line ($y = \delta$) and horizontal blue dashed line ($z = 1.5\delta$) are the vertical and horizontal bounds above $z = Ky$ for the region of existence of negative corner vortex. Thus the

vortex marked Φ_- forms the negative corner vortex with center $(\tilde{y}_-, \tilde{z}_-)$ and the vortex marked Φ_+ forms the positive corner vortex with center $(\tilde{y}_+, \tilde{z}_+)$ as these are the strongest and largest of the vortices lying in their respective domains.

The centers of the vortices are computed by calculating the centroid of the iso-contour closed loop defining the vortices. If $\mathbf{r}_+ = (\tilde{y}_+, \tilde{z}_+)$ and $\mathbf{r}_- = (\tilde{y}_-, \tilde{z}_-)$ represent the position vectors of the positive and negative corner vortex centers for the given instantaneous vector field m, the corner vortex separation distance (γ) is defined by

$$\gamma = |\mathbf{r}_+ - \mathbf{r}_-| \tag{4.25}$$

The position vector of center of circulation $\mathbf{r_{cen}}$ for the corner vortex pair Φ_+ and Φ_- is defined as

$$\mathbf{r}_{cen} = \frac{\mathbf{r}_+(\oint_{A_+} |\omega_{RR_{+L}}| dA_+) + \mathbf{r}_-(\oint_{A_-} |\omega_{RR_{-L}}| dA_-)}{(\oint_{A_+} |\omega_{RR_{+L}}| dA_+) + (\oint_{A_-} |\omega_{RR_{-L}}| dA_-)} \tag{4.26}$$

The corner bisector angle θ_{bis} is then defined as

$$\theta_{bis} = \arg(\mathbf{r}_{cen}) \tag{4.27}$$

4.7 Statistical Study of Corner Vortices

4.7.1 Spatial Phase Averaging and Vortex Statistics

Centers of the corner vortices were determined as per described in section 4.6 for each instantaneous vector field after the scale decomposition was applied. Phase averaging of instantaneous (large-scale) vector fields was conducted in a two step process. First, an average field was constructed in a reference frame shifted to the center of the negative (negative corner vortex centric coordinate system, -CVCCS) or positive corner vortex coordinate system (+CVCCS); thus generating two mean fields, one as seen from the center of the negative corner vortex and the other from the center of the positive corner vortex. Then, the resulting field was shifted back to the original

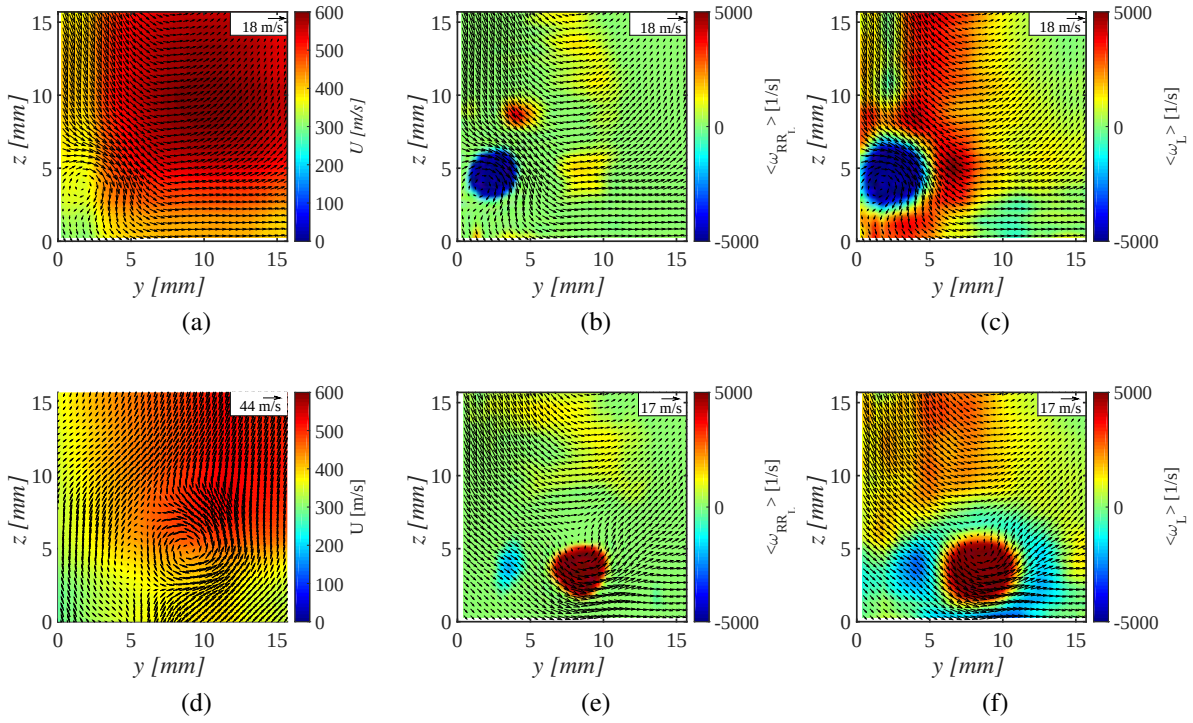

Figure 4.18: Top Row, -CVCCS: (a): Mean flow field, (b):TDM of 4.18a, (c): Mean vorticity of 4.18a. Bottom row, +CVCCS: (d): Mean flow field, (e):TDM of 4.18d, (f): Mean vorticity of 4.18d. All fields at TV1 in Mach 2.75. For reference, $y_T = 57.2$ mm, $z_T = 69.3$ mm.

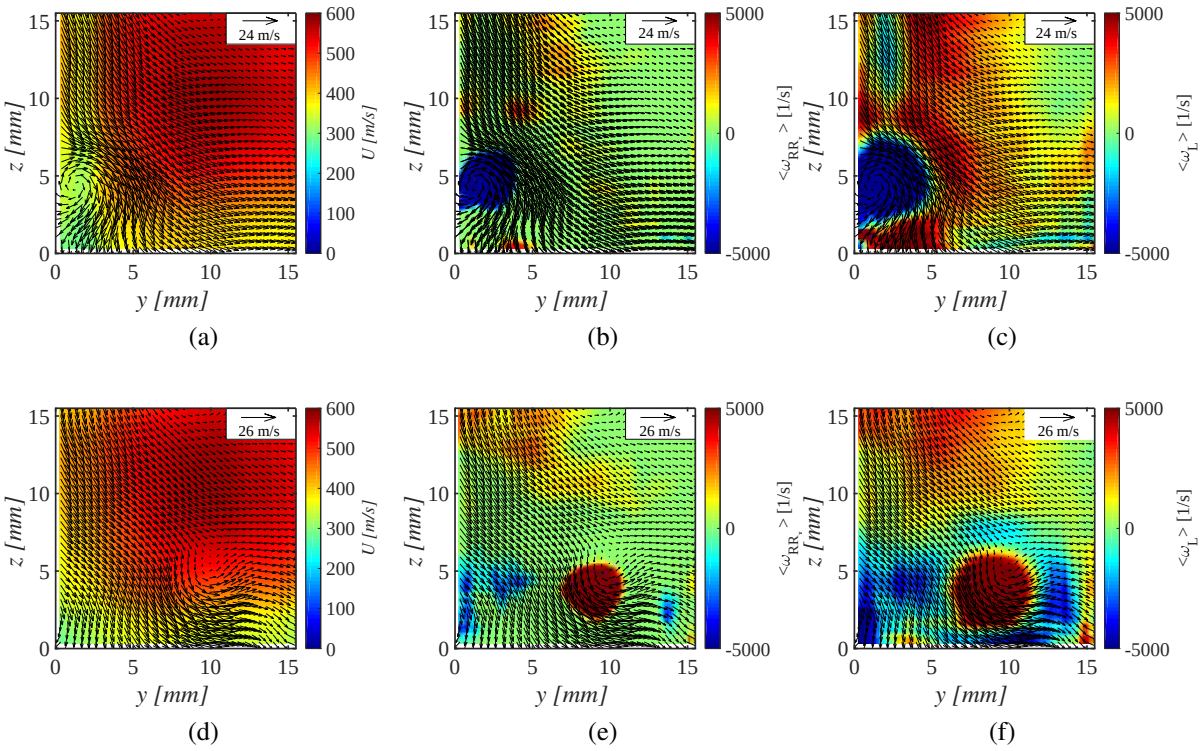

Figure 4.19: Top Row, -CVCCS: (a): Mean flow field, (b):TDM of 4.19a, (c): Mean vorticity of 4.19a. Bottom row, +CVCCS: (d): Mean flow field, (e):TDM of 4.19d, (f): Mean vorticity of 4.19d. All fields at TV2 in Mach 2.75. For reference, $y_T = 57.2$ mm, $z_T = 69.3$ mm.

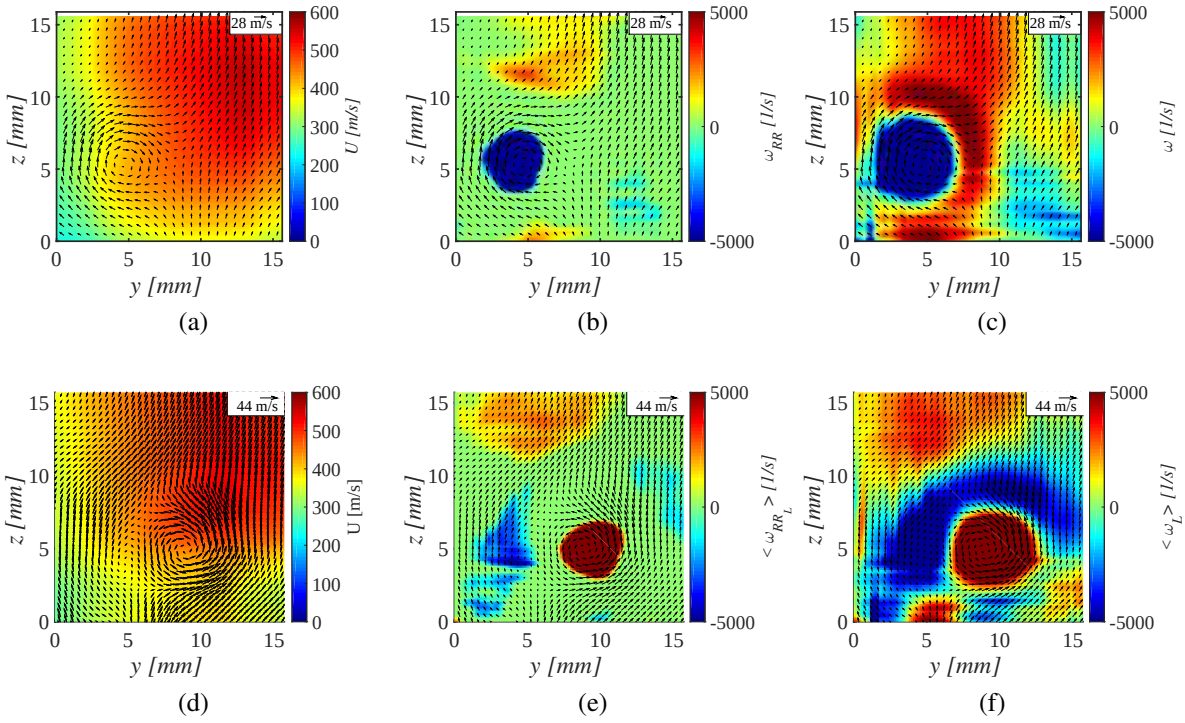

Figure 4.20: Top Row, -CVCCS: (a): Mean flow field, (b):TDM of 4.20a, (c) Mean vorticity of 4.20a. Bottom row, +CVCCS: (d): Mean flow field, (e): TDM of 4.20d, (f): Mean vorticity of 4.20d. All fields at TV3 in Mach 2.75. For reference, $y_T = 57.2$ mm, $z_T = 69.3$ mm.

frame of reference by the average position of each of the two vortices in the pair. These conditionally averaged vector fields are shown in Figures 4.18, 4.19 and 4.20 for the TV1, TV2 and TV3 planes respectively, at Mach 2.75. The spatially phase averaged fields provide a relative measure of how the mean flow looks like around the corner vortex, its scaling and the average strength.

Figure 4.18a shows the average vector field in the vicinity of the negative corner vortex at $x = -100$ mm. The rigid rotation vorticity and conventional vorticity fields associated with the vector field in Figure 4.18a are shown in Figures 4.18b and 4.18c. The circular motion created by the negative corner vortex is well observed in the vector field. The mean position of the vortex center at this location as observed from the instantaneous vector field statistics is $(\bar{y}_n, \bar{z}_n) = (2.63, 4.64)$ mm. Similar properties of the positive and negative corner vortex can be measured at different data plane locations and are tabulated in Table 4.1 for both Mach 2.75 and Mach 2. Note also that the process of phase averaging for the detection of the positive or negative vortex reinforces only the intended vortex, the resulting conditionally averaged field still maintain a signature, albeit weak, of the opposite vortex. As we proceed downstream we can see (Figure 4.20) that both the corner vortices move away from the corner with a slight increasing trend in their characteristic scales in the streamwise direction. This is quantitatively summarized in Table 4.1. Similar observations were made at Mach 2.

The probability density functions (PDF) of the location of corner vortex centers are shown in Figure 4.21. The most probable location of the positive corner vortex lies between the bottom wall and $z = 5$ mm. It moves away from the corner along the bottom wall in the downstream direction. The negative corner vortex has a high probability of residing in the range of $z = 0 - 5$ mm along the sidewall at the first two locations (TV1 and TV2), while at TV3 it appears to become spatially unstable with a larger standard deviation which is also seen in table 4.1. The PDFs of the corner bisector angle (θ_{bis}) and the corner vortex separation distance (γ) for Mach 2.75 and Mach 2 are shown in Figure 4.22 and 4.25. It is worth noting that both the PDFs remain approximately the

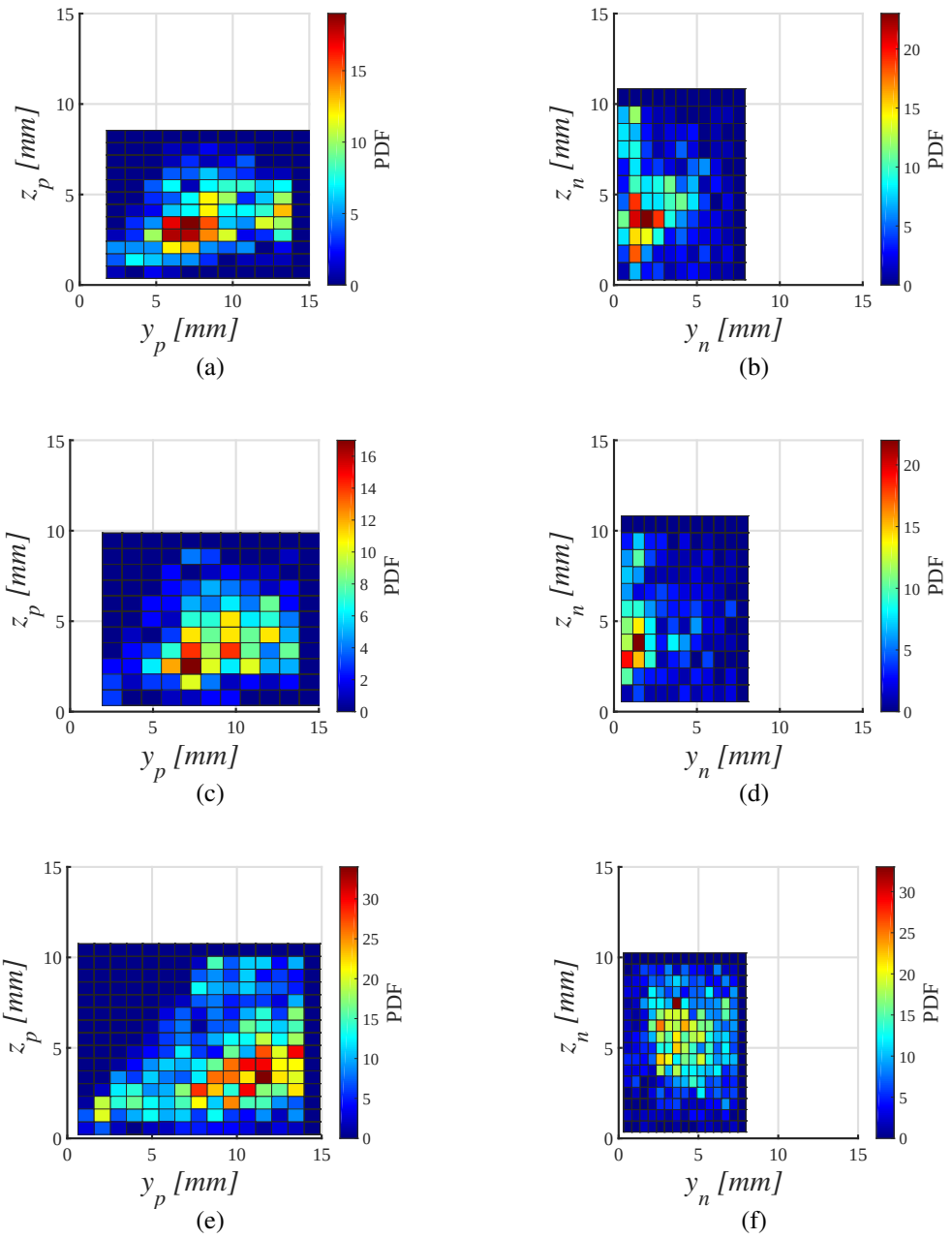

Figure 4.21: PDF of locations of corner vortex centers at Mach 2.75. Left column shows the position statistics of the positive corner vortex while the right one shows statistics of the negative corner vortex. Top row: TV1; Middle row: TV2; Bottom row: TV3. For reference, $y_T = 57.2$ mm, $z_T = 69.3$ mm.

x, mm	$(\bar{y}_+, \bar{z}_+)$, mm	$(\bar{y}_-, \bar{z}_-)$, mm	$\bar{\lambda}_+$, mm	$\bar{\lambda}_-$, mm	$\bar{\sigma}_+$, mm	$\bar{\sigma}_-$, mm
Mach 2.75						
-100 (TV1)	(8.42, 3.76)	(2.63, 4.64)	3.09	2.58	3.25	2.87
-50 (TV2)	(8.93, 4.01)	(2.57, 4.92)	3.1	2.74	3.1	2.91
75 (TV3)	(9.61, 5.16)	(4.26, 5.67)	3.86	3.05	4.06	2.68
Mach 2						
-100 (TV1)	(6.36, 2.39)	(2.52, 3.54)	1.61	2.21	3.14	2.22
-50 (TV2)	(11.66, 5.3)	(4.21, 3.92)	3.23	3.11	3.87	3.11
0 (TV3)	(11.27, 4.1)	(3.77, 5.71)	3.84	3.66	3.76	2.78

Table 4.1: Corner vortex properties at various streamwise locations.

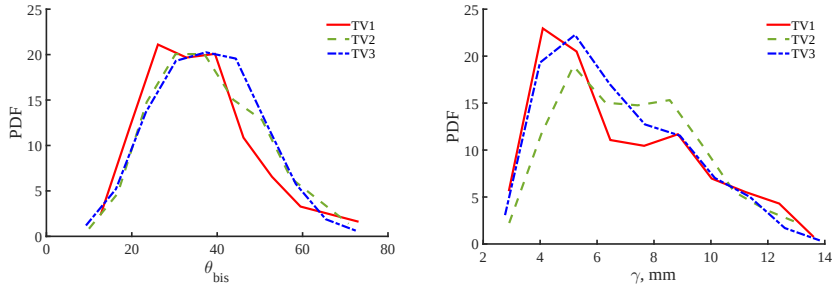

Figure 4.22: Probability density functions at Mach 2.75 of (a): corner bisector angle and (b) corner vortex separation distance. For reference, $y_T = 57.2$ mm, $z_T = 69.3$ mm.

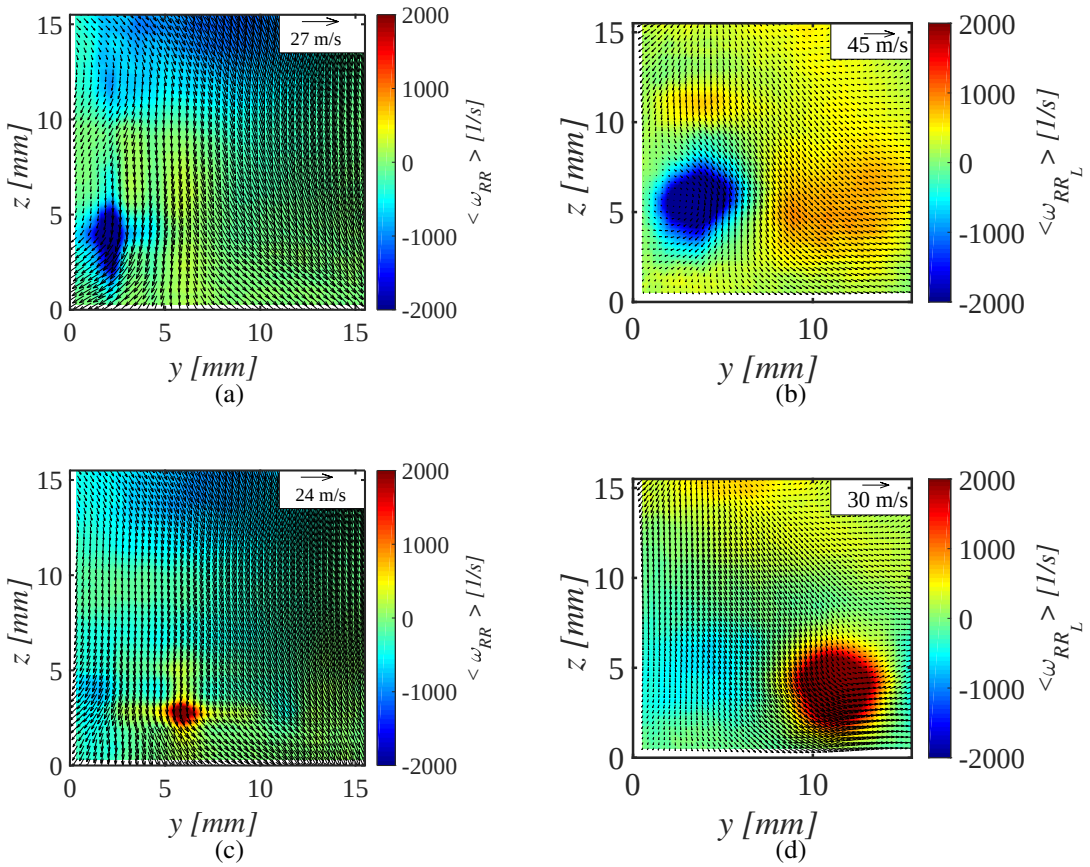

Figure 4.23: Top Row, -CVCCS: (a): averaged ω_{RR_L} at TV1; (b): averaged ω_{RR_L} at TV3. Bottom row, +CVCCS: (c): averaged ω_{RR_L} at TV1; (d): averaged ω_{RR_L} at TV3. All fields at in Mach 2. For reference, $y_T = 57.2$ mm, $z_T = 69.3$ mm.

same at all three streamwise locations. The mean angle of corner bisector stays at about 40°, which is a value approximately equal to $\tan^{-1}(y_T/z_T)$, which is the angle of the diagonal of the rectangular cross-section of the test section. The mean distance between the corner vortex pair stays constant roughly at 6.7 mm.

Results leading to similar conclusions obtained at Mach 2 are shown in Figures 4.23 and 4.25.

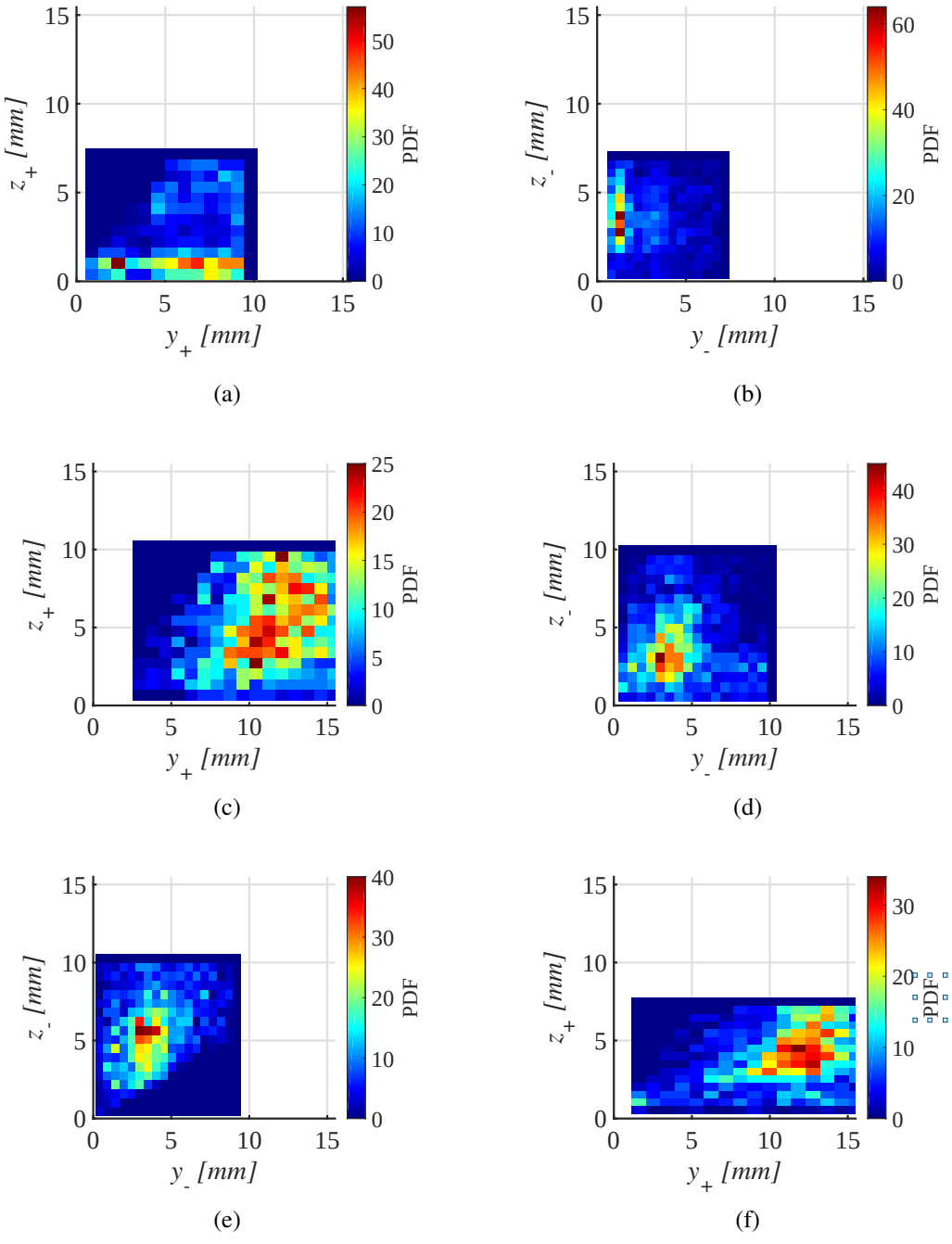

Figure 4.24: PDF of locations of corner vortex centers at Mach 2. Left column shows the position statistics of the positive corner vortex while the left shows statistics of negative corner vortex. Top row: TV1; Middle row: TV2; Bottom row: TV3. For reference, $y_T = 57.2$ mm, $z_T = 69.3$ mm.

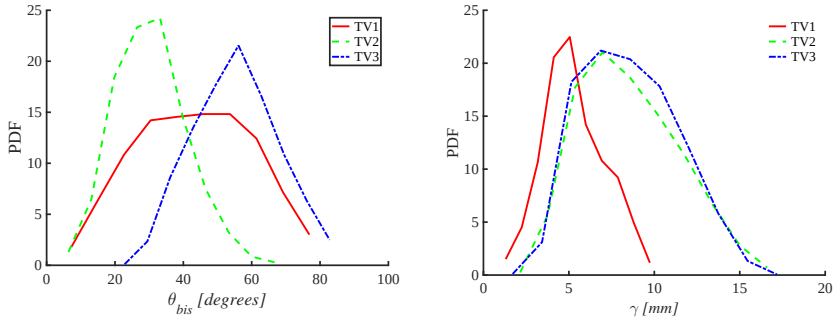

Figure 4.25: Probability density functions in Mach 2 tunnel of (a): Corner bisector angle and (b): Corner vortex separation distance. For reference, $y_T = 57.2$ mm, $z_T = 69.3$ mm.

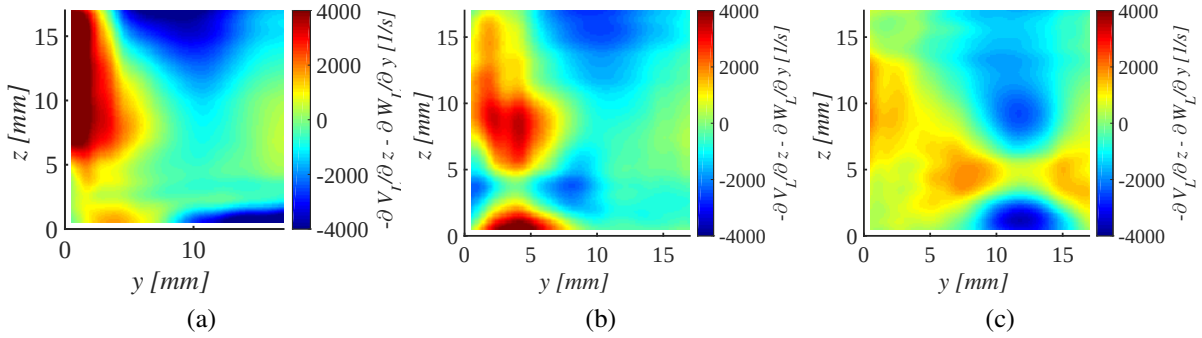

Figure 4.26: Mean $-\frac{\partial V}{\partial z} - \frac{\partial W}{\partial y}$ field at TV2 location in M2 tunnel in (a): laboratory reference frame; (b): -CVCCS; and (c): +CVCCS. For reference, $y_T = 57.2$ mm, $z_T = 69.3$ mm.

4.7.2 Strain Rate Structures in CVCCS

The in-plane strain rate $-\left(\frac{\partial V_L}{\partial z}+\frac{\partial W_L}{\partial y}\right)$ contour plots in the TV2 plane at Mach 2 in the laboratory coordinate system are shown in Figure 4.26a, while Figures 4.26b and 4.26c show the contours in -CVCCS and +CVCCS. There appears to be no special structure in the laboratory frame of reference with high values of strain located near walls. In the CVCCSs (Figs. 4.26b and 4.26c), however we observe a pattern comprising of four lobes of positive and negative values of the strain centered around the location of corner vortices. This pattern is characteristic of a solid body rotation in a cartesian coordinate system caused by increasing value of tangential velocity of the rotating object in the radial direction [121]. They studied the evolution of a wingtip vortex in the wake and found similar structures. Similar structures were observed at other location in both operating conditions.

4.7.3 Organized Motion in Small-scales

In a way similar to the spatial phase averaging of large-scale vortices described in section 4.7.1 instantaneous small-scale velocity fields were spatially averaged by shifting the instantaneous small-scale field by same vector as the corresponding large-scale vector field is shifted (position vector of corner vortex) which is +CVCCS and -CVCCS. The vector field and vortex field corresponding to TV2 plane at Mach 2 are shown in figure 4.27.

The convection of low momentum fluid from near the wall towards the core flow and the convection of high momentum fluid from the core flow towards the corner due to the corner vortices is clearly seen in the U_S fields as shown in Figures 4.27a and 4.27c in the form of negative (blue) and positive (red) regions near the wall respectively. The negative (blue) region that extends from the core flow towards the wall at about z = 5 mm is also characterized by a region of ejection where the conditionally averaged small-scale velocity vectors point away from the wall.

The spatially phase averaged small-scale rigid rotation vorticity fields are characterized by well

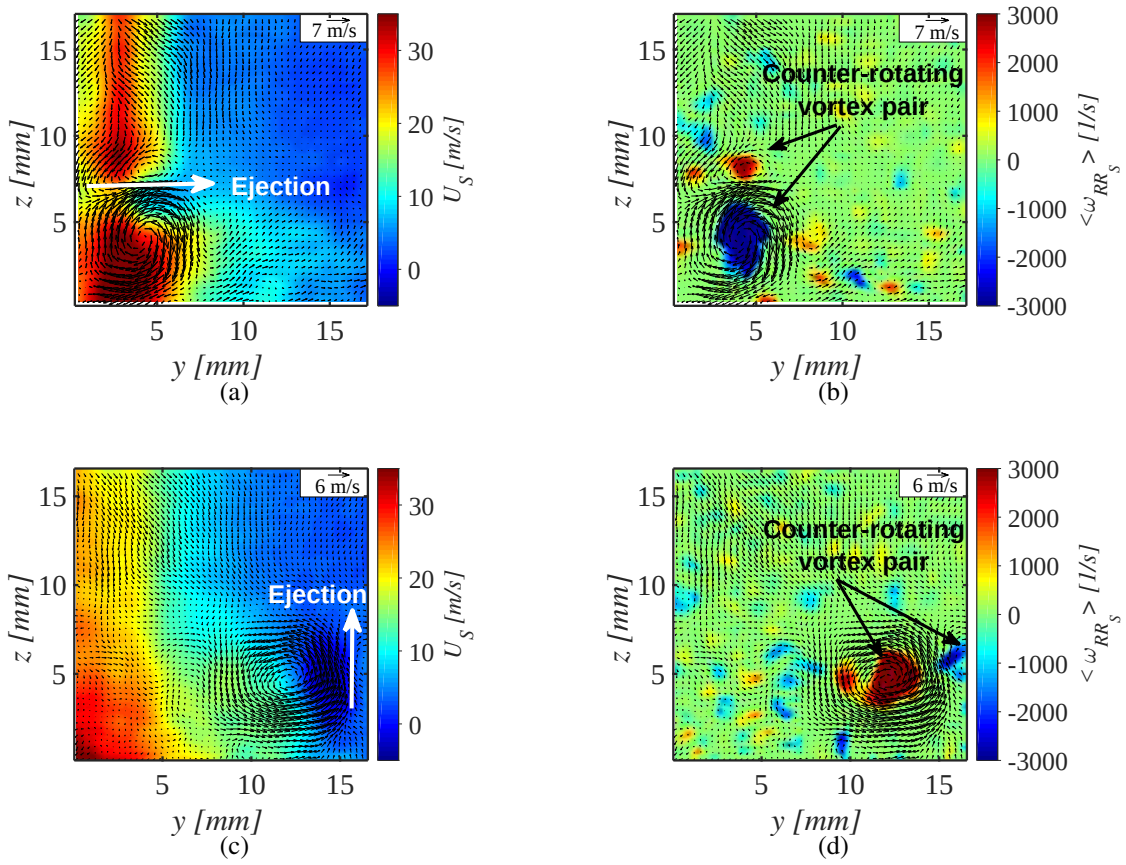

Figure 4.27: Spatially phase averaged small-scale vector fields at TV2 in Mach 2 wind tunnel, (a): mean small-scale vector fields with respect to negative corner vortex, (b): mean small-scale rigid rotation fields with respect to negative corner vortex, (c): mean small-scale vector fields with respect to positive corner vortex, (d): mean small-scale rigid rotation fields with respect to positive corner vortex. For reference, $y_T = 57.2$ mm, $z_T = 69.3$ mm.

defined large-scale counter rotating vortices lying on either side of the ejection in such a way to strengthen the corner vortices as shown in figures 4.27b and 4.27d. The ejection associated with counter rotating vortices associated with strong streamwise aligned vortices lying near wall possibly indicates creation of streamwise vorticity by a mechanism proposed by Bernard [122] which would explain the strengthening of corner vortices in streamwise direction. He observed counter rotating vortex pairs that appear in the ejections associated with the streamwise oriented alternating low and high velocity furrows and the associated streamwise vortices in transitional boundary layers. He proposed a mechanism detailing the increase of streamwise vorticity due to merger of the ejection associated vortices.

Similar ejections and counter rotating vortex systems were also observed at upstream and downstream locations with the systems becoming more prominent downstream.

4.8 Reynolds Stresses and Vorticity Production due to Large-scale Unsteadiness

Large scale Reynolds stresses at Mach 2, TV2 participating in streamwise vorticity creation are shown in figure 4.28. As can be seen from figures 4.28a and 4.28a, the regions of high $v'_L v'_L$ and $w'_L w'_L$ are found mostly conforming slightly lifted the side and bottom walls as would be expected in any turbulent flow. In -CVCCS and +CVCCS a clover-leaf pattern is observed in the stress fields. Contours of $v'_L w'_L$ are observed to be lagging those of $-\left(\frac{\partial V_L}{\partial z} + \frac{\partial W_L}{\partial y}\right)$ by 45°. Chow et al. [121] attribute this behavior to anisotropy of the local turbulence. Similar patterns stronger than the features observed in laboratory coordinate system are also observed at TV3 location where the secondary corner flow is respectively developed, but aren't observed at TV1 location with corners in the nascent stage of development. These four leaf clover patterns are widely observed in turbulence studies of wingtip vortices and have been studied in detail [121, 123].

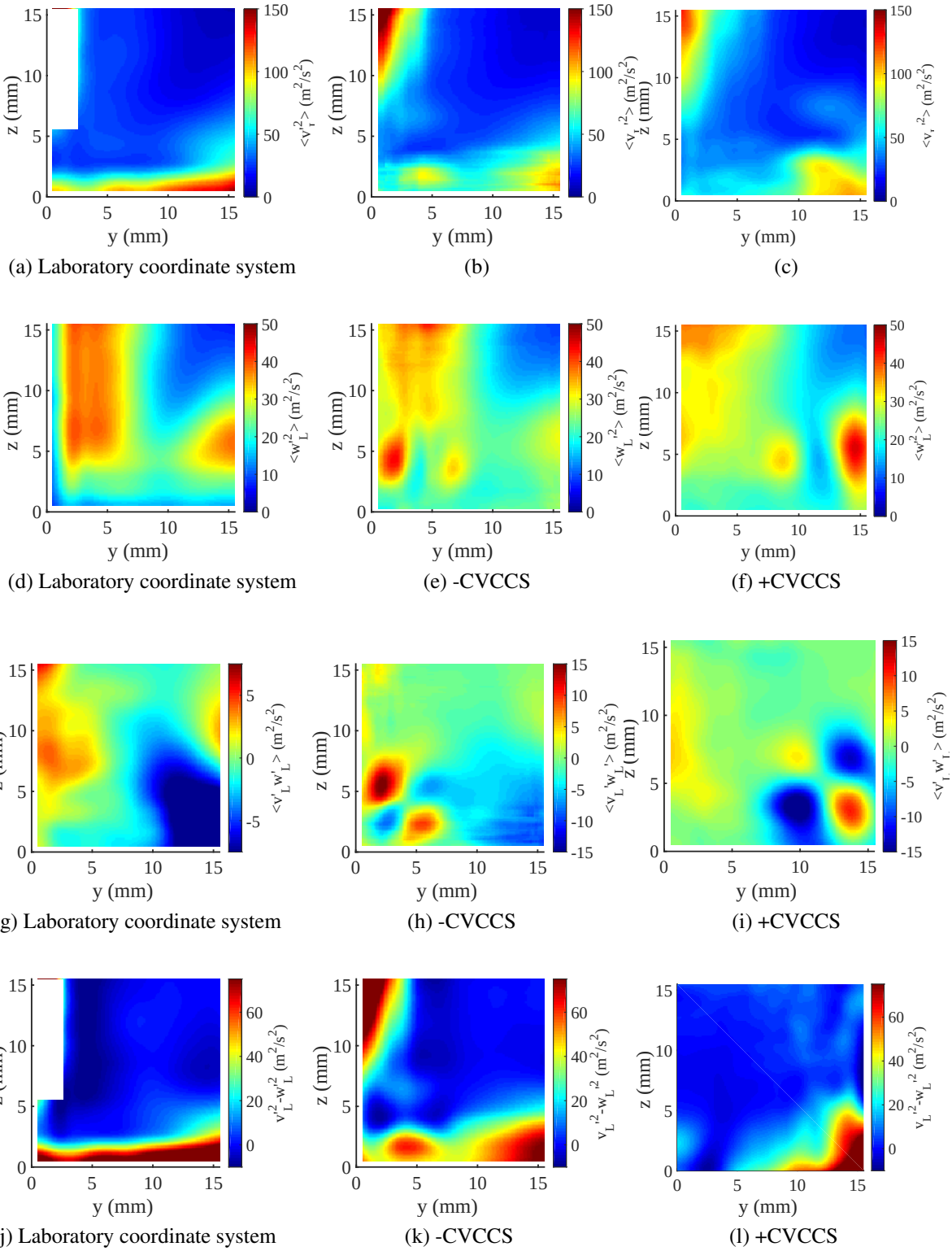

Figure 4.28: Reynolds stress fields at TV2 location in respective coordinate systems at Mach 2. Left column: laboratory coordinate system, middle column: -CVCCS, right column: +CVCCS. For reference, y_T = 57.2 mm, z_T = 69.3 mm.

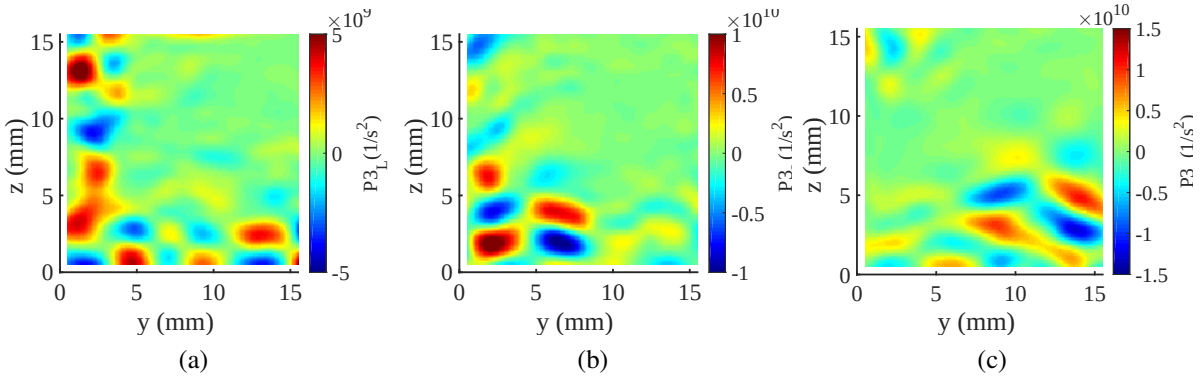

Figure 4.29: $P3_L$ fields at TV2 location in respective coordinate systems at Mach 2. Left column: laboratory coordinate system, middle column: -CVCCS, right column: +CVCCS. For reference, $y_T = 57.2$ mm, $z_T = 69.3$ mm.

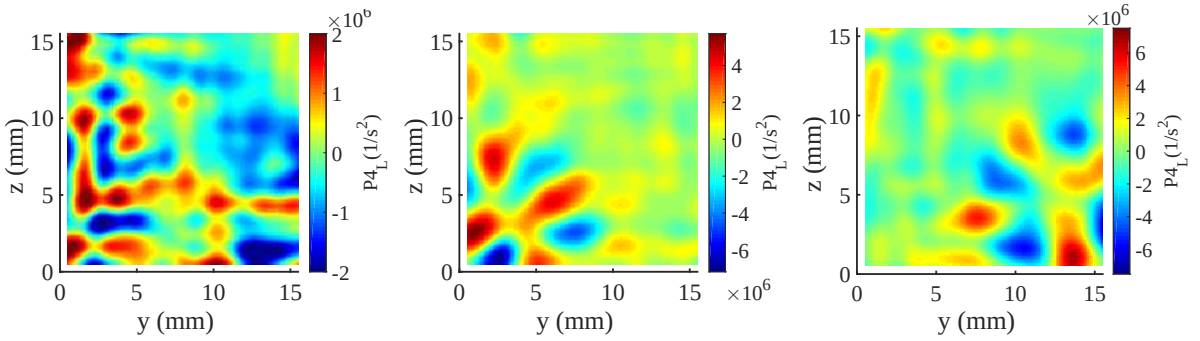

Figure 4.30: $P4_L$ fields at TV2 location in respective coordinate systems at Mach 2. For reference, $y_T = 57.2$ mm, $z_T = 69.3$ mm.

The four leaf clover patterns are also revealed in the large-scale vorticity production fields due to unsteadiness $P3_L$ and $P4_L$ in both the CVCCS at approximate locations of corner vortices, while the $P3_L$ and $P4_L$ fields in laboratory coordinate system do not reveal any special structure (refer figures 4.29 and 4.29). One inference that can be derived from this is that the vorticity production is centered around the corner vortices as high magnitudes of $P3_L$ and $P4_L$ are observed around the vortex centers in CVCCSs. Similar observations are also made in downstream data-plane.

4.9 Strain Rates and Vortex induced Momentum Transport

In-plane strain rate components associated with the streamwise velocity are shown in Figure 4.31. The in-plane streamwise velocity gradients associated with the large-scale fields follow a qualitatively similar but smoother pattern of what shown in Figure 4.31. The in-plane streamwise velocity gradient contour plots are superimposed by iso-contour lines of ω_{RR_L}, with black lines representing the positive vorticity while white lines representing the negative vorticity. It can be observed that in all three locations the regions of high positive $\partial U/\partial z$ are confined near the bottom wall and the thickness of these regions decreases towards the corner. A region of negative $\partial U/\partial z$ can be observed near the sidewall ($z = 2-5$ mm in TV1 and TV2 and around $z = 4-10$ mm in TV3) in the same region where the thickness of the region of positive $\partial U/\partial z$ along the bottom wall starts to drop. It can be observed that mean large-scale negative corner vortex (white iso-contour lines) is seen to reside in this negative region. The negative corner vortex convects lower momentum fluid away from the sidewall creating a decrease in the $U-$velocity as we traverse the positive $z-$direction from the bottom wall near the sidewall. This effect is observed as a dip in the $U(z)$ profiles of Figure 4.5e near the sidewall ($y = 2.5$ &5 mm) and this produces a negative $\partial U/\partial z$ observed at the location of the negative vortex in Figure 4.31h. A similar effect is observed with the positive corner vortex near the bottom wall. Since the $\partial U/\partial y$ field is positive at the location where $\partial U/\partial z$ is negative and vice versa, the product of $\partial U/\partial y$ and $\partial U/\partial z$ would identify the regions where

momentum defects occurs, refer to Figures 4.31c, 4.31f & 4.31i. To further explain this observation, consider as an example the case of TV3 where the secondary flows are most developed, and which presents the case of strongest vortex-induced momentum transport among the three planes. With reference to any vertical line near the sidewall ($y = 0-5$ mm) in Figure 4.31i, the $U-$velocity profile (Figure 4.5e) increases with z until the region with negative (blue) $(\partial U/\partial y)(\partial U/\partial z)$ is encountered, then it decreases until the end of the region of negative $(\partial U/\partial y)(\partial U/\partial z)$. The defect in the streamwise momentum is highest at the end of the negative (blue) region and at the start of the positive (green/red) $(\partial U/\partial y)(\partial U/\partial z)$ region which is located at about $z = 8$ mm along the line $y = 2.5$ mm. It can thus be observed from Figure 4.5e that the streamwise velocity profile reaches a minimum at about $z = 8$ mm and this identifies the location where momentum transport away from the wall due to the vortex is the strongest.

The transport field of streamwise momentum orthogonal to the principal flow direction ($\partial(VU + \overline{u'v'})/\partial y$ and $\partial(WU + \overline{u'w'})/\partial z$) at Mach 2.75 and $x = 75$ mm is shown in Figure 4.32. The quantities represented in both the plots are obtained from the x-momentum conservation equation from the Navier Stokes equations. In both the fields positive regions indicate the transport of momentum away from the walls towards the core flow while the negative regions indicate the transport towards the wall. In Figure 4.32a, which represents the transport of x-momentum in the y-direction, we observe a region of positive values at $z \approx 10$ mm ejecting fluid from near the sidewall towards the core flow. This is also the location of maximum velocity defect and the change of sign of $(\partial U/\partial y)(\partial U/\partial z)$ field from negative to positive vertically traversing away from the bottom wall. It lies at the location from where the negative corner vortex (white contours) scoop out fluid from near the sidewall. A negative region of $\partial(VU + \overline{u'v'})/\partial y$ can be found conforming to the sidewall about $y \approx 3$ mm. This is the region where the negative corner vortex convects fluid towards the sidewall. It can thus be observed that the negative vortex is responsible for momentum transport causing a velocity defect at $z \approx 10$ mm. Similar conclusions can be made from observing vertical

transport of the x-momentum in Figure 4.32b.

4.10 Variation of Skin Friction Coefficient (C_f)

Skin friction coefficient along the side and the bottom wall was computed using the integral method of Mehdi and White [124]. The viscosity was computed using Sutherland law while the density near the wall was computed using the results of Spina et al. [125]. The integral method is derived by simplifying the 2D boundary layer x-momentum equation also considering the Reynolds stress gradients. The final expression of C_f is given as:

$$C_f = 4\int_{\frac{n}{\delta}=0}^{\frac{n}{\delta}=1}\left[1-\frac{n}{\delta}\right]\frac{\partial U}{\partial n}d\left(\frac{n}{\delta}\right)+2\int_{\frac{n}{\delta}=0}^{\frac{n}{\delta}=1}\left[1-\frac{n}{\delta}\right]^2\left(-\frac{\partial^2 U}{\partial n^2}\right)d\left(\frac{n}{\delta}\right) \tag{4.28}$$

where n is the wall normal direction, δ is the 99% boundary layer thickness and U is the mean velocity tangential to the wall, which in our case would be along the bottom wall and along the sidewall. The variation of C_f along the bottom wall at $x = -100$ mm, $x = -50$ mm and $x = 75$ mm at Mach 2.75 is shown in Figure 4.33a. The values of $u_\tau = \sqrt{C_f U_\infty^2/2/\rho}$ corresponding to C_f on the bottom wall away from the corner ($y = 15.5$ mm) are 35 m/s, 45 m/s and 44 m/s at $x = -100$ mm, -50 mm&75 mm, respectively. These values match fairly well with the value reported by Lapsa and Dahm [17] ($u_\tau = 31$ m/s at $x = -81.5$ mm) on the centerline using the same experimental setup but a different approach. The general trend of increase-decrease-increase of C_f away from the corner influence is in agreement with Davis et al. [7], at their upstream locations. The red curve in Figure 4.33a represents the C_f variation at $x = -100$ mm along the bottom wall.

The effect of variation of C_f due to longitudinal vortices imbedded in boundary layer was studied in detail by Shabaka et al. [126]. They found that the regions where the velocity vectors point away from the wall lead to a lower C_f while those with vectors pointing towards the wall lead to higher value of C_f due to convection of lower momentum fluid away from and convection of

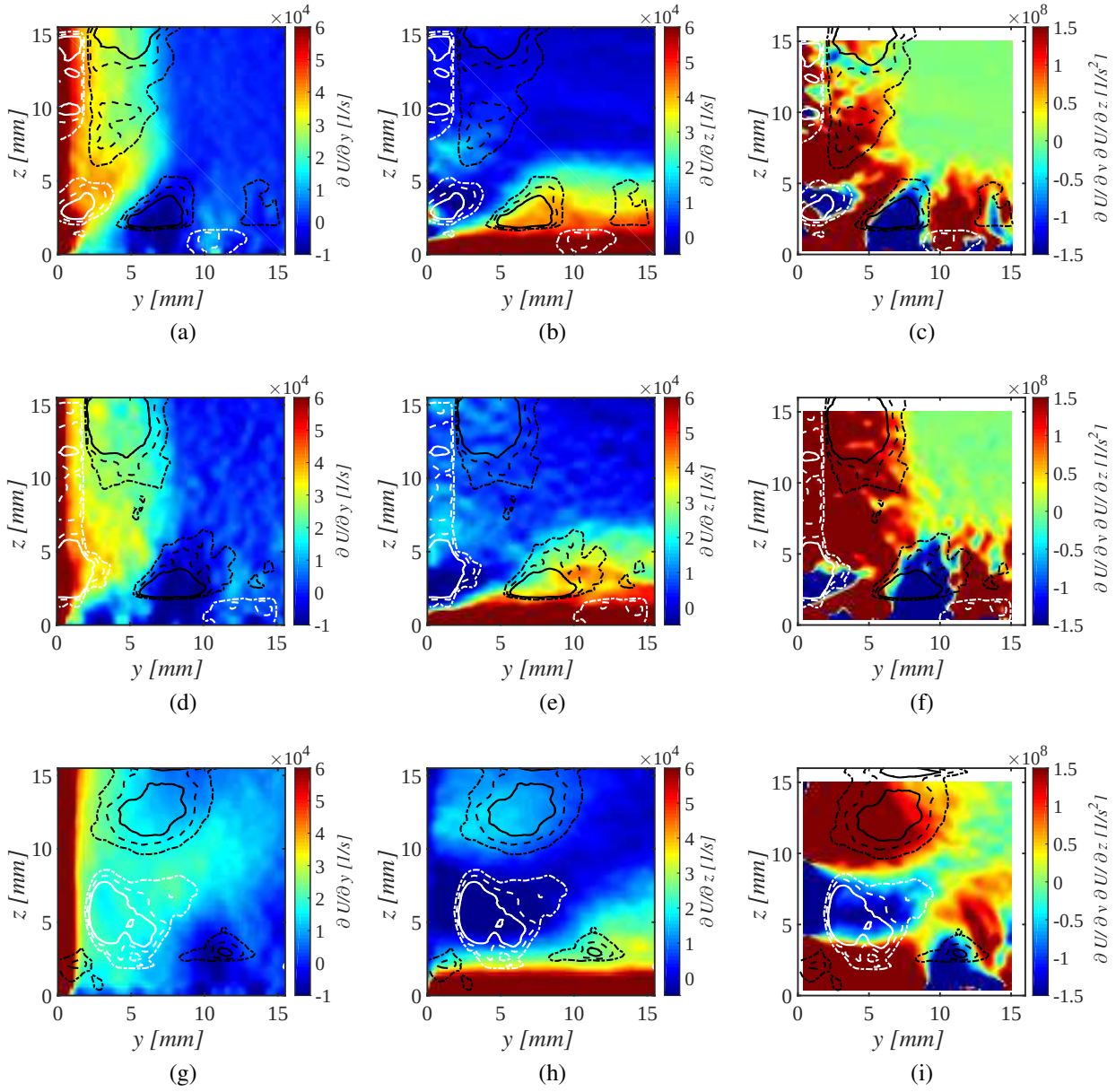

Figure 4.31: In plane gradients of mean streamwise velocity and the product of the velocity gradients superimposed with contour lines of mean rigid rotation vorticity at large-scales, white lines: negative vorticity, black lines: positive vorticity. Top row: TV1; middle row: TV2 and bottom row: TV3. All fields refer to Mach 2.75. For reference, y_T = 57.2 mm, z_T = 69.3 mm.

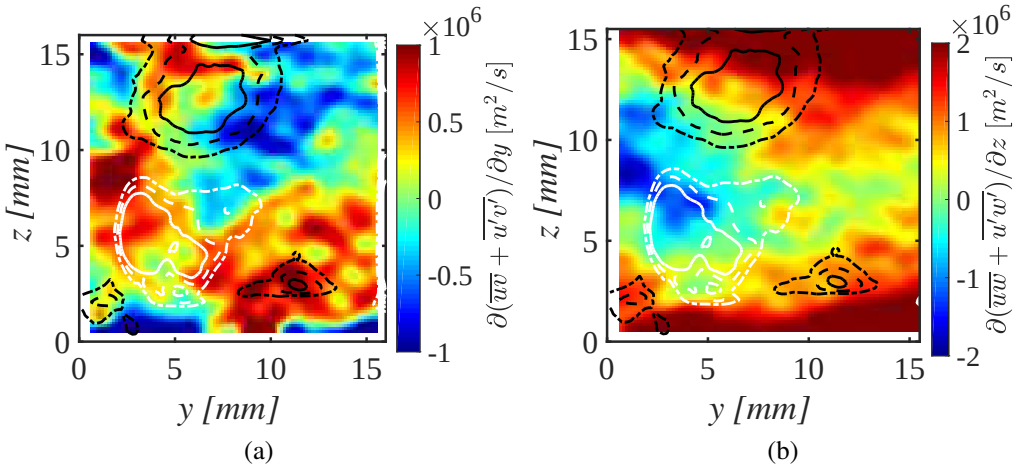

Figure 4.32: Mean transport of streamwise momentum by secondary flows at Mach 2.75, TV3 (x = 75 mm) location: (a): In y-direction and (b): In z-direction. For reference, y_T = 57.2 mm, z_T = 69.3 mm.

higher momentum fluid towards the wall respectively. In accordance to this explanation it can be seen (Figure 4.33a) that the rate of growth of C_f at $x = -100$ mm with respect to y suddenly increases at about $y = 6$ mm which is the region where positive corner vortex would be causing a downwash (refer Figure4.18e, also from table 4.1, we see that $y_+ = 8.42$ mm and $\lambda_+ = 3.09$ mm at $x = -100$ mm, which would cause a downwash at $y = y_+ - \lambda_+ = 5.33$ mm). The positive corner vortex would convect the higher momentum fluid from the core flow towards the bottom wall, which would increase the value of $\partial u/\partial z$ at $y = 6$ mm. Positive corner vortex would have a tendency to cause an upwelling at around $y = 10$ mm convecting the low momentum fluid from the corner towards the core flow, thus reducing $\partial U/\partial z$ and hence C_f. This reduction in C_f is observed in Figure 4.33a. The higher rate of increase of C_f ($x = -50$ mm) may be attributed to strengthening positive corner vortex. However, the location of strong increase of C_f ($y = 6$ mm) and the location of its growth stagnation ($y = 10$ mm) correspond well with the location and characteristic scale of the positive corner vortex (refer table 4.1). It can be seen from Figure 4.33a that the curve of C_f at $x = 75$ mm (well developed corner secondary flow) is mostly higher than those at $x = -100$ mm and $x = -50$ mm, which would be due to the strong development of the negative corner vortex

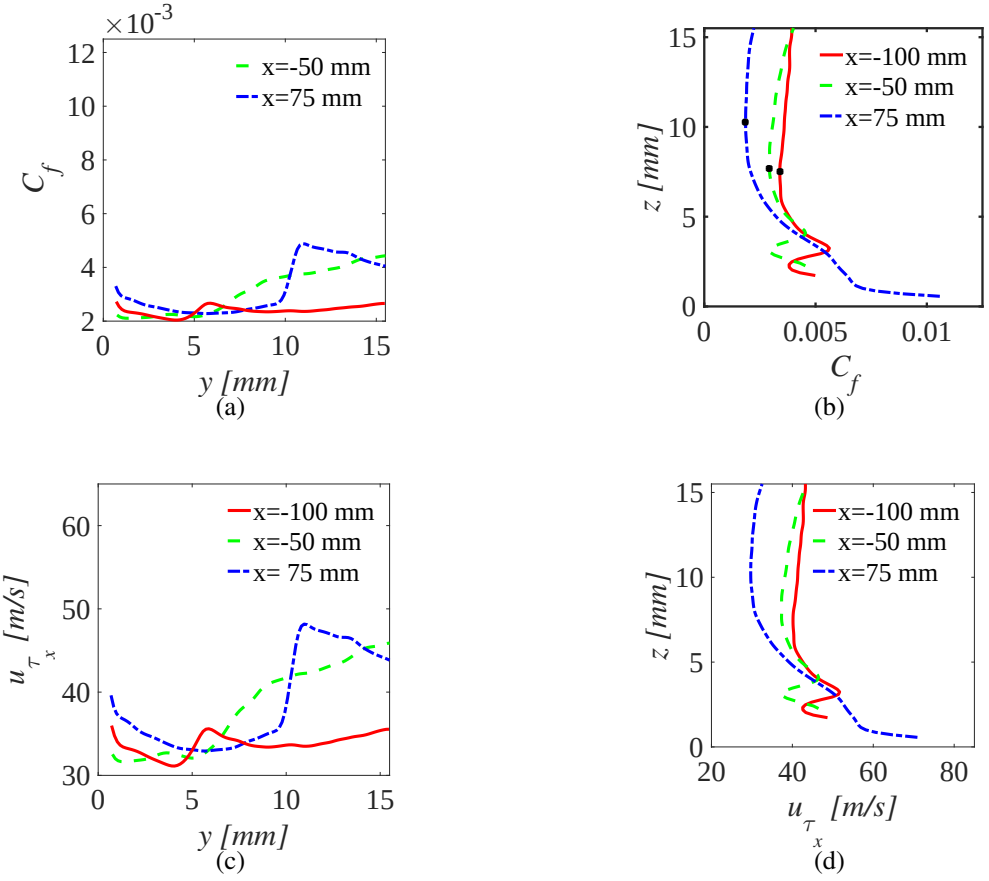

Figure 4.33: Variation of co-efficient of friction along (a): bottom wall, (b): sidewall and variation of friction velocity along (c): bottom wall, (d): sidewall at Mach 2.75. For reference, y_T = 57.2 mm, z_T = 69.3 mm.

leading to a downwash on the bottom wall. The strong peak in C_f ($x = 75$ mm) at about $y = 10$ mm followed by a decreasing trend away from the corner is consistent with the spatial evolution of the positive corner vortex (table 4.1).

Similar inferences can be derived from the variation of C_f profiles on the sidewall shown in Figure 4.33b. The friction velocities along the bottom and side wall obtained from C_f are shown in Figures 4.33c and 4.33c respectively.

It can thus be said that the corner vortices play an important role towards the distribution of C_f around the corner.

4.11 Effect of Secondary Flows on Inner Scale Velocity Profiles

Velocity profiles in inner wall scaling at a spanwise distance of 17 mm and 12 mm from the corner is shown in Figure 4.34. The shear velocity at the wall was obtained from a measure of the skin friction coefficient C_f estimated from the current measurements using the method outlined in section 4.10. It is seen from Figures 4.34a, 4.34b, 4.34e and 4.34f that the boundary layer velocity profile follows the theoretical log-law curve (Cole's Wake law with van Driest's compressible correction) at $x = -100$ mm; strong corner effects are not observed at this location. The velocity profiles at $x = 75$ mm are shown in Figures 4.34c, 4.34d, 4.34g and 4.34h. It can be seen (Figure 4.34c) that the velocity profile downstream is fuller i.e. the velocity profile is above the theoretical curve at $y = 17$ mm with respect to the upstream location. This is due to the net downward flow generated by the stronger negative corner vortex compared to the upstream location, which brings the higher momentum fluid from the core flow towards the wall. In Figure 4.34g, it is observed that the fullness has weakened due to the presence of positive corner vortex at about $y = 12$ mm which tends to cause a convection of low momentum fluid away from the bottom wall at this location. Departure from the theoretical behavior around the logarithmic region is observed in Figures 4.34d

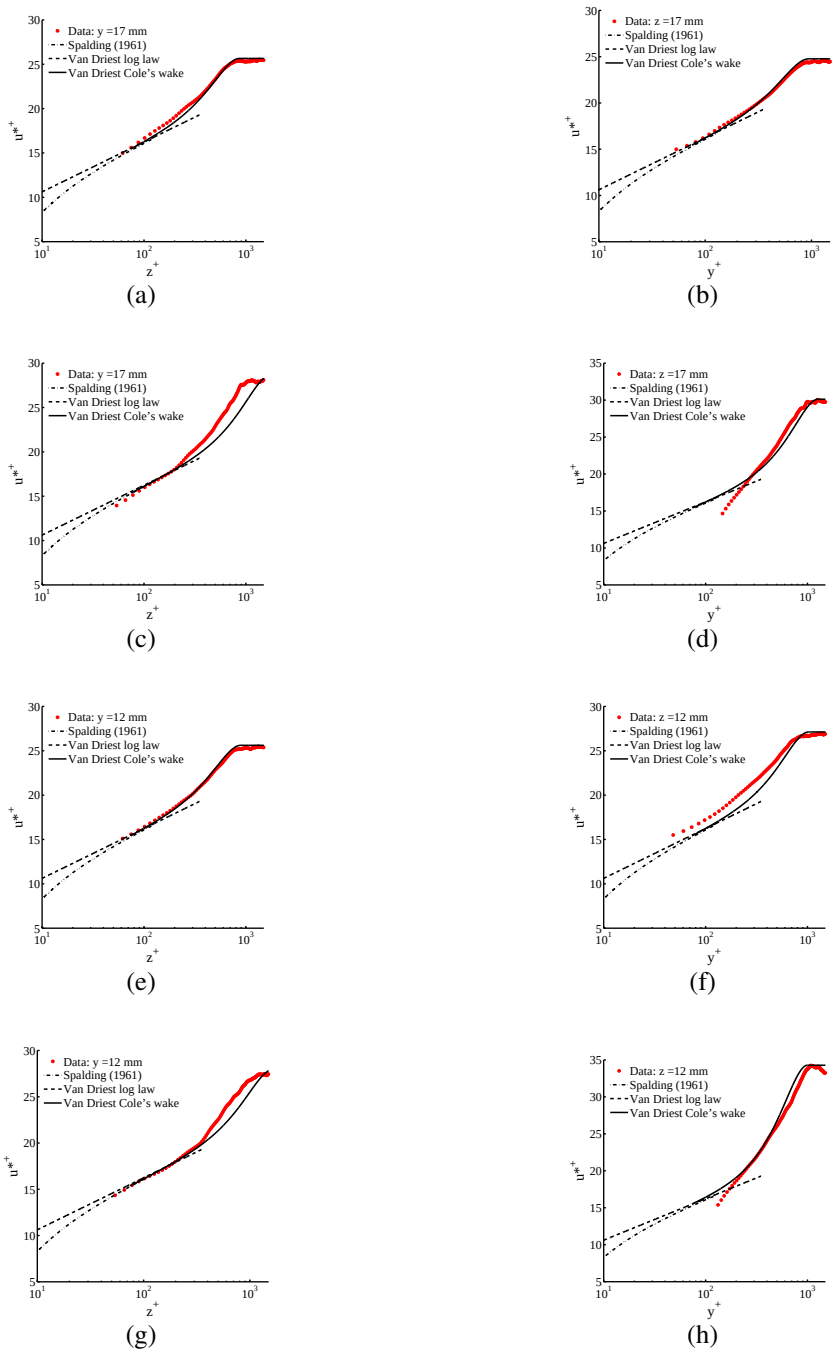

Figure 4.34: Wall normal streamwise velocity profiles in inner scales at Mach 2.75. (a) and (b): u^+ profiles at $y = 17$ mm and $z = 17$ mm respectively at TV1. (c) and (d): u^+ profiles at $y = 17$ mm and $z = 17$ mm respectively at TV3. (e) and (f): u^+ profiles at $y = 12$ mm and $z = 12$ mm respectively at TV1. (g) and (h): u^+ profiles at $y = 12$ mm and $z = 12$ mm respectively at TV3. For reference, $y_T = 57.2$ mm, $z_T = 69.3$ mm.

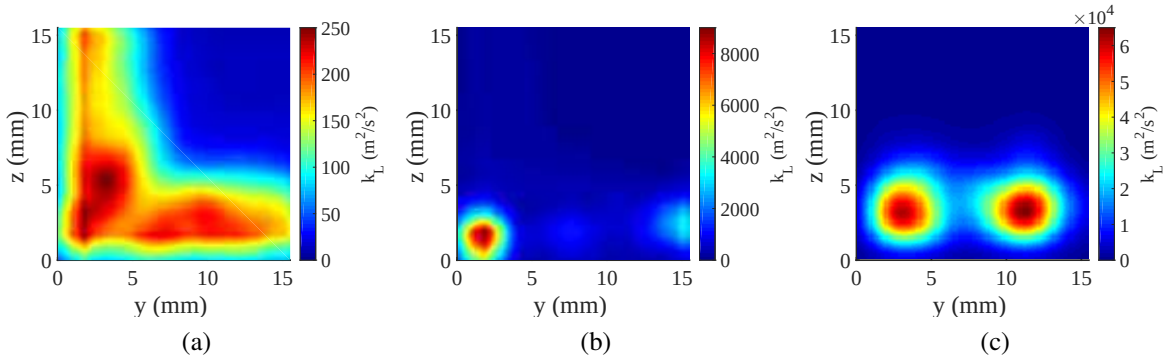

Figure 4.35: Large scale turbulent kinetic energy fields at (a): TV1 ($x = -100$ mm), (b): TV2 ($x = -50$ mm) and (c): TV3 ($x = 75$ mm) at Mach 2.75. For reference, $y_T = 57.2$ mm, $z_T = 69.3$ mm.

and 4.34h which corresponds to the location effected by a developed negative corner vortex. This may be due to the convection of low momentum fluid from near the sidewall towards the core flow due to negative corner vortex causing a momentum defect in the logarithmic region. The velocity profile was observed to not conform to the log law as corner was approached within 5 mm. It was observed to lie above the theoretical curve indicating a net influx of high momentum from the core flow.

4.12 Large-scale Unsteadiness

Large-scale unsteadiness of the secondary flows can be quantified in terms of large scale turbulent kinetic energy which describes the fluctuations in the velocities. Contour plots of mean large-scale turbulence kinetic energy (TKE) is

$$\bar{k_L} = \frac{1}{2}\left(\overline{u_L{'}^2} + \overline{v_L{'}^2} + \overline{w_L{'}^2}\right) \tag{4.29}$$

are shown in Figure 4.35. Small-scale mean turbulent kinetic energy (k_s) fields were computed similarly and are shown in Figure C.3. It can be seen that the large scale unsteadiness increases in intensity at large-scales as we proceed downstream with TV1 containing the least unsteadiness.

However, the relative contribution of small-scale TKE to the total TKE with respect to the large-scale TKE decreases downstream. At the ($x = -50$ mm) location we can observe from Figures 4.35b, that the amplitude of large-scale TKE has increased and most of it is contained in between the zones of high probable positive and high probable negative vortices (see Figures 4.21c and 4.21d). This observation is in support of what was observed by Brundrett and Baines [75]. It can thus be conjectured that the flow is most unsteady at the interface of the two opposing vortices at this location. Similar observations can be made from the contours of TV4 (Figure 4.35c) for one of the regions of high TKE near the corner.

The wall normal profiles of total turbulent kinetic energy (contains large- and small-scales) are shown in Figure 4.36. The profiles of TKE in TV1, do show a canonical peak close to the wall and gradual decay towards the core flow [127]. However it must be noted that this decay in TKE towards the core flow is not monotonic at this location as seen in Figures 4.36c and 4.36b. This effect may be due to the non-equilibrium state of the boundary layer at this location [17, 105]. It can be seen from Figure 4.36e, that the boundary layer has progressed towards equilibrium away from the corner as the profile at ($y = 15$ mm) now shows monotonic decay of TKE towards the core flow. From Figure 4.36h we can see that the boundary layer is close to equilibrium form with the decay of TKE towards the core flow being gradual. Figure 4.36i shows two peaks in the TKE profiles close to the bottom wall. The second peak can be attributed to being a corner effect since it is observed around $y \approx 10$mm which is the location where the positive corner vortex resides.

4.13 Forms of Turbulence

The relative magnitudes of the Reynolds stress components $\overline{u_i' u_j'}$ are of paramount importance for computational studies. The normalized anisotropy a_{ij} tensor introduced by Lumley [128], defined as the deviation from the isotropic state, provides a good way to quantify their relative dominance

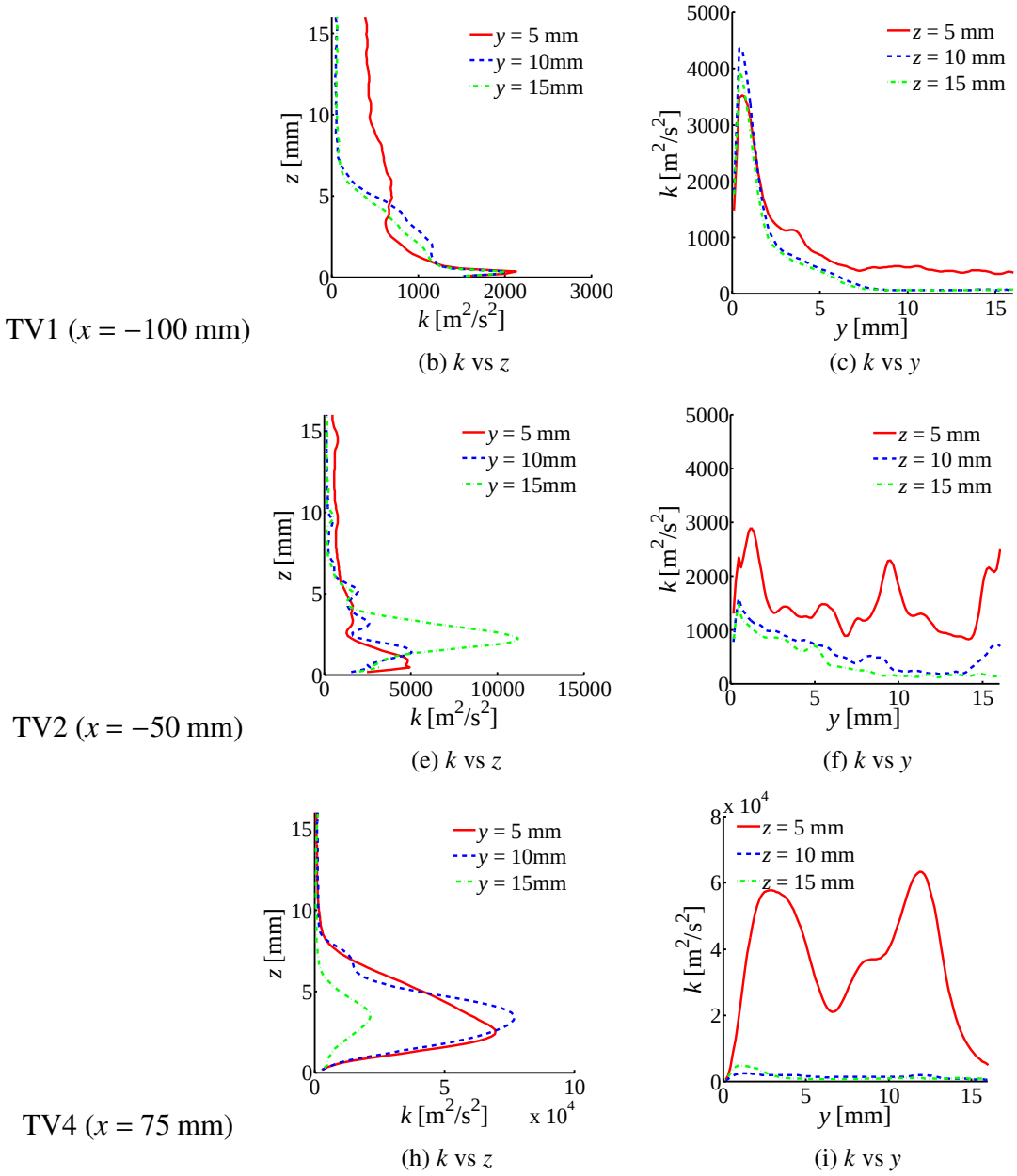

Figure 4.36: Mean turbulent kinetic energy profiles from TV1, TV2 and TV4 dataplanes at Mach 2.75. For reference, $y_T = 57.2$ mm, $z_T = 69.3$ mm.

in the flow field. Its mathematical definition is

$$a_{ij} = \frac{\overline{u_i' u_j'}}{2k} - \frac{\delta_{ij}}{3} \tag{4.30}$$

where $k = \overline{u_i' u_j'}$ and δ_{ij} is the Kronecker delta. The diagonalization of a_{ij} provides us with its eigenvectors (E_1, E_2, E_3) associated with eigenvalues $(\lambda_1, \lambda_2, \lambda_3)$ ordered such that $\lambda_1 \geq \lambda_2 \geq \lambda_3$ and $\lambda_1 + \lambda_2 + \lambda_3 = 0$. The relative values of these eigenvalues provide an insight into the structure of local turbulence. It is given as:

a. One component or cigar shaped: Turbulence along one direction dominates. This state is represented by $\mathbf{X_{1c}}$.
$\lambda = [2/3, -1/3, -1/3]^T$.

b. Two component/axisymmetric or pancake shaped: Turbulence along two directions is equally stronger than the third direction. This state is represented by $\mathbf{X_{2c}}$.
$\lambda = [1/6, 1/6, -1/3]^T$.

c. Isotropic or spherical: Turbulence is equally distributed in all three directions. This state is represented by $\mathbf{X_{3c}}$.
$\lambda = [0, 0, 0]^T$.

The lines joining these points form the boundary of all possible turbulence states and thus define an invariant map. Various maps have been proposed in literature based on the invariants [129, 130]. The points on these invariant maps determine what behavior the turbulence of the flow is undergoing locally. These processes are as follows:

a. Axisymmetric expansion: Lies on the line joining $\mathbf{X_{1c}}$ and $\mathbf{X_{3c}}$.
$0 < \lambda_1 < 1/3$ and $-1/6 < \lambda_2 = \lambda_3 < 0$.

b. Axisymmetric contraction: Lies on the line joining $\mathbf{X_{2c}}$ and $\mathbf{X_{3c}}$.

$-1/3 < \lambda_1 < 0$ and $0 < \lambda_2 = \lambda_3 < 1/6$.

c. Two component: Lies on the line joining $\mathbf{X_{1c}}$ and $\mathbf{X_{2c}}$.

$\lambda_1 + \lambda_3 = 1/3$ and $\lambda_2 = -1/3$.

d. Plane Strain: At least one $\lambda_i = 0$.

The turbulence anisotropy of the corner flow was mapped on to barycentric coordinate system detailed by Banerjee et al. [129] and represented by contours using methodology of Emory and Iaccarino [130]. Figure 4.38 shows the streamwise evolution of turbulence form in the Mach 2 tunnel corner.

The turbulence state profiles across three spanwise (as a function of z) and three heightwise (as a function of y) locations at TV2 plane in Mach 2 empty tunnel are shown in Figure 4.37. At the upstream location (Figure 4.37a) the turbulence state normal to the bottom wall away from the corner ($y = 12$ mm) matches that of a typical undisturbed boundary layer [129] where the turbulence near the wall is 2 dimensional and evolves along the axisymmetric expansion line towards isotropy. This behavior is consistent with the observationf of Lapsa and Dahm [17] on the centerline of the tunnel. The profile is closest to isotropy until $z = 10.39$ after which it is affected by the secondary flow effects of the rectangular channel flow and no longer conforms to an undisturbed boundary layer. Normal to the sidewall (Figure 4.37b) the turbulence state profile is seen to have been affected by the secondary flows with an initial tendency to evolve with the 2D turbulence before turning the tendencies towards one dimensional turbulence. Further downstream it can be seen that the turbulence structure is biased towards one component turbulence for most of the corner flow which is typical of a boundary layer profile. As we traverse away from the walls the profiles initially have a tendency to be biased towards pancake shaped turbulence before undergoing an axisymmetric expansion with a horizontal peak at $y = 12$ mm, $z = 0.76$ mm which is about $y^+ =$

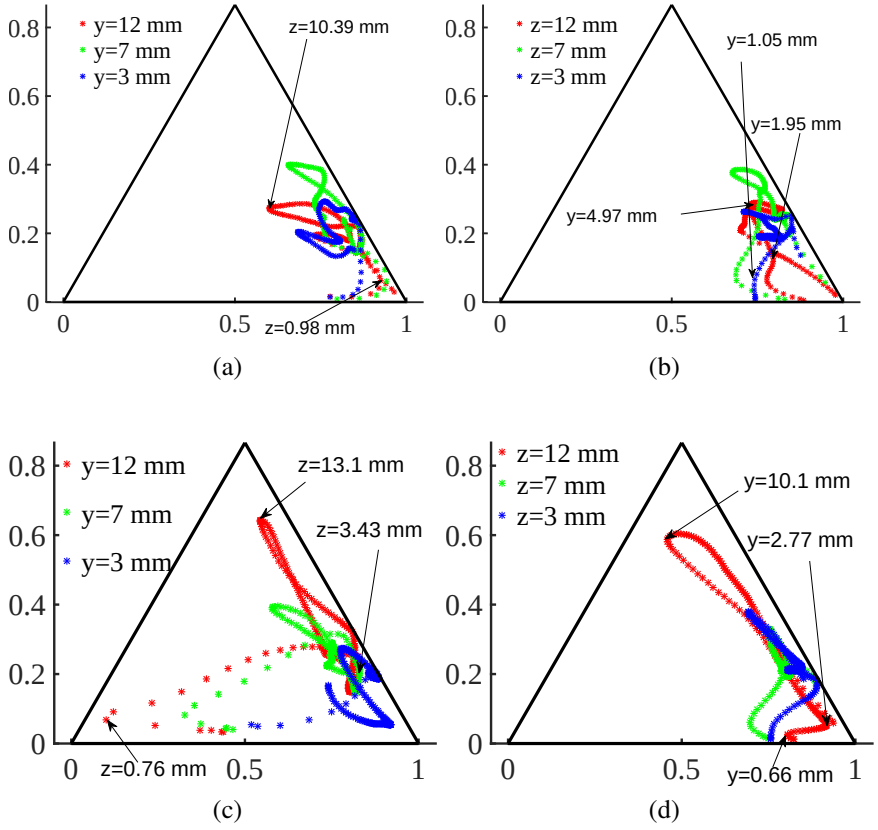

Figure 4.37: Profiles of the turbulence states (a): as functions of z at TV1 and (b): as functions of y at TV1, (c): as functions of z at TV2 and (d): as functions of y at TV2 in barycentric coordinate system in Mach 2.

10240, $z^+ = 0.76$ and $y = 0.66$ mm, $z = 12$ mm about $y^+ = 558$, $z^+ = 8170$. This behavior is atypical of a regular boundary layer and is attributed to the vorticity associated with the corner secondary flows and reaching near isotropy at about $y = 12$ mm, $z = 13.1$ mm which is about $y^+ = 10240$, $z^+ = 8927$ and $y = 0.66$ mm, $z = 12$ mm about $y^+ = 558$, $z^+ = 10142$. The behavior of the turbulence states at TV3 is similar to that observed at TV2.

Figure 4.38a shows the colormap associated with the barycentric coordinate system with $\mathbf{X_{1c}}$, $\mathbf{X_{2c}}$ and $\mathbf{X_{3c}}$ being the limiting states associated with one component or cigar shaped turbulence, axisymmetric two component or pancake shaped turbulence and three component or spherical/isotropic turbulence.

Figures 4.38b, 4.38c and 4.38d show the turbulence forms observed at the location of TV1, TV2 and TV3 respectively. Most of the flow at all three locations is non-isotropic dominated primarily by one component cigar shaped turbulence. All three locations feature yellow/green bands of two component/two component limit turbulence conforming the sidewall near corner which is characteristic of near wall flow where one direction is constrained by the presence of the wall. A prominent axisymmetric 2D turbulence region (green) is observed in TV2 (Figure 4.38c) along the bottom wall away from the influence of corner secondary flows. At TV1 (Fig 4.38b), a pink region of axisymmetric expansion is observed slightly away from the corner which is due to the secondary flows causing increase in in-plane turbulence orthogonal to the principal flow direction (also the direction of 1-component turbulence). Downstream at TV2 (Fig 4.38c) as the corner vortices get stronger and bigger with an increase in spatial unsteadiness as observed in Figures 4.24 and 4.21, the in-plane turbulence contribution to the total turbulence increases and a part of this region (dark blue) develops into three component isotropic turbulence which overlays the region around corner bisector. Further downstream at TV3 (Figure 4.38d) as the corner flow becomes increasingly turbulent in the plane normal to the principal flow, the turbulence in this plane starts dominating over the principal flow direction leading to a development of axisymmetric contraction region (light

blue region). Thus due to the development of secondary flows, the turbulence structure at a fixed point in the corner has a tendency to evolve from a double wall-bounded one-component turbulence to a two-component pancake type turbulence, the path being shown in Figure 4.39. A schematic of evolution of turbulence form of a random point (consider the black dot in Figures 4.38) on the bisectors is shown in Figure 4.40. In Figure 4.40, the black cube represents an element on the bisector plane of the corner while the three orthogonal double headed arrows represent the three eigenvectors $[E_1, E_2, E_3]$ associated with the anisotropy tensor at three streamwise locations in the channel. The relative lengths of the eigenvectors at each of the three locations are related to their corresponding eigenvalues $[\lambda_1, \lambda_2, \lambda_3]$ with the eigenvector having highest eigenvalue represented by the longest double headed arrow. The lengths are also color coded for clarity with red being longer than blue. Extrapolating the observations, the turbulence state at this point will have a tendency to move towards the limiting case of pancake shaped turbulence.

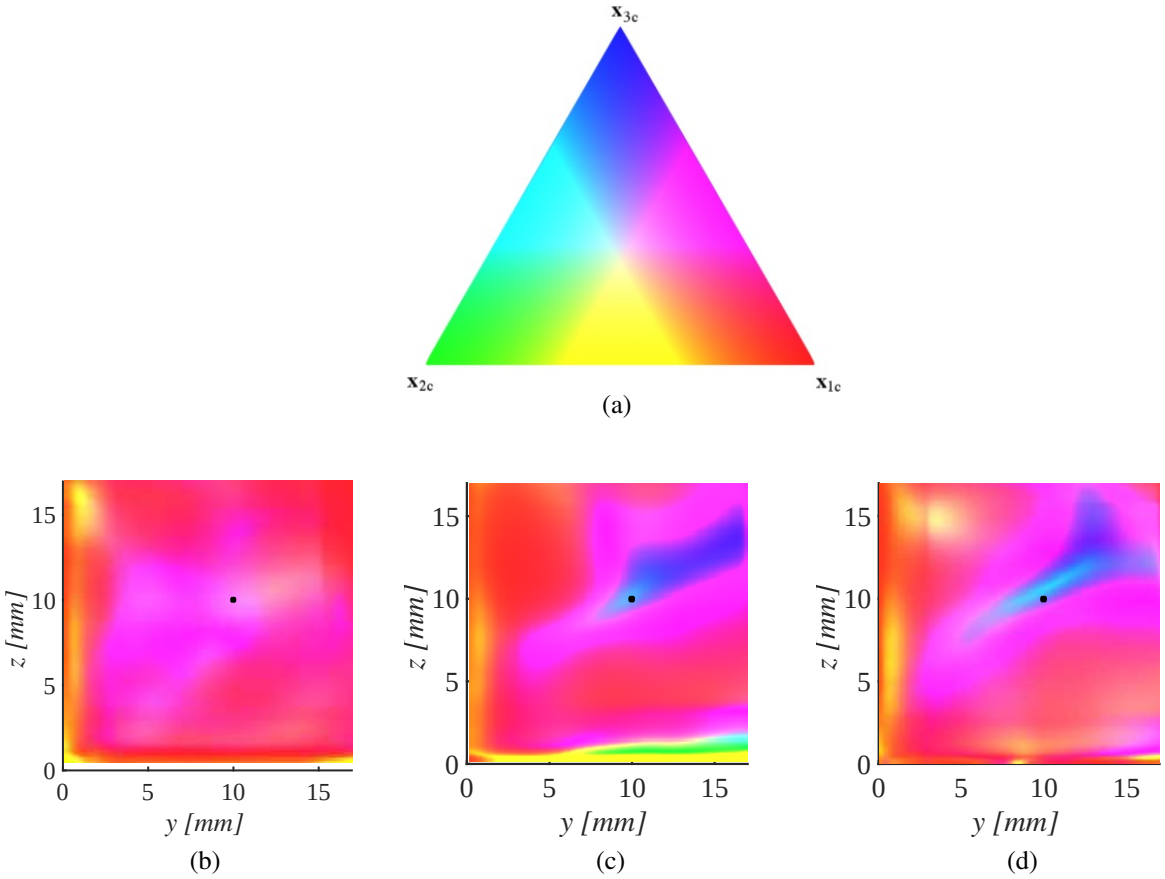

Figure 4.38: Structure of large-scale turb ulence isotropy/anisotropy mapped on to a Barycentric mapping (a): Barycentric colormap: $\mathbf{X_{1c}}$ is the cigar shapped or one-component turbulence, $\mathbf{X_{2c}}$ is the pancake shapped or two-component turbulence, $\mathbf{X_{3c}}$ is the sphere shapped or three-component turbulence; (b): Form of turbulence at TV1; (c): Form of turbulence at TV2; (d): Form of turbulence at TV3. Fields are obtained at Mach 2. For reference, $y_T = 57.2$ mm, $z_T = 69.3$ mm.

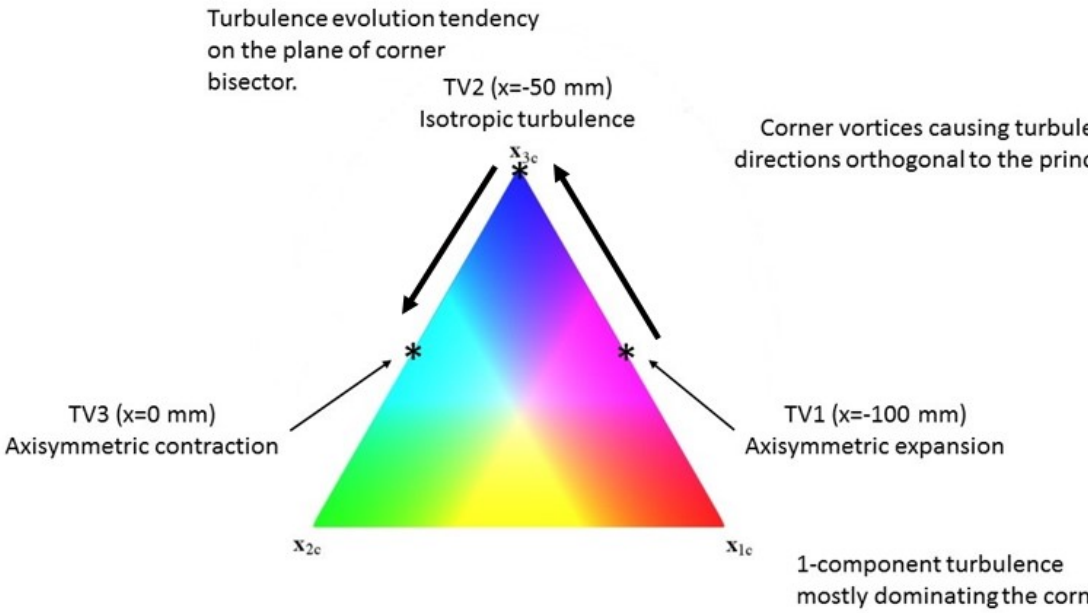

Figure 4.39: Streamwise evolution tendency of the turbulence structure on the corner bisector plane.

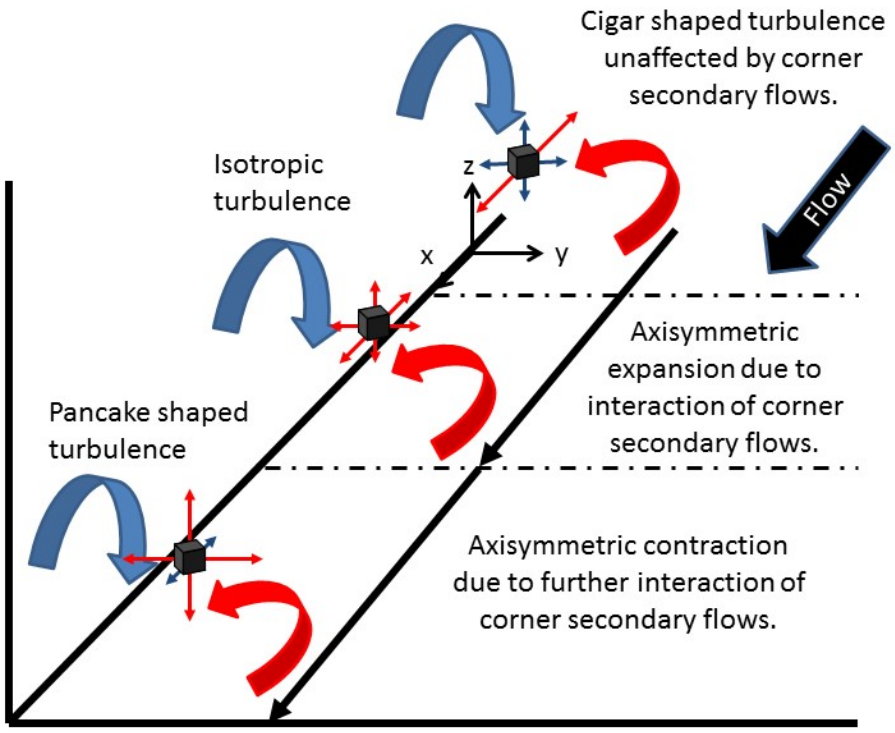

Figure 4.40: Schematic explaining evolution turbulence form on a point on the corner bisector plane.

4.14 Conclusions

Mach 2.75 and Mach 2.0 supersonic turbulent corner flows were experimentally investigated using stereo PIV. Three SPIV data planes orthogonal to the channel walls and the principal flow direction separated by a few boundary layer thicknesses were recorded. The data obtained was used for computing various parameters in order to provide an insight to the turbulent structures which would be characteristic of such a flow field. It was found that,

- No form of symmetry was evident from observing either instantaneous, mean velocity fields or vorticity fields obtained from mean velocity fields in the original form. Decomposing the vector fields into large and small-scales revealed a skewed symmetry, skewed possibly due to the nature of the nozzle or the aspect ratio of the tunnel.

- The instantaneous flow fields consisted of a forest of vortices. Decomposing the velocity field into large and small-scales made it possible to define the corner vortices and study their behavior in the streamwise direction. The average form of the corner vortices was made clear using conditional sampling.

- A statistical analysis revealed that the corner vortices move away from the corner while maintaining a similar probability density function of the inter-vortical distance and the corner bisector angle. The mean corner bisector angle at all the locations was found to be approximately equal to the characteristic angle of the channel aspect ratio. The mean characteristic scaling of the corner vortices was found to be of the same order of magnitude at all three locations with a slight tendency to increase downstream.

- The instantaneous vortex filaments become increasingly unstable downstream as the Reynolds number increases. This is evident from decreasing amplitudes and increasing scales of mean vorticity structures observed in mean vorticity fields as well as the increasing standard devi-

ations in the probable corner vortex center locations in vortex center location PDF fields.

- The effect of vortical momentum transport was observed in the iso-tach lines of streamwise velocity and the in plane strain rates associated with the streamwise velocity component.

- The corner vortices tends to decrease the value of the coefficient of friction in regions it draw the lower momentum fluid away from the wall and increase the coefficient of friction in regions where the higher momentum fluid from the core flow is convected towards the wall. This is consistent with skin friction measurements in boundary layers dominated by vortices [126] and also matches the observations by Davis and Gessner [7].

- The velocity profiles (inner scale normalized) show fuller profiles in the outer wake region when the wall normal velocity vectors point towards the wall, while they show a defect region in the logarithmic region when the wall-normal vectors point away from the wall, indicating momentum transport (upwell/downwash motion) due to the corner vortices.

- The vorticity production fields due to turbulence anisotropy and the cross diagonal turbulence components were found to be orthogonal to each other which corroborates results of Brundrett and Baines [75].

- Small scale coherent structures were found by conditionally averaging scale velocity fields in corner vortex coordinate system. The ejection caused by these structures was associated with a pair of counter rotating vortices with positive vortex lining up with the positive corner vortex and negative vortex lining up with the negative corner vortex.

- Turbulence in the corner was mostly anisotropic primarily dominated by one component cigar shaped turbulence. The region of interaction between the two corner follows a trend of axisymmetric expansion to isotropic turbulence and axisymmetric contraction having a tendency to proceed towards pancake shaped turbulence.

CHAPTER 5

Swept shock-corner flow interactions

This chapter will initially give a description of the flow fields resulting from the stronger (6° deflection) and weak (4.6° deflection) SBLIs at Mach 2.75 with an emphasis on secondary flows. We then investigate the effects of the weak SBLI on the corner vortices. A hypothesis will be presented to explain the role of secondary flows on determining where an open flow separation event is most likely to occur. This hypothesis will then be used for predicting the locations of flow separations from both the cases, as well as to explain flow separation / reattachment in a couple of canonical flow configurations found in the literature.

5.1 Comparison between Strong and Weak SBLI

Figure 5.1 shows the averaged schlieren images of the strong and weak SBLIs. The measured angle of the incident shock wave in strong SBLI case is 25.8° against a computed value of 25.9° while for the weak SBLI while it is measured to be 24.8° against a calculated value of 24.7°. The major difference observed is that the reflected shock wave begins well upstream of the nominal interaction point (I) in case of the stronger (6°) SBLI which is consistent with a separated incident oblique SBLI (see section 1.2.3), while it appears to be reflected at the nominal interaction location in case of weaker (4.6°) SBLI and resembles the structure of a non-separated incident oblique SBLI. The 6° SBLI causes a stronger adverse pressure gradient resulting in a stronger boundary layer

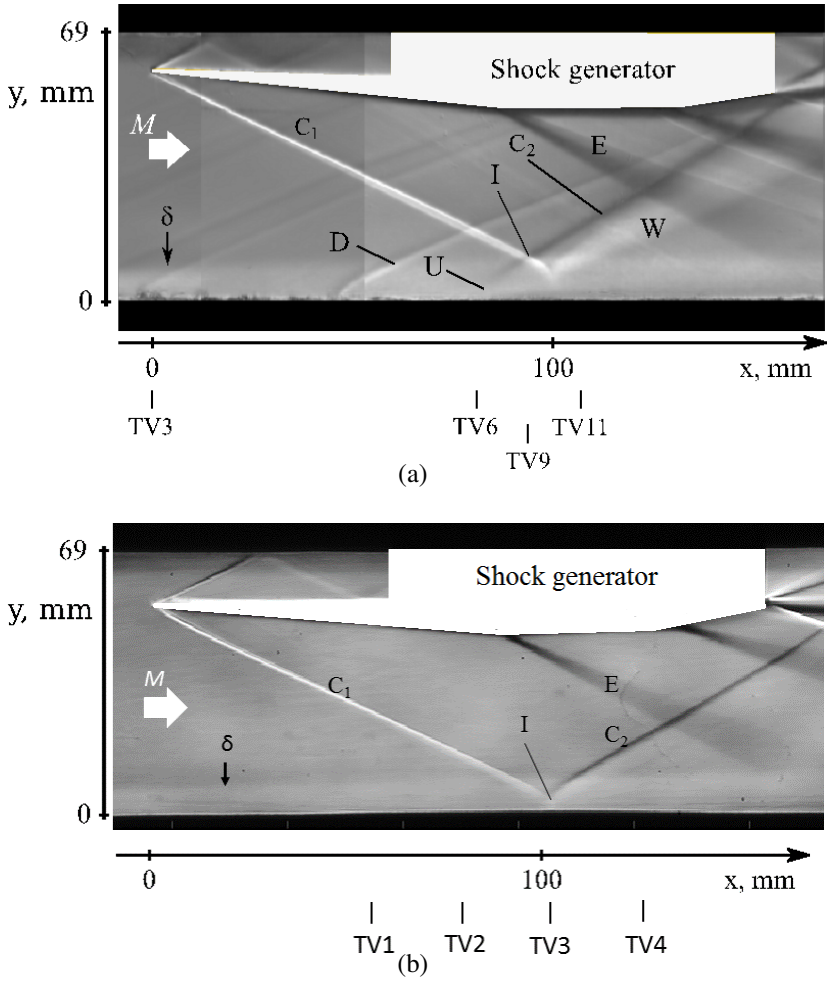

Figure 5.1: Average schlieren images of the (a): 6° SBLI and (b): 4.6° SBLI. For reference, $y_T = 57.2$ mm, $z_T = 69.3$ mm.

thickening and flow separation. This causes the incoming flow to be diverted along the thickened boundary layer resulting in a separation shock (reflected shock) that starts well upstream of the nominal interaction location.

Another major difference in the schlieren images is the presence of the reflected expansion fan W in the 6° SBLI that is not observed in the weaker interaction. This is consistent with the 6° and 4.6° SBLIs being examples of separated and non-separated interactions as has been inferred previously. The separated boundary layer reattaches on the bottom wall causing a downflow of the

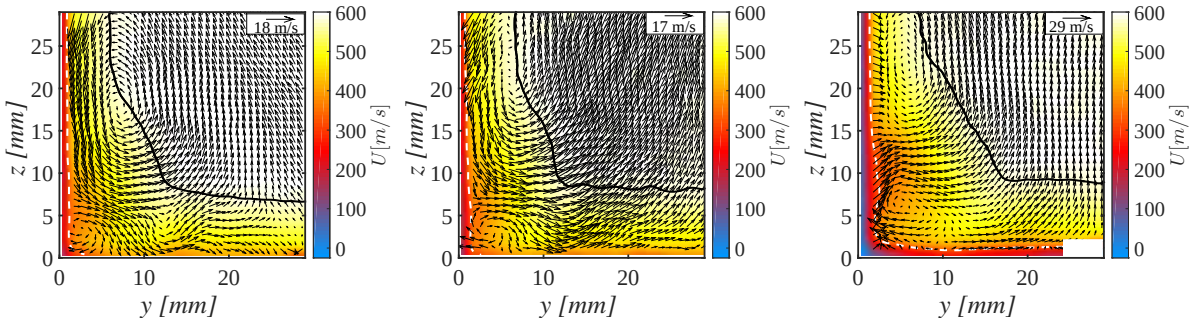

Figure 5.2: Primary flow fields obtained in empty tunnel (a): upstream (x = 82 mm), (b): at (x = 102 mm) and (c): downstream (x = 122 mm) of the nominal interaction location of SBLI with 4.6° flow deflection. For reference, y_T = 57.2 mm, z_T = 69.3 mm.

air resulting in the formation of expansion waves. As per the proposed structure of unseparated incident oblique SBLI (Section 1.2.3, Figure 1.3), the thickened boundary layer recovers downstream as it progresses through the expansion waves. These are reflected from the free surface by the compression waves formed by spreading out of incoming shock. However the expansion waves are completely extinguished by the reflected strong shock wave near the interaction point and are not observed in the schlieren fields.

5.1.1 Primary Flow Fields

5.1.1.1 Empty Tunnel

SPIV data was recorded in the empty tunnel at the same locations where data was recorded for a weak SBLI case in the wind tunnel prior to installing the wedge. Thus the empty tunnel flow recorded in this dataset would correspond to the room and physical conditions that existed during the time weak SBLI case was studied and hence would be a representative of the flow that would have existed without the wedge for the SBLI with 4.6° flow deflection (weak interaction).

The averaged vector fields in the empty tunnel are shown in Figures 5.2a, 5.2b and 5.2c respec-

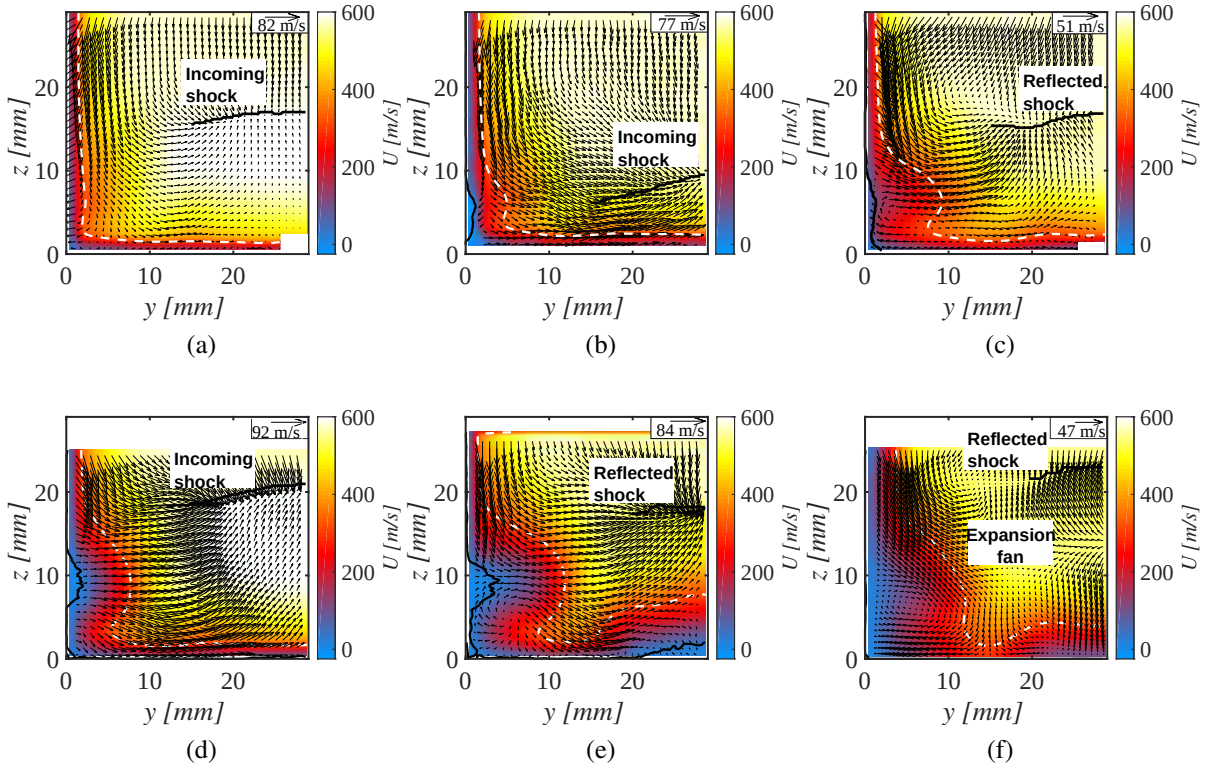

Figure 5.3: Top row: Primary flow fields of 4.6° SBLI at (a): x = 82 mm, (b): x = 102 mm and (c): x = 122 mm. Bottom row: Primary flow fields of 6° SBLI at (d): x = 76 mm, (e): x = 96 mm and (f): x = 115 mm. For reference, y_T = 57.2 mm, z_T = 69.3 mm.

tively. The growth of the corner effect on the primary flow fields follows the discussion in chapter 4.

5.1.1.2 SBLI cases

Averaged velocity fields on cross sectional planes of both cases of SBLI at three locations (2δ upstream, at and 2δ downstream of the point of nominal interaction) are shown in Figure 5.3 where the top row shows the velocity fields for the weak (4.6°) SBLI while the bottom row shows the velocity fields from the stronger (6°) SBLI. The $y = 0$ and $z = 0$ axes represent the locations of the sidewall and the bottom wall as per the coordinate system discussed previously, the white

dotted line is the sonic line, the solid black line in the core flow is the shock and the solid black line conforming the axes is the separation bubble profile (h) averaged by conditionally sampling the separation bubble profile obtained from the separated cases.

The flow field 2δ upstream of the nominal interaction location of the weaker SBLI (4.6° flow deflection) is shown in Figure 5.3a. The flow in the corner ($[0 \leq y \leq 10,\ 0 \leq z \leq 10]$) of the weaker SBLI qualitatively resembles that of an undisturbed corner flow with the major portion of the corner flow dominated by a higher momentum fluid as compared to the corner flow subject to the stronger SBLI (6° flow deflection) at location 2δ upstream of the nominal interaction location. This is evident in the form of region characterized by lower values of U and relatively unaffected sonic line (white dashed). One possible reason for this may be the downward mass flux generated by the weaker incoming swept-oblique shock is lesser than the 6° case. Thus the interaction of this downflow with the corner flows is weaker causing an unobservable convection of low momentum fluid from near the sidewall resulting in an extremely weak low momentum fluid bulge around $z = 8$ mm. The incoming shock associated with the weaker interaction is flatter than the stronger case and nearer to the bottom wall as the angle associated with the shock generated by 4.6° flow deflection is smaller than that generated by 6° flow deflection. The shock is found to be terminating at the boundary layer of the sidewall for both the cases. No flow separation is observed in the weaker case which is due to the weaker adverse pressure gradient and weaker low momentum convection caused by the corner flows associated with the weaker case.

At the location of nominal interaction (point I), the incident shock associated by the weaker SBLI penetrates deeper into the boundary layer, while the incident shock associated with the stronger SBLI is intercepted by a separation shock (U); which originates upstream of I; away from the bottom wall at a higher value of z (see Figure 5.1) which makes it appear that the shock is reflected from a higher point (see figures 5.3b and 5.3e). A separation bubble (incipient) is observed in the conditionally averaged separation bubble profiles of both cases on the sidewall near the region

where the negative corner vortex would exist. The strong SBLI causes a large separation bubble (more probable and spatially larger separation bubble) due to the same reasons as stated for the upstream location. Apart from the separation bubble on the sidewall, the stronger SBLI is also associated with a weaker flow separation on the bottom wall lifting the incoming flow upwards, away from the bottom shock which is manifested in the form of low momentum (blue) region on the bottom wall from starting from $y \approx 20$ mm in Figure 5.3e as well as the upwelling of the sonic line. However no such feature is observed in the weak SBLI case (see Figure 5.3b) where the sonic line is seen conforming to the bottom wall. Another major difference observed in the flow fields at this location is that of the iso-tach profiles of the principal velocity component which qualitatively follow the sonic line profile. The iso-tach profiles associated with strong SBLI resemble those characteristic of a strong secondary corner flow effect, which is caused by the sidewall flow separation convecting some incoming flow towards the core which is evident in the flow vectors in the separated flow region ($z \approx 8$ mm).

Averaged primary flow fields 2δ downstream of the nominal interaction for both weak and strong SBLIs are shown in Figures 5.3c and 5.3f, respectively. At this location the boundary layer is undergoing a recovery process having passed through through the expansion fan. Figure 5.3c shows the flow downstream of the interaction in the weaker SBLI case where the expansion fan has been consumed by the reflected shock. The separation bubble on the sidewall near the corner is now weaker, while the momentum defect region created by the secondary corner flows has expanded away from the walls and it is now affecting the sonic line that has bulged out from the corner into the core flow. This may be a result of the secondary flows interacting with the shock followed by an expansion fan. Figure 5.3f is the flow field downstream of the strong SBLI that features an expansion fan (manifested as a region of diverging vectors) following the reflected/separation shock unlike the non-separated case (weaker SBLI). The flow is almost completely attached with the sonic line curvature nearly relaxing (nearer to bottom wall as compared to the nominal interaction

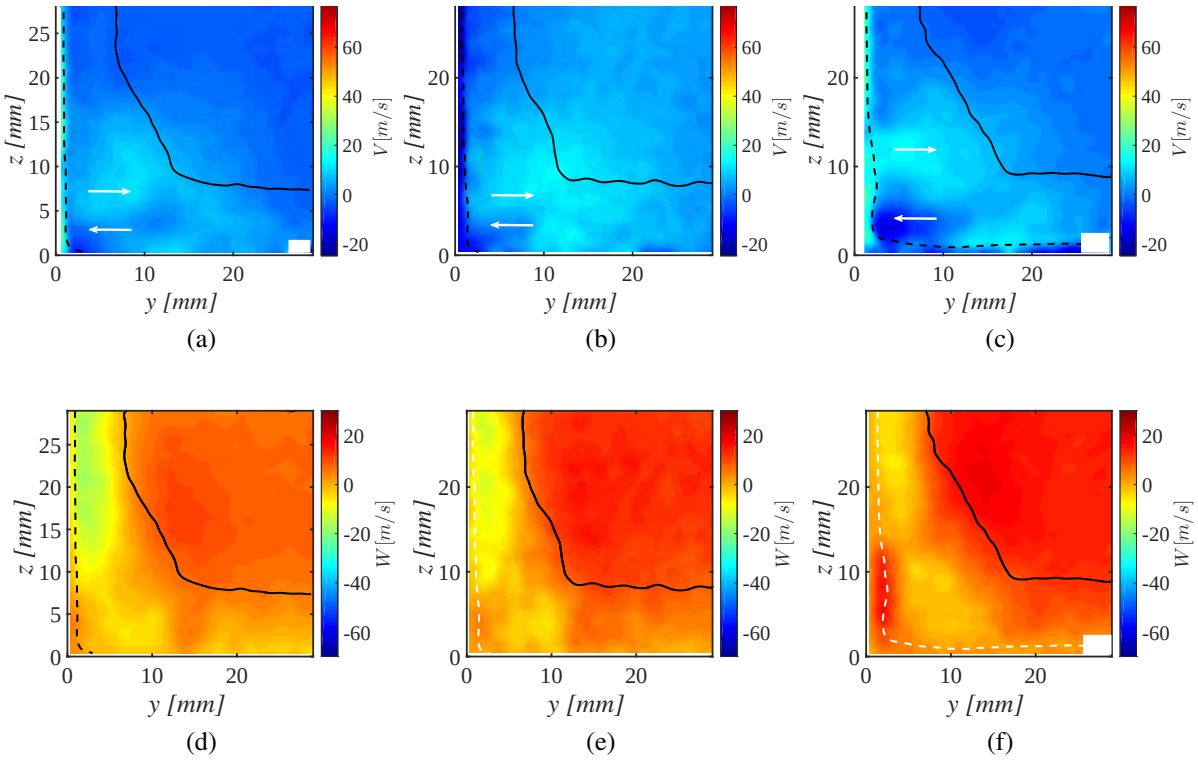

Figure 5.4: Top Row: V-velocity fields obtained in empty tunnel (a): $x = 82$ mm, (b): $x = 102$ mm and (c): $x = 122$ mm. Bottom Row: W-velocity fields obtained in empty tunnel at (d): $x = 82$ mm, (e): $x = 102$ mm and (f): $x = 122$ mm. For reference, $y_T = 57.2$ mm, $z_T = 69.3$ mm.

location) on the bottom wall.

5.1.2 Secondary Flow Fields

5.1.2.1 Empty Tunnel

The contour plots of averaged V and W fields obtained in the empty tunnel are shown in Figure 5.4. A growing and strengthening region of negative V velocity can be seen conforming to the corner characteristic of evolving corner flows. The region of upwash of the fluid pointing away from the sidewall (positive V) starts at about $z \approx 5$ mm and continues moving away from the wall to $z \approx 10$ mm as would be expected from an evolving corner secondary flow. A similar effect of

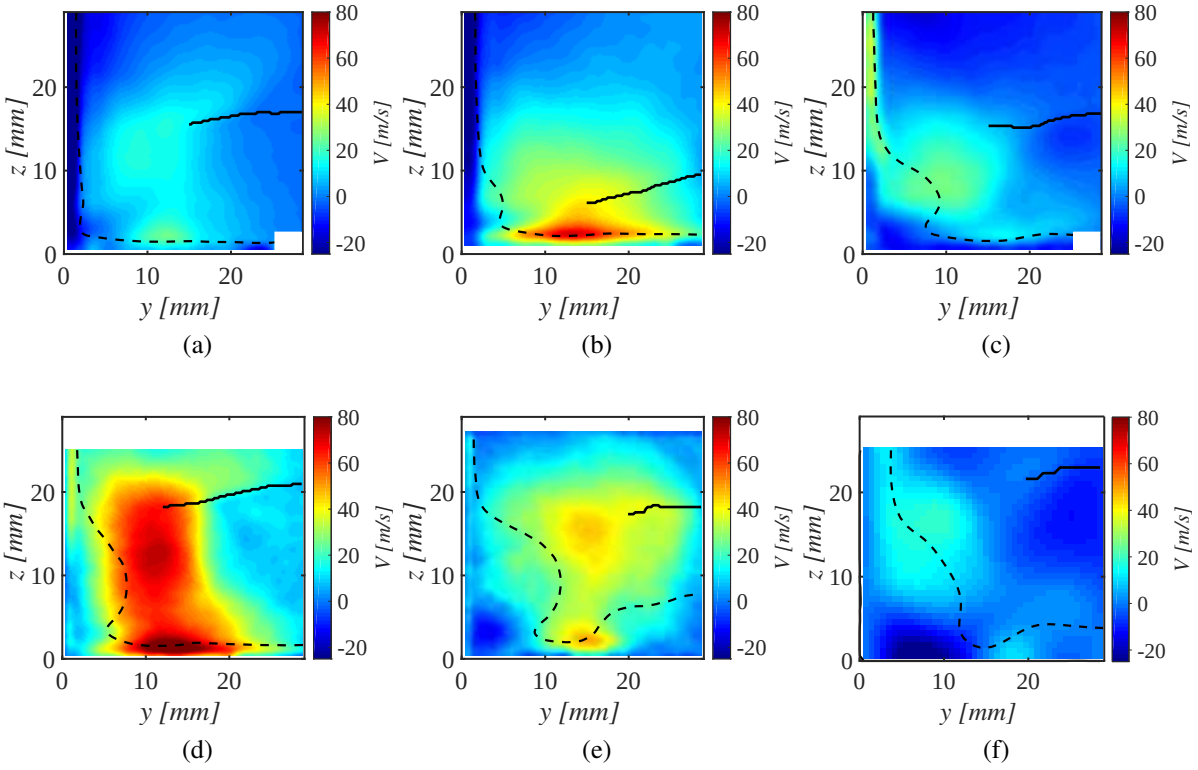

Figure 5.5: Top row: V-velocity fields of 4.6° SBLI at (a): (x = 82 mm), (b): (x = 102 mm) and (c): (x = 122 mm). Bottom row: V flow fields of 6° SBLI at (d): (x = 76 mm), (e): (x = 96 mm) and (f): (x = 115 mm). For reference, y_T = 57.2 mm, z_T = 69.3 mm.

evolving secondary corner flows is observed in the W fields.

5.1.2.2 SBLI

The in-plane averaged velocity fields (V and W) associated with the weak (4.6° deflection) and strong (6° deflection) SBLI are shown in Figures 5.5 and 5.6 respectively.

The averaged V velocity fields 2δ upstream of the nominal interaction location in weak and strong SBLI are shown in Figures 5.5a and 5.5d respectively. As expected the incoming swept shock interacting with the sidewall boundary layer-corner flow system generates a stronger secondary flow away from the sidewall manifested as the larger region occupied by high V values that exist

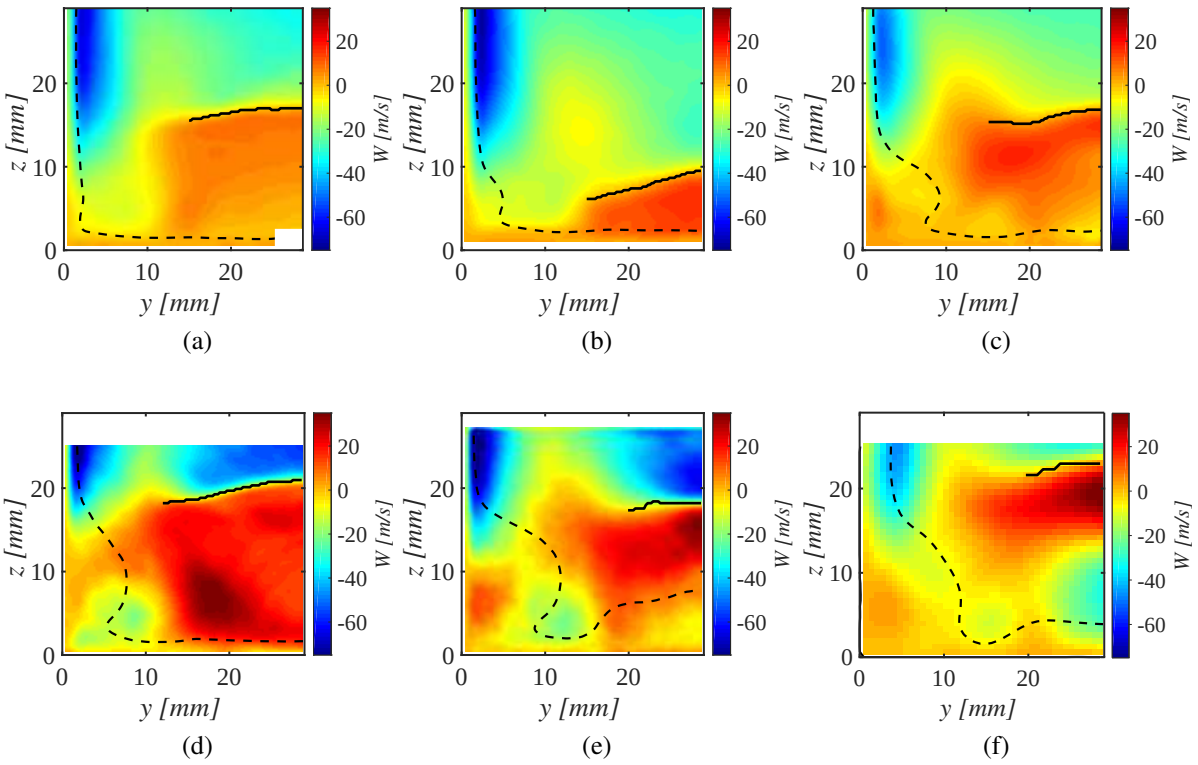

Figure 5.6: Top row: W-velocity fields of 4.6° SBLI at (a): (x = 82 mm), (b): (x = 102 mm) and (c): (x = 122 mm). Bottom row: W-velocity fields of 6° SBLI at (d): (x = 76 mm), (e): (x = 96 mm) and (f): (x = 115 mm). For reference, y_T = 57.2 mm, z_T = 69.3 mm.

between the sidewall and the left limit of the incoming shock wave in the region (7 mm < y < 20 mm, 0 mm < z < 20 mm). The incoming flow is diverted towards the center of the tunnel due to the boundary layer thickening and incipient flow separation in case of the 6° SBLI caused on the sidewall resulting into higher V velocities. However the morphology of this column remains more or less similar in both the cases. It comprises of two prominent regions of high positive values of V: (1) one region characteristic of the positive corner vortex that is found conforming to the bottom wall in the region 9 mm < y < 20 mm; and (2) the region formed due to the swept shock vortex scooping fluid from the sidewall boundary layer towards the core flow observed in the region (9 mm < y < 17 mm, 8 mm < z < 15 mm) which also thickens the subsonic region as seen in Figure 5.5d compared to Figure 5.5a. In case of the weaker SBLI a signature of the negative corner vortex can be observed in the V-velocity fields at $z \approx 3$ mm. It is consistent in magnitude and structure to that observed in the empty tunnel V field of Figure 5.4a. The observed structure of the V-fields for 4.6° and 6° SBLI would be consistent with the surface oil flow structures observed by Bruce et al. [68] for normal shock wave-corner flow studies at low and high Mach numbers. They observed that strong SBLI producing more prominent hourglass oil flow patterns that were observed in the high Mach number cases. The presence of strong V fields (column) would also strengthen the hypothesis suggested by Benek et al. [58] that the interaction taking place on the sidewall affects the interaction on the centerline by deflecting the incoming flow towards the centerline upstream of the shock reaching the bottom wall boundary layer. The stronger shock wave produces a stronger swept SBLI associated with a stronger swept shock vortex (see Alvi and Settles [4]) sweeping down a larger momentum flux. This effect can also be observed in the W-velocity fields at this location shown in Figures 5.6a and 5.6d in the form of a stronger downward velocity (blue region conforming the sidewall above $z \approx 17$ mm) in the stronger SBLI case. Larger magnitudes of positive W-velocity are observed under the shock in the strong SBLI case. They may be due to the thickening and/or incipient flow separation on the bottom wall boundary layer diverting the incoming flow upwards away from the bottom wall. Region of negative W velocities characteristic

of a positive corner vortex can be observed in the corner region $y \lesssim 10$ mm conforming the bottom wall. Unlike the weak SBLI (Figure 5.6a), it appears that the corner flow region upstream of the nominal interaction location in strong SBLI (Figure 5.6d) is coupled with the flow under the shock in the from of a bridge like structure of positive W-velocity values that extends from the corner and away from the sidewall at about $z \gtrsim 10$ mm connecting the core flow. It should be noted that the location of this bridge is also the location of high values of positive V (Figure 5.5d) suggesting convection towards the core flow.

Figures 5.5b and 5.5e show the averaged V velocity fields at the nominal interaction location for the weak and strong SBLI cases respectively. The column of high positive values of V has intensified and the two prominent regions it comprised of have merged in the weak SBLI case and it is seen under the shock conforming to the bottom wall (7 mm $\leq y \leq$ 20 mm). A weak signature of the negative V velocities associated with the negative corner vortex can be observed at $z \approx 3$ mm in Figure 5.5b. In the case of strong SBLI, the column of the positive V velocity has weakened as compared to the upstream field (Figure 5.5d). The two regions of the column are still prominent as the incoming shock is intercepted away from the bottom wall by the separation/reflected shock in the case of strong SBLI before they can merge as observed in the weak SBLI (Figure 5.5b). The negative V velocity region associated with the secondary corner flows convecting fluid into the corner is intensified most likely due to the fact that incipient separation and/or boundary layer thickening on bottom wall diverts the incoming flow away from the separation/thickening region which mostly follows the behavior of the sonic (dashed black) line. In both cases the negative V velocity region associated with the corner flows is observed lying just outside of the convex protuberance of the supersonic region which may attribute the growth of the protuberance to momentum transport caused by the secondary flows. The higher value of negative V velocity causes a transport of high U velocity fluid tending to stretch the sonic line towards the corner. It can also be observed from Figures 5.3b and 5.3e that the conditionally averaged separation bubble profile is alleviated in

the region where this negative V velocity region lies as relatively higher energy fluid is convected towards the separated flow by the velocity vectors pointing towards the sidewall. The averaged W velocity fields at the nominal interaction location for weak and strong cases of SBLI are shown in Figures 5.6b and 5.6e respectively. Larger values of positive W velocity are observed in strong SBLI case with a thicker subsonic region characterized by almost zero W velocity. Negative W values characteristic of a displaced corner vortex are observed on the supersonic side of the protuberance in the sonic line (9 mm $\lesssim y \lesssim$ 12 mm). This region was displaced due to the interaction on the sidewall creating flow separation as seen in Figure 5.3e. The coupling bridge that existed at the upstream location in the strong SLI case is seen to have narrowed.

The averaged V fields for weak and strong SBLI 2δ downstream of the nominal interaction location are shown in Figures 5.5c and 5.5f respectively. As the flow is undergoing relaxation having passed through the interaction, the overall magnitudes of V are lower than the upstream locations for both the cases. The negative V velocity region associated with corner flows has strengthened and grown in area for both the cases and now lies conforming with the bottom wall being pushed down by the shock. The positive V velocity region associated with the swept shock is seen to have weakened and is now moving upwards along with the reflected shock. Mean W velocity fields at this location for both weak and strong SBLIs are shown in Figures 5.6c and 5.6f respectively. The negative W velocity region associated with the swept shock is found conforming to the sidewall at $z \geq 17$ mm. Almost all the flow below the shock displays positive W velocity for weak SBLI. Since this is the location of boundary layer relaxation, the bottom wall boundary layer attachment is manifested as a region of negative W in strong SBLI which exists above the sonic line in the region $y \geq 20$ mm. This is the result of the flow outside boundary separated/thickened boundary layer turning back towards the bottom wall. The region of divergent vectors between the positive W below the shock and the subsequent negative W region below it forms the reflected expansion fan.

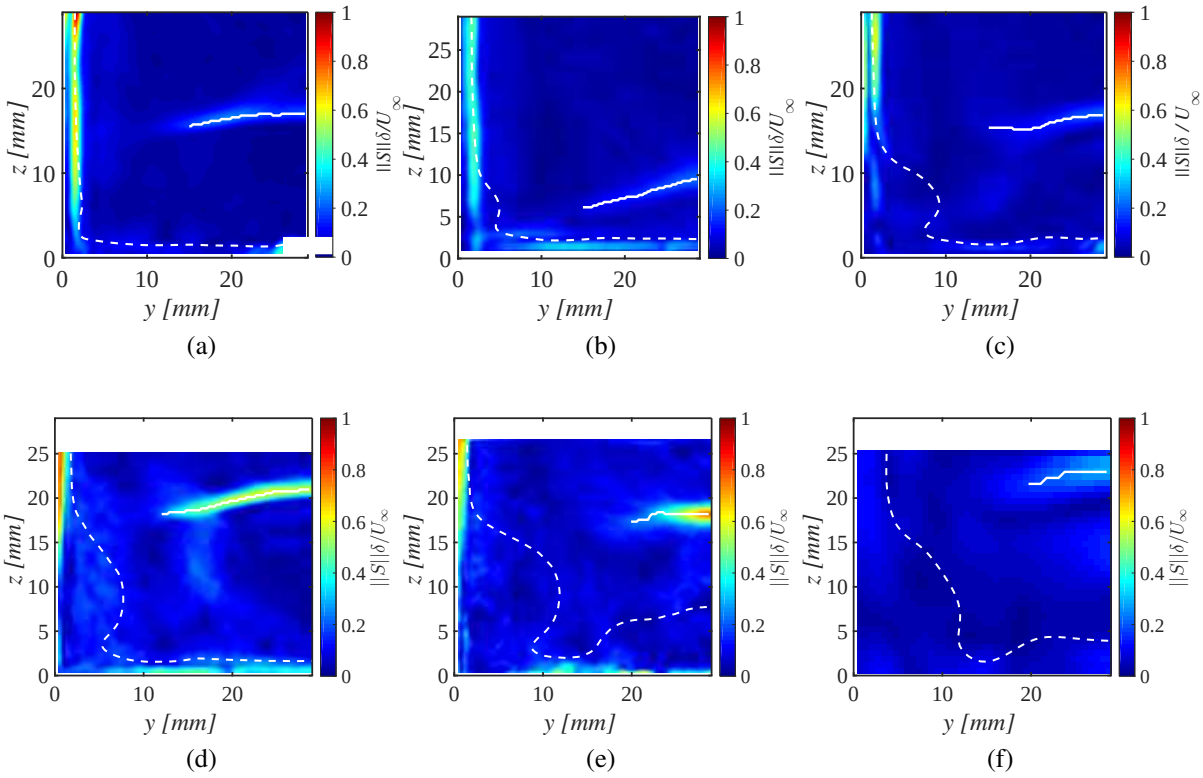

Figure 5.7: Top row: Averaged $||S||$ fields of 4.6° SBLI at (a): $x = 82$ mm, (b): $x = 102$ mm and (c): $x = 122$ mm. Bottom row: Averaged $||S||$ fields of 6° SBLI at (d): $x = 76$ mm, (e): $x = 96$ mm and (f): $x = 115$ mm. For reference, $y_T = 57.2$ mm, $z_T = 69.3$ mm.

5.1.3 Strain Fields and Shock Structure

The in plane strain fields and shock traces as defined in 3.1.4 for the three locations in weak and strong SBLI are shown in Figure 5.7. It can be observed that the shock tends to be less curved in weaker SBLI as compared to the strong SBLI.

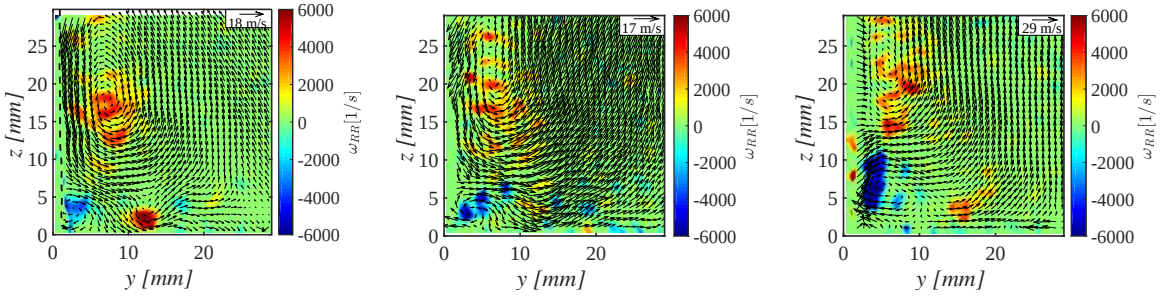

(a) (b) (c)

Figure 5.8: Rigid rotation vorticity fields obtained in empty tunnel at (a): x = 82 mm, (b): x = 102 mm and (c): x = 122 mm. For reference, y_T = 57.2 mm, z_T = 69.3 mm.

5.1.4 Vortex Fields and the Effects of SBLI on Corner Vortices

5.1.4.1 Empty Tunnel

The rigid rotation vortex fields obtained from mean vector fields in empty tunnel at different locations where data is recorded for the weak (4.6° deflection) SBLI are shown in Figure 5.8. The corner vortices were observed to follow the evolution trends discussed in Chapter 4.

5.1.4.2 SBLI

The rigid rotation vorticity fields obtained from mean vector fields (Figure 5.3) of weak and strong SBLI are shown in Figure 5.9. The case of the stronger SBLI is characterized by stronger streamwise oriented vortices.

At the location upstream of the nominal interaction, for both weak and strong SBLI, the incoming positive swept shock vortex (vortex C as described in section 3.4.2) and the positive vortex (vortex B) associated with the secondary corner flows are prominent while only weak signs indicating the presence of the negative corner vortex (B) can be seen. It should be noted that the location of the positive corner vortex does not seem to be significantly affected by the incoming shock at this location in both the cases (as compared to the empty tunnel, Figure 5.8a). The negative corner

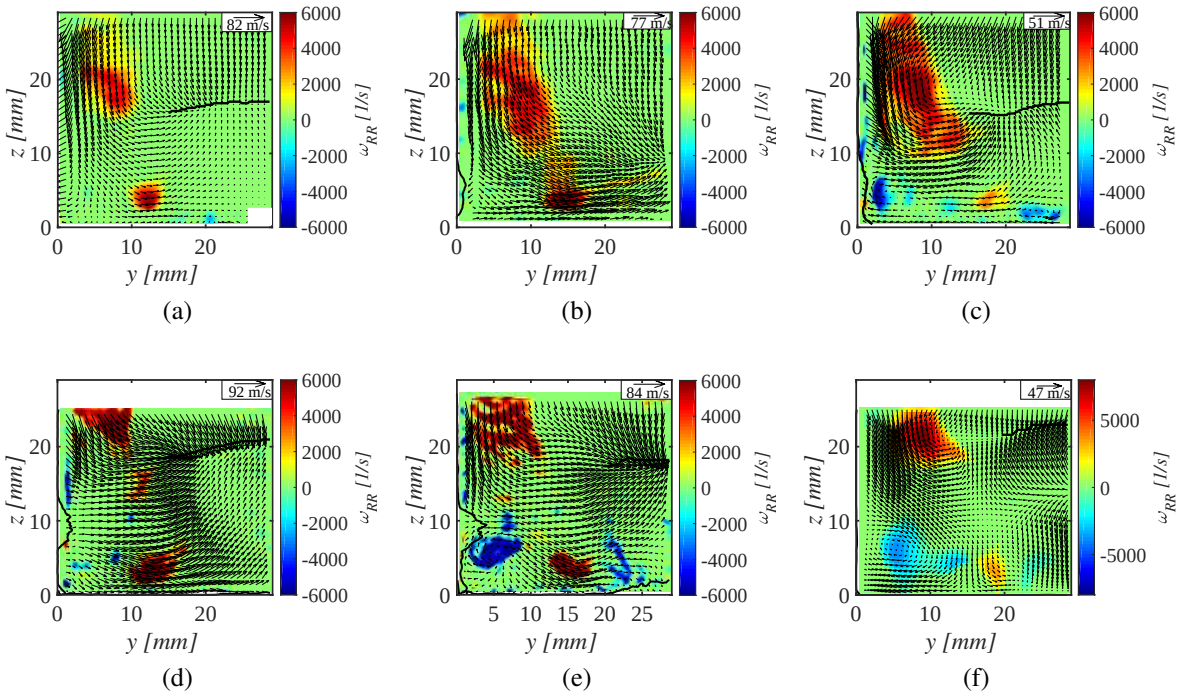

Figure 5.9: Top row: ω_{RR}-fields obtained from obtained from mean vector fields of 4.6° SBLI at (a): x = 82 mm, (b): x = 102 mm and (c): x = 122 mm. Bottom row: ω_{RR}-fields obtained from obtained from mean vector fields of 6° SBLI at (a): x = 76 mm, (b): x = 96 mm and (c): x = 115 mm. For reference, y_T = 57.2 mm, z_T = 69.3 mm.

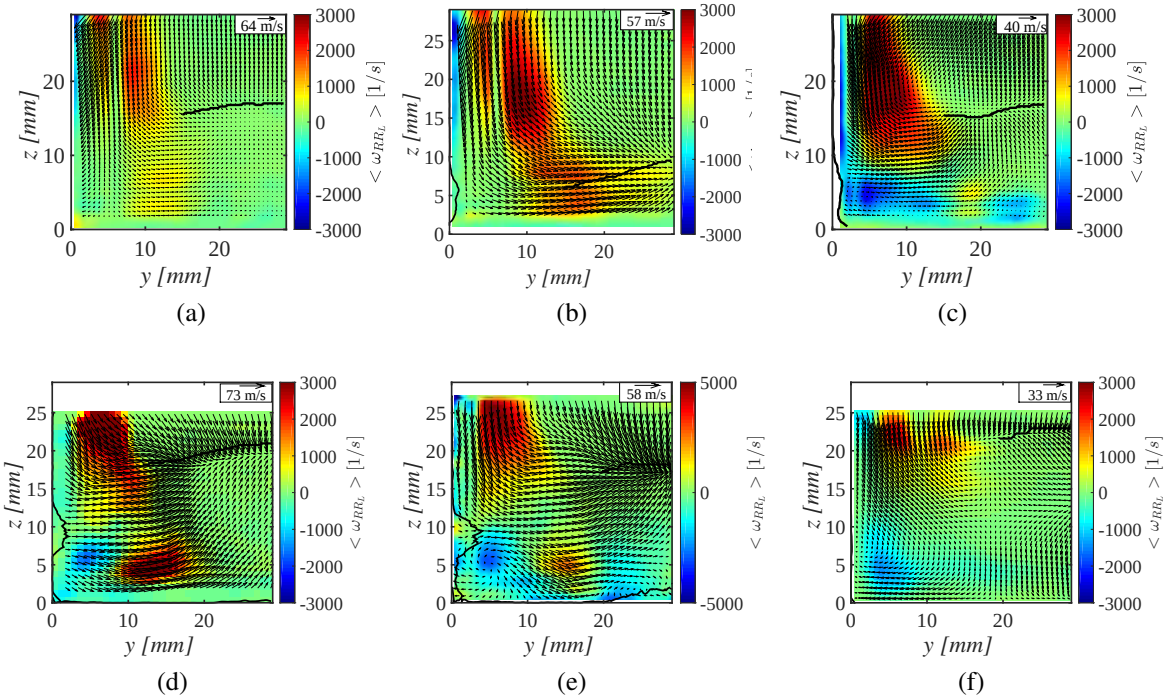

Figure 5.10: Top row: Averaged ω_{RR_L}-fields obtained from obtained from large-scale vector fields of 4.6° SBLI at (a): x = 82 mm, (b): x = 102 mm and (c): x = 122 mm. Bottom row: Averaged ω_{RR_L}-fields obtained from large-scale vector fields of 6° SBLI at (a): x = 76 mm, (b): x = 96 mm and (c): x = 115 mm. For reference, y_T = 57.2 mm, z_T = 69.3 mm.

vortex becomes clearer for the strong SBLI case in the averaged large-scale rigid rotation voticity fields shown in Figure 5.10 while an extremely weak signature of large-scale negative corner vortex is visible for the weak SBLI at $z \approx 2$ mm conforming to the sidewall for the upstream location (Figure 5.10a). In Figure 5.10d, the maximum extent of the averaged flow separation bubble towards the core is observed at the location where the negative corner vortex and the incoming swept shock vortex would transport the low momentum fluid towards the core flow.

Figures 5.10b and 5.10e show the rigid rotation vorticity fields obtained by decomposing the mean vector fields shown in Figures 5.3b and 5.3e. At this location, the positive corner vortex associated with both the cases has been slightly displaced from its laboratory position observed in the undisturbed flow (empty tunnel); towards the core flow. This is due to the incoming flow being convected from the sidewall towards the core flow as the velocity vectors indicate. The swept shock vortex (C) associated with the weaker interaction is found to be closer to the bottom wall as compared to the stronger interaction where the incoming shock is intercepted by the separation shock. Negative corner vortex is still not prominent in the weaker SBLI with only faint traces observed at $z \approx 3.5$ mm conforming to the sidewall while it has strengthened in the stronger SBLI. This may be a result of the flow being processed by the separation shock at this location. For both the cases sidewall flow separation bubble exists at the location from where the negative corner vortex is scooping low momentum fluid away from the sidewall. Similarly, in the stronger SBLI case, the bottom wall flow separation bubble is seen to start at about $y \approx 20$ mm from where the positive corner vortex is seen scooping low momentum fluid away from the bottom wall towards the core flow. Figures 5.10b and 5.10e show the averaged large-scale rigid rotation vorticity fields at the nominal interaction locations for the 4.6° and 6° SBLIs respectively. The averaged large-scale negative vortex is observed to be located at approximately the same z-location it was located upstream of the nominal interaction for both the cases however, it has less vorticity associated with it. A trace of negative vortex D (see section 3.4.3) is observed at the nominal interaction location

conforming to the bottom wall at $y \approx 22$ mm. It should be noted that the bottom wall flow separation bubble starts where the vortex D and vortex A (positive corner vortex) act together to scoop low energy fluid from along the bottom wall towards the core flow.

The rigid rotation vorticity fields obtained from mean vector fields 2δ downstream of the nominal interaction location for weak and strong SBLI are shown in Figures 5.9c and 5.9f while the averaged large-scale vorticity profiles are shown in Figures 5.10c and 5.10f. The negative corner vortex has now recovered for the weak SBLI and is found by the sidewall at about $z \approx 5$ mm which is closer to the bottom wall than its natural position $z \approx 8$ mm in the empty tunnel at this location (Figure 5.8c). This might be due to the downward flux of fluid caused by the shock system on the sidewall as seen in Figure 5.6c pushing the negative corner vortex towards the bottom wall. Its large-scale morphological structure (Figure 5.10c) seems to be a highly distorted vortex structure after a moderate to strong streamwise vortex-oblique shock wave interaction as observed in the numerical studies by Zudov and Pimonov [110] who observed the splitting of the vortex core into two for moderate to strong interactions. The resulting distorted structure is characterized by two cores of high values of vorticity, which may be distorted by the presence of walls and a complicated secondary flow field while the positive corner vortex would be unaffected as observed in the weak streamwise vortex-oblique shock wave interaction cases. The magnitudes of the vortices in the weak SBLI case are higher than those in the strong SBLI case at this location. This may be due to the absence of an expansion wave that would smear out the velocity fields, reducing their gradient magnitudes. Due to absence of an expansion fan the flow recovery is slower in the weak SBLI and flow separation is still observed on the sidewall in the region where the negative corner vortex convects low energy flow away from the sidewall. The negative corner vortex associated with the downstream location of the strong SBLI also shows two lobe structure (Figure 5.9f) associated with a strong streamwise vortex-oblique shock wave interaction. However it has been weakened after passing through the expansion fan and the structure becomes less prominent in the large-scale

	Empty tunnel					
	Φ_-			Φ_+		
	$\overline{z_-}$ mm	$\overline{A_-}$ mm^2	$\overline{Wt_-}$ mm^2/s	$\overline{y_+}$ mm	$\overline{A_+}$ mm^2	$\overline{Wt_+}$ mm^2/s
TV2	4.75	13.32	5.75×10^4	9.99	12.07	4.95×10^4
TV3	5.3	9.23	2.92×10^4	7.75	4.96	1.66×10^4
TV4	6.25	20	8.75×10^4	11.48	12.11	4.37×10^4
	SBLI					
TV2	3.78	3.76	1.05×10^4	12.13	23.97	3.93×10^4
TV3	3.71	2.17	6.97×10^3	11.77	10.25	2.18×10^4
TV4	5.24	18.52	9.19×10^4	15.84	9.95	3.67×10^4

Table 5.1: Effect of SBLI on corner vortices.

fields. The positive corner vortex is observed to have been displaced further towards the channel centerline on the bottom wall for both the cases.

Due to the availability of the empty tunnel corner flows at the location of dataset recording for weak SBLI, we are presented with an opportunity to study the effect of SBLI on corner vortices. Various properties of corner vortices with and without the SBLI are tabulated in Table 5.1 while the histograms of the properties at two locations one upstream and another downstream of the interaction are shown in Figures 5.11 and 5.12 respectively. The effect of the shock system pushing the negative corner vortex towards the bottom wall can be observed in the form of a shift to the left of the pdfs of z_- both upstream and downstream of interaction (Figures 5.11a and 5.12a). This is attributed to the downward velocity flow that is found conforming to the sidewall as has been observed in Figure 5.6c. Similarly the positive corner vortex is displaced away from the sidewall towards the centerline which is observed as a rightward shift of the pdfs in Figures 5.11d and 5.12d. Upstream of the interaction the negative corner vortex affected by the shock wave is seen to have a decreased area and weights. Vortex weight is defined as $Wt = \int_{A_\Phi} |\omega_{RR_L}| dA_\Phi$ or the net

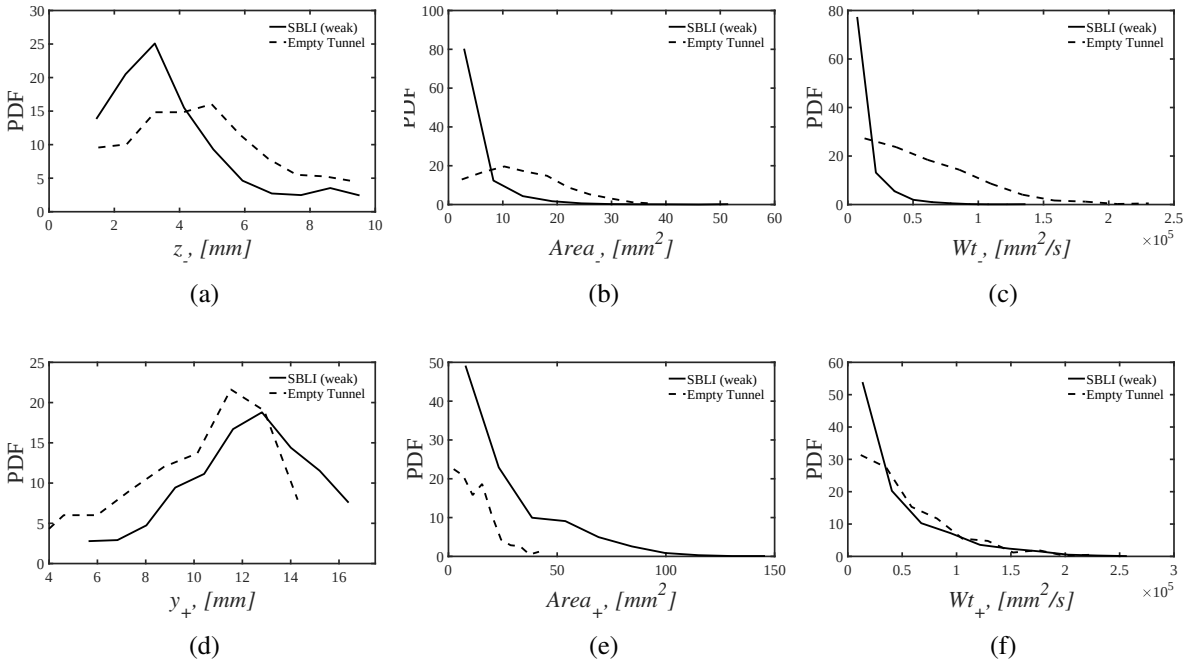

Figure 5.11: Effect of weak SBLI on various corner vortex properties 2δ upstream of interaction (TV2 x = 82 mm). Top row: negative corner vortex, bottom row: positive corner vortex.

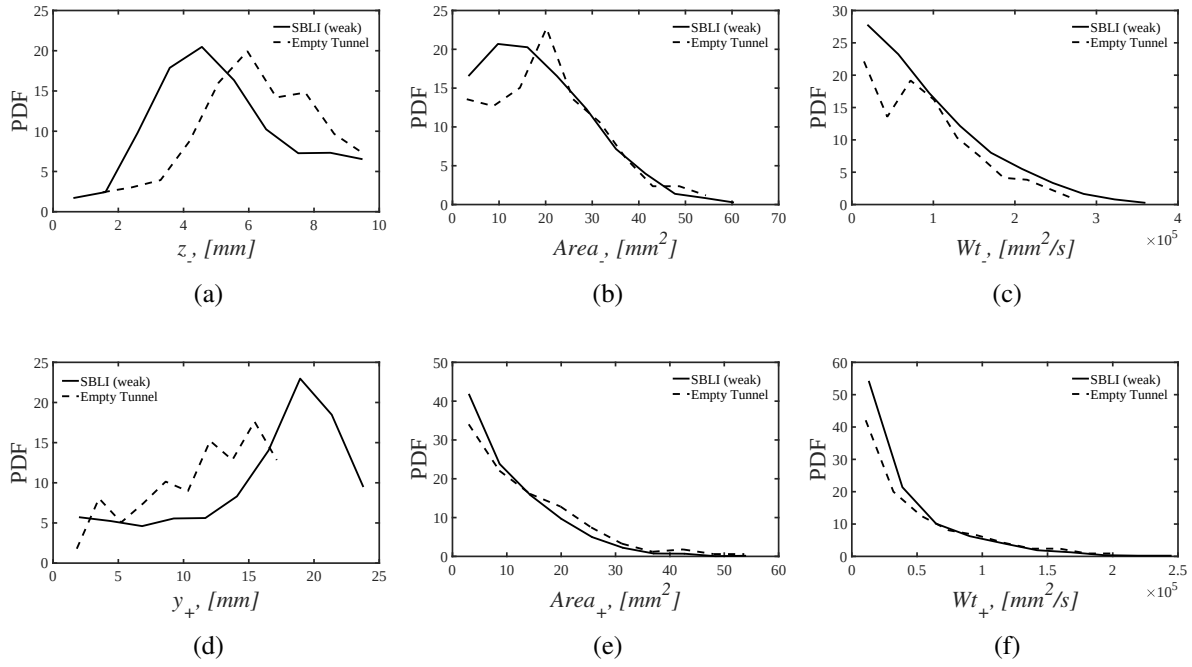

Figure 5.12: Effect of weak SBLI on various corner vortex properties 2δ downstream of interaction (TV4 x = 102 mm). Top row: negative corner vortex, bottom row: positive corner vortex.

rigid rotation vorticity content of a vortex. It is similar to circulation but computed using rigid rotation vorticity. as seen in Figures 5.11b and 5.11c respectively. This may indicate a vortex breakdown into smaller scales as the size and the net vorticity content of the vortex decreases. A possible reason for this may be the shock wave imposing an adverse pressure gradient and/or flow separation on the sidewall which has been observed to cause vortex breakdowns by Sarpkaya [131]. Sarpkaya observed that increasing adverse pressure gradient leads to vortex breakdown into smaller scales at further upstream locations. The positive vortex on the other hand expands in size (Figure 5.11e). However its weight approximately follows the same PDF (Figure 5.11f), which would indicate that vortex straining is affecting the positive vortex by expanding its size while conserving the net vortex weight in the positive corner vortex. At the downstream location both the positive and negative vortices are observed to be recovering to the default state (empty tunnel) with the PDFs affected by the SBLI tending towards those observed in empty tunnel corner vortices. The independence of the corner vortex properties whose PDFs are plotted in Figures 5.11 and 5.12 at lower values of threshold for $|\omega_{RR}|$ is shown in Appendix C.1.

5.2 Hypothesis to explain the Mechanisms of Flow Separation

5.2.1 Principle and Background

Our hypothesis is that secondary flows in the form of vortices near the walls scoop out low energy fluid from near the wall towards the freestream. This creates regions of low energy fluid extending normal to the walls. These regions have high probability to separate if a sufficiently strong pressure gradient is applied.

Shabaka et al. [126] studied in detail the effects of having a vortex close to a bounding surface in a flow. A vortex that exists close to a bounding surface transports lower momentum fluid from the wall to the core on the downwash side, thus modifying the velocity profile to be less full, while

transports higher momentum fluid from the core towards the wall on the upwash other side, thus making the velocity profile fuller. This results in an increase in skin friction coefficient (C_f) on the fuller side, and a decrease on the other side. The side with net lower C_f is more susceptible to flow separation than the rest of the flow, while the region of maximum C_f represents a region with higher resistance to flow separation. This is schematically shown in Figure 5.13a.

In the case two (counter-rotating) vortices lie in close proximity to each other (Figure 5.13), two possibilities arise: (1) the region of common flow upwash (see Figure 5.13b) [132] and (2) the region of common flow downwash (see Figure 5.13c). The case where flow upwash exists is associated with an intensification of the decrease in C_f because the two vortices increase the strength of the low momentum flow transport away from the wall. The SBLI problem studied here exists at the location where the positive vortex along the sidewall interacts with the negative corner vortex. This results in increased likelihood of flow separation (see Figures 3.6, 3.12 and 3.18). This is associated with a point of minimum C_f, which makes the flow more prone to separation. In the opposite case where downwash exists, the flow has a higher resistance to separation and corresponds to a local maximum in C_f. It should be noted that although the vortex causes a local decrease and increase of C_f, the net spatial average effect is an overall increase in C_f as noted by Shabaka et al. [126]. The second case is observed in the corner of a rectangular duct that features counter-rotating corner vortices with common flow towards the corner.

5.2.2 Criterion to identify Locations of Most Probable Flow Separation

We now proceed to establish a criterion that can be used to evaluate the location where separation most likely can occur. This criterion is established from observations and discussions conducted in previous sections. We assume that the pocket of flow field with low kinetic energy fluid when applied with adverse pressure gradient is most likely to separate. Such a region of low kinetic energy fluid corresponds to a region of velocity defect in the cross-sectional velocity

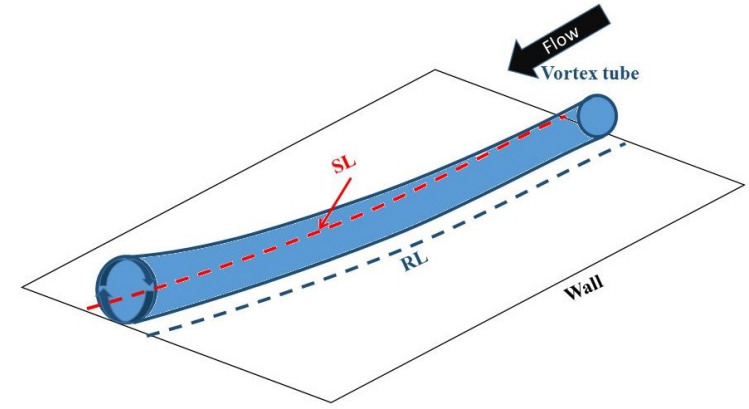

(a)

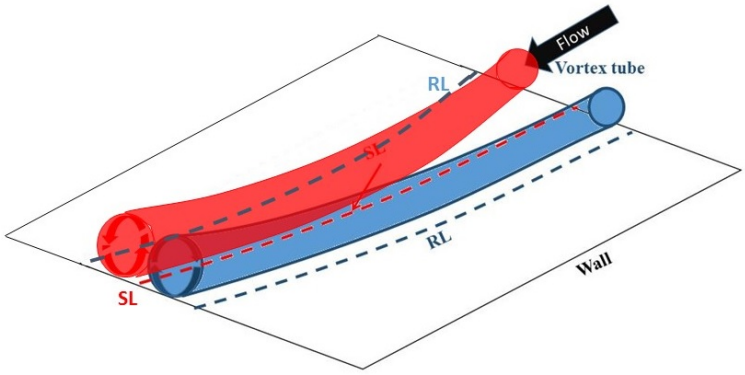

(b)

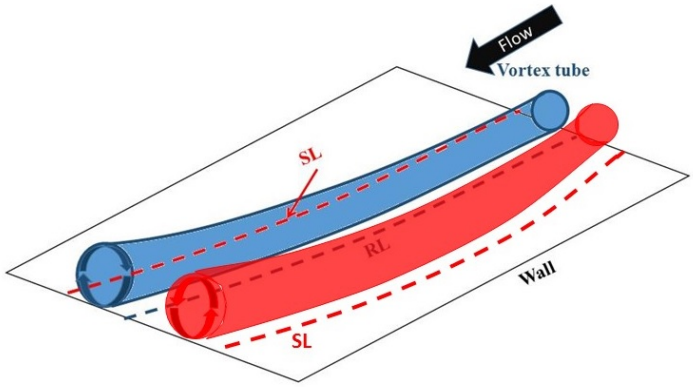

(c)

Figure 5.13: Simple examples of potential flow separation and re-attachment lines.

field. Our investigation into the empty tunnel corner flows (Chapter 4) revealed that the upwash created by the interaction of corner vortices and the counter rotating vortex pair (negative corner vortex and positive vortex on the side wall) within the boundary layer along the walls results into such a streamwise velocity defect region (see Section 4.9). From Section 4.9, it was found that $(\partial U/\partial y)(\partial U/\partial z)$ serves as a good indicator to locate the regions of maximum velocity defect. The locations where the quantity $(\partial U/\partial y)(\partial U/\partial z)$ reverses sign from negative to positive traversing in the positive direction, or $(\partial^2 U/\partial y^2)$ or $(\partial^2 U/\partial z^2)$ are positive are the locations of local maximum streamwise velocity defect. This can be explained by considering the U-velocity profiles (Figure 5.20) and the $(\partial U/\partial y)(\partial U/\partial z)$ fields shown in Figure 5.21. As we traverse the U-profiles in the $+z$-direction away from the bottom wall, streamwise velocity increases until it reaches a local maximum at about $z \approx 3$ mm for $x = 82$ mm and $x = 102$ mm and $z \approx 5$ mm at $x = 122$ mm. This region of increasing streamwise velocity constitutes a positive $(\partial U/\partial z)$. Traversing further in the $+z$-direction the $(\partial U/\partial z)$ changes its sign to negative until the local minimum is reached at $z \approx 5$ mm for $x = 82$ mm and $x = 102$ mm and $z \approx 10$ mm at $x = 122$ mm. Proceeding further into the region of increasing streamwise velocity values, $(\partial U/\partial z)$ will be positive. This point of sign reversal from negative to positive values of $(\partial U/\partial z)$ represents the maximum local streamwise velocity defect as the U-velocity is at a local minimum. Since the flow around these regions is characterized by lower kinetic energy flow compared to flows away from the corner effects, it is most likely to separate at these locations along the walls. This effect has been sourced to the momentum transport caused by the corner secondary flows as is discussed in Section 4.9. The location of local maximum streamwise velocity defect is also the location of the local minimum in C_f as is observed in Section 4.10.

A generalized version explaining how $(\partial U/\partial y)(\partial U/\partial z)$ parameter locates velocity defect will now be discussed. Consider a wall shown by the thick black horizontal lines in Figure 5.14 and coordinate system with t-axis tangential to the wall and n-axis normal to the wall. Let there be a

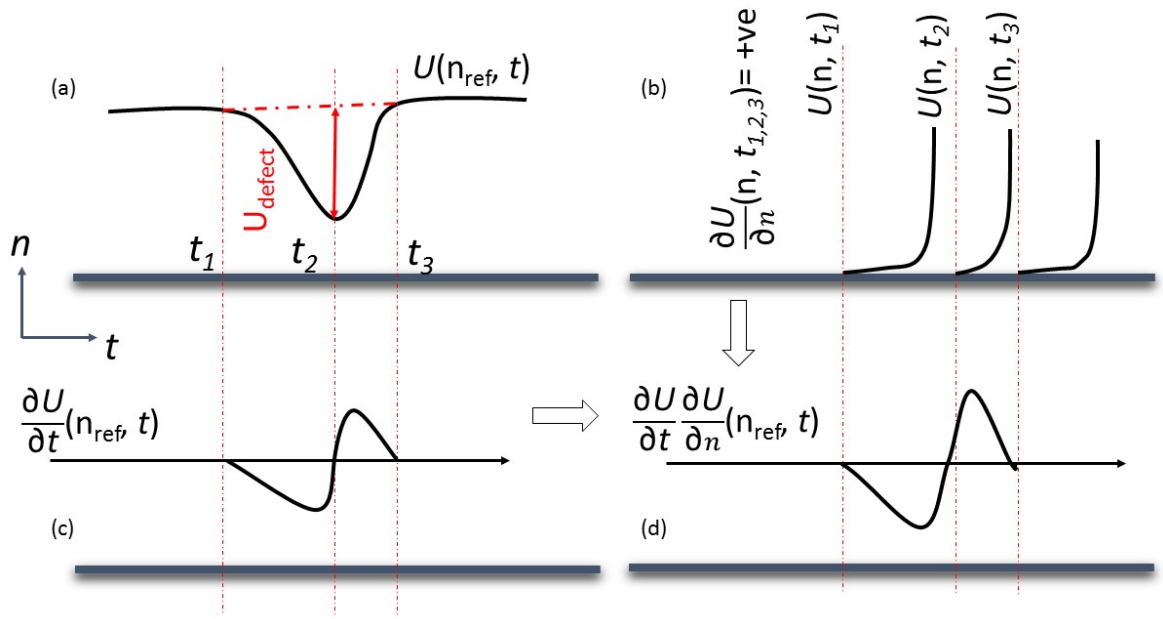

Figure 5.14: A schematic explaining how $(\partial U/\partial y)(\partial U/\partial z)$ locates velocity defect.

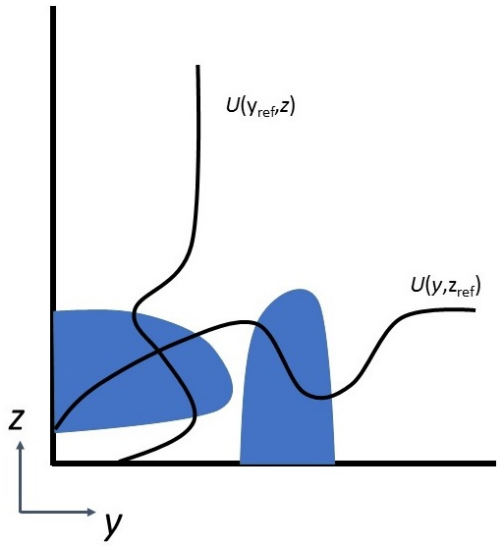

Figure 5.15: A schematic explaining how $(\partial U/\partial y)(\partial U/\partial z)$ locates velocity defect in a cross-section with complex flow fields.

flow with arbitrary velocity profile U characterized by velocity defect over this wall with U being directed out of the plane. Let $U(n_{ref},t)$ at some $n = n_{ref}$ be as shown in Figure 5.14a. Let $t = t_1$

be the coordinate of where the velocity U starts reducing in t direction, $t = t_2$ be the coordinate of maximum defect and $t = t_3$ be the location of complete recovery of U in the t direction. If we calculate the gradient $\partial U/\partial t$ along $n = n_{ref}$, it will be negative after $t = t_1$ until $t = t_2$ as the magnitude of U decreases along t in this region. After $t = t_2$, the value of U starts increasing in the t-direction and thus $\partial U/\partial t$ will be positive until it completely recovers at $t = t_3$. There is a reversal of signs of $\partial U/\partial t$ at $t = t_2$ as shown in Figure 5.14c. Figure 5.14b shows the U as a function of n plotted at $t = t_1$,$t = t_2$ and $t = t_3$. There exists no velocity defect along n and U monotonically increases to freestream value away from the wall. Thus $\partial U/\partial n$ is monotonically positive. Thus if we are to determine the regions of velocity defect in a cross-sectional plane, we take the product of $\partial U/\partial t$ and $\partial U/\partial n$ and the parameter $(\partial U/\partial t)(\partial U/\partial n)$ becomes a good indicator of such regions. The variation of this parameter along t at a slice $n = n_{ref}$ is shown in Figure 5.14d, and it changes sign from negative to positive traversing along t at the location of maximum defect.

Now let us consider a complex flow field with velocity defects that are possible in multiple directions, such as what is shown in Figure 5.15. Here we have a velocity defect as we are traversing along the side and one as we traverse along the bottom wall. Thus, either $\partial U/\partial y$ or $\partial U/\partial z$ are negative. However if we take the product of the gradients $(\partial U/\partial y)(\partial U/\partial z)$, we obtain a parameter that can locate the local maximum velocity defects on the cross-sectional plane. The defects are maximum if $(\partial U/\partial y)(\partial U/\partial z) = 0$ and $(\partial^2 U/\partial y^2) > 0$, $(\partial^2 U/\partial z^2) > 0$. In Figure 5.15 the negative zones of $(\partial U/\partial y)(\partial U/\partial z)$ are shown by color blue while everything else is positive. We thus see how $(\partial U/\partial y)(\partial U/\partial z)$ enables us to locate the minima in a 2D cross-sectional plane, constituting the criterion to detect locations of most probable flow separation.

5.2.3 Lines of Potential Separation and Reattachment

A line of potential separation (SL) is defined as the locus of local minimum of C_f, and identify a line along which the flow would begin to separate or is characterized by intermittent separation or

in general, has the highest tendency to separate. Such a line would be typical of a configuration of a streamwise-oriented vortex tube near a wall as shown in Figure 5.13.

As seen in Figure 5.13, a vortex tube that exists close to a wall and within a boundary layer, would draw the lower momentum fluid from near the wall towards the freestream on one side, thus increasing the potential of flow to separate. The locus along which this effect is the strongest is referred to as the line of potential separation (SL). Thus, using the criterion defined in section 5.2.2 a potential separation line (SL) can be defined as the locus of points where $(\partial U/\partial y)(\partial U/\partial z)$ reverses sign from negative to positive while traversing in a positive direction of the coordinate system along the wall. If a counter-rotating vortex exists, this tendency would be reinforced in the region of common upwash (Figure 5.13b). Here, the line of potential separation of relatively weak isolated vortices is referred to as SL', while that caused by adverse pressure gradient or close proximity of two counter rotating vortices is referred to as SL. Conversely, on the other side of the vortex tube, higher momentum fluid from the free stream is drawn towards the wall, thus decreasing the tendency to separate. The region is here referred to as the line of reattachment (RL). The RL also correspond to the line of local maximum C_f. Thus a potential reattachment line (RL) can be defined as the locus of points where $(\partial U/\partial y)(\partial U/\partial z)$ reverses sign from positive to negative while traversing in a positive direction of the coordinate system along the wall. If a counter rotating vortex pair exits to mutually cause a downwash in between them, the reattachment tendency will be amplified leading to a common reattachment line (Figure 5.13c). A schematic diagram showing the map of lines of potential separation and reattachment of the SBLI problem considered here are shown in Figure 5.16.

In Figure 5.16 SL1 is a result of the adverse pressure gradient of the swept shock and the associated Vortex C. The vortex C transports higher momentum fluid towards the sidewall causing a reattachment line RL1. SL'1 (dashed line becoming solid once it encounters adverse pressure gradient due to the shock) is caused by the corner vortex B, which then merges into SL1 producing a stronger

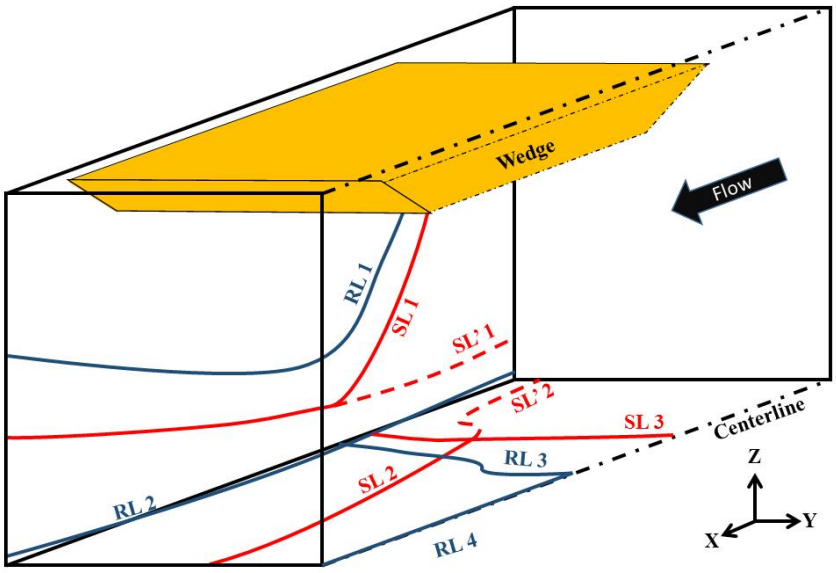

Figure 5.16: Lines of potential separation and reattachment in a 3D SBLI setting.

potential to separate as a result of the close proximity of near wall counter-rotating vortices B and C as was seen in Figure 3.16.

Both the corner vortices A and B convect high-momentum fluid towards the corner of the tunnel producing RL2. SL'2(dashed line) is caused only by the relatively weak corner vortex A. SL'2 merges into a stronger SL2, which is a result of the interaction between two counter-rotating vortices A and D. Vortex D and its counterpart which would exist in the other half of the domain, would form a counter-rotating pair which would form a strong reattachment line (RL4) on the centerline of the tunnel if the spacing were sufficiently small. SL3 is produced by the incident oblique shock and the span-wise vortex which exists at the foot of this shock, while RL3 is the reattachment line caused by this vortex. Based on this view, the potential to separate in the SBLI region would be greatest where most of the potential separation lines are in close proximity to each other as shown in Figure 5.16. In the case shown here, it is the region where the swept shock vortex C is closest to the bottom wall, and thus closest to the spanwise vortex and the corner vortices A and

B. Such region would be found around $x/\delta = 10$. Thus, the sudden increase in separation bubble cross-section area in Figure 3.12 may be attributed to this phenomenon of vortex interaction.

In the next few sections we will explore this hypothesis from the set of measurements available at strong and weak SBLIs as well as present a few canonical flow examples where the mechanism proposed would have an impact.

5.2.4 Flow Separation Predictions using the Hypothesis

Because the likelihood of flow separation is believed to be associated with the large-scale vortical structures present in the flowfield, we extract additional flow properties after scale decomposition is performed. This approach follows the study of the structure of the corner flow (chapter 4) by first performing a scale decomposition. It is the large-scale contribution that is responsible for the evolution of the corner vortex system; while the small-scale captures the underlying turbulent features. The large-scale vortex features were then extracted after applying the the TDM, from which rigid rotation vorticity ω_{RR} is extracted. From the observations of Chapter 3, we believe that the flow separation is likely caused by the configuration of large-scale vortical configurations and not by the turbulent small-scales. The identification of the corner vortex then followed using the definition introduced in Chapter 4.

5.2.4.1 Strong SBLI (6° deflection)

The mean flowfield obtained at $x = 75$ mm in the empty tunnel is shown in Figure 4.3c. The wall normal mean streamwise velocity profiles are shown in Figures 4.5e and 4.5f. The defect in the streamwise velocity profile near sidewall ($y = 5$ mm) created due to the negative corner vortex can be observed in Figure 4.5e at about ($z = 5 - 10$ mm). As per the hypothesis presented this region would be a candidate for the existence of a line of separation potential.

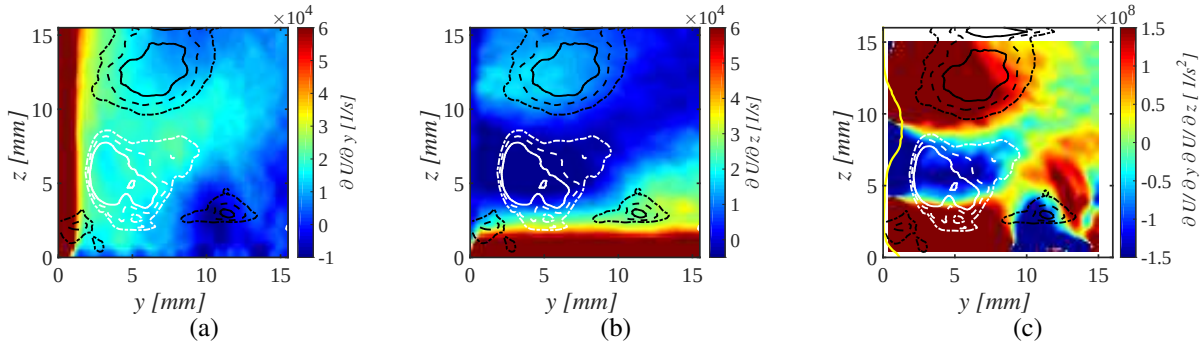

Figure 5.17: Mean streamwise in-plane velocity gradients and the product of the velocity gradients superimposed with contour lines of mean rigid rotation vorticity at large-scales. White iso-contour line: negative vorticity; black iso-contour line: positive vorticity from the empty tunnel data at $x = 75$ mm. (a) $\partial U/\partial y$; (b) $\partial U/\partial z$; and (c) $(\partial U/\partial y)(\partial U/\partial z)$. The yellow line is the mean separation profile obtained from the SBLI data at the same streamwise location. For reference, $y_T = 57.2$ mm, $z_T = 69.3$ mm.

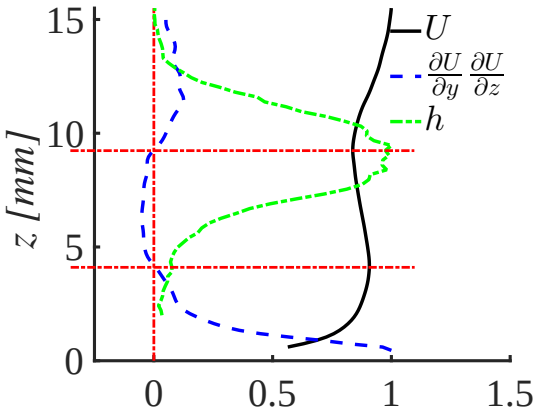

Figure 5.18: Plot to correlate $(\partial U/\partial y)(\partial U/\partial z)$, U defect observed in empty tunnel and h observed in 6° SBLI. $(\partial U/\partial y)(\partial U/\partial z)$ and U profiles are plotted at $y = 1$ mm. All profiles have been normalized by their maximum values.

The effect of momentum transport due to corner vortices is observed in the streamwise velocity gradients. The velocity gradient fields overlapped with iso-contours of mean large-scale rigid rotation vorticity fields for empty tunnel at $x = 75$ mm are shown in Figures 5.17a and 5.17b. The negative corner vortex shown by the white iso-contour lines convects lower momentum fluid away from the sidewall creating a decrease in the $U-$velocity as we traverse in $+z$-direction from the bottom wall near the sidewall. This effect is observed as a dip in the $U(z)$ profiles shown in Figure 4.5e near sidewall ($y = 2.5$ and 7.5 mm) and thus, produces a negative $\partial U/\partial z$ at the location of the vortex in Figure 4.31h. A similar effect is observed with the positive corner vortex near the bottom wall. Since the $\partial U/\partial y$ field is positive at the location where $\partial U/\partial z$ is negative and vice versa, the product of $\partial U/\partial y$ and $\partial U/\partial z$ would identify the region with momentum defect in Figure 5.17c. Thus, observing Figure 5.17c with reference to a vertical line (i.e., any line in the range $y = 0-5$ mm) near the sidewall, the U velocity profile continues to increase until we encounter the region with negative (blue) $(\partial U/\partial y)(\partial U/\partial z)$, it then begins to decrease until the end of the region of negative $(\partial U/\partial y)(\partial U/\partial z)$. The defect in the streamwise momentum is the highest between the end of the region of negative $(\partial U/\partial y)(\partial U/\partial z)$ and the start of the region of positive $(\partial U/\partial y)(\partial U/\partial z)$. A normalized near sidewall ($y = 10$ mm) slice of Figure 5.17c, along with normalized plot of U, and h as a function of z is shown in Figure 5.18. It can be seen that $(\partial U/\partial y)(\partial U/\partial z)$ reverses sign from negative to positive while traversing in $+z$-direction at $z = 9$ mm which correlates well with maximum defect in U-velocity. This location (around $z = 9$ mm) would mark a point on the line of separation potential and would be most likely to separate should an adverse pressure gradient be applied (e.g., a shock wave sweeping through this region). By comparison with the incident SBLI data at this location, it is found that this is indeed the case. We overlay the mean sidewall separation bubble profile (yellow line in Figure 5.17c and green line in Figure 5.18) found from the 6° incident SBLI case at this measurement plane to the data from the empty tunnel of Figure 5.17c. In the incident SBLI case, an adverse pressure gradient is created by the incident shock and its influence is felt upstream through the subsonic region of the boundary layer [27]. It can thus

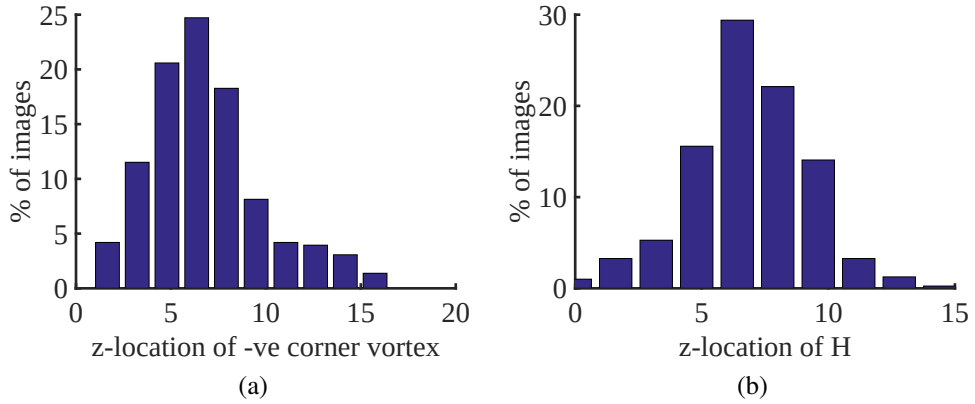

Figure 5.19: Relation between the location of flow separation bubble and the negative corner vortex in an empty tunnel flowfield: (a) Histogram of z-location of negative corner vortex in empty tunnel at $x = 75$ mm; and (b) Histogram of z-location of the maximum extent of the separation bubble (H) at $x = 76$ mm.

be concluded that the upstream sidewall separation observed in the incident SBLI study may be primarily a consequence of the structure of the corner flow region where the flow at the corner is more likely to separate as the adverse pressure due to the incident shock is (externally) applied to the corner flow field.

The region with streamwise velocity component less than 25 m/s ($u \leqslant 25$ m/s) was considered to be separated flow while the maximum extent the separated flow region away from the wall was defined as the height of separation bubble (H) [15]. The separation bubble height was then used to correlate the likelihood of flow separation with the presence of the corner vortex system disturbed by the pressure gradient imposed by the incident shock. The z-location of the negative corner vortex center in the empty tunnel was compared with the z-location of the point of maximum separation height (H) on the sidewall separation region on the $x = 75$ mm measurement plane. Histograms of these two quantities are shown in Figure 5.19. It can be seen from the figure that the most probable location of the negative vortex in the empty tunnel is approximately the same to the most probable position of the point of maximum separation height. We take this as an

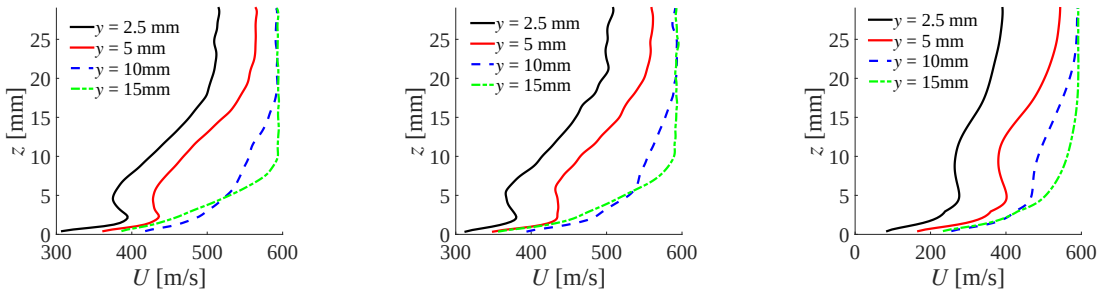

Figure 5.20: Mean streamwise velocity profile normal to bottom wall from the empty tunnel data at (a): $x = 82$ mm, (b): $x = 102$ mm and (c): $x = 122$ mm. For reference, $y_T = 57.2$ mm, $z_T = 69.3$ mm.

initial indication supporting the hypothesis that the location of separation depends on the vortex arrangement of the flow in the corner region. We now proceed to apply this hypothesis to connect the flow separation to vortex configuration to the 4.6° SBLI that has SPIV data available in empty tunnel at the locations where the SBLI data was recorded.

5.2.4.2 Weak SBLI (4.6° deflection)

Since the empty tunnel measurements are available for the weak SBLI case at the locations where SBLI data was recorded, this section will attempt to use the empty tunnel secondary flow data to predict the locations of potential flow separation on the sidewall. It should be noted that without the 3D effects there should be no flow separation for the weak SBLI case as per the Korkegi's model (Figure 1.9) discussed in section 1.2.4. The primary flow fields in the empty tunnel at $x = 82$ mm, $x = 102$ mm and $x = 122$ mm are shown in Figure 5.2 while the wall normal secondary flows are shown in Figure 5.4. The primary flow profiles normal to the bottom wall are shown in Figure 5.20. The streamwise velocity defect created by the corner secondary flows is observed in the velocity profiles at $y = 2.5$ mm and $y = 5$ mm at $z \approx 5 - 10$ mm (Figure 5.20). According to the hypothesis presented in section 5.2, the site of maximum defect would be a potential location for a

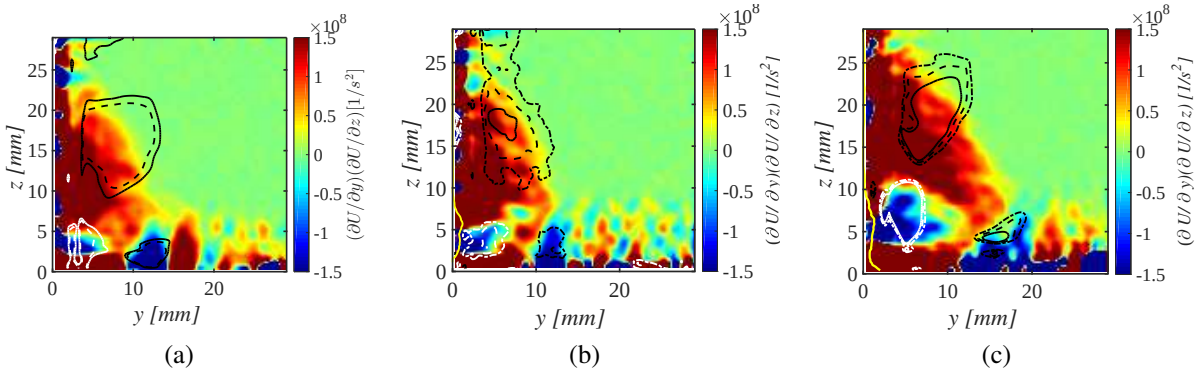

Figure 5.21: Mean streamwise in-plane product of the velocity gradients $(\partial U/\partial y)(\partial U/\partial z)$ superimposed with contour lines of mean rigid rotation vorticity at large-scales. White iso-contour line: negative vorticity; black iso-contour line: positive vorticity from the empty tunnel data at (a): x = 82 mm, (b): x = 102 mm and (c): x = 122 mm. The yellow line is the mean separation profile obtained from the SBLI data at the same streamwise location. For reference, y_T = 57.2 mm, z_T = 69.3 mm.

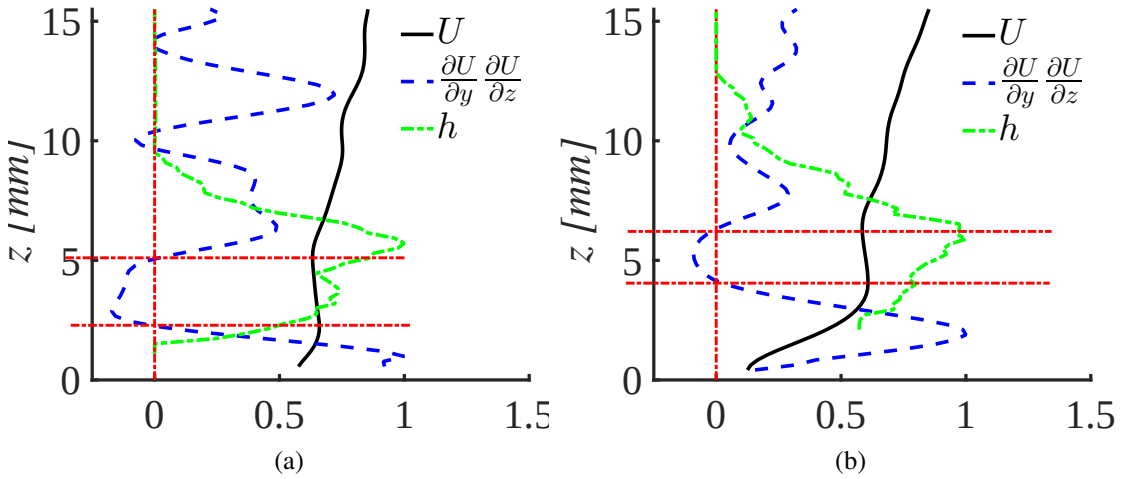

Figure 5.22: Plot to correlate $(\partial U/\partial y)(\partial U/\partial z)$, U defect observed in empty tunnel and h observed in 4.6° SBLI. $(\partial U/\partial y)(\partial U/\partial z)$ and U profiles are plotted at y = 1 mm. All profiles have been normalized by their maximum values. (a): x = 102 mm and (b): x = 122 mm.

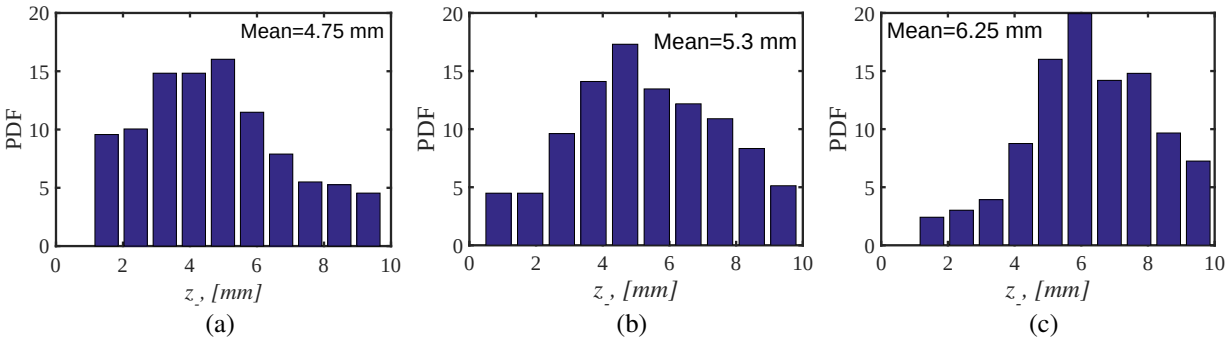

Figure 5.23: Histogram of the z-location of negative corner vortices in empty tunnel at (a): x = 82 mm, (b): x = 102 mm and (c): x = 122 mm.

flow separation event to take place.

According to the discussion in the case of strong SBLI, the fields of products of in-plane streamwise velocity $((\partial U/\partial y)(\partial U/\partial z))$ along with the separation bubble profile and iso-contours of vorticity are shown in Figure 5.21 with conditionally averaged separation bubble profile (yellow line) and iso-contours of mean large-scale rigid rotation vorticity superimposed (white is negative vorticity and black is positive vorticity). Similar to the Figure 5.17c, negative regions of $(\partial U/\partial y)(\partial U/\partial z)$ are observed in the regions where the corner vortices scoop low energy fluid from near the bottom and sidewalls. These are observed at about ($z \approx 3-5$ mm and $y \approx 10-13$ mm) at TV2 and TV3 planes (x = 82 mm and x = 102 mm respectively) and $z \approx 4-7$ mm and $y \approx 10-20$ mm at TV4 (x = 122 mm). The locations of momentum defect and thus the negative $(\partial U/\partial y)(\partial U/\partial z)$ are in fair agreement with the locations where the corner vortices would scoop low momentum fluid away from the wall as shown in Table 5.1 and Figure 5.23. According to the hypothesis the locations along the walls where the $(\partial U/\partial y)(\partial U/\partial z)$ fields change sign from negative to positive traversing away from the corner are the locations where maximum streamwise velocity defect exists (see also Figure 5.20) and mark the locations of lines of potential separation. Further clarification is made by taking slices of the normalized Figures 5.21b and 5.21c and normalized $U(z)$ profiles near the sidewall (y = 1 mm) shown in Figures 5.22a and 5.22b respectively. Consistent with the observa-

tions in the 6° SBLI case, sign reversal from negative to positive of $(\partial U/\partial y)(\partial U/\partial z)$ is observed at z = 5 mm and z = 6.5 mm at x = 102 mm and x = 122 mm respectively. These points are also consistent with the local minimum of the U-velocity and would constitute two points on the potential separation line where flow is most likely. Flow separation is indeed observed at these locations in TV3 (Figure 5.21b) and TV4 planes (Figure 5.21c) for the weak SBLI case where no separation should be observed in absence of the secondary corner flows as per the Korkegi's map (Figure 1.9). Flow separation location was thus successfully predicted using empty tunnel data. Thus it can be concluded that the primary velocity defects caused by the streamwise momentum transport by the secondary flows that are observed of an empty duct govern the locations that are most likely to separate should a sufficient adverse pressure gradient be introduced.

5.2.4.3 Other Cases from the Literature

Case 1: Vortex Generator Microramps inducing an Upwards Common Flow

The first case refers to the experimental results by Blinde et al. [11] on flow separation control using micro ramp vortex generators in a problem of incident oblique SBLI. Consider the flow field shown in Figure 5.24 taken at a height of 0.6δ with respect to the floor from their results. The vortex generators are depicted by black triangles that generate counter-rotating vortices with common flow being lifted. Thus, there is a flow upwards out of the plane behind the streamwise oriented vertex of the vortex generator. As per our hypothesis, this will cause a momentum defect directly downstream of a vortex generator, a feature that is observed in the U/U_∞ field shown. The locus of the maximum defect will form the line of most probable separation which is also observed in the $\partial U/\partial z$ plot obtained upstream of the SBLI at $x = x_{ref}$, changing its sign (as well as$(\partial U/\partial z)(\partial U/\partial y)$) from negative to positive at such a location. There are three such locations of potential separation observed that are shown as red lines in Figure 5.24. In fact the flow does have the highest probability to separate along these lines as seen in Figure 5.25. Thus it can be said

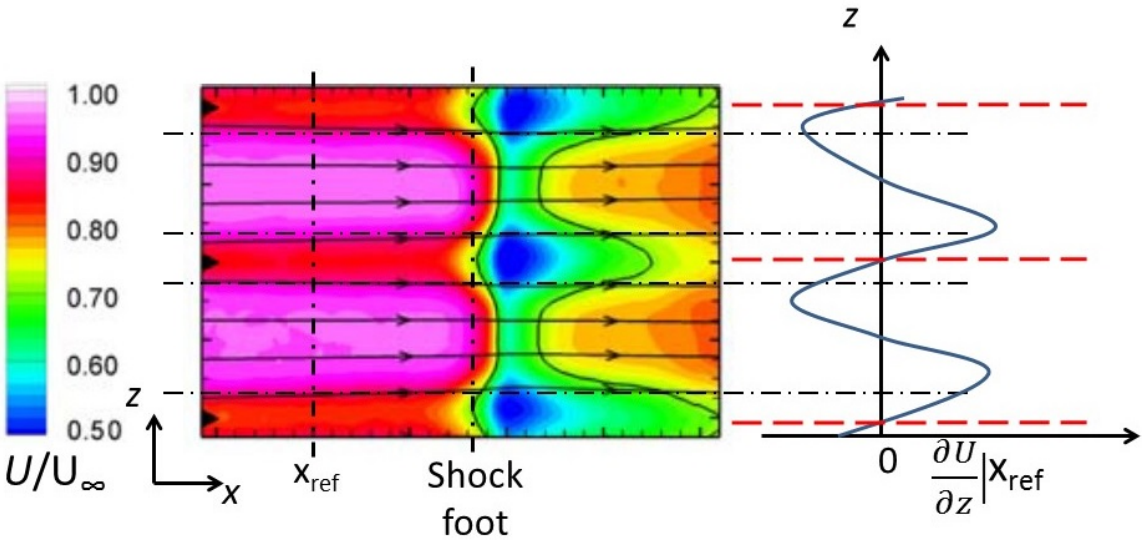

Figure 5.24: Top view flow field obtained from experiment by Blinde et al. [11].

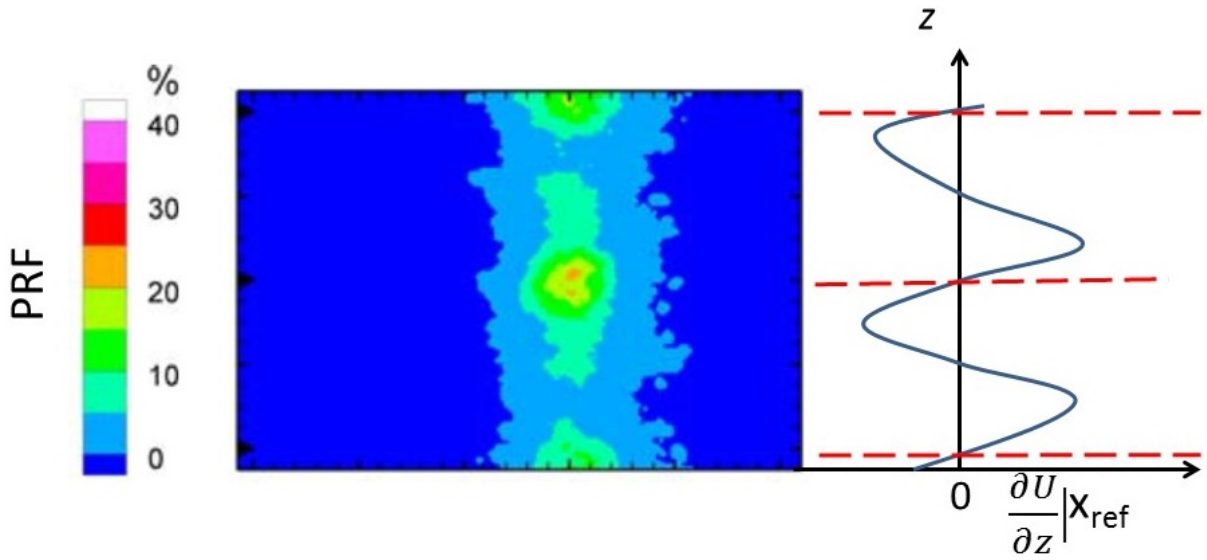

Figure 5.25: Probability of reverse flow map obtained from experiment by Blinde et al. [11].

that the hypothesis explains the location of flow separation in this case. It should be noted that the shocked flow field is separated without the vortex generators in this case and we are assuming that the flow field processed by the vortex generators incoming in the SBLI is completely independent of the baseline case.

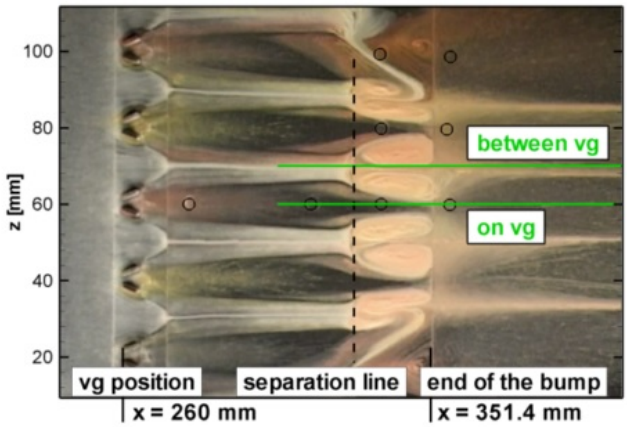

Figure 5.26: Surface oil flow and PIV plane locations for the separation control experiment. Figures taken from Sartor et al. [12].

Case 2: Vortex Generator Vanes inducing Downwards Common Flow

For this case we will consider the experimental work by Sartor et al. [133]. They study the effect of vortex generators on a transonic separated flow on a backward facing corner. It should thus be noted that the streamwise oriented vortices are subject to change in wall curvature and it is assumed that this will have negligible effect on the behavior of the vortices. The two locations where they obtain PIV data along with surface oil-flow visualization are shown in Figure 5.26. Flow reversal can be seen in the oil flow images in the region that is between two vanes from where the generated vortices will cause an upwash introducing a streamwise velocity defect. The defect will be maximum at the point equidistant from two adjacent vanes and this is the location where the flow will have the maximum probability to separate.

The velocity profiles at a point upstream (x = 320 mm) of the SBLI but downstream of the vortex generators are shown in Figure 5.27. The streamwise velocity profile in between two vortex generators is consistently at lower values than the one on the vortex generator. Thus $\partial U/\partial z$ will be negative in the direction from the plane on the vortex generator to the plane in between two vortex

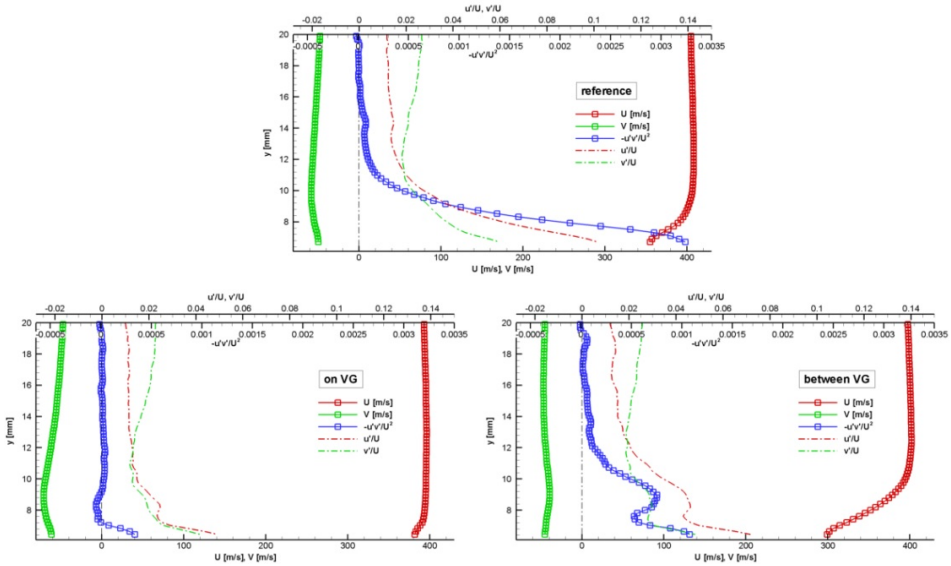

Figure 5.27: Velocity profiles obtained from PIV upstream of the interaction and downstream of the vortex generators. Figures taken from Sartor et al. [12].

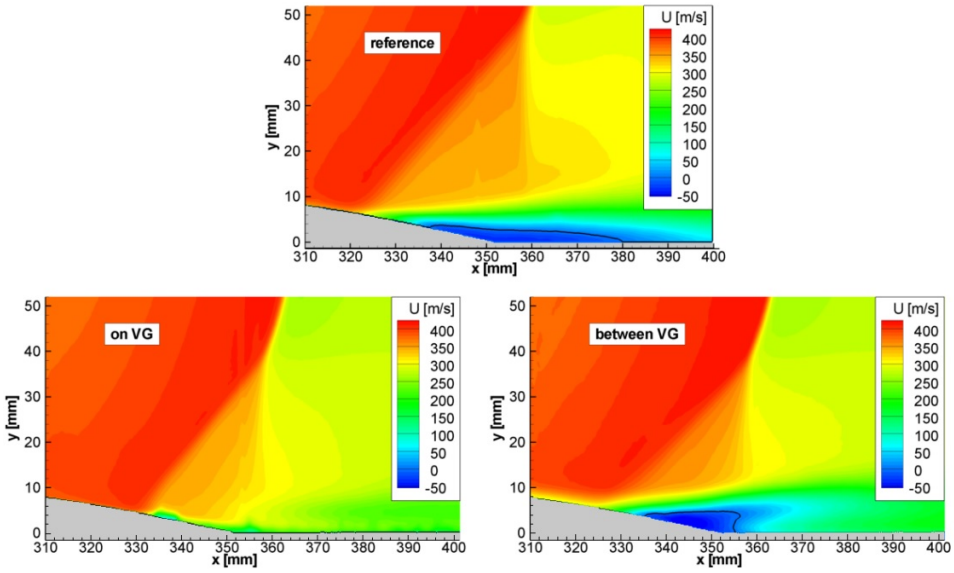

Figure 5.28: Velocity fields and superimposed separation bubble obtained from PIV upstream of the interaction and downstream of the vortex generators [12].

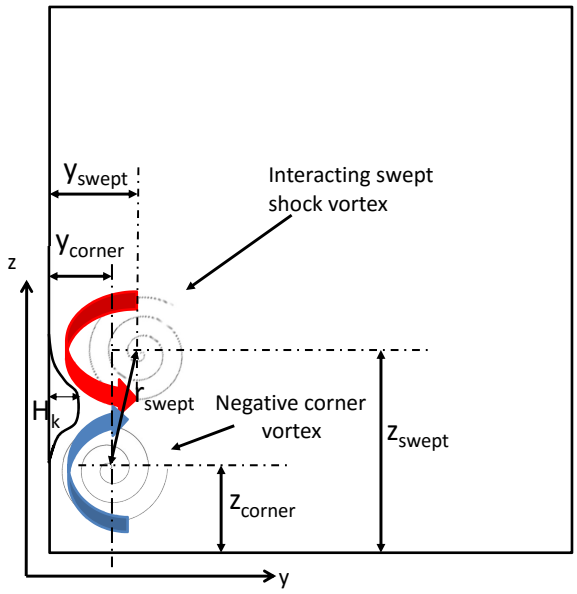

Figure 5.29: Schematic of parameters influencing vortex pair interaction with sidewall boundary layer).

generators. Assuming symmetry this will be the point of maximum velocity defect and $\partial U/\partial z$ will be positive proceeding further. Thus the location in between the vortex generator is a likely candidate to observe flow separation as $(\partial U/\partial z)(\partial U/\partial y)$ changes sign from negative to positive. Flow separation is indeed found at this location as seen in Figure 5.28. The hypothesis thus stands valid for this flow field. However, it should be noted that the flow is already separated without the vortex generators due to the shock and introduction of the vortices governs where the flow will separate instead of being separated over the full span.

5.2.5 Correlation Efforts

While Section 5.2.4 addresses the question "Where and how flow separates?", this section will attempt to address "When does the flow separate?".

Based on physical model it was postulated that a parameter ($\Lambda = \frac{|\Omega_{RR+}|\,|\Omega_{RR-}|}{y_{swept}\, y_{corner}\, r_{swept}}$) with the variable definitions as shown in Figure 5.29 and $|\Omega_{RR}| = \frac{\int_{A_\Phi} |\omega_{RR_L}| dA_\Phi}{\int_{A_\Phi} dA_\Phi}$. The value of this parameter would

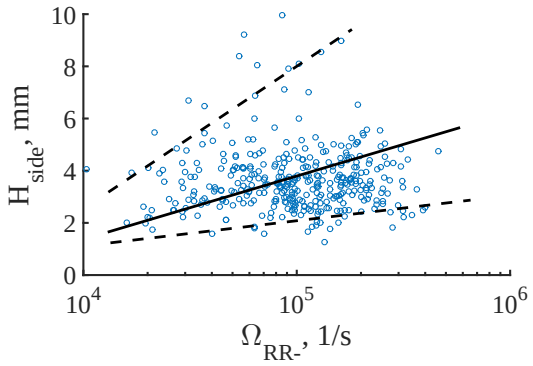

Figure 5.30: Scatter plot between strength of negative corner vortex and extent of separation at $x = 75$ mm.

be instrumental in determining the relationship between instantaneous flow configuration and the instantaneous separation strength (H). The parameter Λ would have a larger value due to strong interacting vortices with large $|\Omega_{RR}|$ which would cause a stronger momentum transport, scooping more low momentum fluid away from the wall. It is inversely proportional to the distance of the vortices to the sidewall and the distance between the interacting vortices as the closer the interacting vortices are to each other and to the wall stronger will be the scooping effect. However, no such correlation was observed in any of the analyzed data planes. This may be due to the inherent temporal phase lag in between occurrence of an interacting vortices configuration and the event of flow separation caused by it. As the presence of a separation bubble would affect the neighboring flow structure and hence the vortices B and C. The flow separation caused by this interaction would act as a bluff body and force the vortices B and C away from each other which would cause the separation bubble and the instantaneously observed vortex structure at the time of flow separation to be uncorrelated. Another possible reason might be the dependence on local instantaneous pressure gradient that would be an important factor to determine if the flow separates and is not available currently.

Correlations between the separation size (H) and various parameters describing the vortex interactions were attempted and proved unpromising. However, an extremely weak trend was observed

between the instantaneous mean vorticity of the corner vortex (Ω_{RR-}) and the local extent of the separation bubble (H). A scatter plot of these quantities obtained at $x = 75$ mm for the strong SBLI is shown in 5.30.

5.3 Conclusions

The Mach 2.75, 6° and 4.6° angle of deflection incident SBLI cases was studied using SPIV measurements to quantify the importance of the interaction of the swept shock with the corner flows. The 3 dimensionality of the SBLI was found to increase with its strength as a stronger adverse pressure gradient generated by the swept SBLI propagates upstream affecting the corner secondary flows. The SBLI was found to cause a decrease in size and circulation of the negative corner vortex which is directly influenced by the swept shock on the sidewall while it expands the positive corner vortex while conserving the net vorticity content of the positive corner vortex.

An hypothesis explaining the underlying mechanism of flow separation due to vortical momentum transport was put forth and tested. The flow structure obtained from empty tunnel measurements was used to determine the location of most probably observing flow separation in the case an adverse pressure gradient would be applied, as for example when the swept-shock on the sidewall reaches the corner region. The predicted point of separation on the sidewall agrees with the observed point of separation from the incident SBLI measurements, thus providing some initial support to the proposed mechanism. The hypothesis was also tested on other work from the literature. Although no perfect setups were found to test the hypothesis, those that were analyzed proved to strengthen the hypothesis. However the hypothesis in its current form falls short of predicting when the separation event takes place.

CHAPTER 6

Conclusions and suggested Future Direction

A detailed study was conducted to investigate the three-dimensional flow structure of corner flows in supersonic duct flows and how they affect the three-dimensionality of shock boundary layer interactions in low aspect ratio channels. The 3D SBLI is composed of three unit physics problems: (1) Oblique-incident SBLI on the bottom wall, (2) Swept/fin type SBLI on the sidewalls and (3) Corner flows on the corners of sidewall and bottom wall. These unit physics are coupled with each other due to their vicinity to each other in a low aspect ratio channel. From this study we particularly learnt about the role played by the corner flows by coupling with the swept SBLI in governing the flow separations associated with the 3D SBLI system.

Non-intrusive high resolution SPIV measurments were conducted in the streamwise corner of a supersonic rectangular channel at two Mach numbers (2 and 2.75) to study the secondary flows associated with the duct flow. In order to study the SBLI problem, SPIV measurements were initially conducted for the incipiently separated SBLI (Mach 2.75 6° deflection) case at three orthogonal orientations in order to completely extract the underlying large-scale flow structure including the statistics, location and extent of the local flow separation bubble. The separation bubble location was then related to the vortex skeleton of the SBLI flow structure in order to construct a hypothesis that relates separation location to secondary flows. This hypothesis was then tested on the SPIV results obtained in the weaker SBLI (Mach 2.75 4.6° deflection). The major findings of this thesis are summarized as follows:

6.1 Corner Flows of Supersonic Rectangular Channels

a. The limited work that previously has considered the secondary flows generated at the corner of a supersonic duct flow has proposed the existence of a well-defined vortex pair. In this study, where we gather instantaneous measurements of the flow in a corner, we have identified that the instantaneous structure of the flow can be described as the superposition of a large-scale counter rotating vortex pair that defines the secondary flow, and a forest of small-scale vortical features that are generated by the underlying small-scale turbulence. A decomposition of scales that is based on this view was proposed as a convenient tool to separate the two properties of the flow into the large and small-scales allowing us to investigate the properties of each scale. This approach allowed us to mathematically define a corner vortex pair (based on the large-scale flowfield), and thus investigate its properties statistically.

b. In our study the corner vortices were observed to have a tendency to grow in the streamwise direction and move away from the corner becoming increasingly spatially unstable and increasingly affecting the primary flows by creating regions of velocity defects.

c. Corner secondary flows cause a momentum transport away from the side and bottom wall at locations the velocity vectors point away from the wall towards the freestream and causing a momentum transport into the corner from the freestream This transport of low energy boundary layer fluid from near the walls caused a defect in the streamwise velocity profiles. The skin friction coefficient profile along the walls was affected by the momentum transport and a minima was introduced at the location of the defect.

d. Some effect of the momentum transport was observed in normalized inner scale velocity profiles. Momentum transport towards the wall was responsible for fuller profiles in the outer wake region while the momentum transport away from the wall introduced a defect in

the logarithmic region.

e. Small scale coherent structures were observed in the spatially averaged flow fields. Ejections away from the walls and associated counter-rotating vortex pairs were observed in these structures.

f. The turbulence state in corner flows is highly anisotropic. For a fixed point on the corner bisector, the state of turbulence is initially (outside of the corner flow region) dominated by one component cigar shaped turbulence. As the flow evolves in the streamwise direction, axisymmetric expansion to an isotropic state followed by an axisymmetric compression to a pancake type turbulence state is found.

6.2 SBLI

a. The incoming shock for the stronger of the two SBLIs studied was found to be curved. In both cases the shock penetrated the same length into the sidewall boundary layer. However the shock associated with the centerline attached flow SBLI (weaker) was observed to penetrate deeper into the bottom wall boundary layer due to absence of a separation shock from the oblique-incident SBLI.

b. Contrary to the two dimensional models [21, 40], in our study, flow was found to be incipiently separated for both the cases whereas it should have been attached for the weaker SBLI. This establishes that the flow separation in the 3D SBLI case is governed by the coupling between the multiple SBLI unit physics problems.

c. Statistically studying the effect of the incoming shock on the corner vortices in our experiments revealed that the negative corner vortex that interacts with the swept SBLI on the side wall decreases in size as well as circulation while the positive corner vortex expands

conserving its net circulation. The incoming shock also pushes the negative corner vortex towards the bottom wall and the positive vortex away from the corner towards the centerline.

d. In our study, the highest likelihood of flow separation was found to be on the sidewall in the region affected by the corner secondary flows. This suggested a role of corner secondary flows on determining the location and possibility of flow separations. Also flow separation was observed upstream of the shock location for the stronger SBLI.

e. A hypothesis was proposed to explain the location of the flow separations by observing the flow separation map and the vortex structure associated with the SBLI. It was proposed that the velocity defect created by the momentum transport caused by streamwise oriented vortex tubes embedded inside a boundary layer were sites of potential separation. These sites constitute the lines of potential separation which lie on the walls bounding the flow. They quantitatively locate the regions in the flow that would separate first or are more likely to separate should a sufficiently strong adverse pressure gradient be applied. A criterion was developed to locate the regions of most probable flow separation in a three dimensional flow field.

6.3 Future Work

While this work answers a few questions, like dependence of flow separation on the secondary flows, related to the secondary flows in a rectangular channel and the three dimensionality of a coupled SBLI, a lot of questions remain unanswered.

Current analysis completely avoids the discussion into three dimensional compressibility effects of the SBLI and corner flows due to the lack of information available. It would thus be beneficial to conduct simultaneous SPIV and Rayleigh scattering measurements to obtain instantaneous density and velocity measurements which would make available the density gradients and fluctuations thus

improving the approximations associated with transport and production terms in both SBLIs and corner flows. This would provide a deeper insight into formation of supersonic corner vortices and compressibility effects in a 3D SBLI.

The out of plane gradients are currently the missing terms limiting the analysis of the corner vortex formation apart from the limited SPIV resolution. Use of dual plane SPIV [134] or tomographic PIV [135] would fill in the current gaps providing complete strain rate and Reynolds stress tensors helping further investigate the formation and orientation of corner secondary flows.

The vortex structure put forth in chapter 3 (Figure 3.16) interpolates a splitting of spanwise vortex D_o into D and D' without providing a direct proof. Filling in this gap by use of tomographic PIV would help in validating this arguemnt and understanding the dynamics of the splitting of the large-scale vortices generated by the SBLI.

The hypothesis provided (Section 5.2) was able to statistically predict the mean location of flow separation, however did not completely answer the question of when an event of separation takes place. Possible reasons for this lack of answer were suggested to be a phase delay between the instantaneous interacting vortex configuration and the observed event of separation and the lack of instantaneous local pressure gradient. A simultaneous time resolved SPIV coupled with pressure sensitive paint measurements would be helpful in completely validating the hypothesis presented and perhaps even establish a complete version of separation parameter Λ proposed in Section 5.2.5 including the local pressure gradients and/or phase delay factors.

Another possible path would be attempting to alleviate the flow separations by installing boundary layer control devices (like vortex generators) on the sidewall in order to affect the corner vortices and the incoming swept shock vortex reducing the strength of the upwash caused by the interacting swept shock and corner vortices. A study of the resulting fluid dynamics would be intriguing.

Appendices

Appendix A

Pressure Measurements

A.1 Placement and Resolution of Pressure Taps

Pressure taps were fixed on the bottom wall and sidewall which profiled both empty tunnel as well as the SBLI problem. Further experiments were conducted to ascertain the significance of the errors arising due the inter-tap streamwise distance or the spatial resolution of pressure measurements. A set of runs were made to obtain pressure readings at different resolutions on the bottom plug in the empty tunnel and the results of each run then compared to make a conclusion.

The presence of a pressure tap essentially a hole disturbs the natural flow field by bending the near wall streamlines just above the hole inwards as discussed by Mckeon et al. [94]. The effect of this disturbance can extend downstream of the tap influencing the measurements recorded downstream. This study shows that the inter-hole distance used in our static pressure measurements is sufficient to not be influenced by this effect.

A.1.1 Apparatus and Methodology

21 holes as per Figure A.1 were drilled on the bottom plug at y=28.575 mm (global co-ordinate system) at 0.25 inches from each other in stream-wise direction. Lapsa et al. [17] report flow parameters as:

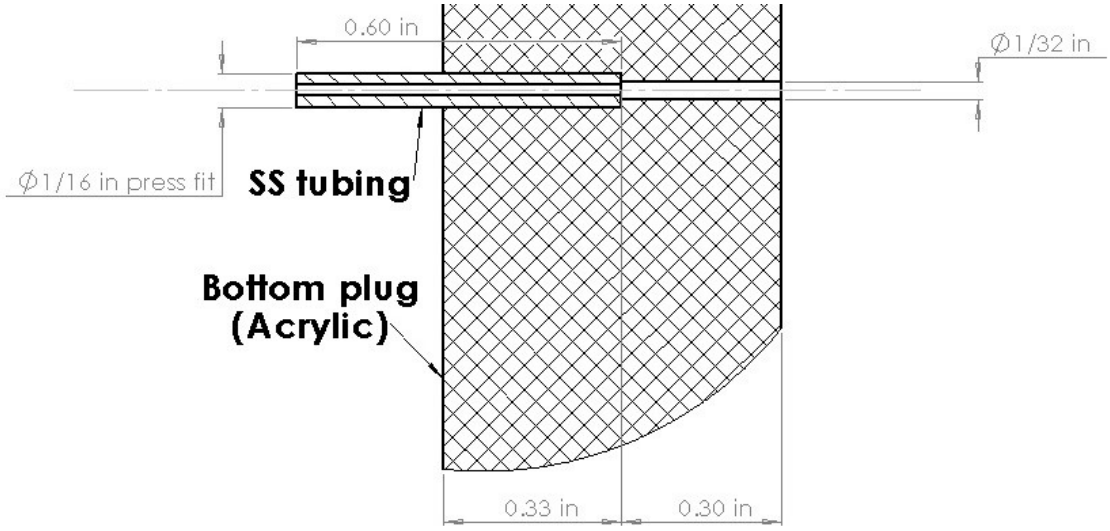

Figure A.1: Pressure port geometry.

- U_τ(friction velocity) = 31.3 m/s
- ν_w(dynamic viscosity at wall) = 2.74×10^{-4} m^2/s
- τ_w(wall shear stress) = 42.8 Pa

Using these values the tap Reynolds no. defined as:

$$Re_{tap} = \frac{U_\tau d}{\nu_w} \tag{A.1}$$

where d is the tap diameter exposed to the flow (1/32 in). Thus as per the results of Shaw [96] we would have a non-dimensional pressure error; defined as Π:

$$\Pi = \frac{\Delta P}{\tau_w} \tag{A.2}$$

where ΔP is the recorded error in pressure measurements; to be about 0.125. When translated into pressure units it comes to about 5.35 Pa, while we have a free stream static pressure of 4.3 kPa at Mach 2.75. Thus the static pressure error analytically resulting from the effects of tap diameter would be about 0.12%. Chue [95] notes that for a deep square edged hole, the depth of the hole is

unimportant, however Shaw [96] suggests keeping the depth of the tap to tap diameter ratio(l/d) above 1.5 while Mckeon [94] suggests to keep it above 2 in order to minimize the non-dimensional error. The l/d ratio used in our experiments is 9.23.

Stainless steel tubing (ID: 1/16 in, OD: 0.02 in) is press fitted in all the holes drilled in order to ensure good sealing of the taps. Tygon B-44-4X flexible tubing (ID: 1/16 in, OD: 1/8 in) manufactured by Saint Gobain is used to connect the pressure taps to differential pressure sensor array, DSA 3217 manufactured by Scanivalve. The pressure sensor array is referenced to the free stream pressure of 4.3 kPa(absolute) which stays fairly constant throughout the run. A set of about 1000+ readings are noted for each run. Runs are repeated after the initial run($resolution$ = 0.25 in) by sealing the taps with modeling clay in order to get a resulting resolution of 0.5 in and 1 in. Excess clay is removed using a sharp knife edge and buffing in order to insure that the fill stays flush with the exposed surface of the bottom plug.

A.1.2 Results

The results obtained from the pressure tap resolution experiments are summarized in Figure A.2a The error between different runs was computed by comparing the readings with the 0.25 in resolution run since values at all locations are available. The maximum error in between all the runs is 0.82% at the most upstream tap, while the average error is about 0.342%.

Two independent measurements at a resolution of 0.25 in with a few overlapping pressure tap measurements were also conducted to check for repeatability. The plots of the pressure distribution with 0.5% error bars are shown in Figure A.2b

The figures A.2a and A.2b show that the pressure measurements are repeatable within 0.5% of normalized pressure readings.

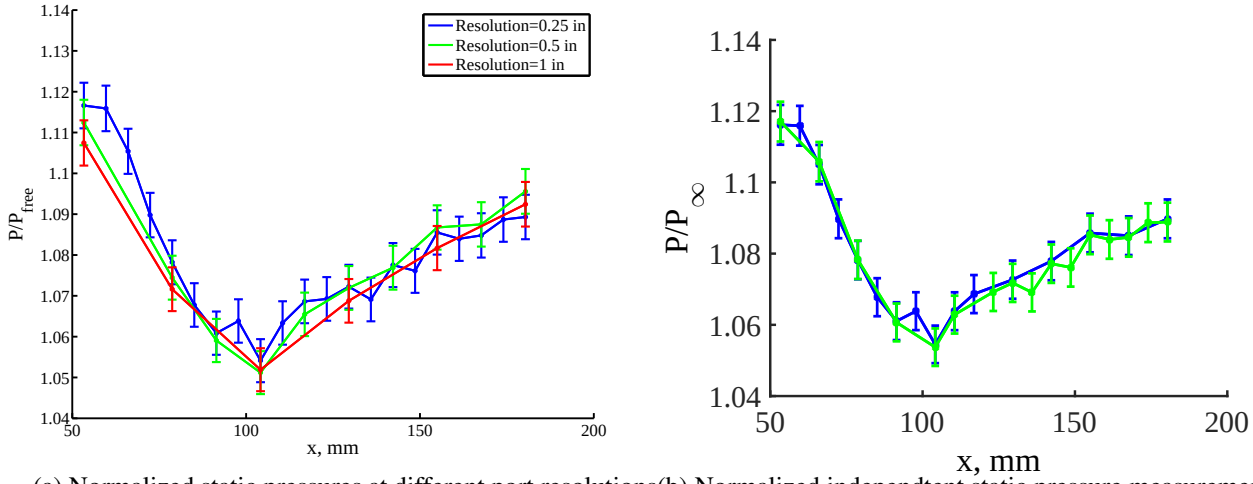

(a) Normalized static pressures at different port resolutions with 0.5% error bars.

(b) Normalized independtent static pressure measurements with 0.5% error bars.

Figure A.2: Pressure recording error brackets.

A.2 Pressure Sensor Calibration

A.2.1 Omega DPG 2001B-30A

Both the omega absolute pressure gauges were checked with respect to the MKS Baratron 627D sensors with an accuracy of 0.12% of the reading. A control volume was created using the plastic tubing to which all 4 pressure sensors were connected. Two runs were conducted by pumping down this control volume using a Cenco Pressovac vacuum pump and one run using the Hy-Vac 14 vacuum pump. The readings from the Baratrons and the Omega digital pressure gauges matched fairly well except at near vacuum conditions possibly because the baratrons arent zeroed. The calibration curves of all three runs overlapped and are as shown

A.2.2 Scanivalve DSA 3217 Differential Pressure Sensor Array

A differential pressure was created by creating two independent control volumes by connecting the pressure tubing to the upstream (P=1) and downstream (P=2) top ports on the wind tunnel as per

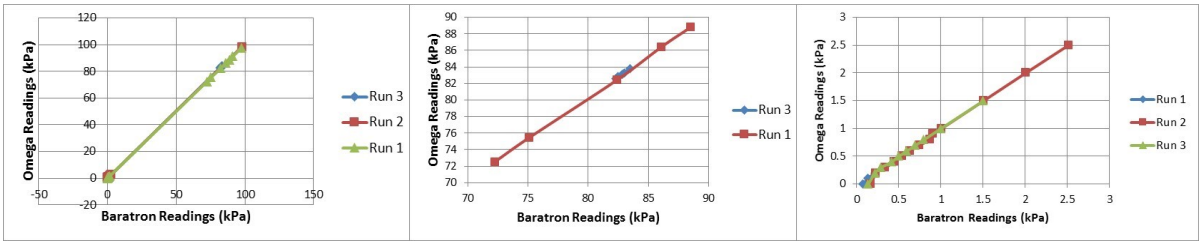

(a) (b) (c)

Figure A.3: Omega DPG 2001B-30A calibration at three different pressure ranges.

the circuit shown in figure A.4a.

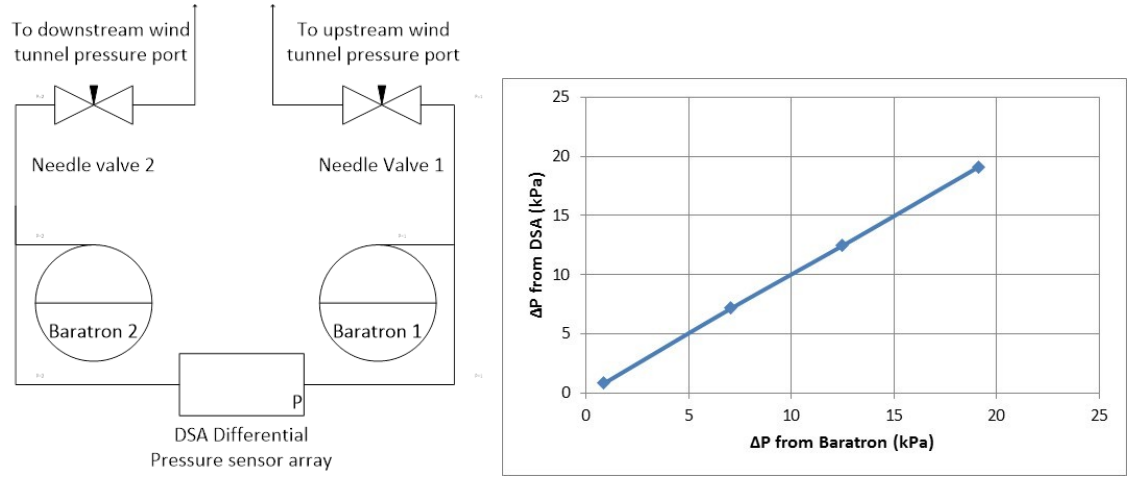

(a) pneumatic circuit used for checking differential pressure sensor array calibration.

(b) DSA scanivalve calibration curve.

Figure A.4: Scanivalve calibration circuit and curve.

The needle valves served as a protection for baratrons from the sudden pressure rise resulting from the shock as well as a way to control the pressure in each line independently. All 16 ports of the DSA pressure array were connected to a manifold which was connected to the downstream (P=2) line, while the reference port of the DSA pressure array was connected to the upstream (P=1) pressure line. The pressures in each line were then manually varied using the needle valve and then noting the stabilized pressures on each baratron and recording the pressures from the DSA array. Four such runs were conducted. The calibration curve obtained by averaging the 16 readings

from the DSA ports v/s the difference in pressure displayed by baratrons is as follows:

The highest error was around 0.015 kPa whereas the percentage error was highest at 4.21% for the lowest differential pressure reading of 0.88 kPa while for all other points it was less than 1.5%, except for the last point (19 kPa) where it was 1.9%, however this point falls just outside the specified range(2.5 psi) of the sensor array.

Appendix B

Stereo Particle Image Velocimetry (SPIV)

B.1 Laser Sheets

The laser sheet energy profiles were obtained (Figure B.1) by traversing a knife edge through the beam sheets near the interrogation region. Energy content per pulse was measured using a power meter (Scientech Vector S310) as the knife edge was traversed through the beam sheets produced by the two lasers in order to determine the overlap and sheet thickness. A custom function

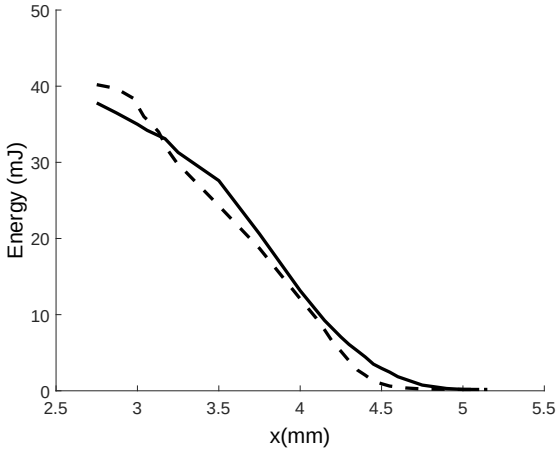

Figure B.1: Laser power profiles obtained from traversing knife edge.

$\left[f(x) = \left(1 - erf\left(\frac{\sqrt{2}(x-b)}{c}\right)\right)\right]$ was fit over the normalized energy profiles in (Figure B.1. A fit with $R^2 = 0.995$ was obtained for the GCR with normalized function $P_{GCR} = 1 - erf\left(\frac{\sqrt{2}(x-3.61)}{1.56}\right)$, thus

the $1/e^2$ radius of the beam produced by the GCR laser is 1.56 mm. A fit with $R^2 = 0.999$ was obtained for the Quanta Ray with normalized function $P_{QRay} = 1 - erf\left(\frac{\sqrt{2}(x-3.7)}{1.44}\right)$, thus the $1/e^2$ radius of the beam produced by the Quanta Ray laser is 1.44 mm.

B.2 Seed Particles

A TDA-4B portable Laskin nozzle aerosol generator manufactured by ATI Techniques Inc. was used to seed the flow. The generator uses Poly-alpha olefin (PAO) oil ($\rho = 819\,\mathrm{kg/m^3}$) to create sub-micron droplets using 6 laskin nozzles. The mean particle diameter specified by the manufacturer is 0.281 μm. However a thorough analysis was conducted on velocity decay across the shock wave to obtain particle sizing in order to make sure that particle size after allowing for coagulation is as per the requirement.

B.2.1 Instantaneous and Statistical Analysis

SV1 data plane was used for analyzing the ability of seed particles to follow the flow due to the presence of shock. The seed particle characteristics were obtained from the behavior of velocity after the shock. The entire co-ordinate system was rotated by $(shock\ angle - \pi/2)$ for every image. Shock angle was obtained using the S_{zz} planar distribution independently for each image of the dataset. An exponential curve fit was then made between the minimum value of $\frac{\partial^2 u_n}{\partial n^2}$ and minimum value of shock normal velocity component (u_n) in the core flow. Also note the rise of the normal velocity after the decay as a function of the normal co-ordinate in couple of the instances shown in figure B.2 along with the exponential curve fit shown by dashed lines. Such behavior was observed in a few randomly selected instantaneous images. A similar behavior is also observed in one of the cases shown by Elsinga et al. [136] which is sourced to aero-optical effects(AOE). In their paper Elsinga et al. did a few computations on expansion fan and the localized peak in velocities

became more prominent for more concentrated cases of expansion fans. Since the recorded particle velocity profiles are similar and the localized peak is towards the denser side in both the studies it is believed that this behavior is due to aero-optical effects. The distance between the max and the

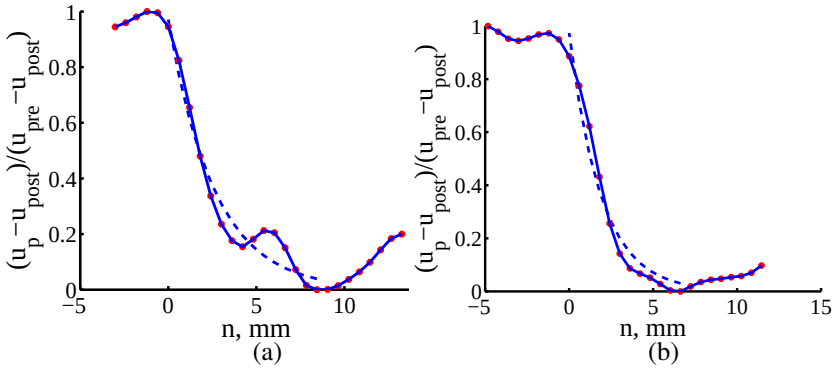

Figure B.2: Couple of instances of particle velocity decay across shock and exponential fits(dashed).

min values of the shock normal velocity is defined as the relaxation distance, the pdf of which in global co-ordinates is shown in figure. Mean shock normal particle relaxation distance was found to be 6.4458 mm, which reduces to 3 mm in x direction.

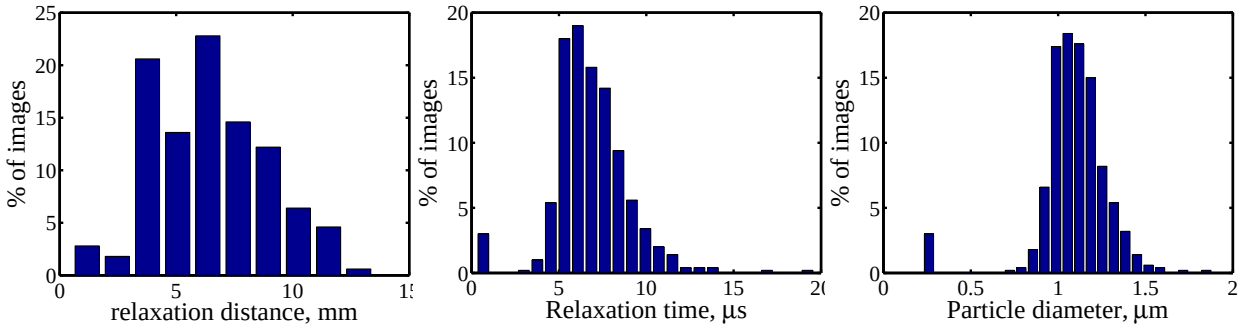

(a) Particle relaxation distance PDF (b) Particle relaxation time PDF (c) Particle diameter PDF

Figure B.3: PDFs of various seed particle characteristics.

Particle relaxation time was then computed using equation B.1 as shown below:

$$\frac{u_p - u_{post}}{u_{pre} - u_{post}} = exp\left(-\frac{n}{u_{pre}\tau_v}\right) \tag{B.1}$$

where u_p is the local shock normal velocity, u_{post} is the shock normal velocity after passing through shock or the minimum velocity in this case and u_{pre} is the shock normal velocity of free stream(max velocity) and τ_v is the relaxation time. It was obtained by an exponential curve fit as shown in fig. B.2.Mean relaxation time was found to be 6.83 μs. The Stokes no. which represents the ability of the particle to closely follow the fluid flow defined as:

$$St = \frac{\tau_v}{\tau_f} \tag{B.2}$$

where τ_f is the characteristic flow time scale which in our case is 17 μs as reported by Lapsa and Dahm [17]. The resulting Stokes no. is 0.4 which falls within the acceptable zone ($St <$ 0.5) suggested by Samimy and Lele [137]. The pdf of relaxation time of paricles obtained from instantaneous analysis of SV1 is as shown in Figure B.3b. The relaxation time as reported by Lapsa [17] was 5.5 μs which was computed from an average velocity field.

Particle diameter was then computed using equations 2.4 and 2.5,

$$\tau_p = \frac{\rho_p d_p^2}{18\mu_f}\left(1 + 3.4\sqrt{\gamma\frac{u_{pre} - u_{post}}{a_{pre}Re_{dp}}}\right) \tag{B.3}$$

where d_p is the particle diameter, μ_f is the free stream air dynamic viscosity ($8.21 \times 10^{-}6$ Pa$-$s), ρ_p is the particle density (819 kg/m^3 for PAO) , τ_p is the particle relaxation time, γ is the gas constant (1.4 for air) a_{pre} is the pre-shock sonic velocity(taken to be constant 217.1 m/s, computed using a stagnation temperature of 296 K and free stream velocity of 597 m/s) and Re_{dp} is the droplet Reynolds number in pre shock state. The pdf of particle diameters thus computed is shown in figure B.3c. The mean diameter was found out to be 0.78 μm against 0.57 μm which reported by Lapsa [17] which was computed from the mean flow field.

B.2.2 Mean Analysis

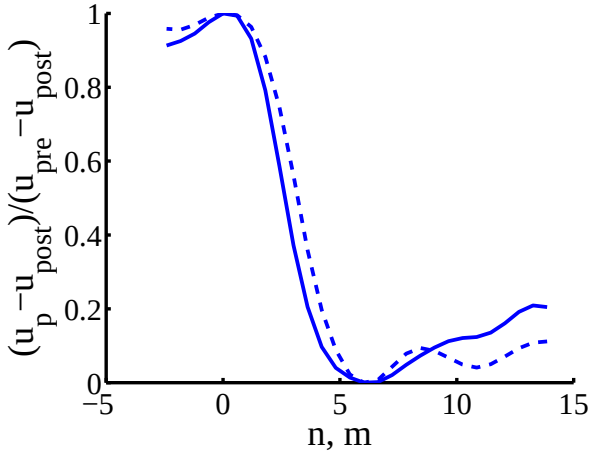

Figure B.4: Mean particle velocity decay across shock and exponential fit(dashed).

The curve fit was made using the same parameters on the mean flow field of SV1 as shown in figure B.4. The relaxation time found from this exponential fit was 5.88 μs which is fairly close to that reported by Lapsa and Dahm [17] while the corresponding particle diameter computed was 0.75 μm.

Thus it was found that the particle sizes would result in Stokes numbers within the acceptable values as recommended by Samimy and Lele [137].

B.3 Uncertainty in Location of Calibration Plate with respect to the Laser Beam Sheet

The location of the laser beam sheet with respect to the first plane of calibration plate was artificially displaced by 0.5 mm in order to study the effects of errors in calibration plate placement. Calibration was repeated for both configurations using the same set of calibration images selecting the same reference points on the calibration plate, followed by multiple steps of stereo-PIV

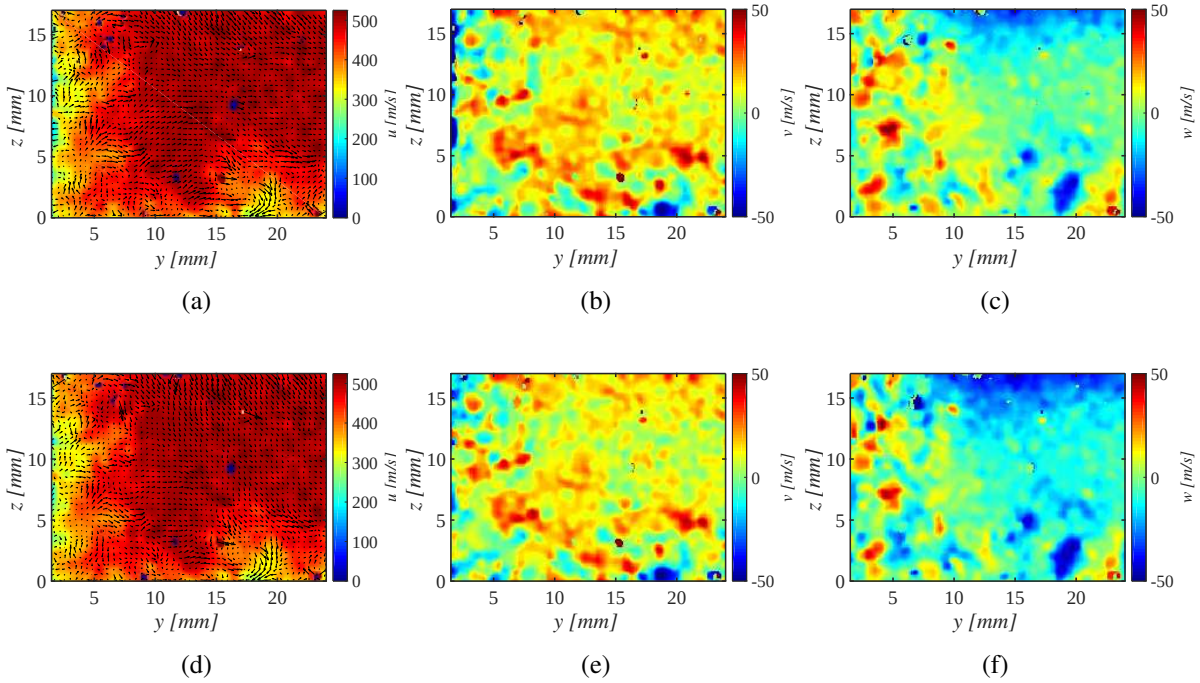

Figure B.5: Unfiltered unshifted velocity fields (a)-(c): Original fields, (d)-(f): Fields with artificial beam displacement of 0.5 mm.

self-calibration in a decreasing size of interrogation window ($128\times128 \rightarrow 64\times64 \rightarrow 32\times32$). The origin of vector fields presented in Figure B.5 has not been remapped to the side and bottom wall of the tunnel in order to determine the shift of vectors (or flow features) if any. It is observed that the locations and morphology of the flow features remain unchanged, however the magnitudes of the velocity components vary by a small margin. The images were then shifted to the physical origins, the regions of interest extracted, validated, interpolated and filtered as per the process outlined in Section 2.1.1.6. Error was then computed from the artificially shifted fields and the original fields. Figure B.6 shows the RMS error fields obtained from the 100 images. The RMS error values of u and v in most of the flow field are ≤ 5 m/s or $0.97\%U_\infty$ while that of w are ≤ 7 m/s or $1.36\%U_\infty$. Higher values are conforming to the sidewall which may be sourced to the laser reflections, these regions are deleted from the analysis.

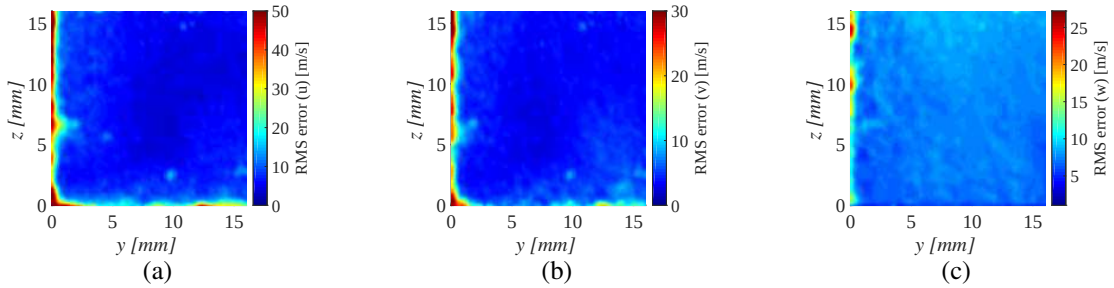

Figure B.6: RMS error fields arising from mis-location of laser sheet by 0.5 mm.

B.4 Sampling Uncertainty

Uncertainty analysis is performed on the values of U, V and W that are reported throughout this work. The finite number of recorded datasets cause a small uncertainty in the reported values which have been quantified in this section. Uncertainty analysis was carried out on the TV1 plane in Mach 2.75 empty tunnel which is considered as the worst case given that it contains least number of good (> 97% valid vectors each realization) instantaneous flow field (about 489), whereas most of the other datasets contain about 1500 instantaneous realizations. For the worst case scenario the maximum value of the standard deviation of v-velocity $\sigma_v/\sqrt{N}$ is used($N = 489$), which is found to be 0.65 m/s in the freestream. Thus a confidence interval of 98% is $\pm 2.33\frac{\sigma_v}{\sqrt{N}} = \pm 1.51$ m/s = $\pm 0.25\% U_\infty$. $U_\infty = 593 \pm 2$ m/s as has been estimated previously. Similar uncertainty analyses were conducted for other quantities in different regions viz. sidewall boundary layer ($y \leq \delta, z \geq \delta$), bottom wall boundary layer ($y \geq \delta, z \leq \delta$) and corner ($y \leq \delta, z \leq \delta$). Sampling uncertainty in the Reynolds stresses is determined in the freestream region and compared with U_∞^2. E.g. Consider the Reynolds stress $v'v'$, the maximum value of standard deviation $\sigma_{v'^2}/\sqrt{N}$ was found to be 23.51 m^2/s^2. The 98% confidence interval associated with this value is ± 54.78 m^2/s^2 which is $\pm 0.016\% U_\infty^2$. The results of the uncertainty analyses at worst case are tabulated in table B.1.

Convergence plots of the turbulence quantities for TV1 plane in Mach 2 empty tunnel are shown

98% C.I.	**Free stream**	**Side-wall boundary layer**	**Bottom-wall boundary layer**	**Corner**
U	$0.2\%U_\infty$	$0.93\%U_\infty$	$1.13\%U_\infty$	$1.55\%U_\infty$
V	$0.25\%U_\infty$	$0.56\%U_\infty$	$0.55\%U_\infty$	$0.74\%U_\infty$
W	$0.22\%U_\infty$	$0.62\%U_\infty$	$0.33\%U_\infty$	$0.48\%U_\infty$
$\overline{u'^2}$	$0.023\%U_\infty^2$	$0.19\%U_\infty^2$	$0.53\%U_\infty^2$	$0.75\%U_\infty^2$
$\overline{v'^2}$	$0.016\%U_\infty^2$	$0.0012\%U_\infty^2$	$0.095\%U_\infty^2$	$0.16\%U_\infty^2$
$\overline{w'^2}$	$0.024\%U_\infty^2$	$0.001\%U_\infty^2$	$0.089\%U_\infty^2$	$0.14\%U_\infty^2$

Table B.1: ±98% confidence intervals on mean values due to finite sampling at Mach 2.75 empty tunnel TV1 ($x = -100$ mm).

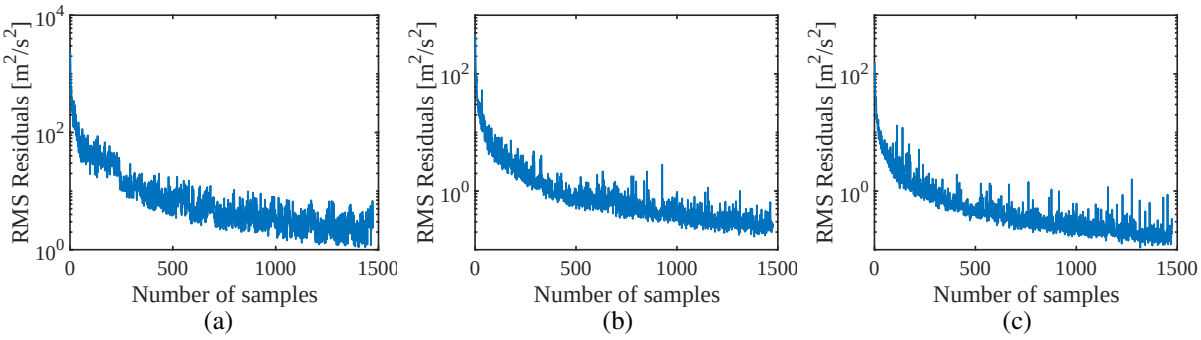

Figure B.7: Convergence plots showing the residuals for (a): $\overline{u'^2}$, (b): $\overline{v'^2}$, (c): $\overline{w'^2}$.

in Figure B.7. Increasing number of samples were used to compute the mean turbulence quantities $\overline{u'^2}$, $\overline{v'^2}$ and $\overline{w'^2}$. The difference in the averages obtained by using n samples and $n-1$ samples termed as residuals were used to evaluate the convergence of the Reynolds stresses. The RMS values of the entire residual fields is plotted as a function of number of samples used in Figure B.7. $\overline{v'^2}$ and $\overline{w'^2}$ both have converged to within 1 m^2/s^2 while the $\overline{u'^2}$ has converged within 50 m^2/s^2.

B.5 Peak Locking

Peak locking or pixel locking is a significant bias error associated with PIV measurements. It is the biasing of particle displacements towards integer pixel values and shows up as regularly spaced peaks in velocity histograms. The primary reasons attributed to peak locking are particle image diameters that are smaller than a pixel and/or inadequate seeding density. Further details about peak locking can be found in Raffel [8], Adrian and Westerweel [138] and Christensen [139].

Christensen [139] reports that even in the case of absolute peak locking mean velocity is not affected. Thus there is no uncertainty arising from peak locking in mean velocity profiles.

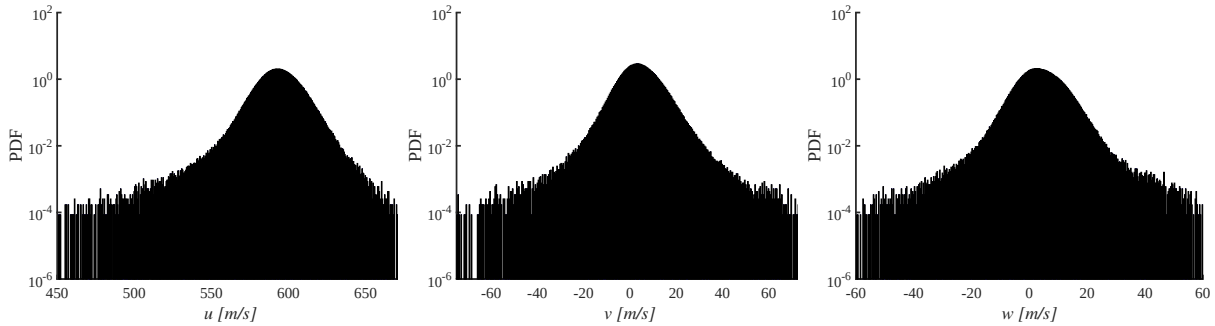

Figure B.8: Unfiltered validated velocity histograms at TV1 plane in Mach 2.75 empty tunnel.

Validated, unfiltered velocity component histograms were checked for peak locking in one of the data sets. The data acquisition arrangement remains more or less unchanged throughout all the datasets except for the SBLI dataset where the images would be zoomed out to cover a larger area. Figure B.8 shows that no peak locking was observed in histograms of validated unfiltered velocity components in TV1 plane ($x = -100$ mm) recorded in empty Mach 2.75 tunnel.

B.6 Errors associated with SPIV Geometry

This section covers the systematic uncertainties arising due to the Stereo PIV geometry. This experiment is conducted using an angular Stereo PIV setup which offers a greater out of plane accuracy than a translational SPIV setup [140–142]. Lawson and Wu [140] derived the error ratio of the out of plane component to in-plane component $e_r = \frac{\sigma_u}{\sigma_v \, or \, \sigma_w} = \frac{1}{tan(\alpha)}$, while Zang and Prasad [143] suggest that this can be improved to $e_r = \frac{1}{\sqrt{2}tan(\alpha)}$ using scheimpflug mounts and geometry. The out of plane velocity component's accuracy is the best at $\alpha = 45°$ The SPIV geometry employed for recording data utilizes cameras oriented at an angle of 33° in scheimpflug arrangement with respect to the object plane normal (arrangement shown in Figure 2.4) which leads to an error ratio of $e_r = 1.09$. Lawson and Wu [141] reported best camera angle to minimize the in plane velocity errors is $\alpha \approx 20°$, thus $\alpha = 33°$ was found to be a good trade off for optimizing both in-plane and out-plane velocity errors. As per their work [141] the RMS in-plane displacement error at $\alpha = 33°$ would be about 1.75% and the corresponding out of plane RMS displacement error would be 1.9%. Lawson and Wu [141] reported an optimum performance of the system for camera angles $20° \lesssim \alpha \lesssim 30°$ which is in good agreement with the current configuration.They also suggest a camera $f > 16$ which is in agreement with the configuration of $f22$ used to record all the datasets in the present work. The small aperture has an additional advantage of reducing image aberrations such as coma and astigmatism.

B.7 System Test at Zero Velocity

The SPIV system was tested by running the tunnel with seeding on and turning off the wind tunnel and the seeding in order to check the performance of the SPIV system. 50 images were recorded of the suspended seed particles at theoretical zero velocity using the same recording, processing and post-processing parameters as were used for the dataset recorded as a part of this

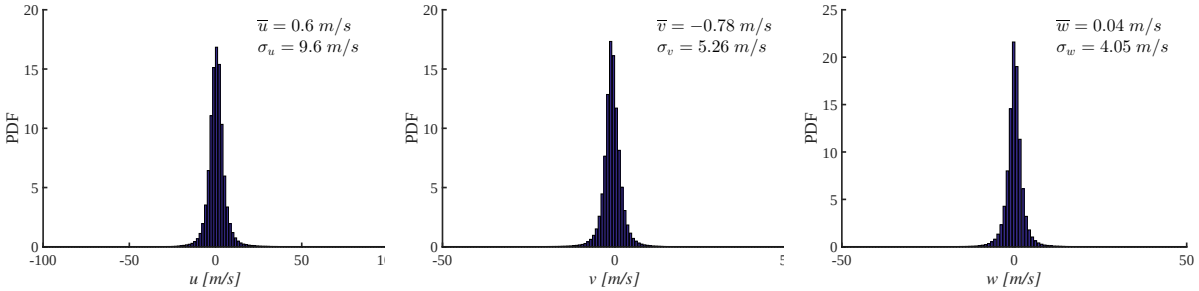

(a) (b) (c)

Figure B.9: Unfiltered validated velocity histograms at zero velocity.

Uncertainty source	Peak locking	Sampling	Sheet location	Geometry	0 velocity test	Net uncertainty
U	0	$1.55\%U_\infty$	$0.97\%U_\infty$	$1.9\%U_\infty$	$1.6\%U_\infty$	$3\%U_\infty$
V	0	$0.74\%U_\infty$	$0.97\%U_\infty$	$1.75\%U_\infty$	$0.89\%U_\infty$	$2.3\%U_\infty$
W	0	$0.62\%U_\infty$	$1.36\%U_\infty$	$1.75\%U_\infty$	$0.68\%U_\infty$	$2.4\%U_\infty$

Table B.2: Net uncertainty on mean values.

work. The histograms of the validated unfiltered velocity components are shown in Figure B.9. The Root Mean Squared (RMS) errors in the velocity components are σ_u = 9.6 m/s = $1.6\%U_\infty$, σ_v = 5.26 m/s = $0.89\%U_\infty$ and σ_w = 4.05 m/s = $0.68\%U_\infty$ at Mach 2.75.

B.8 Net Uncertainty in Mean Velocities

The worst case uncertainties from various sources are combined to obtain the net uncertainty which is tabulated in Table B.2. A second order accurate least square stencil was used for computing the gradients as it is best suited for minimizing the effect of random measurement errors, while forward/backward difference is used at the edges. The uncertainty associated with least square stencil is $\frac{\epsilon_U}{\Delta x}$, where ϵ_U is the net measurement uncertainty of the velocity component involved in gradient computation, while Δx is the vector resolution. In a very conservative way, the maximum

uncertainty observed in the velocity components as tabulated in table B.2 is $3\%U_\infty$, while the highest vector resolution is about 0.1 mm. Thus the maximum uncertainty expected in the gradients would be 1.7×10^4 s^{-1} which is about 10% of the instantaneous rigid rotation vorticity magnitudes observed.

Appendix C

Further Analysis of Corner Flows

C.1 Effect of Thresholding $|\omega_{RR_L}|$ for defining Corner Vortices

Large scale rigid rotation vorticity fields obtained from empty tunnel measurement plane at x = 122 mm for studying the interaction of 4.6° deflection SBLI with corner flows are considered for investigating the effects of thresholding of $|\omega_{RR_L}|$ to define corner vortices explained in Section 4.6. Streamwise oriented vortices are identified from the large-scale vorticity field using thresholds of $|\omega_{RR_L}|$ = 10 s^{-1}, 100 s^{-1}, 1000 s^{-1}. Negative corner vortices are then identified from these sets of vortices as per the definition and their statistical properties studied. The PDF distributions of the z_-, A_- and Wt_- obtained from the various thresholds tested are shown in Figures C.1a, C.1b and C.1c respectively. It can be seen that the PDFs of all the properties are retained through different thresholds. The PDFs at threshold values of $|\omega_{RR_L}|$ = 10 s^{-1}, 100 s^{-1}, equivalent to 1/1000th and

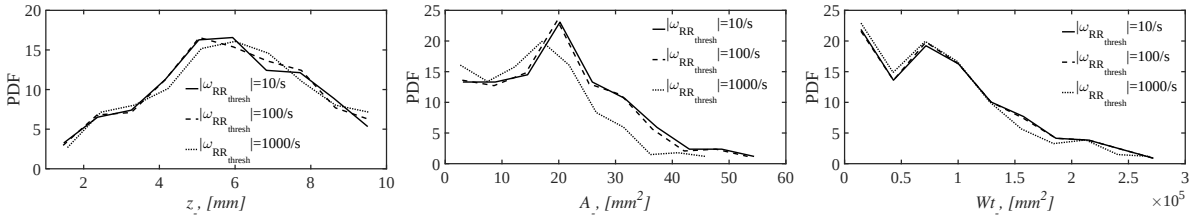

(a) (b) (c)

Figure C.1: Effect of different threshold values of $|\omega_{RR_L}|$for defining a vortex on various corner vortex properties. (Studied for negative corner vortex).

1/100th of the peak values of $|\omega_{RR_L}|$ are almost overlapping. The properties of the corner vortex can thus be considered independent of the thresholding for a threshold value of $|\omega_{RR_L}| \leq 10\ \mathrm{s}^{-1}$.

C.2 Conservation of Turbulent Moments

From equations 1.1,1.4 and 1.5, the turbulent terms that contribute the most towards vorticity production appear to be $\overline{v'^2} - \overline{w'^2}$ and $\overline{v'w'}$. Further mathematical analyses on these two terms is performed in this section. General equation of turbulence moment transport is given as:

$$\begin{aligned}\frac{D\overline{u_i'u_j'}}{Dt} = &-\left[\overline{u_j'u_k'}\frac{\partial U_i}{\partial x_k} + \overline{u_i'u_k'}\frac{\partial U_j}{\partial x_k}\right] - 2\nu\overline{\frac{\partial u_i'}{\partial x_k}\frac{\partial u_j'}{\partial x_k}} + \overline{\frac{p'}{\rho}\left[\frac{\partial u_i'}{\partial x_j} + \frac{\partial u_j'}{\partial x_i}\right]} \\ &-\left[\frac{\partial \overline{u_i'u_j'u_k'}}{\partial x_k} - \nu\frac{\partial \overline{u_i'u_j'}}{\partial x_k} + \frac{1}{\rho}\left(\frac{\partial \overline{p'u_i'}}{\partial x_j} + \frac{\partial \overline{p'u_j'}}{\partial x_i}\right)\right]\end{aligned} \tag{C.1}$$

Using the above equation C.1, the turbulent moment transport equation for $\overline{v'w'}$ is given by,

$$\begin{aligned}\frac{D\overline{v'w'}}{Dt} = &-\left[\overline{v'^2}\frac{\partial W}{\partial y} + \overline{w'^2}\frac{\partial V}{\partial z} + \overline{v'w'}\left(\frac{\partial V}{\partial y} + \frac{\partial W}{\partial z}\right) + \overline{u'v'}\frac{\partial W}{\partial x} + \overline{u'w'}\frac{\partial W}{\partial y}\right] + \overline{\frac{p'}{\rho}\left[\frac{\partial v'}{\partial z} + \frac{\partial w'}{\partial y}\right]} \\ -2\nu&\left[\overline{\frac{\partial v'}{\partial x}\frac{\partial w'}{\partial x}} + \overline{\frac{\partial v'}{\partial y}\frac{\partial w'}{\partial y}} + \overline{\frac{\partial v'}{\partial z}\frac{\partial w'}{\partial z}}\right] - \left[\frac{\partial \overline{u'v'w'}}{\partial x} + \frac{\overline{v'^2w'}}{\partial y} + \frac{\overline{v'w'^2}}{\partial z}\right] + \nu\Delta\overline{v'w'} - \frac{1}{\rho}\left(\frac{\partial \overline{p'w'}}{\partial y} + \frac{\partial \overline{p'v'}}{\partial z}\right)\end{aligned} \tag{C.2}$$

For computing the conservation equation for $\overline{v'2} - \overline{w'2}$, the conservation equation of $\overline{w'2}$ is subtracted from that for $\overline{v'2}$. The conservation equations are as follows:

$$\begin{aligned}\frac{D\overline{v'^2}}{Dt} = &-\left[2\overline{u'v'}\frac{\partial V}{\partial x} + 2\overline{v'^2}\frac{\partial V}{\partial y} + 2\overline{v'w'}\frac{\partial V}{\partial z}\right] - 2\nu\left[\overline{\left(\frac{\partial v'}{\partial x}\right)^2} + \overline{\left(\frac{\partial v'}{\partial y}\right)^2} + \overline{\left(\frac{\partial v'}{\partial z}\right)^2}\right] + \overline{\frac{p'}{\rho}\left(2\frac{\partial v'}{\partial y}\right)} \\ &-\left[\frac{\partial \overline{u'v'^2}}{\partial x} + \frac{\partial \overline{v'^3}}{\partial y} + \frac{\partial \overline{v'^2w'}}{\partial z}\right] + \nu\Delta\overline{v'^2} - \frac{2}{\rho}\left[\frac{\partial \overline{p'v'}}{\partial y}\right]\end{aligned} \tag{C.3}$$

The conservation equation for w'^2 is obtained similarly as:

$$\frac{D\overline{w'^2}}{Dt} = -\left[2\overline{u'w'}\frac{\partial W}{\partial x} + 2\overline{v'w'}\frac{\partial W}{\partial y} + 2\overline{w'^2}\frac{\partial W}{\partial z}\right] - 2\nu\left[\overline{\left(\frac{\partial w'}{\partial x}\right)^2} + \overline{\left(\frac{\partial w'}{\partial y}\right)^2} + \overline{\left(\frac{\partial w'}{\partial z}\right)^2}\right] + \overline{\frac{p'}{\rho}\left(2\frac{\partial w'}{\partial z}\right)} - \left[\frac{\partial \overline{u'w'^2}}{\partial x} + \frac{\partial \overline{v'w'^2}}{\partial y} + \frac{\partial \overline{w'^3}}{\partial z}\right] + \nu\Delta\overline{w'^2} - \frac{2}{\rho}\left[\frac{\partial \overline{p'w'}}{\partial z}\right] \tag{C.4}$$

Subtracting equation C.4 from C.3 and using the quasi streamwise assumption ($\partial V/\partial x = \partial W/\partial x = 0$) we obtain the conservation equation for $\overline{v'2} - \overline{w'2}$ as:

$$\begin{aligned}\frac{D(\overline{v'^2} - \overline{w'^2})}{Dt} = {} & 2\overline{v'w'}\left[\frac{\partial V}{\partial z} - \frac{\partial W}{\partial y}\right] - 2\left[\overline{v'^2}\frac{\partial V}{\partial y} - \overline{w'^2}\frac{\partial W}{\partial z}\right] + \overline{\frac{2p'}{\rho}\left(\frac{\partial v'}{\partial y} - \frac{\partial w'}{\partial z}\right)} + \nu\Delta(\overline{v'^2} - \overline{w'^2}) \\ & - \left[\frac{\partial \overline{u'(v'^2 - w'^2)}}{\partial x} + \frac{\partial \overline{v'(v'^2 - w'^2)}}{\partial y} + \frac{\partial \overline{w'(v'^2 - w'^2)}}{\partial z}\right] - \frac{2}{\rho}\left[\frac{\partial \overline{p'v'}}{\partial y} - \frac{\partial \overline{p'w'}}{\partial z}\right] \\ & - 2\nu\left[\overline{\left(\frac{\partial v'}{\partial x}\right)^2} - \overline{\left(\frac{\partial w'}{\partial x}\right)^2} + \overline{\left(\frac{\partial v'}{\partial y}\right)^2} - \overline{\left(\frac{\partial w'}{\partial y}\right)^2} + \overline{\left(\frac{\partial v'}{\partial z}\right)^2} - \overline{\left(\frac{\partial w'}{\partial z}\right)^2}\right] \\ & = 2\overline{v'w'}\omega_x + ...\end{aligned} \tag{C.5}$$

Let the terms be named as Turbulent production A, turbulent convection B, viscous diffusion C, turbulent barotropic production and redistribution D and dissipation E.

$$\begin{aligned} A &= 2\overline{v'w'}\omega_x - 2\left[\overline{v'^2}\frac{\partial V}{\partial y} - \overline{w'^2}\frac{\partial W}{\partial z}\right] \\ B &= \left[\frac{\partial \overline{u'(v'^2 - w'^2)}}{\partial x} + \frac{\partial \overline{v'(v'^2 - w'^2)}}{\partial y} + \frac{\partial \overline{w'(v'^2 - w'^2)}}{\partial z}\right] \\ C &= \nu\Delta(\overline{v'^2} - \overline{w'^2}) \\ D &= \overline{\frac{2p'}{\rho}\left(\frac{\partial v'}{\partial y} - \frac{\partial w'}{\partial z}\right)} - \frac{2}{\rho}\left[\frac{\partial \overline{p'v'}}{\partial y} - \frac{\partial \overline{p'w'}}{\partial z}\right] \\ E &= -2\nu\left[\overline{\left(\frac{\partial v'}{\partial x}\right)^2} - \overline{\left(\frac{\partial w'}{\partial x}\right)^2} + \overline{\left(\frac{\partial v'}{\partial y}\right)^2} - \overline{\left(\frac{\partial w'}{\partial y}\right)^2} + \overline{\left(\frac{\partial v'}{\partial z}\right)^2} - \overline{\left(\frac{\partial w'}{\partial z}\right)^2}\right] \end{aligned} \tag{C.6}$$

C.3 Conservation of Enstrophy

Taking the scalar product of the equation 4.9 with $\overline{\omega_j}$ we get the mean enstrophy ($\frac{1}{2}\overline{\omega_j^2}$) conservation equation as,

$$\overline{u_i}\frac{\partial}{\partial x_i}(\frac{1}{2}\overline{\omega_j^2}) = (\bar{\omega}_j\bar{\omega}_i)\frac{\partial\overline{u_j}}{\partial x_i} + \overline{\omega_j}\left[\frac{\partial}{\partial x_i}\left[\overline{\omega_i'u_j'} - \overline{\omega_j'u_i'}\right]\right] + \nu\left[\frac{\partial^2}{\partial x_i^2}(\frac{1}{2}\overline{\omega_j^2}) - \left(\frac{\partial\overline{\omega_j}}{\partial x_i}\right)^2\right] \tag{C.7}$$

Using continuity ($\nabla.(u_L' + u_S') = 0$) and ($\nabla.(\nabla\times\mathbf{u}) = 0$), the above equation can be written as,

$$\overline{u_i}\frac{\partial}{\partial x_i}(\frac{1}{2}\overline{\omega_j^2}) = (\bar{\omega}_j\bar{\omega}_i)\frac{\partial\overline{u_j}}{\partial x_i} + \frac{\partial}{\partial x_i}[\overline{\omega_j}(\overline{\omega_i'u_j'})] - (\overline{\omega_i'u_j'})\frac{\partial\overline{\omega_j}}{\partial x_i} + (\overline{\omega_j'u_i'})\frac{\partial\overline{\omega_j}}{\partial x_i} - \frac{\partial}{\partial x_i}[\overline{\omega_j}(\overline{\omega_j'u_i'})] + \nu\left[\frac{\partial^2}{\partial x_i^2}(\frac{1}{2}\overline{\omega_j^2}) - \left(\frac{\partial\overline{\omega_j}}{\partial x_i}\right)^2\right] \tag{C.8}$$

$$\overline{u_i}\frac{\partial}{\partial x_i}(\frac{1}{2}\overline{\omega_j^2}) = (\bar{\omega}_j\bar{\omega}_i)\frac{\partial\overline{u_j}}{\partial x_i} + \frac{\partial}{\partial x_i}[\overline{\omega_j}(\overline{\omega_i'u_j'} - \overline{\omega_j'u_i'})] + \frac{\partial\overline{\omega_j}}{\partial x_i}[(\overline{\omega_j'u_i'}) - (\overline{\omega_i'u_j'})] + \nu\left[\frac{\partial^2}{\partial x_i^2}(\frac{1}{2}\overline{\omega_j^2}) - \left(\frac{\partial\overline{\omega_j}}{\partial x_i}\right)^2\right] \tag{C.9}$$

Using the Einstein notations for vorticity $\omega_i = \epsilon_{ijk}\frac{\partial u_k}{\partial x_j}$ where ϵ_{ijk} is the Levi-Civita symbol, the enstrophy conservation equation can be simplified as:

$$\overline{u_i}\frac{\partial}{\partial x_i}(\frac{1}{2}\overline{\omega_j^2}) = (\bar{\omega}_j\bar{\omega}_i)\frac{\partial\overline{u_j}}{\partial x_i} + \epsilon_{jki}\frac{\partial\overline{u_i}}{\partial x_k}\left[\frac{\partial}{\partial x_i}\left[\overline{\epsilon_{ijk}\frac{\partial u_k'}{\partial x_j}u_j'} - \overline{\epsilon_{jki}\frac{\partial u_i'}{\partial x_k}u_i'}\right]\right] + \nu\left[\frac{\partial^2}{\partial x_i^2}(\frac{1}{2}\overline{\omega_j^2}) - \left(\frac{\partial\overline{\omega_j}}{\partial x_i}\right)^2\right] \tag{C.10}$$

Using continuity equation $\frac{\partial u_i'}{\partial x_i} = 0$

$$\overline{u_i}\frac{\partial}{\partial x_i}(\frac{1}{2}\overline{\omega_j^2}) = (\bar{\omega}_j\bar{\omega}_i)\frac{\partial\overline{u_j}}{\partial x_i} + \left[\epsilon_{jki}\epsilon_{ijk}\frac{\partial\overline{u_i}}{\partial x_k}\frac{\partial^2\overline{u_k'u_j'}}{\partial x_i\partial x_j} - \epsilon_{jki}\epsilon_{jki}\frac{\partial\overline{u_i}}{\partial x_k}\frac{\partial^2\frac{(u_i')^2}{2}}{\partial x_i x_j}\right] + \nu\left[\frac{\partial^2}{\partial x_i^2}(\frac{1}{2}\overline{\omega_j^2}) - \left(\frac{\partial\overline{\omega_j}}{\partial x_i}\right)^2\right] \tag{C.11}$$

$$\overline{u_i}\frac{\partial}{\partial x_i}(\frac{1}{2}\overline{\omega_j^2}) = (\bar{\omega}_j\bar{\omega}_i)\frac{\partial\overline{u_j}}{\partial x_i} + \epsilon_{jki}\epsilon_{jki}\frac{\partial\overline{u_i}}{\partial x_k}\left[\frac{\partial^2\overline{u_k'u_j'}}{\partial x_i\partial x_j} - \frac{\partial^2\frac{(u_i')^2}{2}}{\partial x_i x_j}\right] + \nu\left[\frac{\partial^2}{\partial x_i^2}(\frac{1}{2}\overline{\omega_j^2}) - \left(\frac{\partial\overline{\omega_j}}{\partial x_i}\right)^2\right] \tag{C.12}$$

$$\overline{u_i}\frac{\partial}{\partial x_i}(\frac{1}{2}\overline{\omega_j^2}) = (\bar{\omega}_j\bar{\omega}_i)\frac{\partial\overline{u_j}}{\partial x_i} + \begin{vmatrix}\delta_{jj} & \delta_{jk} & \delta_{ji}\\ \delta_{kj} & \delta_{kk} & \delta_{ki}\\ \delta_{ij} & \delta_{ik} & \delta_{ii}\end{vmatrix}\frac{\partial\overline{u_i}}{\partial x_k}\left[\frac{\partial^2\overline{u_k'u_j'}}{\partial x_i\partial x_j} - \frac{\partial^2\frac{(u_i')^2}{2}}{\partial x_i x_j}\right] + \nu\left[\frac{\partial^2}{\partial x_i^2}(\frac{1}{2}\overline{\omega_j^2}) - \left(\frac{\partial\overline{\omega_j}}{\partial x_i}\right)^2\right] \tag{C.13}$$

$$\overline{u_i}\frac{\partial}{\partial x_i}(\frac{1}{2}\overline{\omega_j^2}) = (\bar{\omega}_j\bar{\omega}_i)\frac{\partial\overline{u_j}}{\partial x_i} + 6\frac{\partial\overline{u_i}}{\partial x_k}\frac{\partial^2(\overline{u_k'u_j'} - \frac{(u_i')^2}{2})}{\partial x_i\partial x_j} + \nu\left[\frac{\partial^2}{\partial x_i^2}(\frac{1}{2}\overline{\omega_j^2}) - \left(\frac{\partial\overline{\omega_j}}{\partial x_i}\right)^2\right] \tag{C.14}$$

Following the enstrophy conservation equation, C.14, the second term on the right hand side represents the turbulent enstrophy creation. Following the streamwise quasi steadiness assumption or ($\frac{\partial}{\partial x} = 0$), the turbulent production of enstrophy (T_{ω^2}) can be simplified as:

$$\begin{aligned} T_{\omega^2} = {} & \frac{\partial\overline{v}}{\partial y}\frac{\partial^2}{\partial y^2}\left[\overline{v'^2} - \frac{1}{2}\overline{v'^2}\right] + \frac{\partial\overline{v}}{\partial z}\frac{\partial^2}{\partial y^2}\left[\overline{v'w'} - \frac{1}{2}\overline{v'^2}\right] + \frac{\partial\overline{v}}{\partial y}\frac{\partial^2}{\partial y\partial z}\left[\overline{v'w'} - \frac{1}{2}\overline{v'^2}\right] + \frac{\partial\overline{w}}{\partial y}\frac{\partial^2}{\partial y\partial z}\left[\overline{v'^2} - \frac{1}{2}\overline{w'^2}\right] + \\ & \frac{\partial\overline{w}}{\partial z}\frac{\partial^2}{\partial z^2}\left[\overline{w'^2} - \frac{1}{2}\overline{w'^2}\right] + \frac{\partial\overline{w}}{\partial y}\frac{\partial^2}{\partial z^2}\left[\overline{v'w'} - \frac{1}{2}\overline{w'^2}\right] + \frac{\partial\overline{w}}{\partial z}\frac{\partial^2}{\partial y\partial z}\left[\overline{v'w'} - \frac{1}{2}\overline{w'^2}\right] + \frac{\partial\overline{v}}{\partial z}\frac{\partial^2}{\partial z\partial y}\left[\overline{w'^2} - \frac{1}{2}\overline{w'^2}\right] \end{aligned} \tag{C.15}$$

The turbulent enstrophy production fields at TV1, TV2 and TV3 are shown in figure C.2. Turbulent dissipation is observed in the corner (negative blue region) in all three locations with dissipation

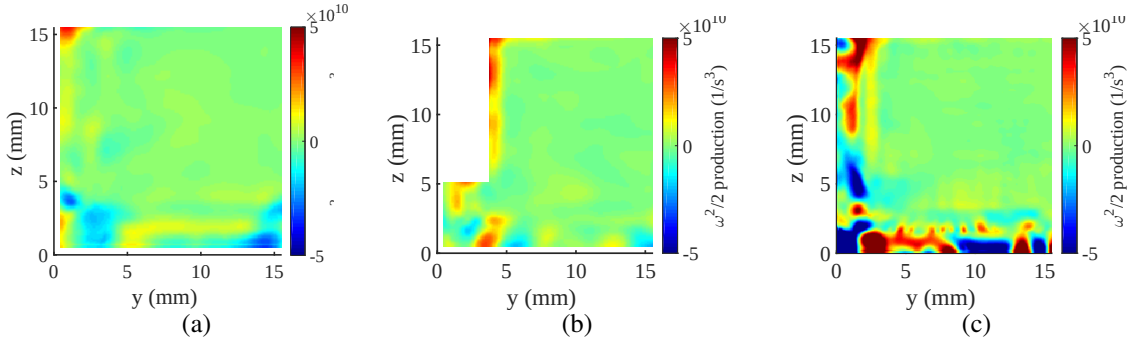

Figure C.2: Mean turbulent enstrophy production field on (a): TV1 ($x = -100$ mm); (b): TV2 ($x = -50$ mm); and (c): TV3 ($x = 0$ mm) at Mach 2.

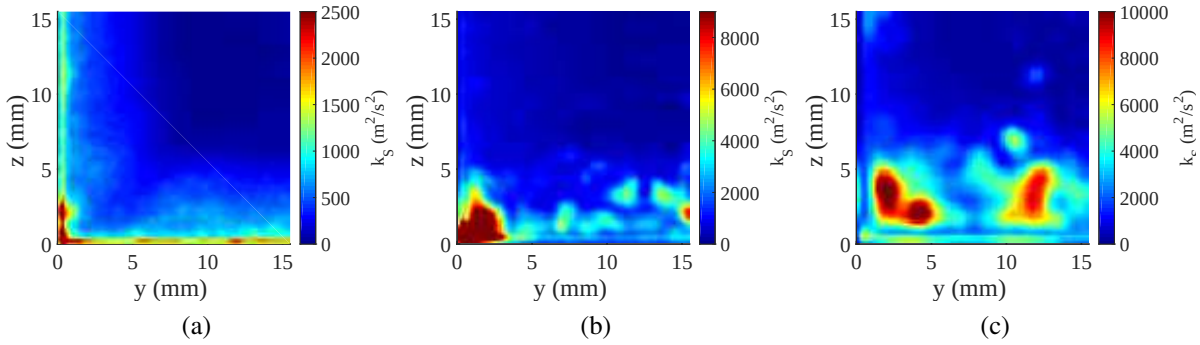

Figure C.3: Small scale turbulent kinetic energy fields at (a): TV1 ($x = -100$ mm), (b): TV2 ($x = -50$ mm) and (c): TV3 ($x = 75$ mm) at Mach 2.75.

strengthening in the downstream direction. The dissipation region is neighbored by enstrophy production (positive red region) on both side and bottom walls immediately away from the corner.

C.4 Small Scale Kinetic Energy Fields

C.5 Turbulent Kinetic Energy Production and Dissipation

The kinetic energy dissipation (ϵ) is approximated as

$$\epsilon = \nu \overline{\frac{\partial u_i\prime}{\partial x_j} \frac{\partial u_i\prime}{\partial x_j}} \tag{C.16}$$

Incompressible turbulence assumption was used in order to estimate the out of plane derivatives as the turbulent Mach number $M' < 0.3$. Thus substituting,

$$\frac{\partial u\prime}{\partial x} = -\left(\frac{\partial v\prime}{\partial y} + \frac{\partial w\prime}{\partial z}\right) \tag{C.17}$$

in equation C.16, we get,

$$\epsilon = \nu \left[2\overline{\left(\frac{\partial v\prime}{\partial y}\right)^2} + 2\overline{\frac{\partial v\prime}{\partial y}\frac{\partial w\prime}{\partial z}} + 2\overline{\left(\frac{\partial w\prime}{\partial z}\right)^2} + 2\overline{\left(\frac{\partial v\prime}{\partial z}\right)^2} + 2\overline{\left(\frac{\partial u\prime}{\partial z}\right)^2} + \overline{\left(\frac{\partial u\prime}{\partial y}\right)^2} + \overline{\left(\frac{\partial w\prime}{\partial y}\right)^2} \right] \tag{C.18}$$

The viscosity was computed using Sutherland law while the density near the wall was computed using th e results of Spina et al. [125]. The dissipation fields obtained from Equation C.18 are shown in Figure C.4. It can be seen that the dissipation field is pretty ordinary with TKE being dissipated near walls. Downstream at TV2, where the corner flow begins to develop, the highest dissipation takes place in the corner, while in the most downstream plane, the stronger TKE dissipation zones are observed at the interface of region with a high probability of vortex and a wall.

Production of turbulent kinetic energy (P) is computed using the definition,

$$P = -\overline{u_i\prime u_j\prime} \frac{\partial U_i}{\partial x_j} \tag{C.19}$$

using an assumption that the streamwise gradient of secondary velocity components is small ($\frac{\partial V}{\partial x} \approx$

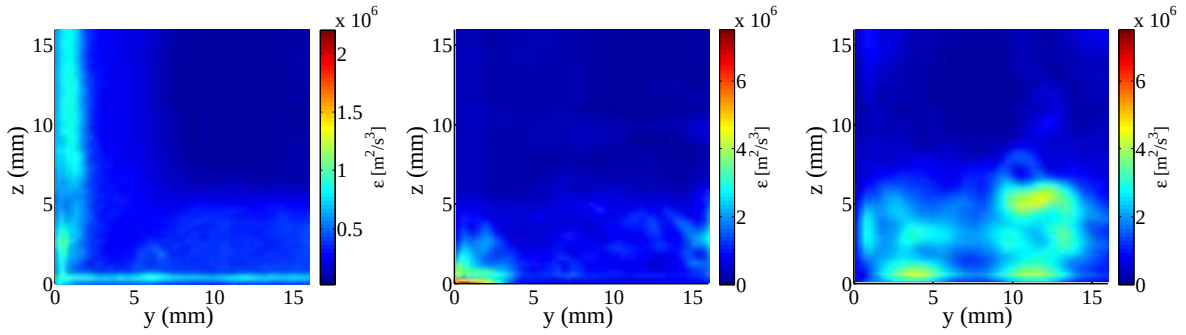

Figure C.4: Turbulent kinetic energy dissipation ϵ fields at (a): TV1, (b): TV2 and (c): TV3 obtained at Mach 2.75.

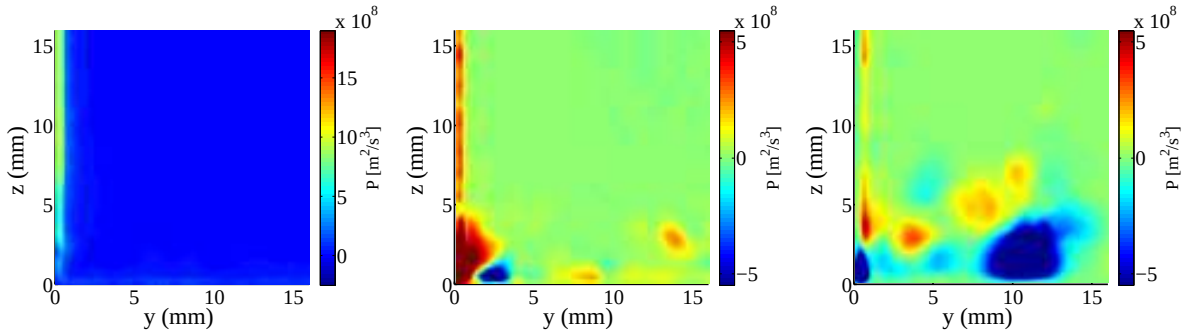

Figure C.5: Turbulent kinetic energy production P fields at (a): TV1, (b): TV2 and (c): TV3 obtained at Mach 2.75.

$\frac{\partial W}{\partial x} \approx 0$). The production fields thus obtained are shown in Figure C.5. The production of TKE at $x = -100$ mm is small compared to the distribution found at the downstream planes. In TV2 and TV4, it can be seen from Figures C.5b and C.5c, that most of the production takes place at the location of the vortices. Positive vortex is responsible for negative production and vice versa.

C.6 Vorticity Production Fields

As described in section 4.3, the vorticity production terms are decomposed into large, small and interscales. Most of the vorticity production takes place in the large-scales and interscale while

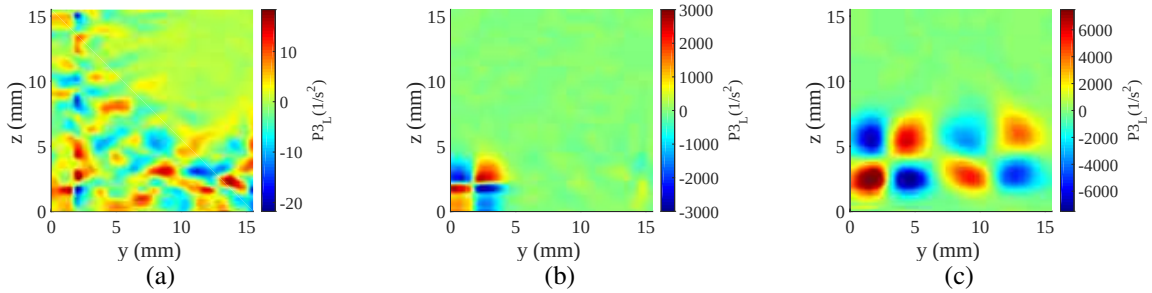

Figure C.6: Large scale vorticity production $P3_L$ fields at (a): TV1, (b): TV2 and (c): TV3 at Mach 2.75.

the small-scale production although of comparable magnitude lacks structure and appears random. Thus only the large and inter-scale vorticity production terms will be presented.

The vorticity production fields associated with large-scale anisotropy are shown in Figure C.6. It is observed that at TV1 ($x = -100$ mm) the field appears unstructured and weak as compared to the downstream planes where vorticity production takes place around the regions of high turbulence fluctuations. Vorticity production due to interscale anisotropy is stronger than that in the large-scales and follows similar trend as can be observed in Figure C.7.

The vorticity production caused by the cross diagonal components of large-scale turbulence are shown in Figure C.8. It can be observed that these fields are of the same orders of magnitude as the $P3_L$ fields and are also primarily driven by the sites of higher values of turbulent fluctuations. It is worth noting that the anisotropic vorticity production fields and the fields of vorticity production due to cross diagonal turbulence terms are orthogonal to each other which was also observed by Brundrett and Baines [75]. Similar to the $P3$ fields the contribution from the interscale terms is an order of magnitude higher than the large-scale terms.

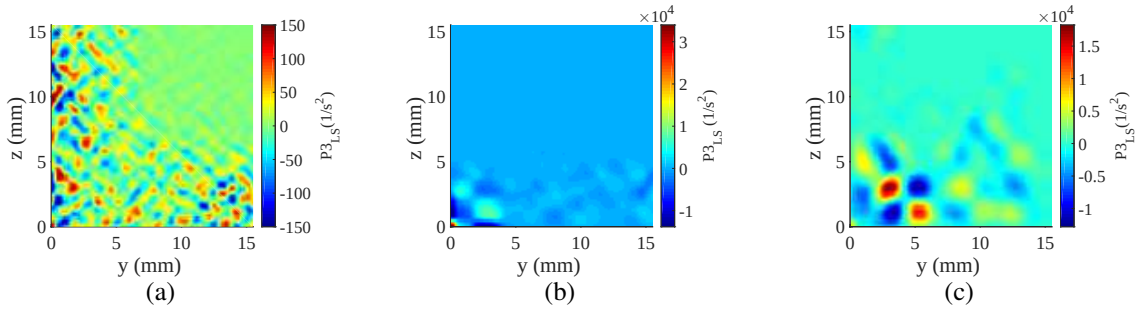

Figure C.7: Interscale vorticity production $P3_{LS}$ fields at (a): TV1, (b): TV2 and (c): TV3 at Mach 2.75.

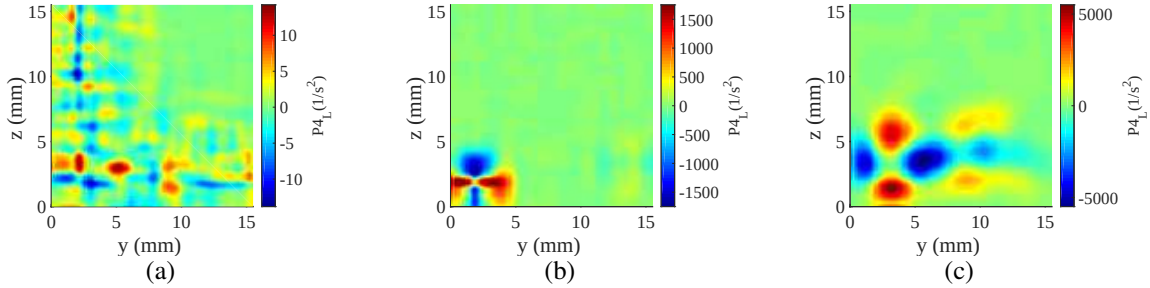

Figure C.8: Large scale vorticity production $P4_L$ fields at (a): TV1, (b): TV2 and (c): TV3 at Mach 2.75.

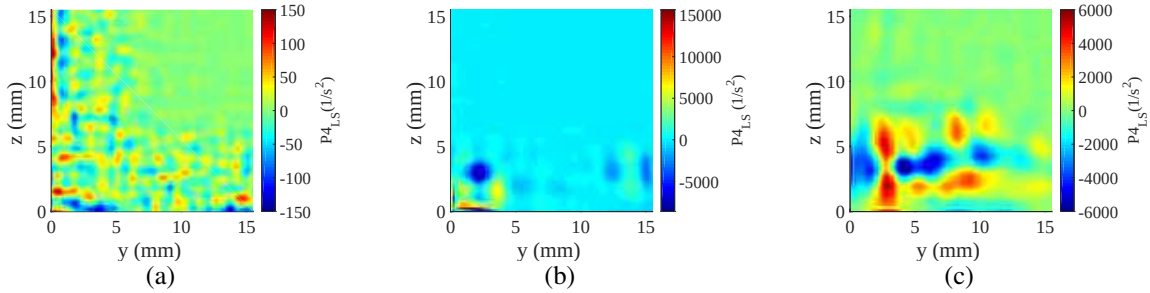

Figure C.9: Interscale vorticity production $P4_{LS}$ fields at (a): TV1, (b): TV2 and (c): TV3 at Mach 2.75.

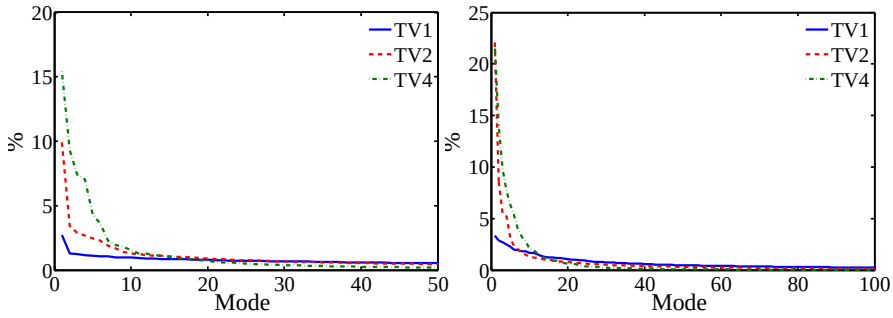

(a) Modal contributions to conventional vorticity fields (b) Modal contributions to vector fields

Figure C.10: Modal contributions of the first 50 modes.

C.7 Proper Orthogonal Decomposition (Proper Orthogonal Decomposition (POD))

Preferred modes of flow were extracted from the data at the TV1, TV2 and T4 planes using the algorithm developed by Gurka et al. [144]. The algorithm was applied to the three component vector fields, conventional vorticity fields and the rigid rotation fields at TV1, TV2 and TV3 to elucidate the most prominent modes. It was observed that the highest contribution by a mode obtained from the rigid rotation vorticity fields in all of the data planes was less than 8%, which would be due to the relatively smaller scales associated with rigid rotation vortex as compared to a conventional vortex. The modal contributions of the first 50 modes obtained from the vorticity fields and the vector fields are shown in Figure C.10. It can be observed that the contribution of the most dominant mode in TV1 is less than 5% while it increases as we proceed downstream. The number of modes contributing significantly also increases in the downstream plane as is evident from Figure C.10. First three modes obtained on plane TV2 and TV4 are shown in Figure C.11.. We can see that first two modes (consisting of antisymmetric vortex pair) obtained from the conventional vorticities bear certain similarities in TV2 and TV4. It is therefore ascertained that these modes are the dominant ones in the global flow-field. More robust analysis will be conducted to ascertain

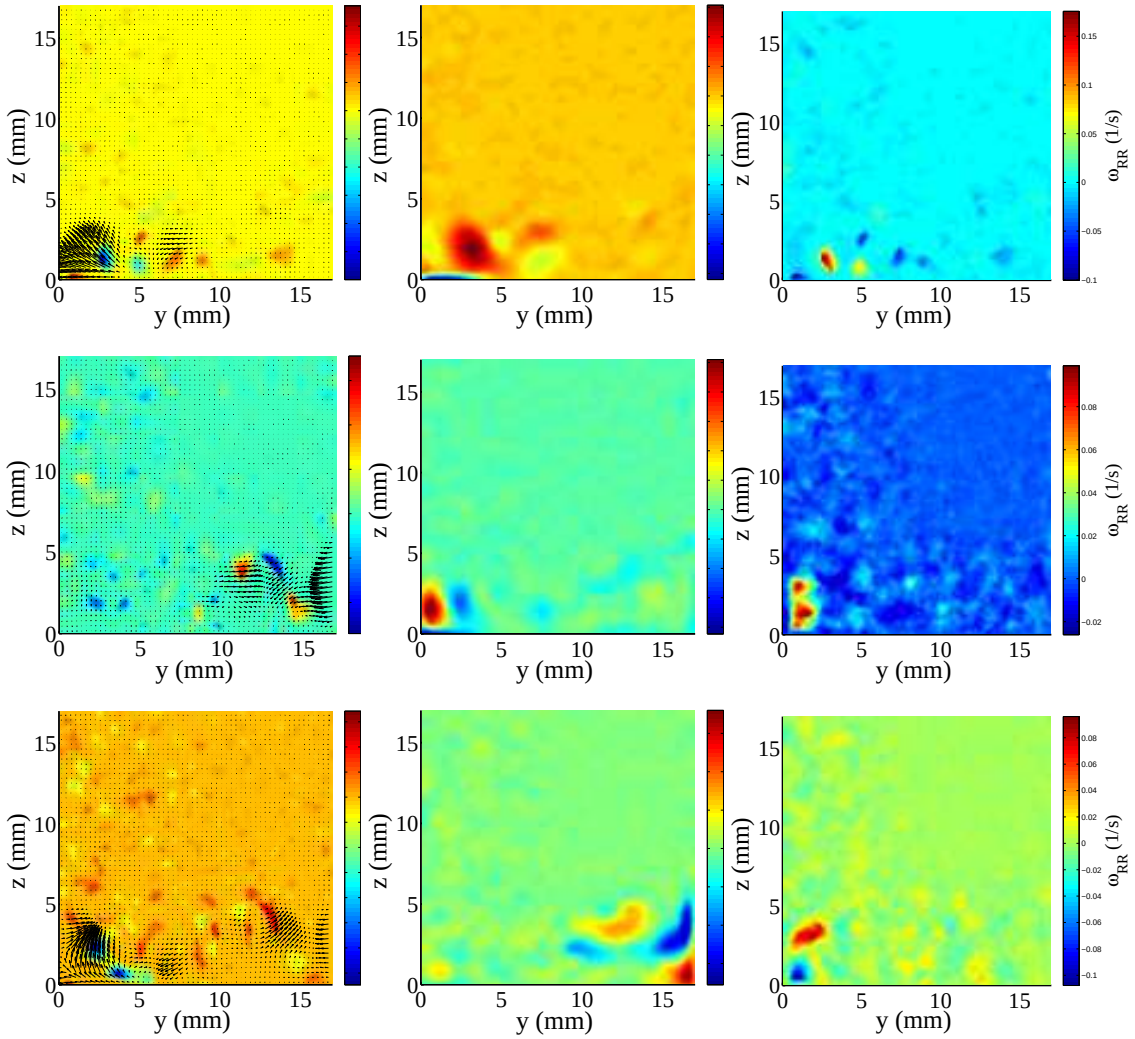

Figure C.11: First 3 dominant modes in TV2 ($x = -50$ mm) at Mach 2.75. Mode number decreases top to bottom and first column represents the modal vector fields, second column represenst the modal conventional vorticity and the third column is the modal rigid rotation vorticity.

similar modes using cross correlations.

Appendix D

A Criterion for Stable Existence of Researchers

In this section we present a model to define allowable zones of existence for a researcher. The current form of model is a result of modifications to the original model following extensive, intensive and deep discussions with Sen. Fabian Chacon. The model gives a correlation between caffeine intake and amount of sleep needed for the given caffeine intake in order to divide th domain into various zones of existence.

The inequality of the model is given as:

$$\frac{sleep\,(caffeine\ +1)}{k} \geq c \tag{D.1}$$

where *sleep* is in hours of sleep needed , $caffeine$ in mg of caffeine ingested and

$$k = f\left(\int_{t=0}^{t\,=\,present} (caffeine\ - at)dt\right) \tag{D.2}$$

which models the number of cortisol receptors in the brain and a is the rate of decay of the cortisol receptors. k can be considered as the tolerance for caffeine developed due to sustained caffeine intake. c would be the natural number of hours of sleep a person requires without the use of or history of any caffeine. For an average person c = 8 hours.

Based on the proposed model we propose a map of different states in which a researcher would exist at any given time. The map is shown in Figure D.1.

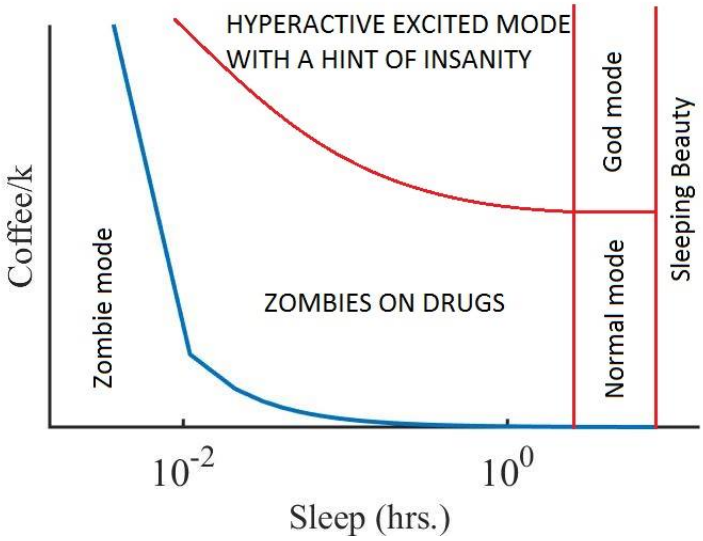

Figure D.1: Map of existence of a researcher in caffeine-sleep space.

BIBLIOGRAPHY

[1] Délery, J. and Bur, R., "The physics of shock wave/boundary layer interaction control: last lessons learned," *European Congress on Computational Methohd in Applied Sciences and Engineering*, , No. September, 2000, pp. 11–14.

[2] Ostlund, J. and Muhammad-Klingmann, B., "Supersonic Flow Separation with Application to Rocket Engine Nozzles," *Applied Mechanics Reviews*, Vol. 58, No. 3, 2005, pp. 143.

[3] Kubota, H. and Stollery, J. L., "An experimental study of the interaction between a glancing shock wave and a turbulent boundary layer," *Journal of Fluid Mechanics*, Vol. 116, 1982, pp. 431–458.

[4] Alvi, F. S. and Settles, G. S., "Physical Model of the Swept Shock Wave / Boundary-Layer Interaction Flowfield," *AIAA Journal*, Vol. 30, No. 9, 1992, pp. 2252–2258.

[5] Batcho, P. and Sullivan, J., "The 3-D Flowfield in a Supersonic Shock Boundary Layer Corner Interaction," *AIAA 26th Aerospace Sciences Meeting*, Reno, Nevada, 1988.

[6] Eagle, W. E. and Driscoll, J. F., "Shock waveboundary layer interactions in rectangular inlets: three-dimensional separation topology and critical points," *Journal of Fluid Mechanics*, Vol. 756, sep 2014, pp. 328–353.

[7] Davis, D. O. and Gessner, F. B., "Further Experiments on Supersonic Turbulent Flow Development in a Square Duct," *AIAA JOURNAL*, Vol. 27, No. 8, 1989, pp. 1023–1030.

[8] Raffel, M., Willert, C. E., Wereley, S. T., and Kompenhans, J., *Particle Image Velocimetry*, Springer, 2nd ed., 2007.

[9] Karasu, I., Genc, M. S., and Acikel, H. H., "Numerical Study on Low Reynolds Number Flows Over an Aerofoil," *Journal of Applied Mechanical Engineering*, Vol. 02, No. 5, 2013, pp. 1–7.

[10] Kolá, V., "Vortex identification: New requirements and limitations," *International Journal of Heat and Fluid Flow*, Vol. 28, No. 4, aug 2007, pp. 638–652.

[11] Blinde, P. L., Humble, R. A., van Oudheusden, B. W., and Scarano, F., "Effects of micro-ramps on a shock wave/turbulent boundary layer interaction," *Shock Waves*, Vol. 19, No. 6, 2009, pp. 507–520.

[12] Sartor, F., Losfeld, G., Leclaire, B., and Bur, R., "Characterization by PIV of the Effect of Vortex Generators in a Transonic Separated Flow," *10TH Internationnal symposium on particle image velocimetry -PIV13*, 2013.

[13] Bruce, P. J. K., Burton, D. M. F., Titchener, N. a., and Babinsky, H., "Corner effect and separation in transonic channel flows," *Journal of Fluid Mechanics*, Vol. 679, may 2011, pp. 247–262.

[14] Benek, J. a., Suchyta, C. J., and Babinsky, H., "The Effect of Wind Tunnel Size on Incident Shock Boundary Layer Interaction Experiments," *51st AIAA Aerospace Sciences Meeting*, No. AIAA 2013-0862, 2013.

[15] Morajkar, R. R., Klomparens, R. L., Eagle, W. E., Driscoll, J. F., Gamba, M., and Benek, J. A., "Relationship Between Intermittent Separation and Vortex Structure in a 3D Shock Wave - Boundary Layer Interaction," *AIAA Journal*, Vol. 54, No. 6, 2016, pp. 1862–1880.

[16] Wagner, J. L., Yuceil, K. B., Valdivia, A., Clemens, N. T., and Dolling, D. S., "Experimental Investigation of Unstart in an Inlet/Isolator Model in Mach 5 Flow," *AIAA Journal*, Vol. 47, No. 6, 2009, pp. 1528–1542.

[17] Lapsa, A. P. and Dahm, W. J. A., "Stereo particle image velocimetry of nonequilibrium turbulence relaxation in a supersonic boundary layer," *Experiments in Fluids*, Vol. 50, No. 1, jun 2010, pp. 89–108.

[18] Ferri, A., "Experimental results with airfoils tested in the high-speed tunnel at Guidonia," *NACA Technical Reports*, Vol. 946, 1940.

[19] Green, J. E., "Reflexion of an oblique shock wave by a turbulent boundary layer," *Journal of Fluid Mechanics*, Vol. 40, 1970, pp. 81–95.

[20] Settles, G. S., Fitzpatrick, T. J., and Bogdonoff, S. M., "A Detailed Study of Attached and Separated Compression Corner Flowfields in High Reynolds Number Supersonic Flow," *AIAA 11th fluid and plasma dynamics conference*, 1978.

[21] Chapman, D. R., Kuehn, D. M., and Larson, H. K., "Investigation of separated flows in supersonic and subsonic streams with emphasis on the effect of transition," *NACA Technical Report 1356*, NACA, 1957, pp. 421–460.

[22] Adamson, T. C. and Messiter, A. F., "ANALYSIS OF TWO- DIMENSIONAL INTERACTIONS BETWEEN SHOCK WAVES AND BOUNDARY LAYERS," *Annu. Rev. Fluid Mech.*, Vol. 12, No. 1939, 1980, pp. 103–138.

[23] Korkegi, R. H., "Comparison of Shock-Induced Two- and Three-Dimensional Incipient Turbulent Separation," *AIAA Journal*, Vol. 13, No. 4, 1974.

[24] Zheltovodov, A. A., "Shock waves / turbulent boundary-layer interactions - Fundamental studies and applications," *AIAA, Fluid Dynamics Conference, 27th*, No. June, New Orleans, LA, 1996.

[25] Dolling, D. S. and Clemens, N. T., "Experimental Study of the Structure of Shock-Induced Turbulent Separated Flow and Its Role in Flowfield Unsteadiness," Tech. Rep. 0704, 2002.

[26] Délery, J. and Dussauge, J.-P., "Some physical aspects of shock wave/boundary layer interactions," *Shock Waves*, Vol. 19, No. 6, jul 2009, pp. 453–468.

[27] Babinsky, H. and Harvey, John, K., *Shock Wave-Boundary-Layer Interactions*, Cambridge University Press, 2011.

[28] Dolling, D. S., "Fifty Years of Shock-Wave/Boundary-Layer Interaction Research: What Next?" *AIAA Journal*, Vol. 39, No. 8, aug 2001, pp. 1517–1531.

[29] Clemens, N. T. and Narayanaswamy, V., "Low-Frequency Unsteadiness of Shock Wave/Turbulent Boundary Layer Interactions," *Annual Review of Fluid Mechanics*, Vol. 46, No. 1, jan 2014, pp. 469–492.

[30] Settles, G. S., Vas, I. E., and Bogdonoff, S. M., "Details of a Shock-Separated Turbulent Boundary Layer at a Compression Corner," *AIAA Journal*, Vol. 14, No. 12, 1976, pp. 1709–1715.

[31] Bookey, P., Wyckham, C., Smits, A., and Martin, P., "New Experimental Data of STBLI at DNS/LES Accessible Reynolds Numbers," *43rd AIAA Aerospace Sciences Meeting and Exhibit*, No. January, 2005, pp. 1–18.

[32] Wu, M. and Martin, M., "Direct Numerical Simulation of Supersonic Turbulent Boundary Layer over a Compression Ramp," *AIAA Journal*, Vol. 45, No. 4, 2007, pp. 879–889.

[33] Priebe, S. and Martín, M. P., "Low-frequency unsteadiness in shock waveturbulent boundary layer interaction," *Journal of Fluid Mechanics*, Vol. 699, 2012, pp. 1–49.

[34] Hankey, W. L. J. and Holden, M. S., "Two-dimensional shockwave boundary layer interactions in high-speed flows," *AGARDograph*, Vol. 203, 1975.

[35] Délery, J. M., Marvin, J. G., and Reshotko, E., "Shock-wave boundary layer interactions," *AGARDograph*, Vol. 280, 1986.

[36] Lu, F. K., "Quasiconical free interaction between a swept shock and a turbulent boundary layer," *AIAA Journal*, Vol. 31, No. 4, apr 1993, pp. 686–692.

[37] Panaras, A. G., "The effect of the structure of swept-shock-wave/turbulent-boundary-layer interactions on turbulence modelling," *Journal of Fluid Mechanics*, Vol. 338, may 1997, pp. 203–230.

[38] Knight, D. D., Horstman, C., Bogdonoff, S., and Shapey, B., "Structure of supersonic turbulent flow past a sharp fin," *AIAA Journal*, Vol. 25, No. 10, oct 1987, pp. 1331–1337.

[39] Dou, H.-s., Khoo, B. C., Yeo, K. S., and Laboratories, T., "Incipient Separation in Shock Wave / Boundary Layer Interactions as Induced by Sharp Fin," *Physics of Fluids*, 2008, pp. 1–28.

[40] Korkegi, R. H., "A Simple Correlation for Incipient Turbulent Boundary-Layer Separation due to a Skewed Shock Wave," *AIAA Journal*, Vol. 11, No. 11, 1973, pp. 1578–1579.

[41] Dann, A. G. and Morgan, R. G., "Analytical Method of Prediction of Turbulent Boundary-Layer Separation in Hypersonic Flows," *AIAA Journal*, Vol. 49, No. 9, 2011, pp. 2068–2072.

[42] Bogdonoff, S., *Preliminary investigations of spiked bodies at hypersonic speeds*, Ph.d. thesis, Princeton University, 1955.

[43] Kistler, A. L., "Fluctuating Wall Pressure under a Separated Supersonic Flow," *The Journal of Acoustical Society of America*, Vol. 36, No. 3, 1963, pp. 543–550.

[44] Dolling, D. S. and Or, C. T., "Experiments inFluids ©," *Experiments in Fluids*, Vol. 3, No. 1, 1985, pp. 24–32.

[45] Beresh, S. J., Clemens, N. T., and Dolling, D. S., "Relationship Between Upstream Turbulent Boundary-Layer Velocity Fluctuations and Separation Shock Unsteadiness," *AIAA Journal*, Vol. 40, No. 12, dec 2002, pp. 2412–2422.

[46] Ganapathisubramani, B., Clemens, N. T., and Dolling, D. S., "Effects of upstream boundary layer on the unsteadiness of shock-induced separation," *Journal of Fluid Mechanics*, Vol. 585, No. 2007, 2007, pp. 369–394.

[47] Erengil, M. E., Dollingt, D. S., and Dolling, D. S., "Unsteady Wave Structure near Separation in a Mach 5 Compression Ramp Interaction," *AIAA Journal*, Vol. 29, No. 5, 1990, pp. 728–735.

[48] Touber, E. and Sandham, N. D., "Large-eddy simulation of low-frequency unsteadiness in a turbulent shock-induced separation bubble," *Theoretical and Computational Fluid Dynamics*, Vol. 23, No. 2, 2009, pp. 79–107.

[49] Hadjadj, B. A., Larsson, J., Morgan, B. E., Nichols, J. W., and Lele, S. K., "Large-eddy simulation of shock / boundary-layer interaction," *Center for Turbulence Research, Proceedings of the Summer Program 2010*, 2010.

[50] Dupont, P., Haddad, C., and Debiève, J. F., "Space and time organization in a shock-induced separated boundary layer," *Journal of Fluid Mechanics*, Vol. 559, jul 2006, pp. 255.

[51] Piponniau, S., Dussauge, J. P., Debiève, J. F., and Dupont, P., "A simple model for low-frequency unsteadiness in shock-induced separation," *Journal of Fluid Mechanics*, Vol. 629, jun 2009, pp. 87–108.

[52] Souverein, L. J., Dupont, P., Debiève, J.-F., Van Oudheusden, B. W., and Scarano, F., "Effect of Interaction Strength on Unsteadiness in Shock-Wave-Induced Separations," *AIAA Journal*, Vol. 48, No. 7, jul 2010, pp. 1480–1493.

[53] Gessner, F. B., Eppich, H. M., and Lund, E. G., "Reynolds Number effects on near wall structure of turbulent flow along a streamwise corner," *Near-Wall Turbulent Flows*, 1993, pp. 965–975.

[54] Reda, D. C. and Murphy, J. D., "Sidewall Boundary-Layer Influence on Shock Wave / Turbulent Boundary-Layer Interactions," *AIAA Journal*, Vol. 11, No. 10, 1973, pp. 1367–1368.

[55] Bruce, P. J. K. and Babinsky, H., "An experimental study into the flow physics of three-dimensional shock control bumps," *49th AIAA Aerospace Sciences Meeting*, No. January, 2011, pp. 1–17.

[56] Burton, D. M. F. and Babinsky, H., "Corner separation effects for normal shock wave/turbulent boundary layer interactions in rectangular channels," *Journal of Fluid Mechanics*, Vol. 707, aug 2012, pp. 287–306.

[57] Eagle, W. E., Driscoll, J. F., and Benek, J. A., "Experimental Investigation of Corner Flows in Rectangular Supersonic Inlets with 3D Shock-Boundary Layer Effects," *49th AIAA Aerospace Sciences Meeting including the New Horizons Forum and Aerospace Exposition*, No. January, American Institute of Aeronautics and Astronautics, Orlando, Florida, 2011, pp. AIAA 2011–857.

[58] Benek, J. A., Suchyta, C. J., and Babinsky, H., "The Effect of Wind Tunnel Size and Shock Strength on Incident Shock Boundary Layer Interaction Experiments," *44th AIAA Fluid Dynamics Conference, AIAA Aviation*, 2014, pp. AIAA Paper No. 2014–3336.

[59] Helmer, D. B., Campo, L. M., and Eaton, J. K., "Three-dimensional features of a Mach 2.1 shock/boundary layer interaction," *Experiments in Fluids*, Vol. 53, No. 5, aug 2012, pp. 1347–1368.

[60] Morgan, B., Kawai, S., and Lele, S. K., "A Parametric Investigation of Oblique Shockwave / Turbulent Boundary Layer Interaction Using LES," *41st AIAA Fluid Dynamics Conference and Exhibit*, No. June, AIAA, Honolulu, Hawaii, 2011, pp. 1–19.

[61] Morgan, B., Duraisamy, K., Nguyen, N., Kawai, S., and Lele, S. K., "Flow physics and RANS modelling of oblique shock/turbulent boundary layer interaction," *Journal of Fluid Mechanics*, Vol. 729, jul 2013, pp. 231–284.

[62] Bermejo-Moreno, I., Larsson, J., Campo, L., Bodart, J., Vicquelin, R., Helmer, D. B., and Eaton, J. K., "Wall-modeled large eddy simulation of shock / turbulent boundary-layer interaction in a duct," *Center for Turbulence Research Annual Research Briefs*, 2011, pp. 49–62.

[63] Doerffer, P. and Dallmannt, U., "Reynolds Number Effect on Separation Structures at Normal Shock Wave/Turbulent Boundary-Layer Interaction," *AIAA Journal*, Vol. 27, No. 9, 1988, pp. 1206–1213.

[64] Eagle, W. E., Driscoll, J. F., and Benek, J. A., "3-D Inlet Shock-Boundary Layer Interactions - PIV Database for the Second SBLI Workshop," *30th AIAA Applied Aerodynamics Conference*, No. June, American Institute of Aeronautics and Astronautics, New Orleans, LA, 2012.

[65] Cresci, R. J., Rubin, S. G., Nardo, C. T., and Lin, T. C., "Hypersonic Interaction along a Rectangular Corner," *AIAA Journal*, Vol. 7, No. 12, 1969, pp. 2241–2247.

[66] Doerffer, P. and Dallmann, U., "Reynolds Number Effect on Separation Structures at Normal Shock Wave/Turbulent Boundary-Layer Interaction," *AIAA Journal*, Vol. 27, No. 9, 1988, pp. 1206–1213.

[67] Morris, M. J., Sajben, M., and Kroutilj, J. C., "Experimental Investigation of Normal-Shock/Turbulent-Boundary-Layer Interactions with and without Mass Removal," *AIAA Journalnal*, Vol. 30, No. 2, 1992.

[68] K. Bruce, P. J., Babinsky, H., Tartinville, B., and Hirsch, C., "Corner Effect and Asymmetry in Transonic Channel Flows," *AIAA Journal*, Vol. 49, No. 11, nov 2011, pp. 2382–2392.

[69] Eagle, W. E., Driscoll, J., and Benek, J., "3-D Inlet Shock-Boundary Layer Interactions - PIV Database for the Second SBLI Workshop," *30th AIAA Applied Aerodynamics Conference*, New Orleans, LA, 2012, pp. AIAA 2012–3214.

[70] Ridha, A., "Flow along streamwise corners revisited," *Journal of Fluid Mechanics*, Vol. 476, mar 2003, pp. 223–265.

[71] Rubin, S. G., "Incompressible flow along a corner," *Journal of Fluid Mechanics*, Vol. 26, No. 01, mar 1966, pp. 97.

[72] Bradshaw, P., "Turbulent Secondary Flows," *Annual Review of Fluid Mechanics*, Vol. 19, No. 1, jan 1987, pp. 53–74.

[73] Gessner, F. B., "The origin of secondary flow in turbulent flow along a corner," *Journal of Fluid Mechanics*, Vol. 58, No. 1, 1972, pp. 1–25.

[74] Perkins, H. J., "The formation of streamwise vorticity in turbulent flow," *Journal of Fluid Mechanics*, Vol. 44, No. 4, 1970, pp. 721–740.

[75] Brundrett, E. and Baines, W. D., "The production and diffusion of vorticity in duct flow," *Journal of Fluid Mechanics*, Vol. 19, No. 3, 1963, pp. 375– 394.

[76] Kornilov, V. I. and Kharitonov, a. M., "Investigation of the structure of turbulent flows in streamwise asymmetric corner configurations," *Experiments in Fluids*, Vol. 2, No. 4, 1984, pp. 205–212.

[77] Alizard, F., Robinet, J.-C., and Rist, U., "Sensitivity analysis of a streamwise corner flow," *Physics of Fluids*, Vol. 22, No. 1, 2010, pp. 014103.

[78] Zamir, M., "Similarity and stability of the laminar boundary layer in a streamwise corner," *Proceedings of the Royal Society: Mathematical, Physical and Engineering Sciences*, Vol. 377, 1981, pp. 269–288.

[79] Balachandar, S. and Malik, M. R., "Inviscid instability of streamwise corner flow," *Journal of Fluid Mechanics*, Vol. 282, apr 2006, pp. 187–201.

[80] Kornilov, V. I., "Correlation of the separation region length in shock wave / channel boundary layer interaction," *Experiments in Fluids*, Vol. 23, No. 6, 1997, pp. 489–497.

[81] Park, D. H., Park, S. O., Kwon, K. J., and Shim, H. J., "Particle Image Velocimetry Measurement of Laminar Boundary Layer in a Streamwise Corner," *AIAA Journal*, Vol. 50, No. 4, apr 2012, pp. 811–817.

[82] Uruba, V., Hladík, O., and Jonáš, P., "Dynamics of Secondary flow in rectangular channel," *Colloquium FLUID DYNAMICS 2011, Institute of Thermomechanics AS CR*, Prague, 2011, pp. 1–7.

[83] Melling, A., "Tracer particles and seeding for particle image velocimetry," *Measurement Science and Technology*, Vol. 8, No. 12, 1997, pp. 1406–1416.

[84] Scarano, F., "Overview of PIV in supersonic flows," *Particle Image Velocimetry: New Developments and Recent Applications*, Vol. 112, 2008, pp. 445–463.

[85] Zucrow, M. J. and Hoffman, J. D., *Gas Dynamics*, John Wiley & Sons, 1976.

[86] Adrian, R. J., "Particle-image techniques for experimental fluid mechanics," *Annual Review of Fluid Mechanics*, Vol. 23, 1991, pp. 261–304.

[87] Adrian, R. J., Christensen, K. T., and Liu, Z., "Analysis and interpretation of instantaneous turbulent velocity fields," *Experiments in Fluids*, Vol. 29, No. 95, 2000, pp. 275–290.

[88] Nogueira, J., Lecuona, A., and Rodriguez, P. A., "Data validation , false vectors correction and derived magnitudes calculation on PIV data," *Measurement Science and Technology*, Vol. 8, 1997, pp. 1493–1501.

[89] D'Errico, J., "inpaint_nans (Interpolation function)," *Matlab Central File Exchange*, Vol. https://ww.

[90] Moisy, F., "PIVMAT toolbox," .

[91] Whittaker, E., "On a new method of graduation," *Proceedings of the Edinburgh Mathematical Society 41*, 1923, pp. 62–75.

[92] Garcia, D., "Robust smoothing of gridded data in one and higher dimensions with missing values," *Computational Statistics & Data Analysis*, Vol. 54, No. 4, apr 2010, pp. 1167–1178.

[93] Garcia, D., "A fast all-in-one method for automated post-processing of PIV data," *Experiments in Fluids*, Vol. 50, No. 5, 2011, pp. 1247–1259.

[94] McKeon, B. J. and Smits, A. J., "Static pressure correction in high Reynolds number fully developed turbulent pipe flow," *Measurement Science and Technology*, Vol. 13, No. 10, oct 2002, pp. 1608–1614.

[95] Chue, S., "Pressure probes for fluid measurement," *Progress in Aerospace Sciences*, Vol. 16, No. 2, jan 1975, pp. 147–223.

[96] Shaw, R., "The influence of hole dimensions on static pressure measurements," *Journal of Fluid Mechanics*, Vol. 7, No. 04, 1960, pp. 550.

[97] Klomparens, R. L., Driscoll, J. F., and Gamba, M., "Response of a shock train to downstream back pressure forcing," *AIAA SciTech 2016*, AIAA, San Diego, California, USA, 2016.

[98] Morajkar, R., Klomparens, R., Eagle, E., Driscoll, J., and Gamba, M., "Flow Separation Associated with 3 - D Shock - Boundary Layer Interaction (SBLI)," *AIAA SciTech 2014*, American Institute of Aeronautics and Astronautics, Harbor Town, 2014, pp. AIAA Paper 2014–1138.

[99] Morajkar, R. R. and Gamba, M., "Swept shock/corner flow interacions," *54th AIAA Aerospace Sciences Meeting, SciTech 2016*, No. AIAA 2016-1165, San Diego, Ca, 2016, pp. AIAA 2016–1165.

[100] Ronald L. Panton, "Incompressible Flow," 2013.

[101] Chakraborty, P., Balachandar, S., and Adrian, R. J., "On the relationships between local vortex identification schemes," *Journal of Fluid Mechanics*, Vol. 535, jul 2005, pp. 189–214.

[102] Graftieaux, L., Michard, M., and Grosjean, N., "Combining PIV, POD and vortex identification algorithms for the study of unsteady turbulent swirling flows," *Measurement Science and Technology*, Vol. 12, No. 9, sep 2001, pp. 1422–1429.

[103] Jeong, J. and Hussain, F., "On the identification of a vortex," *Journal of Fluid Mechanics*, Vol. 285, 1995, pp. 69–94.

[104] Horiuti, K. and Takagi, Y., "Identification method for vortex sheet structures in turbulent flows," *Physics of Fluids*, Vol. 17, No. 12, 2005, pp. 1–4.

[105] Lapsa, A. P., *Experimental Study of Passive Ramps for Control of Shock Boundary Layer Interactions by*, Ph.D. thesis, University of Michigan, 2009.

[106] Sebacher, D. I. and Lee, L. P., "Crossflow in Two-Dimensional Asymmetric Nozzles," *NASA Technical Note*, Vol. TN D-7999, 1975.

[107] Wang, B., Sandham, N., Hu, Z., and Liu, W., "Numerical study of oblique shock-wave/boundary-layer interaction considering sidewall effects," *Journal of Fluid Mechanics*, Vol. 767, feb 2015, pp. 526–561.

[108] Lu, F. K., Pierce, A. J., Shih, Y., Liu, C., and Li, Q., "Experimental and Numerical Study of Flow Topology Past Micro Vortex Generators," *AIAA 40th Fluid Dynamics Conference and Exhibit*, No. July, Chicago, Illinois, 2010, pp. 1–13.

[109] Mccormick, D. C., "Shock/boundary-layer interaction control with vortex generators and passive cavity," *AIAA Journal*, Vol. 31, No. 1, jan 1993, pp. 91–96.

[110] Zudov, V. N. and Pimonov, E. A., "Interaction of a Streamwise Vortex with an Oblique Shock Wave," *Journal of Applied Mechanics and Technical Physics*, Vol. 44, No. 4, 2003, pp. 461–470.

[111] Wang, K. C., "Separation Patterns of Boundary Layer over an Inclined Body of Revolution," *AIAA Journal*, Vol. 10, No. 8, aug 1972, pp. 1044–1050.

[112] Wang, K. C. and Diego, S., "On the Disputes About Open Separation," *AIAA 21st Aerospace Sciences Meeting*, AIAA, Reno, Nevada, 1983.

[113] Tobak, M. and Peake, D. J., "Topology of three-dimensional separated flows," *Annual Review of Fluid Mechanics*, Vol. 14, 1982, pp. 61–85.

[114] Wu, J. Z., Tramel, R. W., Zhu, F. L., and Yin, X. Y., "A vorticity dynamics theory of three-dimensional flow separation," *Physics of Fluids*, Vol. 12, No. 8, 2000, pp. 1932–1954.

[115] Eagle, W. E., *An Experimental Study of Three-Dimensional Inlet Shock-Boundary Layer Interactions*, Ph.d. thesis, University of Michigan, Ann Arbor, 2012.

[116] Tropea, C. and Martinuzzi, R., "The Flow Around Surface- Mounted , Prismatic Obstacles Placed in a Fully Developed Channel Flow," *Journal of Fluids Engineering*, Vol. 115, No. 1, 1993, pp. 85–92.

[117] Chou, J. H. and Chao, S. Y., "Branching of a horseshoe vortex around surface-mounted rectangular cylinders," *Experiments in Fluids*, Vol. 28, No. 5, may 2000, pp. 394–402.

[118] Bermejo-Moreno, I., Campo, L., Larsson, J., Bodart, J., Helmer, D., and Eaton, J., "Confinement effects in shock wave/turbulent boundary layer interactions through wall-modelled large-eddy simulations," *Journal of Fluid Mechanics*, Vol. 758, oct 2014, pp. 5–62.

[119] Spina E., Smits A., R. S., "The physics of supersonic turbulent boundary layers," *Annual Review of Fluid Mechanics*, Vol. 26, 1994, pp. 287–319.

[120] Morajkar, R. R., Driscoll, J. F., and Gamba, M., "Experimental study of supersonic turbulent corner flow evolution in a low aspect ratio rectangular channel," *AIAA SciTech 2015*, No. AIAA Paper 2015-0542, Kissimmee, Fl, 2015, pp. AIAA Paper 2015–0542.

[121] Chow, J., Zilliac, G., and Bradshaw, P., "Mean and Turbulence measurements in the near field of a wingtip vortex," *AIAA Journal*, Vol. 35, No. 10, 1997, pp. 1561–1567.

[122] Bernard, P. S., "Vortex Dynamics in Transitional and Turbulent Boundary Layers," *50th AIAA Aerospace Sciences Meeting*, No. January, Nashville, Tennessee, 2012, pp. 1–26.

[123] Igarashi, H., Durbin, P. A., Hu, H., Waltermire, S., and Wehrmeyer, J., "The Effects of Wind Tunnel Walls on the Near-field Behavior of a Wingtip Vortex," *49th AIAA Aerospace Sciences Meeting*, Vol. AIAA 2011-, Orlando, Florida, 2011.

[124] Mehdi, F. and White, C. M., "Integral form of the skin friction coefficient suitable for experimental data," *Experiments in Fluids*, Vol. 50, No. 1, may 2010, pp. 43–51.

[125] Spina, E. F., Smits, A. J., and Robinson, S. K., "THE PHYSICS OF SUPERSONIC TURBULENT BOUNDARY LAYERS," *Annual Review of Fluid Mechanics*, Vol. 26, 1994, pp. 287–319.

[126] Shabaka, I. M. M. A., Mehta, R. D., and Bradshaw, P., "Longitudinal vortices imbedded in turbulent boundary layers . Part 1 . Single vortex," *Journal of Fluid Mechanics*, Vol. 155, 1985, pp. 37–57.

[127] Spalart, P. R., "Direct Simulation of a Turbulent Boundary Layer up to Re = 1410," *Journal of Fluid Mechanics*, Vol. 187, 1988, pp. 61–98.

[128] Lumley, J. L., "Computational modeling of turbulent flows," *Advances in applied mechanics*, Vol. 18, 1979, pp. 123–176.

[129] Banerjee, S., Krahl, R., Durst, F., and Zenger, C., "Presentation of anisotropy properties of turbulence, invariants versus eigenvalue approaches," *Journal of Turbulence*, Vol. 8, No. March 2015, 2007, pp. N32.

[130] Emory, B. M. and Iaccarino, G., "Visualizing turbulence anisotropy in the spatial domain with componentality contours," *Center for Turbulence Research Annual Research Briefs*, 2014, pp. 123–137.

[131] Sarpkaya, T., "Effect of the Adverse Pressure Gradient on Vortex Breakdown," *AIAA Journal*, Vol. 12, No. 5, 1974, pp. 602–607.

[132] Mehta, R. D. and Bradshaw, P., "Longitudinal vortices imbedded in turbulent boundary layers Part 2. Vortex pair with 'common flow' upwards," *Journal of Fluid Mechanics*, Vol. 188, 1988, pp. 529–546.

[133] Sartor, F., Losfeld, G., and Bur, R., "PIV study on a shock-induced separation in a transonic flow," *Experiments in Fluids*, Vol. 53, No. 3, jun 2012, pp. 815–827.

[134] Hu, H., Saga, T., Kobayashi, T., Taniguchi, N., and Yasuki, M., "Dual-plane stereoscopic particle image velocimetry: System set-up and its application on a lobed jet mixing flow," *Experiments in Fluids*, Vol. 31, No. 3, 2001, pp. 277–293.

[135] Scarano, F., "Tomographic PIV: principles and practice," *Measurement Science and Technology*, Vol. 24, No. 1, 2012, pp. 012001.

[136] Elsinga, G. E., Oudheusden, B. W., and Scarano, F., "Evaluation of aero-optical distortion effects in PIV," *Experiments in Fluids*, Vol. 39, No. 2, 2005, pp. 246–256.

[137] Samimy, M. and Lele, S. K., "Motion of particles with inertia in a compressible free shear layer," *Physics of Fluids*, Vol. 3, No. 8, 1991, pp. 1915.

[138] Adrian, R. J. and Westerweel, J., *Particle Image Velocimetry*, Cambridge University Press, 2010.

[139] Christensen, K. T., "The influence of peak-locking errors on turbulence statistics computed from PIV ensembles," *Experiments in Fluids*, Vol. 36, No. 3, 2004, pp. 484–497.

[140] Lawson, N. J. and Wu, J., "Three-dimensional particle image velocimetry : error analysis of stereoscopic techniques," *Measurement Science and Technology*, Vol. 8, No. 8, 1997, pp. 894.

[141] Lawson, N. J. and Wu, J., "Three-dimensional particle image velocimetry : experimental error analysis of a digital angular stereoscopic system," *Measurement Science and Technology*, Vol. 8, No. 12, 1997, pp. 1455.

[142] Prasad, A. K., "Stereoscopic particle image velocimetry," *Experiments in Fluids*, Vol. 29, No. February, 2000, pp. 103–116.

[143] Zang, W. and Prasad, A. K., "Performance evaluation of a Scheimpflug stereocamera for particle image velocimetry," *Applied Optics*, Vol. 36, No. 33, 1997, pp. 8738–8744.

[144] Gurka, R., Liberzon, A., and Hetsroni, G., "POD of vorticity fields: A method for spatial characterization of coherent structures," *International Journal of Heat and Fluid Flow*, Vol. 27, No. 3, 2006, pp. 416–423.